

# Electron Spin Resonance Investigations on Organic Spin Liquid Compounds

Von der Fakultät Mathematik und Physik der Universität Stuttgart  
zur Erlangung der Würde eines Doktors  
der Naturwissenschaften (Dr. rer. nat.) genehmigte Abhandlung

vorgelegt von

**BJÖRN A. MIKSCH**  
geboren in Ludwigsburg

Hauptberichter: Prof. Dr. Martin Dressel  
Mitberichter: Prof. Dr. Gert Denninger

Tag der mündlichen Prüfung: 28.01.2022  
Prüfungsvorsitzende: Prof. Dr. Maria Daghofer

1. Physikalisches Institut der Universität Stuttgart

2022



# Contents

*Symbols and Abbreviations* • vii

*Introduction and Outline* • xi

*Zusammenfassung* • xv

*Publications* • xix

## 1 *Magnetism in Solids* • 1

- 1.1 Types of Magnetism • 1
  - 1.1.1 Diamagnetism • 2
  - 1.1.2 Paramagnetism • 3
  - 1.1.3 Magnetism in Metals • 4
  - 1.1.4 Exchange Interaction • 4
  - 1.1.5 Magnetic Order • 5
- 1.2 Correlated Electron Systems • 7
- 1.3 Geometrical Frustration • 11
- 1.4 Frustrated Magnets • 12
  - 1.4.1 Spin Liquids • 13
  - 1.4.2 Valence Bond States • 14
  - 1.4.3 Effects of Disorder and Anisotropy • 16
  - 1.4.4 Quantum Spin Liquid Models • 17
  - 1.4.5 Spin Models on Other Lattices • 21

## 2 *Electron Spin Resonance* • 23

- 2.1 ESR in  $S = 1/2$  Systems • 24
- 2.2 Basics of ESR: Bloch Equations • 27
- 2.3 Parameters of ESR Spectra • 31
  - 2.3.1 Fitting ESR Spectra • 34
- 2.4 Conventional ESR Spectrometers • 35
  - 2.4.1 Technical Details • 38

2.5	ESR using Coplanar Waveguides • 39
2.5.1	Frequency-Domain ESR • 42
2.5.2	Coplanar Waveguide Resonators • 52
2.6	Magnetic Field Calibration • 58
3	<i>Materials</i> • 61
3.1	Organic Conductors • 61
3.1.1	Quasi Two-Dimensional Organic Conductors: $\text{ET}_2\text{X}$ • 63
3.1.2	Properties of the $\kappa\text{-ET}_2\text{X}$ Family • 64
3.2	Frustrated Magnetism in $\kappa\text{-ET}_2\text{X}$ • 66
3.2.1	The archetypical quantum spin liquid: $\kappa\text{-ET}_2\text{Cu}_2(\text{CN})_3$ • 66
3.2.2	Introducing Pressure and Disorder: $\kappa\text{-}[\text{ET}_{1-x}\text{STF}_x]_2\text{Cu}_2(\text{CN})_3$ • 74
3.2.3	Deeper in the Mott Insulating State: $\kappa\text{-ET}_2\text{Ag}_2(\text{CN})_3$ • 77
3.3	Studied Samples • 79
4	<i>Gapped Magnetic Ground State in <math>\kappa\text{-ET}_2\text{Cu}_2(\text{CN})_3</math></i> • 81
4.1	ESR Parameters • 83
4.2	Spin Gap • 91
4.2.1	Modelling the Susceptibility • 91
4.2.2	Possible Ground States • 94
4.3	Low-Temperature Contributions • 96
4.3.1	$\text{Cu}^{2+}$ Impurities • 97
4.3.2	Structural Twinning • 98
4.3.3	Defect Signal Contribution • 99
4.3.4	Coupling of Defect Spins to $\text{Cu}^{2+}$ • 104
4.4	Frequency-Dependent Behaviour • 106
4.4.1	Defect Signal • 108
4.4.2	Remaining Signal at $B_{\text{main}}$ • 110
4.5	Low-Temperature Magnetic State • 112
4.5.1	Compatibility to Existing Data • 113
5	<i>ESR on Related <math>\kappa\text{-ET}_2\text{X}</math> Compounds</i> • 117
5.1	Properties of Chemically Substituted $\kappa\text{-}[\text{ET}_{1-x}\text{STF}_x]_2\text{Cu}_2(\text{CN})_3$ • 118
5.1.1	Room Temperature Behaviour • 119
5.1.2	ESR Parameters • 120
5.1.3	Discussion • 125
5.1.4	Conclusions • 127

5.2 Quantum Spin Liquid Candidate  $\kappa$ -ET<sub>2</sub>Ag<sub>2</sub>(CN)<sub>3</sub> • 129

5.2.1 ESR Parameters • 129

5.2.2 Conclusions for the Ground State • 132

6 *Conclusion* • 133

*List of Figures* • 137

*References* • 141



# Symbols and Abbreviations

Listed below are symbols and abbreviations commonly used throughout this thesis.

## SYMBOLS

Symbol	Meaning
$B$	magnetic field, more precise: magnetic flux density
$B_0$	external static magnetic field; in ESR experiments responsible for Zeeman splitting
$B_1$	microwave magnetic field; induces the magnetic transitions in ESR experiments
$B_{\text{res}}$	resonance field in ESR experiments
$c$	speed of light in vacuum, defined value <sup>1</sup> : $2.997\,924\,58 \times 10^8$ m/s
$C$	Curie constant; material property relating magnetic susceptibility to temperature
$e$	elementary charge; defined value <sup>1</sup> : $1.602\,176\,634 \times 10^{-19}$ C
$f_0$	microwave frequency, resonance frequency of the cavity
$f_B$	frequency bandwidth of the microwave cavity
$g, \mathbf{g}$	$g$ -factor, and tensor, relating the magnetic moment to the angular momentum quantum number
$g_e$	spin $g$ -factor for the free electron; value <sup>1</sup> : $-2.002\,319\,304\,362\,56(35)$
$h, \hbar$	Planck constant; defined value <sup>1</sup> : $6.626\,070\,15 \times 10^{-34}$ Js , reduced Planck constant $\hbar = h/(2\pi)$
$H$	magnetic field strength
$J$	exchange coupling
$J, L, S$	total, orbital, and spin angular momentum operator
$k_B$	Boltzmann constant relating temperature and energy; defined value <sup>1</sup> : $1.380\,649 \times 10^{-23}$ J/K
$M$	magnetisation
$m_e$	electron rest mass; value <sup>1</sup> : $9.109\,383\,701\,5(28) \times 10^{-31}$ kg

Symbol	Meaning
$m_{J,L,S}$	projection quantum numbers for total, orbital and spin angular momentum
$t$	transfer integral within the Hubbard model
$T_C$	Curie temperature; ferromagnetic ordering temperature
$T_N$	Néel temperature; antiferromagnetic ordering temperature
$U$	Coulomb repulsion within the Hubbard model
$\gamma$	molecular field constant
$\Theta$	paramagnetic Curie temperature
$\mu$	magnetic moment
$\mu_0$	vacuum permeability, value <sup>1</sup> : $4\pi \times 1.000\,000\,000\,55(15) \times 10^{-7}$ N/A <sup>2</sup>
$\mu_B$	Bohr magneton, value <sup>1</sup> : $9.274\,009\,994(57) \times 10^{-24}$ J/T
$\chi$	volume magnetic susceptibility

<sup>1</sup><sub>2018</sub> CODATA recommended values.

#### ABBREVIATIONS

Abbreviation	Meaning
$\mu$ SR	muon spin rotation
afm	antiferromagnetic
BEDT-STF	bis(ethylenedithio)diselenadithiafulvalene
BEDT-TTF	bis(ethylenedithio)tetrathiafulvalene
CPW	coplanar waveguide
DOS	density of states
DPPH	2,2-diphenyl-1-picrylhydrazyl
EPR	electron paramagnetic resonance
ESR	electron spin resonance
ET	→ BEDT-TTF
fm	ferromagnetic
NMR	nuclear magnetic resonance
QCP	quantum critical point
QSL	quantum spin liquid
RVB	resonating valence bond
SNR	signal-to-noise ratio
STF	→ BEDT-STF

Abbreviation	Meaning
TMTSF	tetramethyl-tetraselenafulvalene
TMTTF	tetramethyl-tetrathiafulvalene
VBG	valence bond glass
VBS	valence bond solid
VNA	vector network analyser
VTI	variable temperature insert
ZFS	zero field splitting

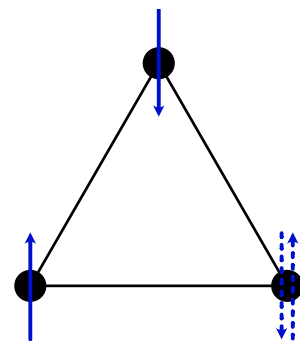


# Introduction and Outline

The search for the quantum spin liquid state – a nonmagnetic state hosted in a strongly interacting spin system – has been a research topic since Anderson’s proposal of the resonating valence bond (RVB) state in 1973 [1]. Various exotic states in interacting spin systems emerging from the interplay of quantum entanglement, geometrical frustration and disorder have been investigated theoretically as well as experimentally for many years.

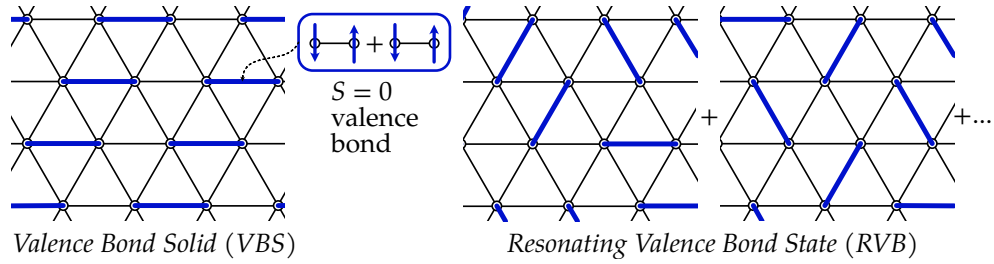
In a system with localised spins subject to exchange interaction, as thermal fluctuations decrease upon cooling, magnetic order eventually sets in below a certain temperature. The sign of the exchange interaction determines whether ferro- or antiferromagnetic ordering is preferred, i.e. whether the spins arrange parallel or antiparallel to one another. However, certain geometrical arrangements can lead to so-called frustrated spins. Competing exchange interactions which cannot be simultaneously satisfied increase the degeneracy of the ground state. The larger number of possible ground state configurations enhances fluctuations which may suppress long-range magnetic ordering.

A simple example – three Ising spins on an equilateral triangle subject to antiferromagnetic exchange – is shown on the right. In the ground state, two of the three spins, can be each in one of the two possible states, “up” or “down”, antiparallel to each other. The remaining one, however, will then always be parallel to one of the others. The result are six degenerate configurations as opposed to the two natural to the Ising symmetry. Extending this concept to a whole lattice leads to a large number of degenerate ground state configurations. Several frustrated lattice geometries with such properties exist in two as well as in three dimensions.



*Frustrated Ising Spins on an Equilateral Triangle*

The basic building block for a nonmagnetic ground state of a frustrated spin system are spin-singlet valence bonds formed by two spins due to the antiferromagnetic exchange interaction. In case an energetically favoured pattern of those valence bonds



exists, a valence bond solid (VBS) can be formed. If, however, many energetically degenerate valence bond patterns exist, a superposition state of those different partitionings of the lattice is a possible ground state. This RVB state is one realisation of a nonmagnetic ground state for a strongly interacting spin system on a frustrated lattice. In such a quantum spin liquid (QSL) ground state the spins are strongly entangled, but nevertheless quantum fluctuations are able to prevent the formation of magnetic order. One main interest in studying QSLs are fractionalised excitations, such as spinons, charge-neutral quasiparticles carrying a spin of  $S = 1/2$ .

In 2003 NMR measurements on the triangular lattice organic charge transfer compound  $\kappa$ -(BEDT-TTF) $_2$ Cu $_2$ (CN) $_3$  have shown no signs of magnetic order for all measured temperatures down to 32 mK [2]. This absence of classical magnetic order at temperatures orders of magnitude below the energy scale of the exchange interactions  $J \approx 250$  K has made the compound one of the prime candidates to host the elusive quantum spin liquid state as its ground state. A number of review articles on quantum spin liquids have paid particular attention to  $\kappa$ -ET $_2$ Cu $_2$ (CN) $_3$  when discussing experimental evidence [3–6]. The compound was over time considered as the textbook example of a quantum spin liquid material.

In spite of the large number of experimental studies since 2003, contradicting conclusions have been drawn and crucial open questions have remained unanswered: What exactly is the system’s magnetic ground state? In what way is magnetic order prevented? What is the nature of the anomalies observed at  $T^* = 6$  K? How does the spin excitation spectrum look like, in particular, is it gapped or not?

Studying the magnetic properties at temperatures below 1 K is challenging. Most of the applicable methods are susceptible to impurity spins. Bulk susceptibility measurements using magnetic torque [7] and SQUID magnetometer [2] cannot distinguish intrinsic from extrinsic contributions. Spectroscopic techniques such as NMR [2, 8, 9] and  $\mu$ SR [10] probe the electron spins indirectly through their interaction with the atomic nuclei respectively the implanted muons which also interact with impurity spins.

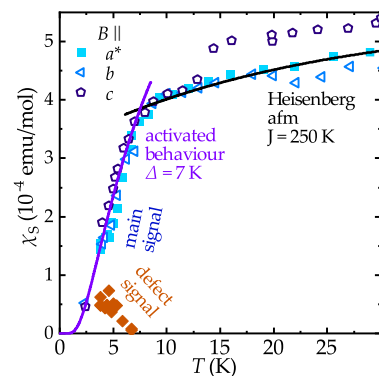
To overcome this issue and tackle the open questions, electron spin resonance (ESR) is the method of choice within this project allowing to directly probe the conduction electrons in  $\kappa\text{-ET}_2\text{Cu}_2(\text{CN})_3$ . The very high sensitivity of conventional instruments, however, comes with the price of a limited operable range in temperature and frequency, respectively magnetic field. A conventional ESR spectrometer employs a microwave cavity as a resonator to enhance the sensitivity. The resonance frequency of the cavity determines the single operational frequency of the instrument. Typical frequencies in the 10 GHz range enforce cavities with geometrical dimensions in the range of several 10 mm.

In order to overcome the restrictions, different techniques based on planar waveguides are employed. A capacitively coupled section of a coplanar waveguide (CPW) can act as a one-dimensional resonator allowing operation at its fundamental frequency as well as the linearly spaced higher harmonics. The one-dimensional nature also allows to fit the resonator in meander shape on compact substrates that fit inside the small operational volume of a  $^3\text{He}/^4\text{He}$  dilution refrigerator.

A novel broadband experimental setup enabling to record ESR spectra with microwave frequency sweeps instead of the commonly used magnetic field sweeps has been developed in the framework of this project [M1]. This enables to continuously explore the temperature/magnetic field phase space. The new setup employs magnetic field modulation and a phase sensitive detection scheme to achieve higher sensitivities compared to previous methods. The sensitivity and operational range of the method is demonstrated with measurements of different standard samples.

Combining measurements with conventional high sensitivity ESR spectrometers and employing the broadband techniques to reach mK temperatures and investigate the field- and frequency-dependence has emerged as a promising approach to investigate the low-temperature magnetic properties of  $\kappa\text{-ET}_2\text{Cu}_2(\text{CN})_3$ .

The results of the ESR experiments promote a ground state scenario for  $\kappa\text{-ET}_2\text{Cu}_2(\text{CN})_3$  that resolves long-standing controversies [M2]. As shown on the right, a rapid drop in the spin susceptibility of the main ESR signal can be identified below  $T^* = 6$  K indicating the opening of a spin gap. The observations are in good agreement with a ground state built from localised valence bonds. An additional “defect signal” in the ESR response starts to dominate when the spin-singlets are formed. Magnetic impurities and a certain amount of intrinsic



Spin Gap in  $\kappa\text{-ET}_2\text{Cu}_2(\text{CN})_3$

disorder lead to the formation of unpaired orphan spins within the otherwise nonmagnetic ground state. These are responsible for the observed defect ESR contribution and other low-temperature properties that have so far led to contradicting interpretations.

To extend the new insights on the low-temperature magnetic properties of  $\kappa\text{-ET}_2\text{Cu}_2(\text{CN})_3$  further into the insulating as well as the metallic side of the phase diagram, ESR measurements have been performed on related frustrated  $\kappa\text{-ET}_2X$  compounds. Applying positive chemical pressure through molecular substitution allows investigating a series of increasingly metallic compounds  $\kappa\text{-}[\text{ET}_{1-x}\text{STF}_x]_2\text{Cu}_2(\text{CN})_3$ . The sister compound  $\kappa\text{-ET}_2\text{Ag}_2(\text{CN})_3$  is instead subject to a stronger influence of electronic correlations. It is, thus, located deeper inside the Mott-insulating state.

## OUTLINE

In chapter 1 basic concepts are introduced to understand the nature of quantum spin liquids. The starting point are the different types of *magnetism in solids* including the peculiarities in correlated electron systems. Afterwards, the concepts of geometrical frustration and valence bond states are briefly explained. In the end, the effect of disorder and anisotropy onto quantum spin liquid states are discussed.

As *electron spin resonance* is the experimental method of choice within the project, the next chapter 2 focuses on the underlying physics as well as the technical aspects of ESR. In addition to the description of the workings of a conventional ESR spectrometer, measurements using coplanar waveguides are introduced including resonant measurements as well as the newly developed frequency-domain setup.

Subsequently, chapter 3 introduces the studied *materials*. First organic conductors are introduced in general followed by the specifics of quasi two-dimensional  $\kappa\text{-ET}_2X$  compounds. Published experimental results for the textbook example of a quantum spin liquid,  $\kappa\text{-ET}_2\text{Cu}_2(\text{CN})_3$ , are summarised followed by previous findings on the two related compounds: the substituted  $\kappa\text{-}[\text{ET}_{1-x}\text{STF}_x]_2\text{Cu}_2(\text{CN})_3$ , and the sister compound  $\kappa\text{-ET}_2\text{Ag}_2(\text{CN})_3$ .

Afterwards the results of the performed ESR experiments on  $\kappa\text{-ET}_2\text{Cu}_2(\text{CN})_3$  are presented and discussed within chapter 4. It is shown to host a *gapped magnetic ground state*. A scenario for the low-temperature magnetic state is proposed as a result of the experiments and finally its compatibility to existing data is discussed.

After that, chapter 5 presents the ESR results obtained for *related  $\kappa\text{-ET}_2X$  compounds*. This includes the substituted  $\kappa\text{-}[\text{ET}_{1-x}\text{STF}_x]_2\text{Cu}_2(\text{CN})_3$  as well as the sister compound  $\kappa\text{-ET}_2\text{Ag}_2(\text{CN})_3$ .

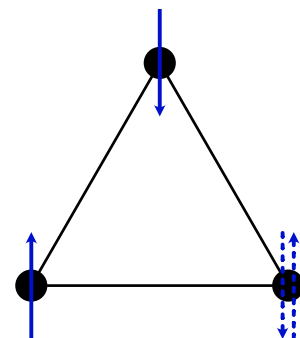
Final *conclusions* are drawn within chapter 6.

# Zusammenfassung

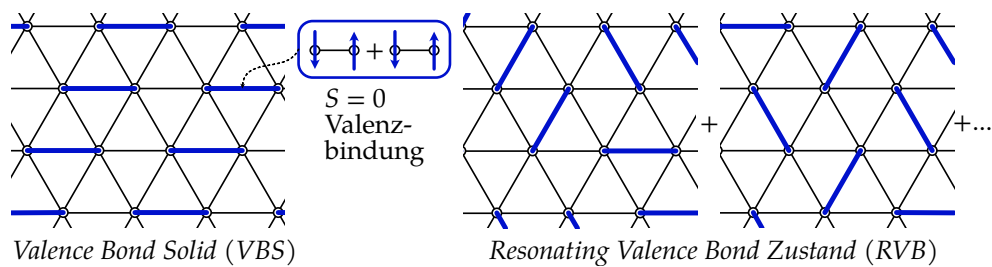
Die Suche nach einer Quantenspinflüssigkeit – einem nichtmagnetischen Zustand in einem stark wechselwirkenden Spinsystem – ist Forschungsgegenstand seit der Einführung des “resonating valence bond state” durch Anderson im Jahr 1973 [1]. Verschiedene exotische Zustände in wechselwirkenden Spinsystemen, die aus dem Zusammenspiel von Quantenverschränkung, geometrischer Frustration und Unordnung entstehen, werden seit vielen Jahren sowohl theoretisch als auch experimentell untersucht.

In einem System mit lokalisierten Spins, die einer Austauschwechselwirkung unterliegen, stellt sich beim Abkühlen unterhalb einer bestimmten Temperatur magnetische Ordnung ein, da die thermischen Fluktuationen abnehmen. Das Vorzeichen der Austauschwechselwirkung bestimmt dabei, ob eine ferro- oder antiferromagnetische Ordnung bevorzugt wird, d.h. ob sich die Spins parallel oder antiparallel zueinander anordnen. Bestimmte geometrische Anordnungen können jedoch zu sogenannten frustrierten Spins führen. Konkurrierende Austauschwechselwirkungen, die nicht gleichzeitig erfüllt werden können, erhöhen die Entartung des Grundzustandes. Die größere Anzahl möglicher Grundzustandskonfigurationen erhöht die Fluktuationen, was die magnetische Ordnung unterdrücken kann.

Ein einfaches Beispiel für geometrische Frustration, sind drei Ising-Spins auf einem gleichseitigen Dreieck, die einer antiferromagnetischen Austauschwechselwirkung unterliegen. Im Grundzustand können zwei der drei Spins jeweils einen der beiden möglichen Zustände einnehmen, nämlich nach “oben” oder “unten” zeigen, antiparallel zueinander. Der verbleibende Spin ist dann jedoch zwangsläufig parallel zu einem der Anderen ausgerichtet. Im Ergebnis erhält man sechs energetisch entartete Konfigurationen im Gegensatz zu den zwei, die aufgrund der Ising-Symmetrie zu erwarten sind. Erweitert man dieses Konzept auf ein ganzes Gitter, so ergibt sich eine große Anzahl entarteter Grundzustandskonfigurationen. Mehrere frustrierte



*Frustrierte Ising Spins  
auf einem gleichseitigen  
Dreieck*



Gittergeometrien mit diesen Eigenschaften existieren sowohl in zwei als auch in drei Dimensionen.

Der Grundbaustein für einen nichtmagnetischen Grundzustand eines frustrierten Spinsystems sind Spin-Singlet-Valenzbindungen, die von zwei Spins aufgrund der antiferromagnetischen Austauschwechselwirkung gebildet werden. Sofern eine bestimmte Partitionierung des Gitters mit Valenzbindungen energetisch begünstigt ist, kann sich ein "valence bond solid" (VBS) Zustand bilden. Gibt es jedoch viele energetisch entartete Partitionierungen, so ist ein Überlagerungszustand dieser ein möglicher Grundzustand. Dieser "resonating valence bond" (RVB) Zustand ist eine der möglichen Realisierungen eines nichtmagnetischen Grundzustands für ein stark wechselwirkendes Spinsystem auf einem frustrierten Gitter. In einem solchen Grundzustand einer Quantenspinflüssigkeit (QSL) sind die Spins quantenmechanisch verschränkt. Trotzdem können Quantenfluktuationen die Ausbildung magnetischer Ordnung verhindern. Ein Hauptinteresse bei der Untersuchung von QSLs gilt fraktionierten Anregungen wie Spinonen, ladungsneutralen Quasiteilchen mit einem Spin von  $S = 1/2$ .

Im Jahr 2003 haben NMR-Messungen an der organischen Ladungstransferverbindung  $\kappa$ -(BEDT-TTF)<sub>2</sub>Cu<sub>2</sub>(CN)<sub>3</sub> mit Dreiecksgitter für alle gemessenen Temperaturen bis hinunter zu 32 mK keinerlei Anzeichen einer magnetische Ordnung gezeigt [2]. Das Ausbleiben einer klassischen magnetischen Ordnung bei Temperaturen, die um Größenordnungen unterhalb der Energieskala der Austauschwechselwirkungen  $J \approx 250$  K liegen, hat die Verbindung zu einem der Hauptkandidaten gemacht, die als Grundzustand eine Quantenspinflüssigkeit ausbilden. In einer Reihe von Übersichtsartikeln über Quantenspinflüssigkeiten wurde  $\kappa$ -ET<sub>2</sub>Cu<sub>2</sub>(CN)<sub>3</sub> bei der Erörterung experimenteller Ergebnisse besondere Aufmerksamkeit geschenkt [3–6]. Im Laufe der Zeit hat sich die Verbindung als Lehrbuchbeispiel einer Quantenspinflüssigkeit herauskristallisiert.

Trotz der zahlreichen experimentellen Studien seit 2003 wurden teils widersprüchliche Schlussfolgerungen gezogen, und entscheidende Fragen blieben unbeantwortet:

Was genau ist der magnetische Grundzustand des Systems? Auf welche Weise wird die magnetische Ordnung verhindert? Was ist die Ursprung der Anomalien, die bei  $T^* = 6$  K beobachtet werden? Wie sieht das Spinanregungsspektrum aus, insbesondere, besitzt es eine Energielücke oder nicht?

Die Untersuchung der magnetischen Eigenschaften bei Temperaturen unter 1 K ist eine technische Herausforderung. Die meisten anwendbaren Methoden sind anfällig für magnetische Verunreinigungen. Suszeptibilitätsmessungen mittels magnetischen Drehmoments [7] oder eines SQUID-Magnetometers [2] können nicht zwischen intrinsischen und extrinsischen Beiträgen unterscheiden. Spektroskopische Verfahren wie NMR [2, 8, 9] und  $\mu$ SR [10] untersuchen die Elektronenspins indirekt durch ihre Wechselwirkung mit den Atomkernen bzw. den implantierten Myonen, die ebenfalls mit den Fremdspins wechselwirken.

Zur Überwindung der genannten Probleme und um die offenen Fragen anzugehen, ist die Elektronenspinresonanz (ESR) die Methode der Wahl. Sie ermöglicht es, die Leitungselektronen in  $\kappa$ - $\text{ET}_2\text{Cu}_2(\text{CN})_3$  direkt zu untersuchen. Die sehr hohe Empfindlichkeit herkömmlicher Spektrometer bedingt einen eingeschränkten Betriebsbereich bei Temperatur und Frequenz bzw. Magnetfeld. Ein herkömmliches ESR-Spektrometer verwendet einen Hohlraumresonator für die Mikrowellen, um die Empfindlichkeit zu erhöhen. Die Resonanzfrequenz des Resonators bestimmt die einzige Betriebsfrequenz des Instruments. Typische Frequenzen im 10 GHz-Bereich erfordern dabei Resonatoren mit Abmessungen im Bereich von mehreren 10 mm.

Um die Beschränkungen zu überwinden, werden verschiedene Techniken auf der Grundlage von koplanaren Wellenleitern eingesetzt. Ein kapazitiv gekoppelter Abschnitt eines koplanaren Wellenleiters (CPW) kann als eindimensionaler Resonator fungieren, der sowohl bei seiner Grundfrequenz als auch bei den höheren Harmonischen in linearem Abstand funktioniert. Die eindimensionale Struktur ermöglicht es, den Resonator mäanderförmig auf kompakten Substraten unterzubringen, die in das begrenzte Probenvolumen eines  $^3\text{He}/^4\text{He}$ -Entmischungskryostaten passen.

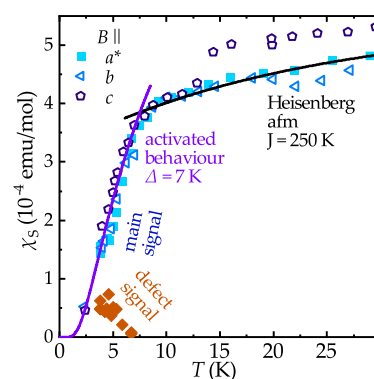
Im Rahmen dieses Projekts wurde ein neuartiger Breitband-Versuchsaufbau entwickelt, der es ermöglicht, ESR-Spektren mit Mikrowellen-Frequenz-Sweeps anstelle der üblicherweise verwendeten Magnetfeld-Sweeps aufzunehmen [M1]. Dies ermöglicht kontinuierliche Untersuchungen im Temperatur/Magnetfeld-Phasenraum. Der neue Aufbau verwendet Magnetfeldmodulation und ein phasenempfindliches Detektionsschema, um höhere Empfindlichkeiten im Vergleich zu früheren Methoden zu erreichen. Die Empfindlichkeit und der Einsatzbereich der Methode wurden anhand von Messungen an verschiedenen Standardproben demonstriert.

Die Kombination von Messungen mit konventionellen hochempfindlichen ESR-Spektrometern und der Einsatz von breitbandigen Techniken, um mK-Temperaturen zu erreichen und die Feld- und Frequenzabhängigkeit zu untersuchen, hat sich als vielversprechender Ansatz zur Untersuchung der magnetischen Eigenschaften von  $\kappa\text{-ET}_2\text{Cu}_2(\text{CN})_3$  bei niedrigen Temperaturen erwiesen.

Die Ergebnisse der ESR-Experimente ermöglichten es, ein Grundzustandsszenario für  $\kappa\text{-ET}_2\text{Cu}_2(\text{CN})_3$  zu entwickeln, das langjährige Kontroversen auflöst [M2]. Es kann ein exponentieller Abfall der Spinsuszeptibilität des ESR-Hauptsignals unterhalb von  $T^* = 6$  K beobachtet werden. Die deutet auf das Vorhandensein einer Energielücke im Spektrum der Spinanregungen hin. Die Beobachtungen sind dabei in guter Übereinstimmung mit einem Grundzustand, der aus lokalisierten Valenzbindungen aufgebaut ist. Ein zusätzliches "Defektsignal" in im ESR-Spektrum taucht auf, sobald die Spin-Singlets gebildet werden.

Magnetische Verunreinigungen und ein gewisses Maß an intrinsischer Unordnung führen zur Bildung ungepaarter Spins im ansonsten nichtmagnetischen Grundzustand. Diese sind für den beobachteten Defekt-ESR-Beitrag und andere Tieftemperatureigenschaften verantwortlich, die bisher zu widersprüchlichen Interpretationen geführt haben.

Um die neuen Erkenntnisse über die magnetischen Eigenschaften von  $\kappa\text{-ET}_2\text{Cu}_2(\text{CN})_3$  bei niedrigen Temperaturen sowohl auf die isolierende als auch auf die metallische Seite des Phasendiagramms zu erweitern, wurden ESR-Messungen an verwandten frustrierten  $\kappa\text{-ET}_2\text{X}$ -Verbindungen durchgeführt. Die analoge molekulare Substitution in  $\kappa\text{-[ET}_{1-x}\text{STF}_x\text{]}_2\text{Cu}_2(\text{CN})_3$  ermöglicht die Einführung von chemischem Druck in die Verbindung und damit eine zunehmend metallische Verbindung. Die Schwesterverbindung  $\kappa\text{-ET}_2\text{Ag}_2(\text{CN})_3$  unterliegt stattdessen einem stärkeren Einfluss von elektronischen Korrelationen. Sie befindet sich daher tiefer im Mott-isolierenden Zustand.



Spin-Energielücke in  $\kappa\text{-ET}_2\text{Cu}_2(\text{CN})_3$

# Publications

Publications related to this thesis:

- [M1] **B. Miksch**, M. Dressel and M. Scheffler, *Cryogenic frequency-domain electron spin resonance spectrometer based on coplanar waveguides and field modulation*, Rev. Sci. Instrum. **91**, 025106 (2020).
- [M2] **B. Miksch**, A. Pustogow, M. Javaheri Rahim, A. A. Bardin, K. Kanoda, J. A. Schlueter, R. Hübner, M. Scheffler and M. Dressel, *Gapped magnetic ground state in quantum spin liquid candidate  $\kappa$ -(BEDT-TTF) $_2$ Cu $_2$ (CN) $_3$* , Science **372**, 276 (2021).

Further publications:

- [M3] M. Hemmida, H.-A. K. von Nidda, **B. Miksch**, L. L. Samoilenko, A. Pustogow, S. Widmann, A. Henderson, T. Siegrist, J. A. Schlueter, A. Loidl and M. Dressel, *Weak ferromagnetism and glassy state in  $\kappa$ -(BEDT-TTF) $_2$ Hg(SCN) $_2$ Br*, Phys. Rev. B **98**, 241202 (2018).
- [M4] L. N. Majer, **B. Miksch**, G. Gorgen Lesseux, G. Untereiner and M. Dressel, *Charge-order phase transition in the quasi one-dimensional organic conductor (TMTTF) $_2$ NO $_3$* , Appl. Magn. Reson. **51**, 1321 (2020).
- [M5] L. N. Majer, **B. Miksch**, O. Iakutkina, T. Kobayashi, A. Kawamoto and M. Dressel, *Interacting electron spins in  $\kappa$ -(BEDT-TTF) $_2$ Cu $_2$ [N(CN) $_2$ ]I investigated by ESR spectroscopy*, Phys. Rev. B **102**, 214430 (2020).
- [M6] M. Prinz-Zwick, B. G. Szigeti, T. Gimpel, D. Ehlers, V. Tsurkan, A. O. Leonov, **B. Miksch**, M. Scheffler, I. Stasinopoulos, D. Grundler, I. Kézsmárki, N. Büttgen and H.-A. Krug von Nidda, *Nuclear and electron spin resonance studies on skyrmion-hosting lacunar spinels*, Phys. Status Solidi B, 2100170 (2021).



# 1 Magnetism in Solids

Our contemporary understanding of magnetism rests on concepts introduced about 100 years ago: the inextricable link between magnetism and electricity expressed in Maxwell's equations; magnetism as a relativistic effect of moving charges; and the concept of spin introduced in quantum mechanics to explain the magnetic dipole moment of several elementary particles by an intrinsic angular momentum. The magnetic properties of solids can vastly differ from the magnetism of atoms or molecules on the microscopic level as collective behaviour plays a crucial role [11]. Many phenomena of magnetism in condensed matter are topical research interests including spin-glasses, skyrmions and magnetism on frustrated lattices. This is driven by an interest in the fundamental physics of the phenomena as well as technological development to find new materials for various applications, e.g. permanent magnets, sensors or magnetic storage.

In this chapter, first a brief introduction to magnetism in solids including the fundamental interactions is given. This is followed by the treatment of correlated electron systems in the framework of the Hubbard model including the ramifications for the magnetic properties. Afterwards magnetism in low-dimensional systems particularly the concept of frustrated lattices is introduced. Lastly an introduction into quantum spin liquids, a peculiar state of matter where magnetic order is suppressed due to geometrical frustration, is given.

## 1.1 Types of Magnetism

This section on different types of magnetism is mainly based on the chapter "*Magnetismus*" from [12] R. Gross and A. Marx, *Festkörperphysik*, 2. ed. (De Gruyter, Berlin Boston, 2014). Statements taken from other sources are explicitly indicated.

The magnetisation  $M$ , the density of magnetic moments in a material, characterises the magnetic properties of a solid in a magnetic field. It can be described by the

derivative of the magnetic moment  $\mu$  with respect to the volume  $V$  as follows

$$M = \frac{d\mu}{dV} \quad (1.1)$$

Inside a magnetised material the magnetic flux density  $\mathbf{B}$  and the magnetic field strength  $\mathbf{H}$ , which are proportional to each other in vacuum, differ by the magnetisation.

$$\mathbf{B} = \mu_0(\mathbf{H} + \mathbf{M}) \quad (1.2)$$

The vacuum permeability  $\mu_0$ , relates  $\mathbf{B}$  and  $\mathbf{H}$  in absence of any magnetisation.

It is common to distinguish three types of magnetism when describing the interaction of an external magnetic field with a solid: *diamagnetism*, *paramagnetism* and magnetism due to co-operating moments, including *ferro-* and *antiferromagnetism*. In diamagnets and paramagnets a linear relation between  $\mathbf{M}$  and  $\mathbf{H}$  exists.

$$\mathbf{M} = \chi\mathbf{H} \quad \mathbf{B} = \mu_0(1 + \chi)\mathbf{H} \quad (1.3)$$

The volume magnetic susceptibility  $\chi$  links the two quantities. Usually  $|\chi| \ll 1$  in the case of dia- and paramagnets. For ferromagnets the relation is generally nonlinear due to saturation and influenced by magnetic hysteresis. For low field it can be linearised with  $\chi$  being much larger in comparison to paramagnets.

The magnetic properties of solids are determined almost exclusively by the electrons, the nuclear magnetic moments can be neglected in most cases. In order to describe the magnetism bound electrons associated with individual lattice sites and quasi-free electrons, e.g. the conduction electrons in metals, are treated differently.

### 1.1.1 Diamagnetism

Applying a magnetic field to a solid induces magnetic moments opposing the external field according to Lenz's law resulting in a negative magnetic susceptibility ( $\chi_{\text{dia}} < 0$ ). In a classical picture the magnetic field leads to a circular current due to the Larmor precession of the electrons; this current in turn leads to a magnetic moment opposing the external field. For closed shell atoms this *Larmor diamagnetism* leads to a negative susceptibility

$$\chi_{\text{dia}} \simeq -\mu_0 \frac{e^2}{6m_e} nZ \langle r^2 \rangle \quad (1.4)$$

with the density  $n = N/V$ , the number of electrons  $Z$  and the mean square distance of the electrons to the nucleus  $\langle r^2 \rangle$ . A diamagnetic contribution is present in all solids at least for the closed inner shells of the atoms. If no magnetic moments are present in absence of an external magnetic field the material behaves purely diamagnetic. If static moments are present the paramagnetism typically dominates.

### 1.1.2 Paramagnetism

Magnetic moments due to orbital motion or spin of the electrons can be present without external magnetic fields in atoms and ions with partially filled outer shells. Typically the orbital angular momentum  $L$  and spin  $S$  of an atom couple to a total angular momentum  $J = L + S$  resulting in a magnetic moment

$$\mu_J = -g_J \mu_B \frac{J}{\hbar} \quad \text{with} \quad g_J = 1 + \frac{J(J+1) + S(S+1) - L(L+1)}{2J(J+1)} \quad (1.5)$$

Here,  $g_J$  is the Landé  $g$ -factor. When an external magnetic field is applied to a paramagnetic material, a material containing magnetic moments, these are oriented along the field leading to a positive magnetic susceptibility ( $\chi_{\text{para}} > 0$ ). For a two-level system with  $J = 1/2$  within an external field  $\mathbf{B}_0 = B_0 \cdot \hat{z}$  only two orientations  $m_J = \pm 1/2$  are allowed. The magnetisation depends on the mean value of  $m_J$  given by the thermal population of the two levels.

$$M = n g_J \mu_B \langle m_J \rangle = n \mu_{\text{eff}} \tanh \frac{\mu_{\text{eff}} B_0}{k_B T} \quad (1.6)$$

with the effective magnetic moment  $\mu_{\text{eff}} = 1/2 g_J \mu_B$ . For large fields all magnetic moments are aligned and the magnetisation saturates at  $M_s = n \mu_{\text{eff}}$ . For low fields ( $\mu_{\text{eff}} B_0 / k_B T \ll 1$ ) *Curie's law* is obtained by using  $\tanh x \simeq x$

$$\chi_{\text{para}} = \mu_0 \left( \frac{\partial M}{\partial B_0} \right)_{T,V} = \frac{\mu_0 n \mu_{\text{eff}}^2}{k_B T} = \frac{C}{T} \quad (1.7)$$

where  $C$  denotes the Curie constant (see Fig. 1.1A). Typical experimental conditions of  $B_0 = 1 \text{ T}$  at  $T = 300 \text{ K}$  are well within the low field regime as  $\mu_{\text{eff}} B_0 / k_B T = 2 \cdot 10^{-3}$ . The magnetisation therefore increases linearly with magnetic field for a paramagnet as in equation 1.3.

### 1.1.3 Magnetism in Metals

In metals the spin of the conduction electrons also leads to paramagnetism. In contrast to localised electrons the magnetic susceptibility in metals is temperature independent. Due to the large Fermi temperature of metals compared to typical experimental temperatures, only a small number of electrons around the Fermi energy can change their spin. This number increases with temperature and compensates the decreasing susceptibility according to Curie's law leading to the temperature independent *Pauli paramagnetism*. Using the density of states (DOS) around the Fermi energy  $D(E_F)$  for the free electron gas the susceptibility is

$$\chi_P = \mu_0 \mu_B^2 \frac{D(E_F)}{V} \stackrel{\text{free electron gas}}{=} n \frac{3\mu_0 \mu_B^2}{2k_B T_F} \quad (1.8)$$

In metals itinerant electrons also contribute to the diamagnetism by their orbital motion leading to *Landau diamagnetism*. For the free electron gas its value is exactly one third of the Pauli paramagnetism; within the periodic potential of a crystal lattice this is altered by the effective mass  $m^*$ .

$$\chi_L = -\frac{1}{3} \chi_P \left( \frac{m}{m^*} \right)^2 \quad (1.9)$$

Combining both effects, a paramagnetic susceptibility remains for the conduction electrons.

### 1.1.4 Exchange Interaction

If finite interactions between magnetic moments are present in a solid, magnetic order as well as an associated finite magnetisation can occur spontaneously, i.e. in absence of an external magnetic field. Different types of magnetic order exist, including but not limited to *ferromagnetism* with *parallel* and *antiferromagnetism* with *antiparallel* alignment of the moments. Thermal energy acts against the ordering process. A phase transition therefore happens from a disordered to an ordered state below a certain temperature. The most important interaction leading to magnetic order is the exchange interaction. Different other possible types of interaction are presented in section 2.1.

The exchange coupling  $J$  can be either ferromagnetic ( $J > 0$ ) or antiferromagnetic ( $J < 0$ ). This can be intuitively explained by considering two electrons which interact

repulsively due to Coulomb interaction and are localised on energetically close orbitals  $\phi_A$  and  $\phi_B$ . Due to Pauli's principle the two-electron state has to be antisymmetric. This can be realised in an antisymmetric spin singlet state ( $|\uparrow\downarrow\rangle, |\downarrow\uparrow\rangle$ ) with symmetric orbital wave function  $\psi_s$  or a symmetric spin triplet state ( $|\uparrow\uparrow\rangle, |\downarrow\downarrow\rangle$ ) with antisymmetric orbital wave function  $\psi_a$ .

$$\psi \propto \phi_A(\mathbf{r}_1)\phi_B(\mathbf{r}_2) \pm \phi_A(\mathbf{r}_2)\phi_B(\mathbf{r}_1) \quad \text{with } + \rightarrow \psi_s, - \rightarrow \psi_a \quad (1.10)$$

Coulomb repulsion between the electrons lifts the degeneracy of the different configurations. The exchange constant  $J$  is defined as the energy difference between the two states. Due to the unambiguous link between the spin and orbital wave functions the exchange interaction can also be expressed by a pure spin Hamiltonian

$$\mathcal{H}_{\text{ex}} = J(\mathbf{S}_1 \cdot \mathbf{S}_2) \quad (1.11)$$

with the spin operators  $S_{1,2}$  of the two electrons. Generalising this concept to arbitrary spin operators leads to the *Heisenberg model* given in equation 1.20.

If the orbitals overlap directly in space, ferromagnetic alignment of the spins to form the antisymmetric orbital wave function  $\psi_a$  reduces the interaction energy, as the orbital wave function vanishes in the centre between the two electrons, where the Coulomb potential is maximal. *Direct exchange* therefore leads to *ferromagnetic* coupling [13]. For spatially separated orbitals increasing the delocalisation can reduce the kinetic energy. Coulomb repulsion however prevents real hopping of the electrons between the sites. Nevertheless virtual hopping within the energy-time uncertainty is possible and reduces the kinetic energy. This process, also called *super-exchange*, is (due to Pauli's principle) only possible in the spin singlet state, thus leading to *antiferromagnetic* exchange coupling [13].

### 1.1.5 Magnetic Order

The interactions between magnetic moments result in magnetic order. In ferromagnetic materials the parallel alignment results in a finite magnetisation in contrast to antiferromagnetic materials for which magnetisation is equal to zero in the ordered state. As thermal fluctuations can destroy the magnetic order, it only develops below a certain critical temperature, called *Curie temperature*  $T_C$  for ferromagnets and *Néel temperature*  $T_N$  for antiferromagnets. To describe the susceptibility in the paramagnetic regime above the ordering temperature, a mean-field approximation can be used. In

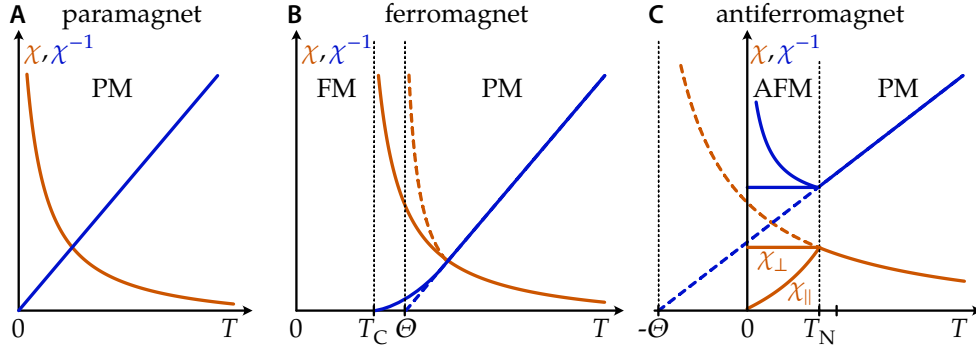


FIG. 1.1 *Curie-Weiss Law* The temperature-dependence of the susceptibility for ferro- (B) and antiferromagnets (C) (solid lines) above the ordering temperature can be approximated by Curie-Weiss law (dashed lines), an extension of Curie's law (A) obtained by the mean-field treatment of the magnetic order. (based on [12])

this approach, the exchange interaction between the individual pairs of moments is treated as an effective molecular field  $\mathbf{B}_{\text{ex}}$  acting on them in addition to the external magnetic field, thus reducing the many-body to a one-body problem. In general, the exchange interaction energy is given by the Heisenberg model. When calculating the interaction energy between in the mean-field approach, the angular momenta  $\mathbf{J}_j$  of the neighbouring atoms are replaced by the mean value  $\langle \mathbf{J}_j \rangle$ . This way one obtains the molecular field

$$\mathbf{B}_{\text{ex}} = \frac{zJ}{ng_J^2\mu_B^2}\mathbf{M} = \mu_0\gamma\mathbf{M} \quad (1.12)$$

where  $z$  is the number of nearest neighbour sites,  $n$  is the density of the lattice sites and  $\gamma$  denotes the molecular field constant. A similar treatment as for the paramagnetic case is now possible by replacing the external field  $B_0$  in equation 1.6 with the effective field  $B_{\text{eff}} = B_0 + B_{\text{ex}}$ . Using the same expansion for low fields it can be shown that spontaneous magnetisation occurs below the Curie temperature

$$T_C = n\gamma \frac{\mu_0 g_J^2 J(J+1)\mu_B^2}{3k_B} = \gamma C \quad (1.13)$$

where  $\gamma$  denotes the molecular field constant and  $C$  is the Curie constant as in equation 1.7. The susceptibility above  $T_C$  is then given by the *Curie-Weiss law*

$$\chi_{\text{fm}} = \frac{C}{T - T_C}. \quad (1.14)$$

When modelling experimental data for large  $T$  with Curie-Weiss law, generally a paramagnetic Curie temperature  $\Theta > T_C$  is obtained as illustrated in Fig. 1.1B.

To treat antiferromagnets the model can be extended to treat the moments on the two sub-lattices  $A$  and  $B$  with opposite spin alignment separately. The ordering temperature in this case depends on the exchange interaction between nearest and next-nearest neighbour sites with molecular field constants  $\gamma_{AB}$  and  $\gamma_{AA} = \gamma_{BB}$  respectively. The Néel temperature is given by

$$T_N = |\gamma_{AB} - \gamma_{AA}|C. \quad (1.15)$$

For the susceptibility *Curie-Weiss law* can be used

$$\chi_{\text{afm}} = \frac{2C}{T + \Theta}. \quad (1.16)$$

The paramagnetic Néel temperature  $\Theta = |\gamma_{AB} + \gamma_{AA}|C$  characterising the temperature-dependence of the susceptibility in the paramagnetic state is always larger than the ordering temperature if both nearest and next-nearest neighbour interactions are antiferromagnetic. The susceptibility for the antiferromagnetic case is illustrated in Fig. 1.1C. Below  $T_N$  the behaviour depends on the orientation of the external field with respect to the spin alignment. For perpendicular alignment the moments get canted resulting in a magnetisation depending linearly on the applied field. The susceptibility is temperature independent in this case. For parallel alignment the susceptibility vanishes as  $T \rightarrow 0$  as no magnetisation can be induced by applying the magnetic field.

## 1.2 Correlated Electron Systems

The properties of many solids can be described in a band theory picture, where electrons are treated solitarily within a periodic potential  $V_{\text{ion}}(\mathbf{x})$  modelling the interactions with the lattice [13]:

$$\mathcal{H}_0 \phi_{k,\sigma}(\mathbf{x}) = \left[ -\frac{\hbar^2}{2m} \nabla^2 + V_{\text{ion}}(\mathbf{x}) \right] \phi_{k,\sigma}(\mathbf{x}) = E_k \phi_{k,\sigma}(\mathbf{x}) \quad (1.17)$$

Here,  $\phi_{k,\sigma}$  and  $E_k$  denote the Bloch wave function respectively the band energy with momentum  $\mathbf{k}$  and spin  $\sigma = \uparrow, \downarrow$ . Electron-electron interactions cannot be taken into account explicitly in the single particle Hamiltonian. A large part of them can however

be incorporated as modifications of the background potential. For many materials this approach is sufficient as electron-electron interactions do not have major consequences due to very effective screening or the vanishing scattering rate near a Fermi surface [14].

For certain phenomena such as the Mott metal-insulator transition and co-operative magnetic properties, electronic correlations play the essential role, thus an explicit treatment, i.e. a many-body theory, is necessary. The *Hubbard model* [15] is the simplest model to explicitly describe interacting electrons on a lattice. On each lattice site one electronic orbital is modelled which can be occupied by a maximum of two electrons with opposite spin according to the Pauli principle. The Hubbard Hamiltonian  $\mathcal{H}_{\text{Hubbard}}$  is composed of two parts [13]: the kinetic term  $\mathcal{T}$ , describing hopping of the electrons between the lattice sites; and the correlation term  $\mathcal{U}$ , describing on-site Coulomb repulsion.

$$\mathcal{H}_{\text{Hubbard}} = - \underbrace{\sum_{\langle ij \rangle \sigma} t_{ij} (c_{i\sigma}^\dagger c_{j\sigma} + c_{j\sigma}^\dagger c_{i\sigma})}_{\mathcal{T}} + U \underbrace{\sum_i n_{i\uparrow} n_{i\downarrow}}_{\mathcal{U}} \quad (1.18)$$

$c_{i\sigma}^\dagger$  and  $c_{i\sigma}$  are the creation and annihilation operators of an electron and  $n_{i\sigma} = c_{i\sigma}^\dagger c_{i\sigma}$  counts the number of electrons at site  $i$  with spin  $\sigma$ . The hopping is parametrised by the transfer integral  $t_{ij}$  measuring the hopping probability between sites  $i$  and  $j$ . The transfer integral is proportional to the electronic bandwidth  $W$ . Creating a double occupancy leads to a Coulomb repulsion  $U$  between the two electrons. The resulting physics is determined by the degree of filling of the lattice sites with electrons and the ratio  $U/t$  of electronic correlations and transfer integral. For large  $U/t$  electrons tend to localise forming a *Mott-insulator*, for small values the system is metallic. For simplicity a half-filled system is considered in the following, i.e. every site is nominally occupied by a single electron. The two extreme cases,  $U \ll t$  and  $U \gg t$ , are illustrated in Fig. 1.2. For  $U \ll t$  a metallic state is realised. In the limit of vanishing interactions  $U = 0$  the model describes the basic Fermi gas. In case of strong interactions  $U \gg t$  the electrons localise and the density of states splits into an occupied band below and an unoccupied band above the Fermi energy separated by a gap. Thus at low energies there are primarily spin excitations. Quantum mechanical tunnelling processes are still allowed between neighbouring sites as far as Pauli's principle is obeyed, i.e. opposite alignment of neighbouring spins is necessary. This *virtual hopping* leads to an antiferromagnetic exchange interaction as discussed in the previous section. The

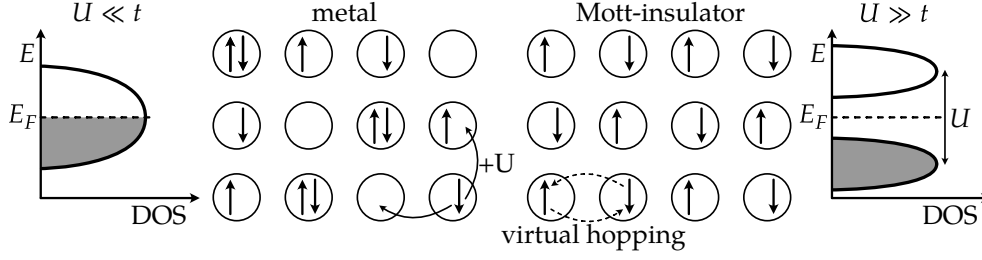


FIG. 1.2 *Hubbard Model for Half-Filling* For small Coulomb repulsion  $U$  electrons can hop between the sites resulting in a metallic state. The kinetic energy gained in this case dominates the Coulomb repulsion paid by the creation of double occupancies. Electrons localise upon increasing  $U$  which opens a gap resulting in insulating behaviour. Virtual hopping can reduce the total energy. As it is only possible between neighbouring sites occupied by electrons of opposite spin an antiferromagnetically ordered state is energetically favourable. (modified from [16])

exchange coupling is given in terms of the Hubbard  $t$  and  $U$  as follows

$$|J_{ij}| = \frac{4t_{ij}^2}{U} \quad (1.19)$$

It can be shown that the Hubbard model for large  $U$  at half filling transforms into the antiferromagnetic  $S = 1/2$  *Heisenberg model* with exchange  $J_{ij}$  [13, 14].

$$\mathcal{H}_{\text{Heisenberg}} = \frac{1}{2} \sum_{ij} J_{ij} \left( \mathbf{S}_i \cdot \mathbf{S}_j - \frac{1}{4} \right) \quad (1.20)$$

Thus systems undergoing the Mott transition generally develop antiferromagnetic order at low temperatures. They are also called *Mott-Heisenberg insulators* for this reason [13]. As  $J$  is much smaller than  $U$  for the Mott insulating state with  $U \gg t$  the Néel transition is typically happening at a temperature  $T_N$  below the Mott metal-insulator transition.

Geometrical frustration can suppress the long range order of the magnetic moments to  $T_N \rightarrow 0$ . In this case magnetic order is absent and a *Mott-Hubbard insulator* is realised as the ground state of the system [13].

A qualitative phase diagram of both cases is shown in Fig. 1.3 indicating the realised states for different temperatures and correlation strengths alongside a sketch of the respective density of states (DOS) in the vicinity of the Fermi level. Both phase diagrams show a conducting region (blue) and the transition to the insulating Mott state (orange) with a gapped DOS. Below the critical temperature  $T_{\text{crit}}$  a first order

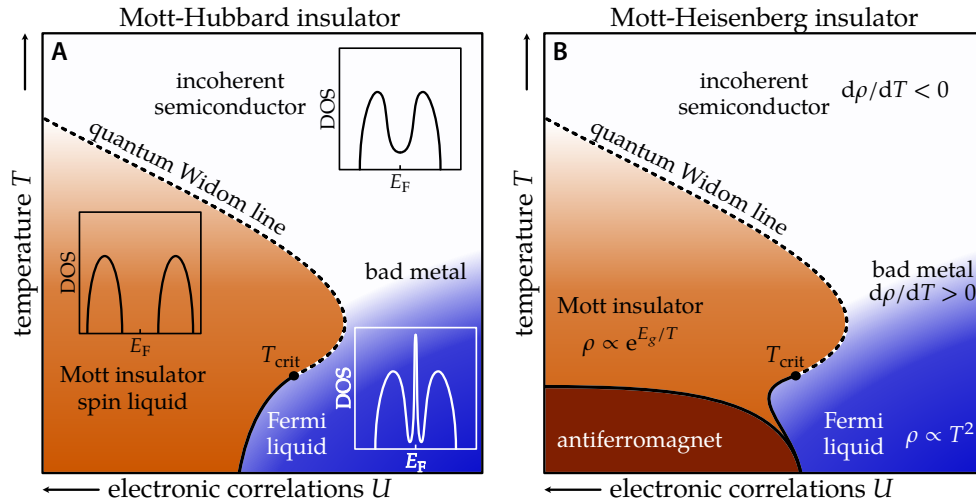


FIG. 1.3 *Schematic Phase Diagram of Mott Insulators* A phase boundary separates insulating (orange) and conducting (blue) regions in both phase diagrams. Below the critical endpoint at  $T_{\text{crit}}$  a first order phase transition is realised (solid line); above it becomes a gradual crossover characterised by the quantum Widom line (dashed line). The low-temperature phase boundary has a different shape in the Mott-Hubbard case (A) and the Mott-Heisenberg case (B). The density of states for the respective phases is sketched in the insets in (A), the characteristic temperature-dependence of the resistivity  $\rho$  is indicated in (B). (based on [17, 18])

phase transition to the metallic state is realised (solid line). This Fermi liquid region is characterised by a Drude peak in the DOS. For higher temperatures the phase boundary becomes a gradual crossover through a quantum critical region around the quantum Widom line (dashed line). The charge transport on the conducting side for higher temperatures is sustained by incoherent thermal fluctuations resulting in a semiconducting behaviour.

For low temperatures the phase diagrams are qualitatively different [13]. Due to the different entropy in the nonmagnetic and the antiferromagnetic ground state the shape of the phase boundary to the metallic side is different as mandated by the Clausius-Clapeyron equation [19]. Without magnetic order the entropy remains larger than in the Fermi liquid regime resulting in a positive slope of the phase boundary. Lifting the geometrical frustration results in an antiferromagnetic ground state. The entropy is thus lowered, implying a negative slope of the phase boundary.

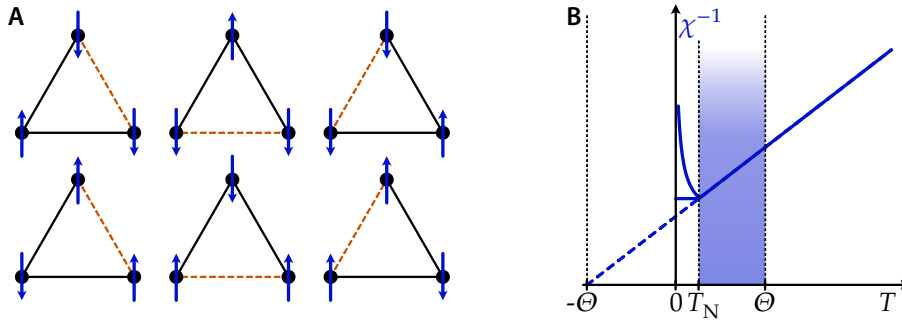


FIG. 1.4 *Geometrical Frustration* (A) Antiferromagnetically interacting Ising spins arranged on a triangle are a simple example of frustration. As the antiparallel alignment cannot be fulfilled on all bonds simultaneously (indicated in orange), the system possesses six degenerate ground states. (B) Inverse susceptibility of a geometrically frustrated antiferromagnet. The shaded region corresponds to the spin liquid regime  $T_N < T < \Theta$  in which magnetic order is suppressed.

### 1.3 Geometrical Frustration

Materials with cooperative magnetism where the moments are arranged in a geometry such that not all exchange interactions can be fulfilled simultaneously are called *geometrically frustrated* magnets. The ground state hosted by frustrated magnets is thus characterised by a large degeneracy. A simple example for geometrical frustration is a system of three antiferromagnetically interacting Ising spins in a triangular arrangement as illustrated in Fig. 1.4A. The preferred antiparallel arrangement cannot be fulfilled on all three bonds resulting in a sixfold degeneracy of the ground state compared to the twofold symmetry intrinsic to the Ising model [3].

Such large degeneracy also occurs in various two- and three-dimensional lattices with the triangle motif as the main building block. In 2D edge sharing triangles lead to a triangular lattice, corner sharing triangles to a kagomé lattice, both depicted in Fig. 1.5. Examples for materials hosting magnetic moments on a triangular lattice are the organic Mott insulators  $\kappa$ -(BEDT-TTF)<sub>2</sub>Cu<sub>2</sub>(CN)<sub>3</sub> and  $\beta'$ -EtMe<sub>3</sub>Sb[Pd(dmit)<sub>2</sub>]<sub>2</sub>. A kagomé type arrangement of the magnetic Cu<sup>2+</sup> ions is present for example in the mineral hebertsmithite ZnCu<sub>3</sub>(OH)<sub>6</sub>Cl<sub>2</sub>. Also in three dimensions geometrical frustration is possible for example in the form of the hyperkagomé lattice a 3D arrangement of corner sharing triangles. This is realised for example in Na<sub>4</sub>Ir<sub>4</sub>O<sub>8</sub> where three out of the four edges of the tetrahedra of the underlying pyrochlore sub-lattice are occupied by the magnetic iridium ions [20].

As discussed in section 1.1 materials hosting local moments interacting antifer-

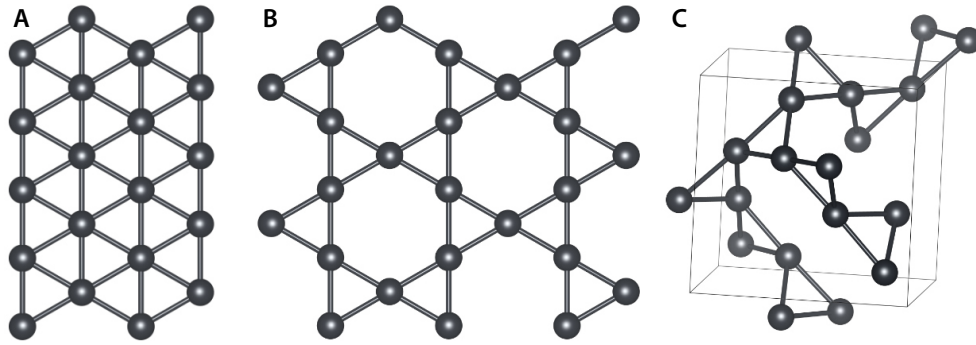


FIG. 1.5 *Frustrated Lattices* Geometrical frustration is possible in two as well as in three dimensions. Typical examples in 2D are the triangular (A) and kagomé lattices. An example in 3D is the hyperkagomé lattice (C) formed by the corner sharing triangles of iridium ions in  $\text{Na}_4\text{Ir}_3\text{O}_8$  [20].

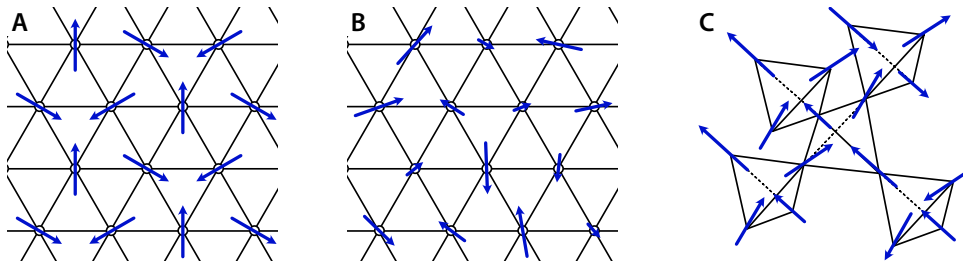


FIG. 1.6 *Frustrated Magnets* A large variety of states exists in frustrated spin systems, e.g. (A) conventional  $120^\circ$  Néel order in a triangular lattice afm Heisenberg model, (B) randomly frozen spins in a spin glass, or (C) a classical spin liquid in the form of spin-ice.

romagnetically via Heisenberg exchange generally develop a magnetically ordered ground state. Ordering happens below the Néel temperature, the high temperature susceptibility can be modelled using Curie-Weiss law characterised by the slightly larger paramagnetic Néel temperature  $T_N \lesssim \Theta$ . Geometrical frustration can suppress the magnetic order to low temperatures  $T_N \ll \Theta$  or even to  $T = 0$  as illustrated in Fig. 1.5B. The quantity

$$f = \frac{\Theta}{T_N} \quad (1.21)$$

can be defined as an empirical measure of frustration [21].

## 1.4 Frustrated Magnets

A large variety of spin states can be realised in frustrated magnets depending on the interplay of the geometrical frustration, the different interactions of the spins,

and the presence of fluctuations and disorder. This section mainly focuses on the case of  $S = 1/2$  spins on a triangular lattice, the situation in other frustrated lattices is discussed briefly in section 1.4.5.

It can be shown that the Heisenberg model on a triangular lattice with nearest neighbour antiferromagnetic exchange leads to a Néel ordered ground state in the case of classical spins  $S \rightarrow \infty$  [22] as well as in the quantum case with  $S = 1/2$  [23]. The coplanar polarised spins form three sub-lattices of collinear spins rotated by  $120^\circ$  with respect to each other [23], as indicated in Fig. 1.6A.

Frustration in magnets can not only occur geometrically due to the underlying lattice. Introducing disorder in the system can lead to the formation of a *spin glass* state under certain prerequisites, as described in [11]. Two possibilities are: randomness in the distances between the spins in a system with competing ferro- and antiferromagnetic interactions, e. g. RKKY-type interaction where the sign of the interaction depends on the spin distance; bond-randomness with varying nearest neighbour exchange interactions. In spin glasses at high temperature thermal fluctuations dominate and the spins are independent leading to paramagnetic behaviour. Upon cooling the spins start to form correlated clusters. The interactions become more and more long range until below a certain temperature the spins eventually freeze into one of the many possible static patterns, as illustrated in Fig. 1.6B. This glassy state is, thus, characterised by the absence of magnetic order and slow relaxation behaviour.

In contrast to that, in a *spin liquid* the constituent spins are also highly correlated, however, they remain fluctuating down to very low temperature [3]. Certain additional conditions have to be fulfilled in order to form a spin liquid state. This intriguing class of states and the prerequisites for their formation are discussed in detail in the following sections.

### 1.4.1 Spin Liquids

The term *spin liquid* is in analogy to liquid matter in which static order of the molecules is absent despite them being highly correlated. The states are characterised by highly entangled spins subject to strong fluctuations, that remain present even below the Curie-Weiss temperature  $\Theta$  [3]. For systems with large spins  $S \gg 1/2$  the fluctuations can be thought of as random reorientation of the spins driven by thermal energy  $k_B T$ .

An example for such a classical spin liquid are the so-called *spin ice* materials described in [3]: In those materials magnetic ions reside on a pyrochlore lattice, a system of corner-sharing tetrahedra. The relevant spins behave like Ising doublets

aligned along the axis connecting the centres of two neighbouring tetrahedra. They are subject to an effective nearest-neighbour ferromagnetic interaction. As a result the energy within a single tetrahedron is minimised in a configuration with two spins pointing inwards and two outwards, as shown in Fig. 1.6C, resulting in six degenerate configurations. This results in a large entropy remaining at low temperature. The spins still behave paramagnetic, however, they are strongly correlated by the “two in–two out”-rule. In the case of spin ice, upon lowering the temperature towards absolute zero, the thermal fluctuations diminish and the spins eventually freeze into one of the many degenerate ordered configurations due to the energy barrier between them [3].

In the case of small spins, especially for  $S = 1/2$ , the quantum mechanical zero-point fluctuations are comparably large. In addition to that, in a system with the full Heisenberg symmetry, no obvious energy barriers exist between different configurations [3]. As the quantum fluctuations persist down to  $T = 0$  K a spin liquid state can be hosted even at zero temperature. This state is then called *quantum spin liquid* (QSL). In essence QSLs host a nonmagnetic ground state built from local magnetic moments [3]. Many intriguing phenomena are predicted for this class of states in particular the presence of exotic fractional excitations [3].

As stated above, however, the ground state of the Heisenberg model on a perfect triangular lattice with antiferromagnetic exchange is the conventional three sub-lattice  $120^\circ$  Néel ordered state. In order to explain the nonmagnetic state observed in real materials, such as the triangular lattice organic conductor  $\kappa$ -(BEDT–TTF) $_2$ Cu $_2$ (CN) $_3$  [2], additional effects have to be considered.

The basic concept of valence bonds and states based on those are introduced in the next section followed by a discussion about the influence of disorder and anisotropy. Finally different QSL models on the triangular lattice and their predictions for the spin excitation spectrum are introduced.

### 1.4.2 Valence Bond States

How can a nonmagnetic ground state be formed from local moments? Two spins subject to antiferromagnetic interaction can form a pair with a  $S = 0$  singlet ground state. Within these pairs, or *valence bonds*, the two spins are maximally entangled. If all spins in a material are part of such valence bonds, it hosts a singlet ground state. Using valence bonds as a building block various possibilities of nonmagnetic states can be imagined [3].

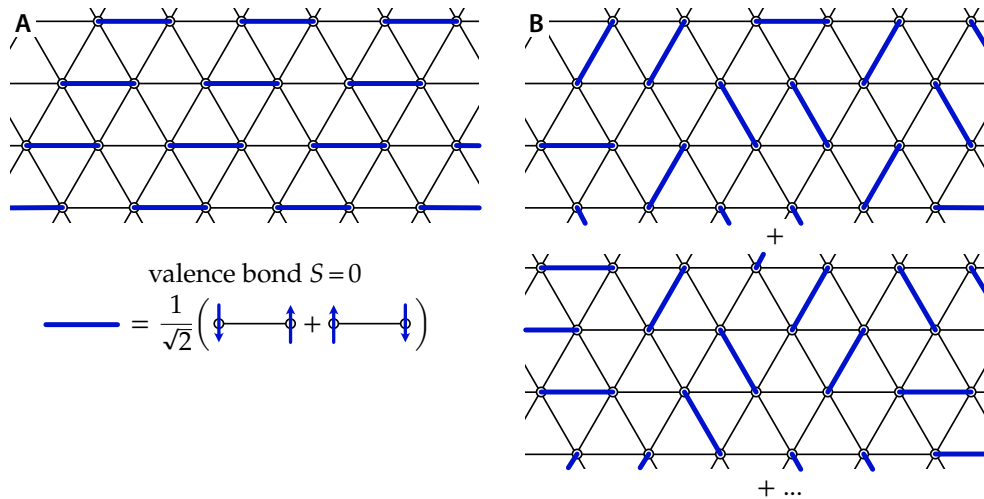


FIG. 1.7 *Valence Bond States*  $S = 0$  valence bonds, highly entangled pairs of spins due to antiferromagnetic exchange, are the building blocks of different valence bond states: (A) a valence bond solid is formed from valence bonds arranged in a specific pattern on top of the triangular lattice; (B) superimposing many different partitionings of the lattice with valence bonds leads to a resonating valence bond state. (based on [3])

A straightforward option is a *valence bond solid* (VBS) state where each spin is part of a specific static and localised valence bond [24]. Since a certain pattern of valence bonds energetically is favoured, a VBS breaks the symmetry of the underlying frustrated lattice as indicated in Fig. 1.7A. An anisotropic contraction or expansion of the lattice can be linked to the formation of the valence bonds in a preferred directions through altered exchange interactions. This is equivalent to the *spin-Peierls* phase known in 1d spin chains [25–28]. In an antiferromagnetically interacting spin chain, a magnetoleastic transition can occur when the energy gained by spins dimerising to  $S = 0$  pairs exceeds the energy cost for the alternating distortion of the underlying lattice. According to [24] the term “valence bond solid” has been used for symmetry preserving singlet phases in earlier literature, e. g. [29], but is now used only for states that break certain lattice symmetries, and thus, synonymous to “spin-Peierls phase”.

In a VBS the configuration of valence bonds is static, thus, each pair of spins in a valence bond is maximally entangled. However, no long-range entanglement between the spins of different valence bonds exists. Fluctuations of the valence bonds are needed in order to form a true quantum spin liquid. In a geometrically frustrated lattice different patterns of valence bonds can be energetically degenerate. One possible ground state wave function incorporating quantum fluctuations of valence bonds is in this case a superposition of different partitionings of the spins into valence bonds as

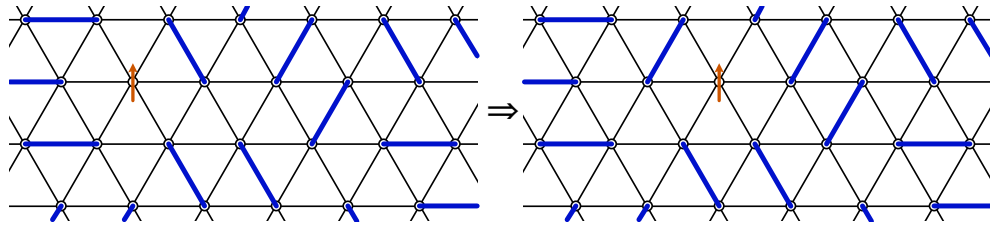


FIG. 1.8 *Spinon Excitations* A spinon excitations (spin  $S = 1/2$ , charge  $q = 0$ ) in a quantum spin liquid can be created as an unpaired spin not part of a valence bond. By local rearrangement of the valence bonds the spinon is able to move through the QSL. (based on [3])

illustrated in Fig. 1.7B. Such a *resonating valence bond* (RVB) state has been proposed by Anderson in 1973 [1]. In case no specific pattern is preferred the valence bonds behave like molecules in a liquid in contrast to a solid as in the case of the VBS.

Many different RVB wave functions have been proposed as ground states of certain specific Hamiltonians including states where valence bonds are formed not only between nearby spins as in the illustration in Fig. 1.7 but also over longer distances [5]. A common feature expected in different models of QSLs are exotic excitations; excitations impossible to construct from the elementary electron- or magnon-like excitations with spin  $S = 1/2$  and charge  $q = \pm e$  respectively spin  $S = 1$  and neutral charge [3]. Breaking a valence bond into two unpaired spins forms a triplet excited state. In a magnetically ordered state the two unpaired spins are bound together forming a magnon excitation [5]. In RVB states the individual spins can move apart simply by rearranging the already fluctuating valence bond pattern as illustrated in Fig. 1.8. Therefore the excitations can be regarded as independent, charge neutral quasiparticles carrying a spin of  $S = 1/2$  – the  $S = 1$  magnons fractionalise into two  $S = 1/2$  *spinons*. The changes in physical properties associated to the existence of spinons, e.g. a low-temperature specific heat contribution, is crucial to the experimental search of QSLs [5].

### 1.4.3 Effects of Disorder and Anisotropy

Small deviations from the perfect triangular symmetry as well as lattice imperfections and impurities present in real materials can significantly alter the experimentally observed ground state. In case of bond anisotropy of the exchange couplings added to the system a certain direction of valence bonds can be energetically favoured. This lifts the degeneracy of the different valence bond patterns and can thus suppress a fluctuating RVB state as illustrated in Fig. 1.9.

Disorder or randomness in real materials effects random modulation of the magnetic interactions between the spin dimers [30]. Consequentially the fluctuating valence bonds of the pure QSL state can be randomly pinned as certain bond interactions are stronger than others. Even for weak disorder, the long-range symmetry-breaking VBS order can be destroyed as smaller domains form around a pinned valence bond separated by defects as illustrated in Fig. 1.9 [24]. Point defects in the form of vortices as well as line defects in the form of domain walls are present in this situation as illustrated in Fig. 1.9 [24, 31]. Both results in unpaired defect spins hosted in the nonmagnetic background. It is even possible to have ordered domains separated from resonating clusters [30]. Increasing the disorder can lead to a fully random pinning of all singlets resulting in a *valence bond glass* (VBG) or *random-singlet* phase [24, 30]. It has been shown that the VBG state is also unstable to the nucleation of  $S = 1/2$  defect monomers [24]. In addition to the random pinning of valence bonds, nonmagnetic spin vacancies can break valence bonds producing local moments as well [31].

At low temperatures where electronic degrees of freedom are frozen even a small number of these local moments can alter the physical properties of materials to a significant extend as a paramagnetic contribution remains even though most of the spins are paired in  $S = 0$  valence bonds.

#### 1.4.4 Quantum Spin Liquid Models

As discussed, taking magnetoelastic coupling as well as the introduction of disorder into consideration, results in valence bond ground states with a static arrangement of valence bonds. Bearing in mind that the antiferromagnetic Heisenberg model on the triangular lattice has conventional Néel order as its ground state, is a quantum spin liquid phase still conceivable in  $S = 1/2$  triangular lattice materials?

The first approach is to consider higher order exchange terms in addition to the nearest neighbour Heisenberg interaction. It has been shown that by adding a four-spin ring exchange term the antiferromagnetic order can be destroyed and a spin liquid state is indeed stable in a certain parameter range. The proposed model by Motrunich [32] is discussed in the following paragraph.

The model Hamiltonian used is the following:

$$\mathcal{H}_{\text{ring}} = J_2 \sum_{\text{---}} P_{12} + J_4 \sum_{\text{◻}} (P_{1234} + P_{1234}^\dagger) \quad (1.22)$$

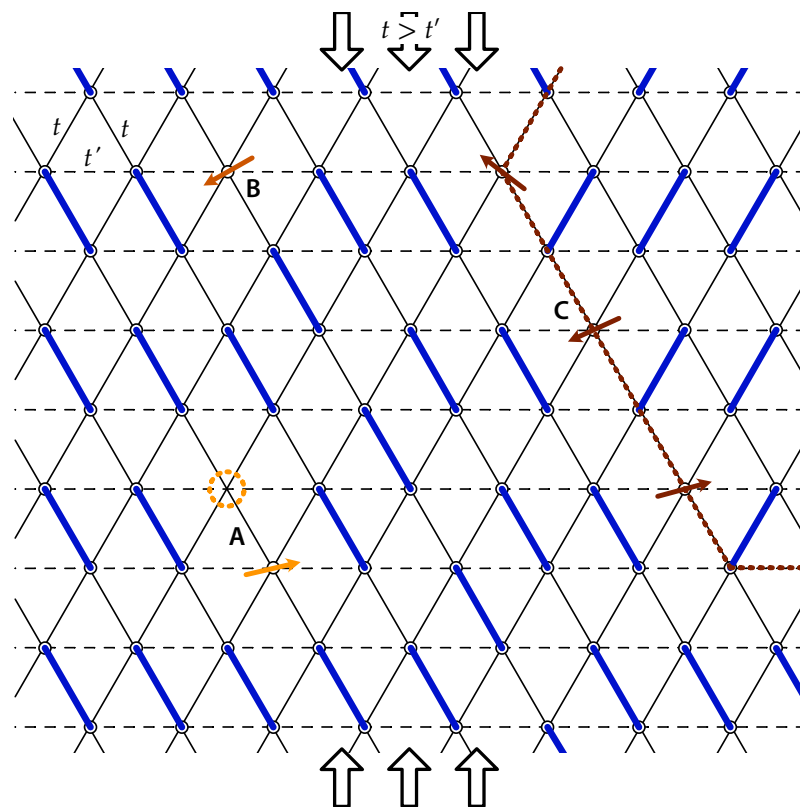


FIG. 1.9 *Adding Anisotropy and Disorder* Distortion (black arrows) of the perfect triangular lattice results in anisotropic transfer integrals and can lead to the formation of a valence bond solid. Unpaired spins can be present either in the vicinity of vacancies (A), or by random pinning of valence bonds (B) or domain walls in the VBS (C) introduced by disorder.

with the two spin Heisenberg exchange between all nearest neighbours with coupling  $J_2$ , and the four spin ring-exchange around all the rhombi of the lattice with coupling  $J_4$ . To find possible ground states for different ratios  $J_4/J_2$ , variational spin liquid states are used as ansätze. These spin liquid trial states are constructed via Gutzwiller-projection from different singlet fermionic mean-field states. The Gutzwiller projection essentially removes all the components of the wave functions with doubly occupied sites, thus leaving only singly occupied sites in the case of half-filling. It is shown, that for  $J_4/J_2 \gtrsim 0.14$  spin liquid states with lower energy than the antiferromagnetically ordered state are found. For larger  $J_4/J_2 \gtrsim 0.3$  the ground state is found to be the projection of the Fermi sea state. The ring-exchange is in an intuitive picture responsible for a tendency to delocalise the fermions, in this case the spinons. Uniform hopping in the form of the projected Fermi sea state is the best description of delocalisation by maximising the kinetic energy. The existence of a ring-exchange term is plausible in view of the underlying Hubbard-model used to describe correlated electron systems, such as the Mott-insulator  $\kappa$ -ET<sub>2</sub>Cu<sub>2</sub>(CN)<sub>3</sub>. It is shown that in the insulating phase determining an effective spin Hamiltonian for the triangular lattice Hubbard model up to order  $t^4/U^3$  indeed contains the model Hamiltonian with ring exchange shown in equation (1.22). Additional second and third neighbour Heisenberg exchange terms also present in the effective Hamiltonian do not alter the ground state in the given parameter range for the Fermi sea regime as these further neighbour correlations are small in the spin liquid regime. The model, thus, proposes a spin liquid ground state with a Fermi surface of spinons. This results in a continuous spin excitations spectrum with no spin gap and thus a finite zero temperature spin susceptibility. Treating the fluctuations and the constraint of no doubly occupied sites accurately requires the spinons to be coupled to a fluctuating gauge field with  $U(1)$  symmetry. As a result, an unusual specific heat contribution  $\propto T^{2/3}$  is expected for low temperatures because of the enhanced entropy due to the spinon excitations.

The spin liquid state with spinon Fermi surface is also found by Lee and Lee [33] by formulating a  $U(1)$  gauge theory for the Hubbard model in the slave-rotor representation. They have shown that for a range of  $U/t$  in the vicinity to the Mott transition charge fluctuations on the insulating side can stabilise the described spin liquid state. From the model a thermal conductivity  $\kappa/T \propto T^{-2/3}$  is predicted with the divergent behaviour cut off by impurity scattering. This bluntly violates the usual Wiedemann-Franz law, that in metals the ratio of thermal and charge conductivity is linear in  $T$  and would thus be a unique experimental signature of the proposed state.

The spin excitation spectrum is responsible for the low-temperature physical proper-

ties as soon as the charge degrees of freedom are frozen. It is, thus, the main signature of a specific spin liquid state. Direct experimental access is possible through neutron scattering and possibly quantum oscillations [34]. In addition to that, the unusual behaviour predicted for different quantities such as specific heat and spin susceptibility can be studied. As discussed, the characteristic of the  $U(1)$  spin liquid state with spinon Fermi surface is the continuous excitation spectrum of the deconfined, gapless spinons. A selection of other models that predict a different spin excitation spectrum and therefore different low-temperature properties are briefly introduced below.

One approach are quantum dimer models. Here, the Hilbert space does not consist of physical spins, but of nearest-neighbour dimer coverings of the lattice [4, 35]. In the following paragraph, the quantum spin liquid phase emerging from a quantum dimer model on the triangular lattice is introduced according to Moessner and Sondhi [35].

The model is motivated by the RVB picture of quantum spin liquids with the spin singlet valence bonds as the basic building blocks. On a triangular lattice, the following Hamiltonian is studied:

$$\mathcal{H}_{\text{dimer}} = \sum_{\triangleleft} \left[ -J(|\nearrow\rangle\langle\triangleleft| + |\triangleleft\rangle\langle\nearrow|) + V(|\nearrow\rangle\langle\nearrow| + |\triangleleft\rangle\langle\triangleleft|) \right] \quad (1.23)$$

where the thick bonds represent links occupied by dimers. Two terms are included in the Hamiltonian:  $J$  flips the dimer on one plaquette,  $V$  penalises plaquettes with parallel and thus flippable pairs of dimers. A RVB spin liquid phase with  $Z_2$  topological order (Ising symmetry gauge theory) is found for  $J \lesssim V$ . The spinons, the  $S = 1/2$  excitations that arise from breaking a valence bond, are shown to not interact beyond on lattice constant, and are thus deconfined as in the case of the  $U(1)$  spin liquid with spinon Fermi surface. However, in contrast to that, the spinon excitation spectrum is gapped.

Lee, Lee and Senthil [36] have shown, that a spin gap possibly also occurs in the  $U(1)$  spin liquid with Fermi surface as a result of spinon pairing. The basic idea is that two spinons with parallel momenta are subject to an attractive interaction similar to the Amperean interaction between two wires carrying parallel currents. The pairing of the spinons on parts of the Fermi surface reduces the  $U(1)$  gauge symmetry to  $Z_2$ , a gapped gauge field. The remaining Fermi surface can, thus, remain gapless restoring Fermi liquid behaviour at low energy. The authors predict a phase transition

or crossover from the high temperature non-Fermi liquid state to the low-temperature Fermi liquid like behaviour which can be understood as the paired spinon state. In accord with that, they predict  $T$ -linear thermal conductivity as in a metal as well as a finite linear specific heat contribution at low temperatures in contrast to the enhanced conductivity and unusual specific heat contribution predicted for the spinon Fermi surface state discussed above.

### 1.4.5 Spin Models on Other Lattices

Spin liquid states are also predicted on frustrated lattices apart from the triangular lattice case. On the related kagomé lattices, with corner sharing triangles as the building block, the situation for the  $S = 1/2$  Heisenberg model still remains under debate [4]: gapped  $Z_2$  QSLs as well as gapless  $U(1)$  states are discussed.

One of the most studied models is Kitaev's model [37] for the honeycomb lattice as it is exactly soluble in contrast to the models discussed for the triangular lattice. Because of its important influence on the field of quantum spin liquids as a proof of principle for the existence of different QSL phases it is briefly introduced in the following along the lines of the review from Savary and Balents [4].

Kitaev's model describes a  $S = 1/2$  systems on a honeycomb lattice, with exchange interactions depending on the bond direction. The following Hamiltonian is studied

$$\mathcal{H}_{\text{Kitaev}} = J_x \sum_{\langle ij \rangle \in x} \sigma_i^x \sigma_j^x + J_y \sum_{\langle ij \rangle \in y} \sigma_i^y \sigma_j^y + J_z \sum_{\langle ij \rangle \in z} \sigma_i^z \sigma_j^z \quad (1.24)$$

with the three different bond directions on the honeycomb lattice labelled with  $\mu = x, y, z$  and the Pauli matrices  $\sigma_i^\mu$ . On the lattice hexagonal plaquettes and a corresponding operator  $W_p = \sigma_1^x \sigma_2^y \sigma_3^z \sigma_4^x \sigma_5^y \sigma_6^z$  can be defined, commuting with the Hamiltonian. These  $W_p = \pm 1$  provide a local  $Z_2$  gauge symmetry for the Hamiltonian. The Hamiltonian can be reduced to a quadratic form by representing the spin operators by Majorana fermion operators. As long as the exchange couplings  $J_x, J_y, J_z$  fulfil the triangle inequalities, a gapless ground state is found. This state and the presence of gapless Majorana fermions is of particular interest as honeycomb materials with strong spin orbit coupling and superexchange, e.g. honeycomb iridates (e.g.  $\text{Na}_2\text{IrO}_3$ ) or  $\alpha\text{-RuCl}_3$ , exist which are well described by Kitaev's model with  $J_x = J_y = J_z$ .

As the ground state should not have any vortices it must be in the subspace where all  $W_p = +1$ .



## 2 Electron Spin Resonance

*Electron spin resonance*, ESR, probes the absorption of microwave radiation by the magnetic moment of the electron spin. Typically electrons form pairs in most compounds which leads to a mutual cancellation of their spins. Unpaired electrons are needed to observe ESR and are present in a range of substances, e.g. conduction electrons in metals, transition metal and rare earth ions with an odd number of electrons, nitrogen oxides and stable free radicals. Measurements are possible in the paramagnetic case but also for magnetically ordered spins in solids. When focusing on the paramagnetic case the method is often called *electron paramagnetic resonance*, EPR.

The basic measurement principle is illustrated in Fig. 2.1. A static magnetic field  $B_0$  is applied to lift the degeneracy of the spin eigenstates. The sample is irradiated with microwave radiation which is absorbed by the excitation of magnetic dipolar transitions between the split levels. The conventional setup, explained in detail in section 2.4, which is commonly realised in commercial spectrometers, utilises a resonant cavity for the microwaves to enhance the sensitivity [39]. The spectrometer is thus operated at a fixed frequency  $f_0$  and spectra are recorded as a function of the applied external magnetic field  $B_0$ . Spectrometers operating at different frequency bands are used, with the X-band (approximately 10 GHz) being the most commonly used.

Another possibility is to use planar waveguides to form one-dimensional microwave resonators (see section 2.5.2). This allows to work not only at the fundamental frequency but also at higher harmonics of the resonator. In addition to that, the small size of these resonators allows them to be implemented in different cryostats to perform experiments in a larger temperature range. Here, such a technique is employed for measurements at different frequencies especially aiming towards millikelvin temperatures in a dilution refrigerator.

A completely different approach is to work with broadband transmission lines sweeping the frequency at fixed magnetic field. A frequency-domain spectrometer has been developed as part of this work [M1]. It is described in detail in section 2.5.1.

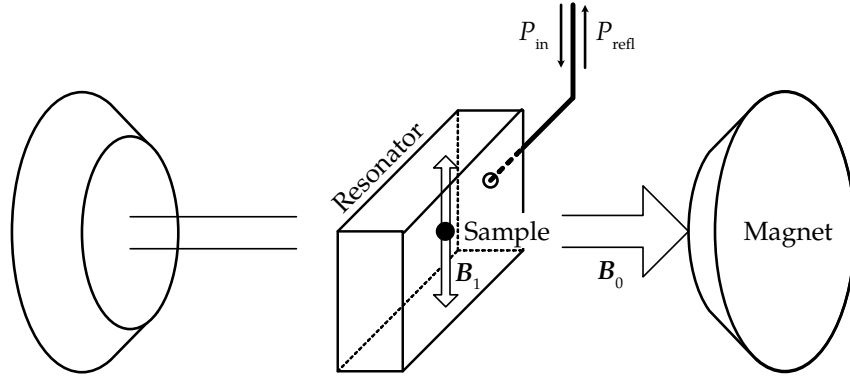


FIG. 2.1 *Basic Experimental Setup* The microwave radiation coupled in to a resonant cavity interacts with the sample by its magnetic field component  $B_1$ . ESR spectra are obtained by measuring the reflected microwave power  $P_{\text{refl}}$  as a function of the applied static magnetic field  $B_0 \perp B_1$  (adapted from [38]).

## 2.1 ESR in $S = 1/2$ Systems

This section on spin- $1/2$  systems is based on the lecture notes on EPR by G. Jeschke [40]. Statements taken from other sources are explicitly indicated.

Electrons carry a spin of  $S = 1/2$  associated with a magnetic moment  $\mu_e = -g\mu_B S$ . In an external magnetic field  $B_0$  the Zeeman effect lifts the degeneracy between the two eigenstates with  $m_S = \pm 1/2$  as shown in Fig. 2.2. The resulting two level system can be described by the *electron Zeeman Hamiltonian*

$$\mathcal{H}_{\text{EZ}} = \frac{\mu_B g}{\hbar} \mathbf{B}_0 \cdot \mathbf{S}_z. \quad (2.1)$$

Here  $g$  denotes the Landé  $g$ -factor and  $\mu_B = e\hbar/(2m_e)$  the Bohr magneton. In case of a free electron, relativistic quantum mechanics provides  $g = 2$ . Exact measurements slightly differ leading to  $g_e = 2.00231930436256(35)$  [41], a value also obtained theoretically by applying corrections from quantum electrodynamics. Transitions between the two eigenstates  $m_S = \pm 1/2$  are detected by ESR. The resonance condition for microwaves with energy  $E = hf_0$  is

$$hf_0 = g\mu_B B_0. \quad (2.2)$$

For microwave radiation in the X-band with a frequency of  $f_0 = 9.5$  GHz the resonance condition for the free electron is fulfilled at a resonance field  $B_0 = 338.98$  mT.

Within single crystals the  $g$ -factor is generally different along different crystallographic axes. Most universally it can be described by a symmetric tensor  $\mathbf{g}$ . The

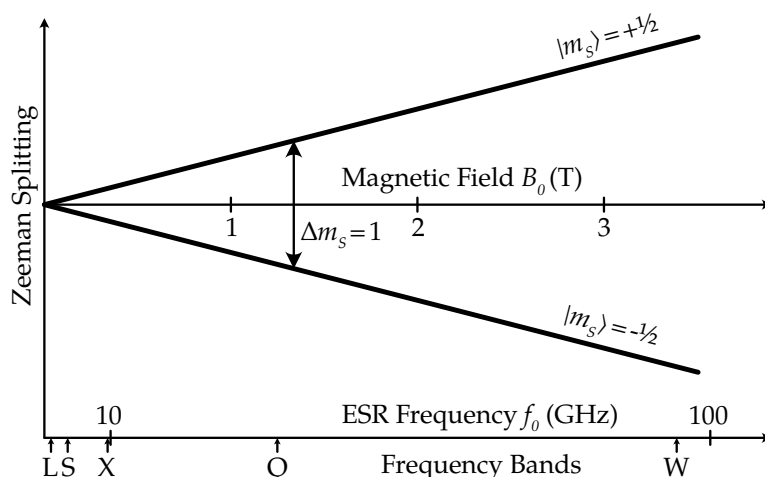


FIG. 2.2 ESR for  $S = 1/2$ . The  $m_S = \pm 1/2$  levels split in magnetic field allowing magnetic dipolar transitions with  $\Delta m_S = 1$  between them. The corresponding resonance frequency for a free electron is shown on the lower abscissa. The commonly used frequency bands in conventional ESR spectrometers are indicated below. (adapted from [40])

electron Zeeman Hamiltonian from equation 2.1 can thus be extended to

$$\mathcal{H}_{EZ} = \frac{\mu_B}{\hbar} \mathbf{B}_0^T \mathbf{gS}. \quad (2.3)$$

The  $g$ -tensor is usually expressed via its diagonal entries as an effective  $g$ -factor

$$g(\theta, \phi) = \sqrt{g_x^2 \sin^2 \theta \cos^2 \phi + g_y^2 \sin^2 \theta \sin^2 \phi + g_z^2 \cos^2 \theta} \quad (2.4)$$

where the  $z$ -direction of the spherical coordinates is given by  $\mathbf{B}_0$ .

The dominant contribution to the  $g$ -shift compared to the free electron  $\Delta g = g - g_e$  is usually the *spin orbit coupling*: Admixture of excited states with orbital momentum to the ground state contribute to the  $g$ -shift. Coupling to unoccupied orbitals leads to negative  $\Delta g$ , whereas coupling to fully occupied orbitals leads to positive  $\Delta g$ . As spin orbit coupling is a relativistic effect its influence generally increases with increasing mass thus  $\Delta g$  is typically small in organic compounds consisting of light elements.

Spins do not only interact with the external magnetic field  $\mathbf{B}_0$  but also with local fields induced by other spins – electron or nuclear – in their vicinity. In case of strong coupling between the electron spins the system is well described by a total spin  $S > 1/2$ . *Zero field splitting*, ZFS, plays a major role in such systems.

## 2 Electron Spin Resonance

For  $S = 1/2$  systems the *electron-electron interactions* are in general described by

$$\mathcal{H}_{\text{EEI}} = \mathbf{S}_k^\top \mathbf{J}_{kl} \mathbf{S}_l \quad (2.5)$$

where the tensor  $\mathbf{J}_{kl}$  describes the total interaction between the spins  $\mathbf{S}_k$  and  $\mathbf{S}_l$  including isotropic, anisotropic and antisymmetric contributions. Typically these interaction are subdivided in: the purely isotropic *exchange interaction*

$$\mathcal{H}_{\text{EX}} = J_{kl} \mathbf{S}_k^\top \mathbf{S}_l \quad (2.6)$$

with the exchange coupling  $J_{kl}$ ; the anisotropic, symmetric part including *anisotropic exchange* and *dipole-dipole interaction*

$$\mathcal{H}_{\text{AI}} = \mathbf{S}_k^\top \mathbf{D}_{kl} \mathbf{S}_l \quad (2.7)$$

where in the spin-polarised high field case (spins oriented along  $\mathbf{B}_0$ ) dipole-dipole interaction is described in the principal axes system by the symmetric tensor

$$\mathbf{D}_{\text{DD},kl} = \frac{\mu_0}{4\pi\hbar} \frac{g_k g_l \mu_B^2}{r^3} \begin{pmatrix} -1 & 0 & 0 \\ 0 & -1 & 0 \\ 0 & 0 & 2 \end{pmatrix} \quad (2.8)$$

and antisymmetric – *Dzyaloshinskii-Moriya*, DM – exchange

$$\mathcal{H}_{\text{DM}} = \mathbf{d}_{kl} \cdot (\mathbf{S}_k \times \mathbf{S}_l) \quad (2.9)$$

with the DM vector  $\mathbf{d}_{kl}$ .

Nuclear spins  $\mathbf{I}_m$  can interact with an electron spin  $\mathbf{S}_k$  via *hyperfine interaction*

$$\mathcal{H}_{\text{HFI}} = \mathbf{S}_k^\top \mathbf{A}_{km} \mathbf{I}_m. \quad (2.10)$$

In addition to that pure nuclear spin interactions have to be taken into account: the *nuclear Zeeman interaction*

$$\mathcal{H}_{\text{NZ}} = \gamma_m \mathbf{B}_0^\top \mathbf{I}_m \quad (2.11)$$

with the nuclear gyromagnetic ratio  $\gamma_m$  for spin  $\mathbf{I}_m$ ; and *nuclear quadrupole interaction* for  $I > 1/2$

$$\mathcal{H}_{\text{NQI}} = \mathbf{I}_m^\top \mathbf{P}_m \mathbf{I}_m. \quad (2.12)$$

At low temperatures the spins can pair due to dimerisation or formation of valence bonds between nearest neighbour spins. This leads to a nonmagnetic singlet  $S = 0$  ground state. In this case ESR can only be observed between the levels of the excited triplet state  $S = 1$ . The triplet is separated from the ground state singlet by a spin gap  $\Delta$ . Upon lowering the temperature  $T \rightarrow 0$  the ESR signal therefore decreases exponentially as the thermally activated triplet state gets depopulated.

## 2.2 Basics of ESR: Bloch Equations

This section on Bloch equations and relaxation is based on the lecture notes on EPR by G. Jeschke [40]. Statements taken from other sources are explicitly indicated.

In this section ESR is described in a classical picture which treats the interaction of the macroscopic magnetisation  $\mathbf{M}$  of a sample with the microwave magnetic field  $\mathbf{B}_1(t)$ . The population of the two spin eigenstates split by  $\Delta E$  in energy through the external magnetic field  $\mathbf{B}_0$  as in equation (2.2) determines the magnetisation of the sample. We assume  $\mathbf{B}_0 = B_0 \cdot \hat{z}$  along the  $z$ -direction. Spins in the energetically higher  $|\alpha\rangle$  state with  $m_s = +1/2$  carry a magnetic moment parallel to the external field whereas spins in the lower lying  $|\beta\rangle$  state with  $m_s = -1/2$  carry an antiparallel magnetic moment. As these moments mutually compensate, only the population difference contributes to the net magnetisation. The populations can be calculated with the Boltzmann statistics

$$p_\alpha = \frac{\exp\left[-\frac{\Delta E}{k_B T}\right]}{1 + \exp\left[-\frac{\Delta E}{k_B T}\right]} \quad (2.13)$$

$$p_\beta = \frac{1}{1 + \exp\left[-\frac{\Delta E}{k_B T}\right]}$$

As the energy difference of the levels is typically small ( $\Delta E/k_B = 0.48$  K for  $f_0 = 9.5$  GHz) compared to the thermal energy at typical experimental conditions, a high temperature approximation can be made: The exponential function is expanded to first order in the polarisation  $\varepsilon = \Delta E/(k_B T) = g_z \mu_B B_0/(k_B T)$  leading to

$$p_\alpha \approx \frac{1 - \varepsilon}{2}$$

$$p_\beta \approx \frac{1 + \varepsilon}{2} \quad (2.14)$$

The magnetisation in thermal equilibrium is then given by the sum of the magnetic moments  $\mu_i$  of the individual spin normalised to the sample volume  $V$ .

$$M_0 = \frac{1}{V} \sum_{i=1}^N \mu_i = \frac{\epsilon N g \mu_B}{2} \hat{z} \quad (2.15)$$

In magnetic field the magnetisation obeys the classical equation of motion

$$\frac{d\mathbf{M}}{dt} = \mathbf{M} \times \frac{-g\mu_B}{\hbar} \mathbf{B}(t) \quad (2.16)$$

In a static magnetic field along  $z$  and in thermal equilibrium  $\mathbf{M}$  is also pointing along  $z$  leading to a vanishing time derivative and therefore a constant magnetisation. When deviating  $\mathbf{M}$  from the  $z$  direction it starts to precess around  $z$  with the Larmor frequency  $\omega_0 = B_0 g \mu_B / \hbar$  according to equation (2.2).

To deviate the magnetisation from the equilibrium position a linearly polarised microwave magnetic field  $\mathbf{B}_1(t)$  is applied in the  $x$  direction.

$$B_{1x}(t) = 2B_1 \cos(\omega_{\text{mw}}t) \quad B_{1y}(t) = B_{1z}(t) = 0 \quad (2.17)$$

Here  $\omega_{\text{mw}}$  denotes the frequency and  $2B_1$  denotes the amplitude of the microwave magnetic field. With a time-dependent magnetic field one cannot solve the equation of motion (2.16) for the magnetisation analytically. Therefore an approximation is employed: the linearly polarised microwave magnetic field is written as a superposition of a right- and left-handed circularly polarised field. The right-handed component follows the precession of the magnetisation whereas the left-handed component rotates in the opposite direction and therefore does on average not markedly change the direction of the magnetisation vector. Neglecting this left-handed component leads to a vanishing time-dependence in the equations of motion (2.16) of the magnetisation vector.

$$\begin{aligned} \frac{dM_x}{dt} &= -(\omega_0 - \omega_{\text{mw}})M_y \\ \frac{dM_y}{dt} &= (\omega_0 - \omega_{\text{mw}})M_x - \omega_1 M_z \\ \frac{dM_z}{dt} &= \omega_1 M_y \end{aligned} \quad (2.18)$$

where  $\omega_1$  denotes the Larmor frequency for the microwave magnetic field  $\omega_1 = B_1 g_x \mu_B / \hbar$ . In the rotating frame the magnetisation precesses around  $z$  with the differ-

ence frequency between the Larmor and the microwave frequency

$$\Omega = \omega_0 - \omega_{\text{mw}} \quad (2.19)$$

In addition to that the magnetisation precesses around  $x$  with the frequency  $\omega_1$  due to the microwave field. In combination this leads to a nutation with frequency  $\omega_{\text{nut}}$  around an axis tilted towards  $x$  by an angle  $\theta$  according to the  $z$ -direction.

$$\omega_{\text{nut}} = \sqrt{\Omega^2 + \omega_1^2} \quad \theta = \arctan\left(\frac{\omega_1}{\Omega}\right) \quad (2.20)$$

On resonance ( $\Omega = 0$ ) it holds  $\theta = 90^\circ$  and  $\omega_{\text{nut}} = \omega_1$  whereas far off resonance  $\theta \approx 0$ , i.e. the magnetisation stays unaffected in its thermal equilibrium position along  $z$ .

In reality relaxation processes drive the magnetisation back to its equilibrium position. Two processes are generally distinguished: longitudinal relaxation driving the magnetisation back to the equilibrium value  $M_0$  along the  $z$ -direction through spontaneous transitions between the energy levels, and transversal relaxation of the  $x$  and  $y$ -components of the magnetisation due to spontaneous transitions of individual spins in addition to flip-flop processes of pairs of spins. In both cases the relaxation happens exponentially in time with associated relaxation times  $T_1$  respectively  $T_2$ . Adding these relaxation processes to the equations of motion for the magnetisation (2.18) leads to the *Bloch equations*

$$\begin{aligned} \frac{dM_x}{dt} &= -\Omega M_y - \frac{M_x}{T_2} \\ \frac{dM_y}{dt} &= \Omega M_x - \omega_1 M_z - \frac{M_y}{T_2} \\ \frac{dM_z}{dt} &= \omega_1 M_y - \frac{M_z - M_0}{T_1} \end{aligned} \quad (2.21)$$

For a continuous wave (CW) ESR experiment a stationary state will eventually develop after irradiating far longer than the characteristic relaxation times  $T_1$  and  $T_2$ . This is illustrated in Fig. 2.3A in the lab frame. In this stationary state the magnetisation vector is constant within the rotating frame, thus the derivatives in the Bloch equations

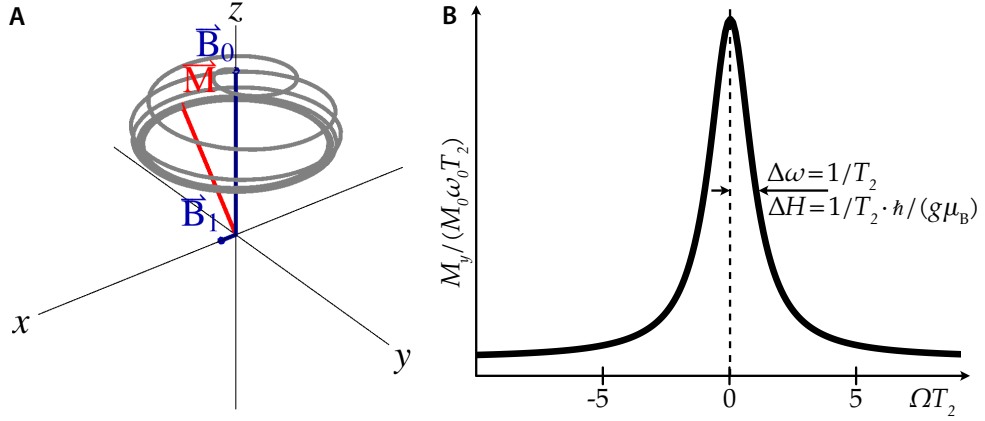


FIG. 2.3 *Bloch Equations: Absorption* (A) *Magnetisation in the Lab Frame* Turning on the microwave irradiation  $B_1$  on resonance ( $\Omega = 0$ ) leads to a deflection of the magnetisation  $M$  from the  $z$ -direction. After some time  $t \gg (T_1, T_2)$  a steady state is established where the magnetisation precesses around  $z$  ( $M_x$  and  $M_y$  constant in the rotating frame) (reproduced from [42], ©2008 Wolfram Demonstrations Project). (B) *Absorption Spectrum* The absorption spectrum possesses a Lorentzian line shape with line width  $1/T_2$ .

vanish. The resulting system of equations can be easily solved

$$\begin{aligned} M_x &= M_0 \omega_1 \frac{\Omega T_2^2}{1 + \Omega^2 T_2^2 + \omega_1^2 T_1 T_2} \\ M_y &= -M_0 \omega_1 \frac{T_2^2}{1 + \Omega^2 T_2^2 + \omega_1^2 T_1 T_2} \\ M_z &= M_0 \frac{1 + \Omega^2 T_2^2}{1 + \Omega^2 T_2^2 + \omega_1^2 T_1 T_2} \end{aligned} \quad (2.22)$$

Here the absorption spectrum is proportional to the  $y$ -component of the magnetisation. For small microwave power, i.e. small  $\omega_1$ , one can neglect the term

$$\omega_1^2 T_1 T_2 \ll 1 \quad (2.23)$$

In this case  $M_z \approx M_0$ , and  $M_x, M_y$  are proportional to  $\omega_1$ . The absorption spectrum in this *linear regime* is then of Lorentzian shape with line width  $\Gamma = 1/T_2$  as shown in Fig. 2.3B

$$M_y(\Omega) = M_0 \omega_1 T_2 \frac{1}{1 + \Omega^2 T_2^2} \quad (2.24)$$

As spectra are typically recorded as a function of the magnetic field  $B_0$  the line width

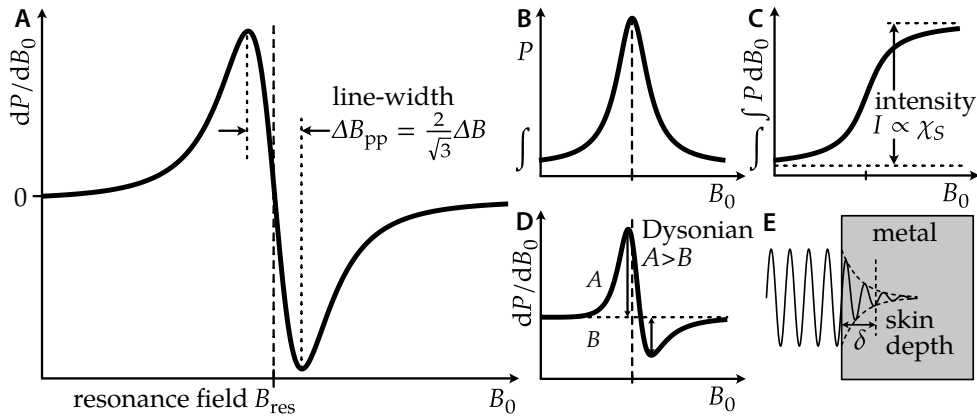


FIG. 2.4 *ESR Spectra* First derivative of the absorbed microwave power for a Lorentzian shaped ESR absorption (A). Integrating the spectrum leads to the absorbed power (B) and further to the intensity (C). Metallic samples show an asymmetric line shape (D) owing to the finite skin depth (E).

translates to

$$\Delta B = \frac{1}{T_2} \frac{\hbar}{g\mu_B} \quad (2.25)$$

in the field-domain.

## 2.3 Parameters of ESR Spectra

This section on ESR parameters is mainly based on the thesis of M. Dumm [38]. Statements taken from other sources are explicitly indicated.

All samples investigated for this thesis are  $S = 1/2$  systems. Four basic parameters characterise a single ESR line in its spectrum as illustrated in Fig. 2.4:

- the *line shape*
- the *ESR intensity*  $I$ , the area under the absorption line, proportional to the *spin susceptibility*  $\chi_S$
- the *resonance field*  $B_{\text{res}}$ , linked to the *g-factor* by the resonance condition  $g = hf_0 / \mu_B B_{\text{res}}$
- the *line width*  $\Delta B$ , defined as the half width at half maximum

### LINE SHAPE

In a homogeneous system, where relaxation processes and internal fields are the same for every spin under observation, the ESR spectrum has the natural Lorentzian shape as discussed in section 2.2. In typical solid state systems however the environment slightly varies for each spin leading to a Gaussian distribution of resonance fields. This inhomogeneous broadening results in the observation of a Gaussian shaped absorption line. Owing to exchange narrowing the spectra of the samples investigated for this thesis are of Lorentzian shape as explained in the paragraph on the line width.

In conductive samples the skin effect has to be taken into account additionally as it can lead to a distortion of the ESR signal as shown in Fig. 2.4D. The shielding currents which lead to the finite skin depth  $\delta \approx \sqrt{\rho/\pi f_0 \mu_0}$ , for resistivity  $\rho$ , cause a phase shift between the microwave electric field  $E_1$  and magnetic field  $B_1$  within the sample. In addition to that, if the skin depth is smaller than the sample's dimensions only a fraction of the sample's volume can be penetrated by the microwave field and thus contribute to the absorption, complicating the correct analysis of the signal's intensity. The resulting ESR line is asymmetric and can be characterised by the ratio  $\alpha$  between dispersion and absorption [39, 43, 44]. The absorbed power in a Dysonian absorption line is described by

$$P(B) \propto \frac{\Delta B + \alpha (B - B_{\text{res}})}{(B - B_{\text{res}})^2 + \Delta B^2} \quad (2.26)$$

For  $\alpha = 0$  the dispersion part vanishes resulting in a pure Lorentzian line shape.

### INTENSITY

The intensity  $I$  of an ESR line is given by the area under the absorption curve (Fig. 2.4B,C). For the typical first derivative spectra integrating the data twice is therefore needed to calculate the intensity. In case of Lorentzian lines, it can also be obtained by fitting the spectra as described in section 2.3.1.

The ESR intensity is directly linked to the spin susceptibility  $\chi_S$  as follows: Averaging over one period of the excitation (2.17) the microwave power absorbed by ESR is [39]

$$P(f_0) = \frac{2\pi f_0 B_1^2}{\mu_0} \chi''(f_0) \quad (2.27)$$

where  $\chi''$  is the imaginary part – the absorption part – of the dynamical susceptibility.

It is related to the spin susceptibility via Kramers-Kronig relations

$$\chi_S = \frac{2}{\pi B_{\text{res}}} \int_{-\infty}^0 \chi''(B_0) dB_0 \propto \int_{-\infty}^0 P(B_0) dB_0 = I \quad (2.28)$$

The spin susceptibility  $\chi_S$  is therefore directly proportional to the ESR intensity  $I$ . As the amplitude of the microwave magnetic field spatially varies and the shape and position of the sample within the resonator are not precisely known, the value of  $B_1$  within the sample cannot be precisely determined. Thus measurements of the spin susceptibility are usually done relative to a known standard.

Determining the spin susceptibility by ESR measurements has several advantages compared to static measurements, e.g. by SQUID magnetometer: With ESR the paramagnetic contributions are measured directly and no diamagnetic background has to be subtracted; additionally as ESR is a spectroscopic method, contributions from different magnetic species can be analysed separately which allows to separate the influence of paramagnetic impurities.

#### RESONANCE FIELD

The effective magnetic field at the spin's position is generally different from the applied external field  $B_0$  due to local fields  $B_{\text{loc}}$ . The resonance field  $B_{\text{res}}$  at which the ESR is observed for a certain frequency  $f_0$  is thus influenced by the different interactions discussed in section 2.1. In absence of spin-spin interactions the local fields are directly linked to the  $g$ -shift  $\Delta g$  via equation (2.2)

$$hf_0 = \Delta g \mu_B B_{\text{loc}} \quad (2.29)$$

Angle-dependent measurements thus allow to determine all 6 independent components of the  $g$ -tensor  $\mathbf{g}$ .

#### LINE WIDTH

One would expect inhomogeneous broadening in typical solids as the environment and thus the resonance frequency  $\Omega$  of each spin is slightly different. In case of large exchange coupling  $J \gg \Delta\Omega$ , i.e. much larger than the distribution of resonance frequencies, the mixing of states results in a Lorentzian absorption line at a central frequency [45]. This effect is called *exchange narrowing*. For the systems investigated for this thesis the condition of large  $J$  is always fulfilled.

As discussed in section 2.2 the excited states have finite lifetimes. Relaxation processes through which the energy is dissipated to the lattice are characterised by the

*spin-lattice relaxation time*  $T_1$ . Spin-spin interaction also causes relaxation characterised by the *spin-spin relaxation time*  $T_2^*$ . Both contribute to broadening of the absorption spectra leading to the line width  $\Gamma = 1/T_2$

$$\frac{1}{T_2} = \frac{1}{2T_1} + \frac{1}{T_2^*} \quad (2.30)$$

Typically in solids  $T_1 \gg T_2$ , e.g. spin-spin processes dominate the line width. In the case of metals this does not hold any more and  $T_1 = T_2$ . According to Elliott [46] phonons modulating the spin orbit coupling are then the dominant contribution to  $T_1$ . Therefore the ESR line width in metals is directly connected to the electron scattering time hence the resistivity  $\rho$

$$\Delta B \propto (\Delta g)^2 \rho \quad (2.31)$$

where  $(\Delta g)^2 \propto Z^4$  ( $Z$ : atomic number) in case of isolated atoms [38]. Heavier elements thus lead to larger line widths due to the larger spin-orbit coupling.

In more resistive samples or for low temperatures, the density of phonons rapidly drops. Therefore, other contributions to the line width become important. For exchange-coupled systems the ESR lines can be described using the Kubo-Tomita theory [47]. For  $S = 1/2$ , thus in absence of single-ion anisotropy, three contributions are discussed for one- and two-dimensional systems in [48, 49]: dipole-dipole interaction, anisotropic exchange interaction, as well as Dzyaloshinskii-Moriya interaction. If nuclear spins would be present, hyperfine interaction would also lead to line broadening. For the analysis the spin Hamiltonian is split into two parts  $\mathcal{H} = \mathcal{H}_0 + \mathcal{H}'$ . The main  $\mathcal{H}_0$  includes the dominating Zeeman and exchange terms. All other terms are contained in the perturbation  $\mathcal{H}'$  and contribute to the line broadening. In the field-domain the line width can be expressed as

$$\Delta B \approx \frac{\hbar^2}{g\mu_B |J|} M_2 (J/k_B T) \quad (2.32)$$

with the second moment  $M_2$  of the relaxation function. The detailed form of  $M_2$  for the different contributions depends on the lattice of the studied system.

### 2.3.1 Fitting ESR Spectra

All ESR spectra have been fitted with the method of least squares using the software Spektrolyst[50]. For the first derivative spectra the following function has been used

for a single ESR line

$$f(B_0) = A \frac{-2 \frac{B_0 - B_{\text{res}}}{\Delta B} + \alpha \left[ 1 - \left( \frac{B_0 - B_{\text{res}}}{\Delta B} \right)^2 \right]}{\left[ 1 + \left( \frac{B_0 - B_{\text{res}}}{\Delta B} \right)^2 \right]^2} + mB_0 + c \quad (2.33)$$

The fit parameters are: the amplitude  $A$ , the resonance field  $B_{\text{res}}$ , the line width  $\Delta B$ , the dispersion-absorption ratio  $\alpha$  and the slope  $m$  and offset  $c$  of a linear background. The intensity can be calculated from the fit parameters as  $I = A\Delta B^2 \sqrt{1 + \alpha^2}$ . The software allows to fit multiple ESR lines in a single spectrum at the same time. For very broad lines with  $\Delta B$  of the order of  $B_{\text{res}}$  or larger, a second term describing the resonance at  $-B_{\text{res}}$  can be added to the function.

## 2.4 Conventional ESR Spectrometers

This section is mainly based on the chapter *An EPR Primer* in Bruker Corporation's EPR user guides by R. Weber [51].

The working principle of conventional CW ESR spectrometers, shown schematically in Fig. 2.5, is explained in the following.

### MICROWAVE BRIDGE

Spectra are recorded as a function of the external magnetic field  $B_0$  swept by an electromagnet. The microwave bridge houses source and detector for the microwave radiation. The source, in modern spectrometers a Gunn diode, emits microwaves at a fixed power. An attenuator is therefore used to change the incident microwave power. A circulator separates the incident and reflected microwaves. Microwaves incident at port 1 are only transmitted to port 2 and the reflected microwaves from the cavity are only transmitted to port 3. A detector diode is used to detect the reflected microwaves. The detector operates in the linear regime (voltage proportional to square root of incident power) around its working point. To ensure linear operation a reference arm is needed to apply a bias to the detector. It is equipped with an attenuator to adjust the bias as well as a phase shifter which allows to adjust the phase of the microwaves from the reference arm to match the phase from the reflected microwaves.

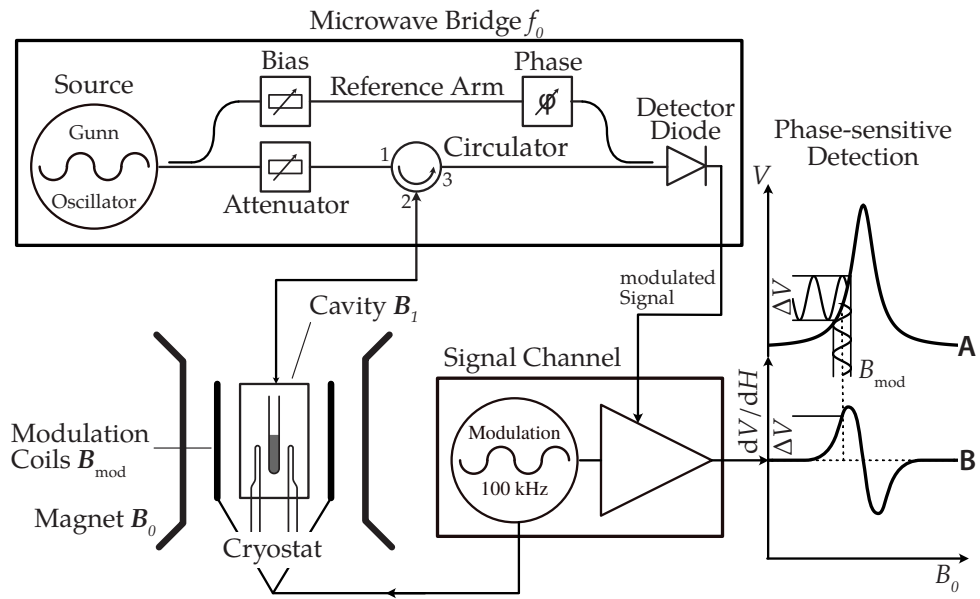


FIG. 2.5 *Conventional CW ESR Spectrometer* In conventional CW ESR spectrometers, spectra are measured as a function of external magnetic field  $B_0$ . A phase-sensitive detection scheme using magnetic field modulation is employed to measure the reflected microwave power from a microwave cavity.

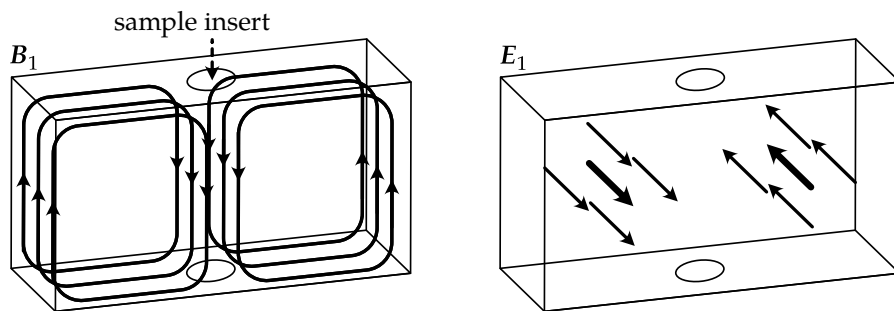


FIG. 2.6 *Rectangular  $TE_{102}$  Cavity* Microwave magnetic field  $B_1$  and electric field  $E_1$  inside a standard ESR cavity. The sample should be placed in the maximum of the magnetic field and minimum of the electric field in the centre of the resonator. (based on [51])

## MICROWAVE CAVITY

The sample is placed inside a cavity resonator. The stored energy inside the resonator leads to an increased microwave magnetic field  $B_1$  at the sample which enhances the coupling of the spins to the microwaves. The resonator is dimensioned in a way that the chosen mode has an antinode of the magnetic field as well as a node of the electric field at the sample position as shown in Fig. 2.6. The suppressed electric field reduces dielectric losses in the sample. Cavities are characterised by their quality factor

$$Q = \frac{f_0}{\Delta f} \quad (2.34)$$

with the resonant frequency  $f_0$  and the bandwidth  $\Delta f$ . When the impedance of the loaded cavity is matched to the impedance of the waveguide no reflection occurs. This critical coupling condition can be achieved by varying the coupling between waveguide and cavity typically done by an adjustable iris. Coupling of the cavity has to be done with the external magnetic field off the ESR resonance of the sample.

When the external field is swept through the ESR absorption, the sample absorbs microwave energy, lowering  $Q$  and changing the impedance of the cavity. It is then no longer critically coupled hence microwaves are reflected to the microwave bridge. An ESR signal can thus be detected.

In addition to the absorption, the  $x$ -component of the magnetisation, the dispersion  $\chi'$ , changes the frequency of the cavity if the excitation is close to the ESR resonance. To compensate for this change, and thus ensure that pure absorption  $\chi''$  is detected without any dispersion  $\chi'$  mixed into the signal, an automatic frequency control circuit is used. It is a closed loop control system which locks the frequency of the microwave source to the resonance frequency of the cavity.

## SIGNAL CHANNEL

As a diode detector is sensitive to signals in a large frequency range it detects noise with large bandwidth besides the ESR signal. To suppress this noise and therefore increase the signal-to-noise ratio, SNR, a phase-sensitive detection scheme is employed. Modulation coils mounted on the cavity create a small magnetic field  $B_{\text{mod}}$  typically alternating with 100 kHz. The signal channel, a lock-in amplifier, is used to demodulate the signal by effectively lowering the detection bandwidth and thus reducing noise. As a result the first derivative of the absorption is recorded. Increasing the modulation amplitude increases the sensitivity, however the line shape can get distorted. Generally

the modulation amplitude should not be chosen larger than  $\Delta B/3$  to not artificially broaden the line [39].

### 2.4.1 Technical Details

A large fraction of the experiments for this project were performed using conventional CW ESR spectrometers. Two instruments at 1. Physikalisches Institut have been employed: a Bruker EMXplus X-band spectrometer operating at  $f_0 \approx 9.5$  GHz as well as a Bruker ELEXYS E680 W-band spectrometer operating at  $f_0 \approx 95$  GHz. The former one utilises an electromagnet for fields up to  $B_0 < 1$  T whereas the latter one is equipped with a superconducting magnet reaching fields up to  $B_0 < 6$  T.

The mainly used X-band spectrometer is normally equipped with a metallic rectangular cavity with TE<sub>102</sub> mode (Bruker ER4102ST) and an unloaded quality factor of approximately 6000. In addition to that, a double rectangular cavity (Bruker ER4105DR) can be utilised for the determination of spin concentrations against a reference sample measured simultaneously. The W-band spectrometer is operated with a cylindrical cavity. Both spectrometer are equipped with a <sup>4</sup>He flow cryostat for temperature control between 4 K and 300 K. The cryostat (Oxford Instruments ESR900) for the X-band spectrometer employs a glass dewar reaching inside the cavity. This allows the cavity to stay at room temperature keeping its properties unaltered while the temperature of the sample is changed. A wire wound heater warms up the helium prior to entering the glass dewar where it flows along the sample tube. Temperature control is achieved with a Cernox® sensor at the helium inlet connected to a temperature controller (Oxford Instruments ITC503). A second cryostat (Oxford Instruments ESR910) which offers the possibility to pump on the helium was used to achieve lower temperatures down to 2 K. A goniometer, motorised for the X-band, manual for the W-band, allows to rotate the sample around the vertical axis, perpendicular to the horizontal magnetic field direction to record spectra as a function of the sample's orientation. The crystals are mounted with Apiezon® N vacuum grease on glass rods which are fixed inside covering glass tubes with paraffin wax. All glass ware has to be fabricated from synthetic quartz in order to be free of paramagnetic impurities interfering with the measurements.

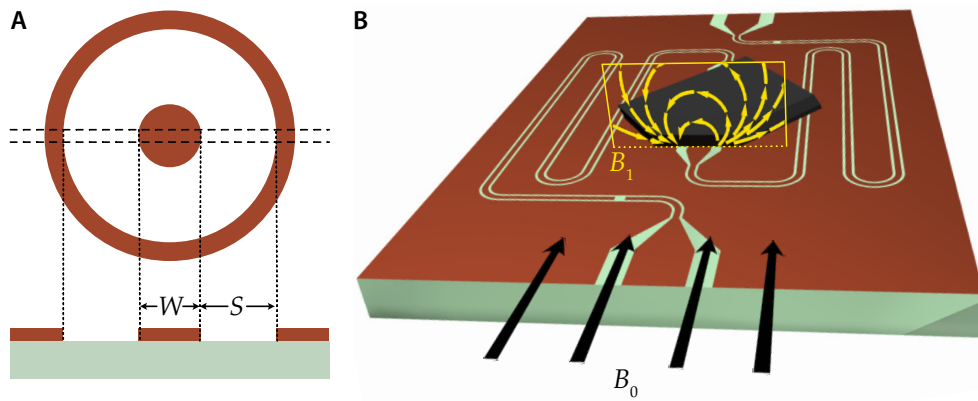


FIG. 2.7 *Coplanar Waveguides* (A) The CPW geometry can be imagined as a horizontal cut through a coaxial cable. The centre conductor width  $W$  and the gap between centre conductor and ground planes  $S$  are the defining dimensions. (B) Coplanar waveguide resonator with mounted sample. The direction of the static magnetic field  $B_0$  is shown in black. The microwave magnetic field  $B_1 \perp B_0$  (yellow) penetrates the sample volume where it is subject to absorption by ESR.

## 2.5 ESR using Coplanar Waveguides

The resonant cavities used in conventional ESR setups to achieve high sensitivity limit the operation of the spectrometers to a single frequency corresponding to a fixed magnetic field as described in the previous section. This mode of operation can be insufficient for the investigation of materials with field-induced phase transitions or large zero-field splitting as multiple frequencies are needed to resolve their whole phase diagram [52–56]. So far a number of magnetic resonance setups have been developed to overcome this limitation. Measurements at multiple frequencies are possible with planar one-dimensional resonators which allow operating at harmonics of their fundamental resonance frequency [57–59]. Numerous approaches have been used to achieve broadband operation: tunable cavities [60], non-resonant coils [61], coaxial lines [62], or planar waveguides [63–68]. In the following, two techniques based on coplanar waveguides, CPWs, are introduced: firstly a newly-developed instrument capable of frequency-domain ESR measurements based on CPWs and field modulation [M1], and secondly using CPW resonators for ESR measurements.

A CPW is a two-dimensional microwave transmission line geometry with planar conductors in a single plane [69, 70]. It can be thought of as a lengthwise slice of a coaxial cable as shown in Fig. 2.7A. CPWs are fabricated by micro-structuring of a metallisation layer on a substrate, typically silicon or sapphire. For this work metallic

(copper) as well as superconducting (niobium and YBCO) waveguides have been employed.

As the magnetic field  $B_1$  extends into the volume above the waveguide, a sample placed on top of the chip can interact with the microwave as illustrated in Fig. 2.7B. In the CPW geometry electromagnetic waves are guided in a quasi-TEM mode. The microwave electric field  $E_1$  is oriented perpendicular to the propagation direction. For the magnetic field  $B_1$  this is only approximately true as there is a small component in the propagation direction alternating with half of the wavelength  $\lambda/2$  resulting in an elliptically polarised magnetic field [71]. As in our case the wavelength  $\lambda$  is typically large compared to the size of the studied samples, the magnetic field component in the propagation direction can also be treated as constant. Due to the quasi-TEM propagation applying a static magnetic field  $B_0$  parallel to the direction of the CPW leads to the standard ESR magnetic field configuration  $B_1 \perp B_0$ .

The geometry of the CPW is defined by two dimensions (see Fig. 2.7A): the inner conductor width  $W$  and the gap size between the inner conductor and the ground planes  $S$ . To couple microwave radiation into the waveguide efficiently, its impedance has to be matched to the standard  $50 \Omega$  of the coaxial feed lines. This can be achieved by a certain ratio of the dimensions, dependent only on the dielectric constant of the substrate  $\epsilon_r$ . The impedance of the waveguide can be calculated using conformal mapping theory [69]. Assuming a thick substrate compared to the CPW dimensions the effective dielectric constant can be approximated as  $\epsilon_{\text{eff}} = (\epsilon_r + 1)/2$  as the field is half in the substrate below and half in the air above the CPW. The characteristic impedance  $Z_0$  is then given by [69]

$$Z_0 = \frac{30\pi}{\sqrt{\epsilon_{\text{eff}}}} \frac{K(k'_0)}{K(k_0)} \quad \text{with} \quad k_0 = \frac{W}{W + 2S} \quad \text{and} \quad k'_0 = \sqrt{1 - k_0^2} \quad (2.35)$$

Here,  $K(k)$  denotes the complete elliptic integral of the first kind<sup>(1)</sup>. Using  $\epsilon_r = 10$  for sapphire,  $Z_0 = 50 \Omega$  is achieved for a ratio  $W/S \approx 2.2$ .

The components of the microwave electric field  $E_1$  as well as magnetic field  $B_1$  above the waveguide can be calculated according to [69, 71]. A plot of the field lines in the plane perpendicular to the propagation direction is shown in Fig. 2.8A. The electric field lines point from the inner conductor towards the ground planes, whereas the magnetic field encircles the inner conductor. The absolute value of the microwave

(1)  $K(k) = \int_0^{\pi/2} 1/\sqrt{1 - k^2 \sin^2(\theta)} d\theta$ . Special care is needed as different definitions of  $K$  exist, e.g. Wolfram Mathematica uses  $K(m) = \int_0^{\pi/2} 1/\sqrt{1 - m \sin^2(\theta)} d\theta$

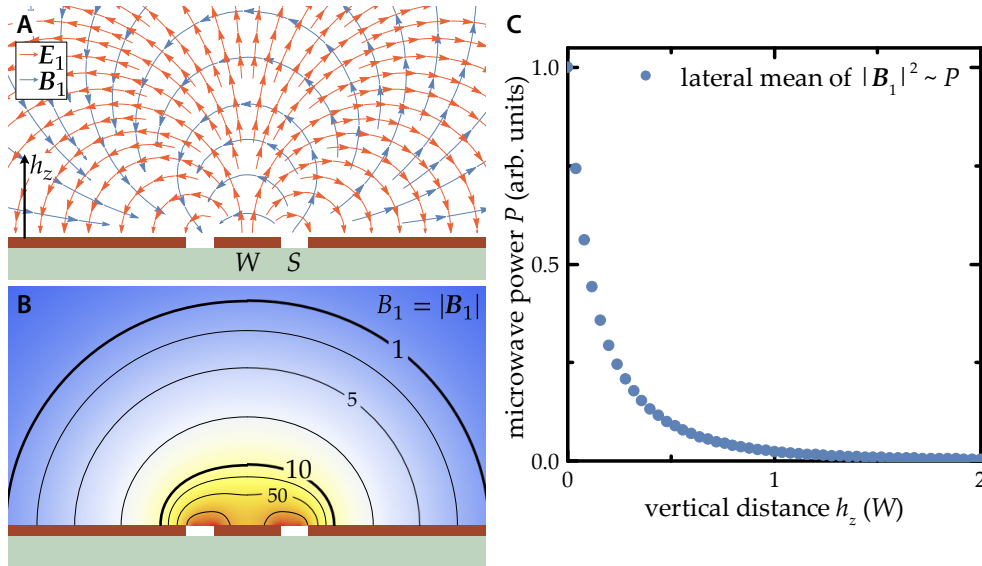


FIG. 2.8 *Coplanar Waveguide Field Components* (A) Field lines of microwave electric  $E_1$  and magnetic field  $B_1$  above a CPW shown in a cut perpendicular to the propagation direction. (B) Magnitude of the microwave magnetic field  $B_1$  in the same view. (C) Lateral mean of the square of the magnetic field  $B_1^2$  as a function of the vertical distance  $h_z$  above the surface of the CPW in units of the inner conductor width  $W$ .

magnetic field  $|B_1|$  within the plane is shown in panel B. The field decreases rapidly when moving away from the surface of the CPW, the thick contour lines correspond to a decrease of a factor of ten each. Concerning the ESR absorption, the relevant physical quantity is the microwave power  $P \propto |B_1|^2$ . The mean value of  $|B_1|^2$  across the vertical direction can be used as an indicator for the dependence of the sensitivity on the distance of the sample to the CPW surface. It is shown as a function of the distance  $h_z$  above the surface of the CPW in units of the inner conductor width  $W$  in Fig. 2.8C. Moving away from the surface by the inner conductor width  $W$  reduces microwave power  $|B_1|^2$  to approximately 2.5% of the values directly at the surface.

Using smaller dimensions increases the magnitude of the microwave magnetic field close to the surface, however the roll-off happens within the smaller dimensions. A small gap of approximately  $20 \mu\text{m}$  always remains between the sample and the surface even when attaching the sample directly on the metallisation layer with the help of vacuum grease [72]. Thus larger widths can be beneficial to study bulk samples as the field can penetrate further into the sample volume.

Two types of ESR experiments can be performed using CPWs. Measuring the transmission through a CPW with attached sample in a fixed external magnetic field  $B_0$  allows to perform ESR measurements as a function of frequency  $f$  as described in

section 2.5.1. Introducing two capacitive coupling gaps into the waveguide results in a one-dimensional resonator. Such a resonator shows equally spaced resonances at harmonics of the fundamental frequency  $f_n = nf_0$  allowing to operate at multiple fixed frequencies. In this case the ESR active sample acts as a perturbation to the resonator and spectra are recorded by measuring the bandwidth  $f_B$  of the resonator as a function the applied external magnetic field  $B_0$  as described in further detail in section 2.5.2.

### 2.5.1 Frequency-Domain ESR

The contents of this section describing the technical details of the instrument have already been published as [M1] **B. Miksch**, M. Dressel and M. Scheffler, *Cryogenic frequency-domain electron spin resonance spectrometer based on coplanar waveguides and field modulation*, Rev. Sci. Instrum. **91**, 025106 (2020) and is reprinted here with the permission of AIP Publishing.

Within the framework of this project an instrument capable of frequency-domain ESR measurements has been newly developed. It builds upon previous work from the institute, where coplanar transmission lines have already been used to demonstrate the possibility of frequency-domain ESR measurements in a large frequency range between 0.1 GHz and 67 GHz [67, 68]. Here, magnetic field modulation is employed allowing for a vastly improved sensitivity. While previous modulation-based on-chip studies focused on thin-film ferromagnetic resonance at room temperature [73–77], we aimed towards a wider parameter range, in particular, low temperatures. This goal has been reached and operation of the instrument between 1.6 K and 300 K in a superconducting magnet allowing for fields up to 8 T could be demonstrated. Measurements of three different samples were performed to present the capabilities of the instrument. The stable free-radical molecule DPPH (2,2-diphenyl-1-picrylhydrazyl) with its narrow line width is used as a standard to calibrate the amplitude of the magnetic field modulation. A single crystalline sample of ruby ( $\text{Cr}^{3+}:\text{Al}_2\text{O}_3$ ) with a concentration of 0.5 % is measured in a broad frequency and temperature range as an example for a material with a more complex energy level scheme. Spectra are taken with as well as without field modulation to demonstrate the SNR enhancement. The overall sensitivity of the instrument is estimated with an easy to handle carbon fibre sample [78].

## EXPERIMENTAL SETUP

The setup of the frequency-domain ESR experiment consists of 3 parts:

- $^4\text{He}$  cryostat with superconducting magnet and variable temperature insert
- ESR insert with probe-head containing the sample box with CPW and attached sample as well as the modulation coil
- Instrumentation for microwave generation and detection as well as driving the modulation field

The working principle of the individual parts is described in the following paragraphs listing the devices used.

The instrument is set up in an Oxford Instruments Integra superconducting magnet in a  $^4\text{He}$  bath cryostat containing a variable temperature insert, VTI, within the magnet bore. Magnetic fields up to 8 T can be applied in vertical direction parallel to the surface of the CPW. Temperatures as low as 1.4 K can be achieved by running liquid helium through a needle valve into the sample space which is pumped by a mechanical pump. A Lakeshore Cernox® CX-1050 Sensor is mounted in a drilled hole in the copper sample stage directly below the sample box to ensure the accurate measurement of the sample temperature. Two resistive heaters can be used to control the temperature via an Oxford Instruments ITC503 temperature controller; one is directly mounted on the sample stage in the ESR insert and used primarily for higher temperatures above 10 K, the other one is mounted on the heat exchanger at the needle valve of the VTI allowing for precise control in the low-temperature range.

From top to bottom the ESR insert is built up as follows: A KF flange seals the VTI exchange gas chamber. It has vacuum feedthroughs for the two 2.18 mm semi-rigid coaxial cables and a hermetically sealed connector for the wires to the thermal sensor and heater as well as the wires carrying the modulation current. The probe-head located in the centre of the magnet bore is attached to the flange via three thin-walled stainless steel tubes which incorporate the wiring. Fig. 2.9 shows a cutaway view of the construction of the probe-head. The sample stage which is manufactured from copper incorporates the thermal sensor and a  $40\ \Omega$  resistive cartridge heater. Within the probe-head two short  $\sim 10$  cm segments of semi-flexible coaxial cable are used as a connection between the sample box and the semi-rigid cables within the insert to allow for different sizes of sample boxes. The modulation coil is wound on a PTFE plastics tube with a length of 60 mm and a radius of 13 mm. It is attached to the inside of the cylindrical cap covering the probe-head. This allows for sliding the coil over

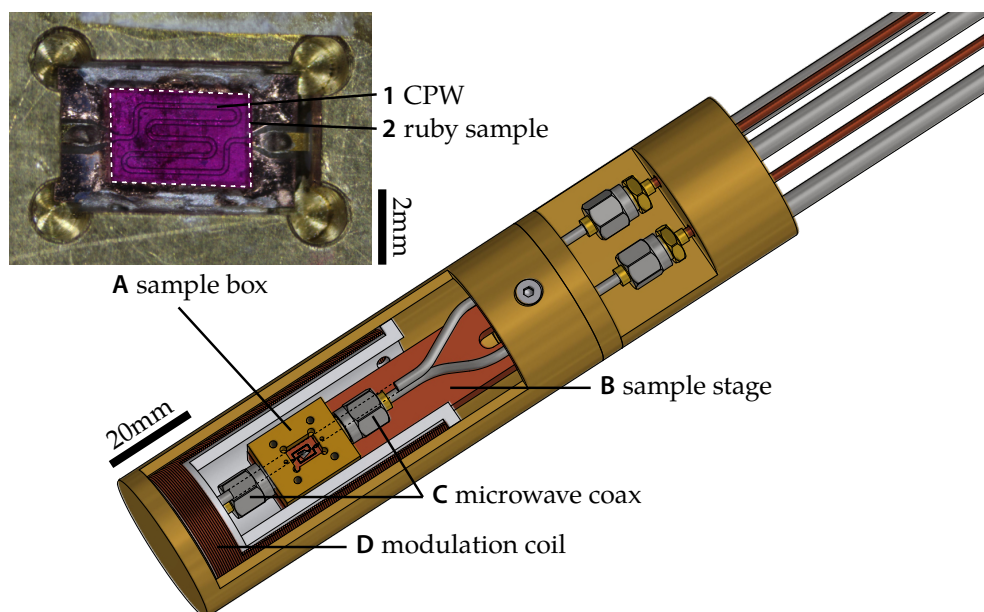


FIG. 2.9 *Frequency-Domain ESR Probe-Head* (A) Picture detail of a sample box with a mounted and contacted CPW (1) and an attached ruby sample (violet cuboid indicated by dashed white line) (2); (B) The copper sample stage contains a resistive heater and a temperature sensor; (C) Microwave coaxial cables for the transmission measurement; and (D) Modulation coil wound on a PTFE plastics tube. (reproduced from [M1], with the permission of AIP Publishing)

the whole assembly after mounting the sample box and ensures the sample box to be centred within the coil.

The CPWs are fabricated from 1  $\mu\text{m}$  copper on R-cut 430  $\mu\text{m}$  sapphire substrates [79]. Unless stated differently, for the data shown in this section the following dimensions are used: 100  $\mu\text{m}$  inner conductor width  $W$  and 42  $\mu\text{m}$  gaps  $S$  between inner conductor and ground planes for a nominal 50  $\Omega$  impedance. The CPW is mounted into a sample box fabricated from brass. The transition from the coaxial cables to the CPW is realised using sparkplug launchers attached to the sample box. The samples are attached to the CPW via Apiezon® N cryogenic vacuum grease. Thermal contact to the sample stage is ensured by the grease as well as the helium exchange gas within the probe-head.

Fig. 2.10 shows a schematic view of the instrumentation of the setup which is controlled by a PC running LabVIEW. The equipment used for the phase-sensitive detection scheme employed for the ESR measurements can be divided in three functional groups: microwave generation, detector and lock-in amplifier, and modulation amplifier. The microwave signal is generated by an Agilent PSG 8257D analog signal generator in the frequency range between 100 kHz and 67 GHz with an output power between  $-20$  dBm and 15 dBm. External power levelling can be used to compensate for changes in the microwave power. In this case a detector diode for levelling is built in the setup with a directional coupler at the output of the insert. To avoid distortion of the ESR signal, the bandwidth of the automatic levelling control circuit of the microwave generator must be limited to a frequency of 1 kHz and thus much lower than the modulation frequency of 30 kHz.

The transmission through the insert is measured with a diode detector (HP 8474E). The voltage from the video output of the detector is directed into a digital lock-in amplifier (Stanford Research SR830) which also generates the sinusoidal modulation signal. A voltmeter (Keithley 2000) can be used to measure the effective value of the transmission signal from the detector directly. The modulation coil is driven by an audio power amplifier which is fed with the modulation signal from the lock-in amplifier. The frequency-swept ESR signal is recorded digitally within the lock-in amplifier and can be directly read out with the controlling PC.

Modulating the magnetic field not only leads to a modulated ESR absorption but also always induces an undesired voltage within the CPW. This induced voltage is amplified by the lock-in amplifier as it oscillates with the modulation frequency. It occurs always  $90^\circ$  out of phase with the modulation field whereas the ESR signal is modulated in phase. With the microwave frequency being detuned from the ESR

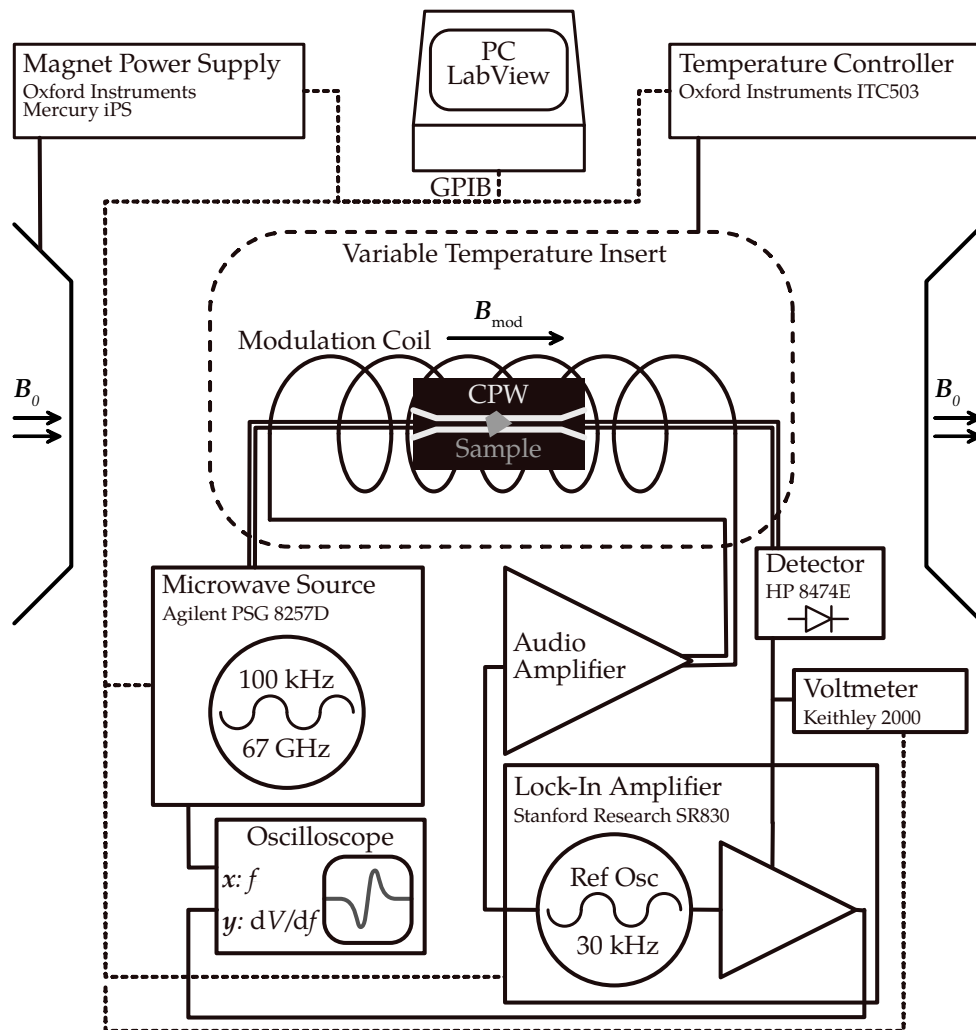


FIG. 2.10 *Schematic View of the Frequency-Domain Instrumentation* The magnet power supply and temperature controller are used to set the external parameters magnetic field and sample temperature. The frequency-swept microwave signal is generated by an analog signal generator and rectified by means of a diode detector. The lock-in amplifier is used to generate the modulation signal as well as to demodulate and record the spectra. An audio amplifier drives the modulation coils. All instruments are computer controlled by a LabView program running an automated measurement sequence. It allows to set all the external parameters, control the microwave measurements, and save the spectra. (reproduced from [M1], with the permission of AIP Publishing)

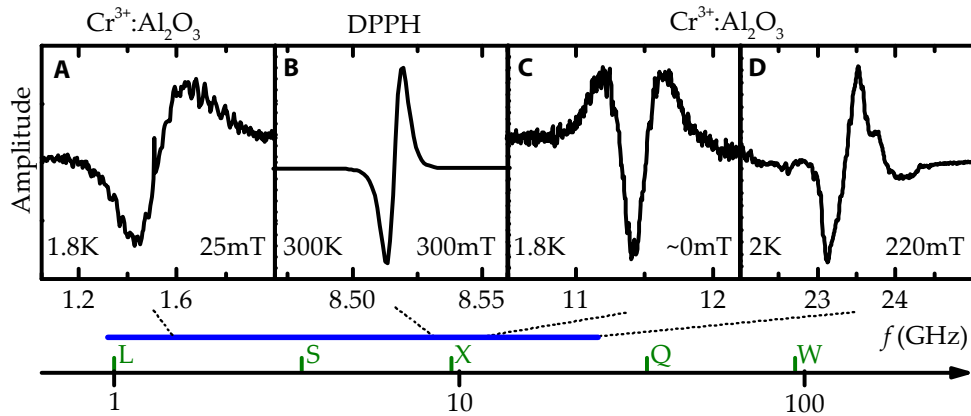


FIG. 2.11 *Demonstration of the Instrument's Parameter Range* (A) and (D) spectra of different transitions in the ruby sample at low temperature, (B) ESR of DPPH at room temperature, and (C) direct measurement of the zero-field splitting in ruby. (reproduced from [M1], with the permission of AIP Publishing)

resonance, only the induced voltage is detected by the lock-in amplifier, and hence, it can be used to adjust the phase of the detection channels to have the ESR signal solely in the Y channel of the lock-in amplifier with correct phase.

#### INSTRUMENT PERFORMANCE

A set of spectra is shown in Fig. 2.11 to demonstrate the capabilities of the instrument. Spectra (A), (C) and (D) are recorded at low temperature and show transitions in the ruby sample at different combinations of frequency and magnetic field; here, (C) demonstrates the benefit of the frequency-domain operation allowing for the direct observation of the zero-field splitting. Spectrum (B) shows the operation around  $g = 2$  with the measurement of a DPPH standard sample at room temperature.

Calibration of the modulation amplitude is done by recording over-modulated spectra of a DPPH powder sample. Spectra recorded with a modulation current between 10 mA and 1000 mA are shown in Fig. 2.12A. Extracting the peak-to-peak line width in frequency-domain and converting it to magnetic field units with  $g_{\text{DPPH}} = 2.0036$  leads to the line width  $\Delta B_{\text{pp}}$  shown in Fig. 2.12B. Fitting the model for the over-modulated Lorentzian line from [39] to the data results in a value of 1.9 mT/A and thus a maximal modulation amplitude of 1.9 mT at a current of 1 A through the coil – a value at which the cryostat is still able to keep the temperature below 1.6 K. The possible modulation amplitude is thus comparable to the one in a standard cavity for a commercial X-band ESR spectrometer, e.g. 3.2 mT in a Bruker ER4102ST rectangular cavity.

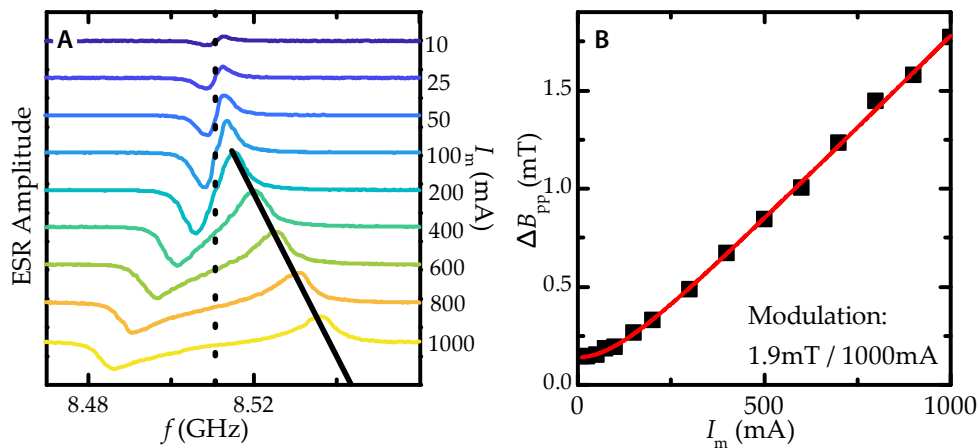


FIG. 2.12 *Calibration of the Modulation Amplitude* The modulation amplitude is calibrated by over-modulating the DPPH ESR signal. (A) Spectra recorded for different modulation amplitudes at  $B_0 = 300$  mT. (B) Fitting the peak-to-peak line width gives a value of 1.9 mT/A for the modulation amplitude  $B_{\text{mod}}$  as well as the true line width  $\Delta B_{\text{pp}} = 0.14$  mT. (reproduced from [M1], with the permission of AIP Publishing)

The broadband operation of the instrument is demonstrated by the measurement of the ruby sample shown in Fig. 2.13. Individual frequency-domain spectra are recorded at increasing magnetic field in steps of 10 mT. One exemplary spectrum for  $B_0 = 450$  mT is shown within the right graph in red. The frequency is swept in the range between 0.1 and 25 GHz. Here 71 spectra are recorded to sample the whole range between 0 and 700 mT. The extracted field-domain spectrum at the X-band frequency of 9.7 GHz is shown in blue in the top graph. The field modulation is set to an amplitude of 0.19 mT at a frequency of 30 kHz and the spectra are recorded with 100 ms integration time of the lock-in amplifier. All six transitions between the four levels of the  $S = \frac{3}{2}$  spin of the  $\text{Cr}^{3+}$  ions are visible in the whole spectrum down to a frequency of 1 GHz [80–82]. The dashed lines show the resonance spectrum calculated with the spin Hamiltonian from [83]. For an angle of  $\theta = 78^\circ$  between the static magnetic field and the cylindrical symmetry axis of the  $\text{Cr}^{3+}$  Hamiltonian – the  $c$ -axis of the  $\text{Al}_2\text{O}_3$  crystal – the calculated spectra coincide well with the measured ones. The horizontal stripes visible in the graph presumably originate from undesired resonant modes within the sample box or the microwave transmission line [68].

In Fig. 2.14 the improvements achieved by field modulation are shown for two examples. The microwave transmission signal  $S_{21}$  always carries a standing wave pattern due to impedance mismatches at the microwave connections contributing to the background of the transmission signal. This background can be seen in the ESR

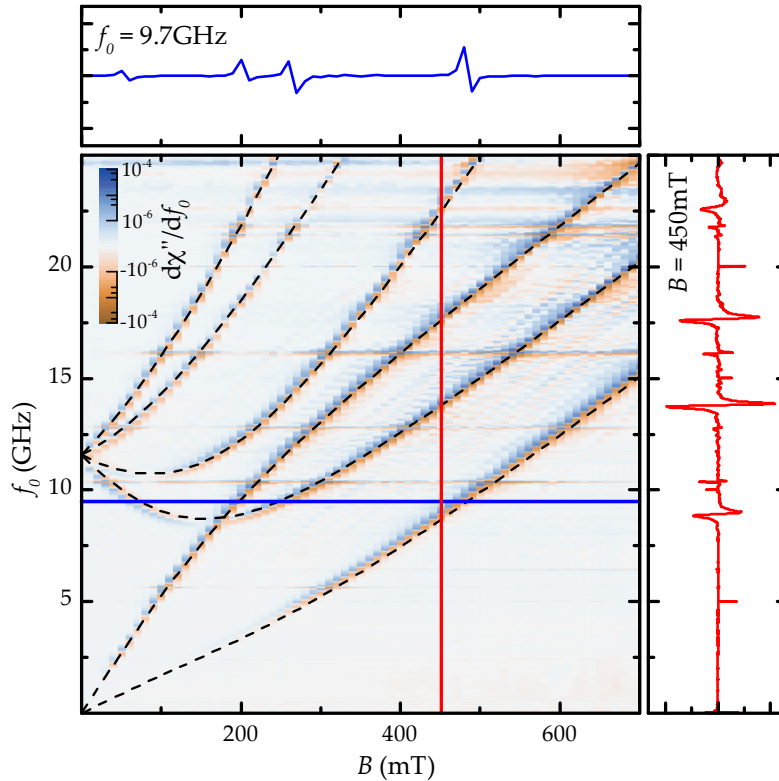


FIG. 2.13 *Frequency-Domain ESR Measurement of Ruby*  $\text{Cr}^{3+}:\text{Al}_2\text{O}_3$  at  $T = 2$  K. An exemplary spectrum at 450 mT is shown in red on the right. A field-domain spectrum can be extracted as shown in blue for the X-band frequency of 9.7 GHz. Dashed lines show the six predicted transitions between the four levels of the  $S = 2$  system for an angle of  $\theta = 78^\circ$  in between the static field and the  $c$ -axis of the crystal. (reproduced from [M1], with the permission of AIP Publishing)

spectrum of DPPH shown in Fig. 2.14B, even though it has already been reduced by dividing the signal at 290 mT by the transmission at 10 mT higher field. As the pattern slightly shifts upon applying magnetic field the background cannot be completely removed by this procedure. Field-modulation allows to effectively suppress any static background from the measurements as seen by the two spectra shown for  $B_0 = 290$  mT and 300 mT.

To demonstrate the reduction of the noise level, field-modulated and pure transmission spectra have been recorded simultaneously. The noise floor is extracted from the data by fitting the Lorentzian absorption and subtracting the fit from the data. The ratio of the signal amplitude and the standard deviation of the noise floor is taken as a measure of the SNR as demonstrated in Fig. 2.14A. Spectra of a selected transition in the ruby sample for three different temperatures are compared in Fig. 2.14C. The

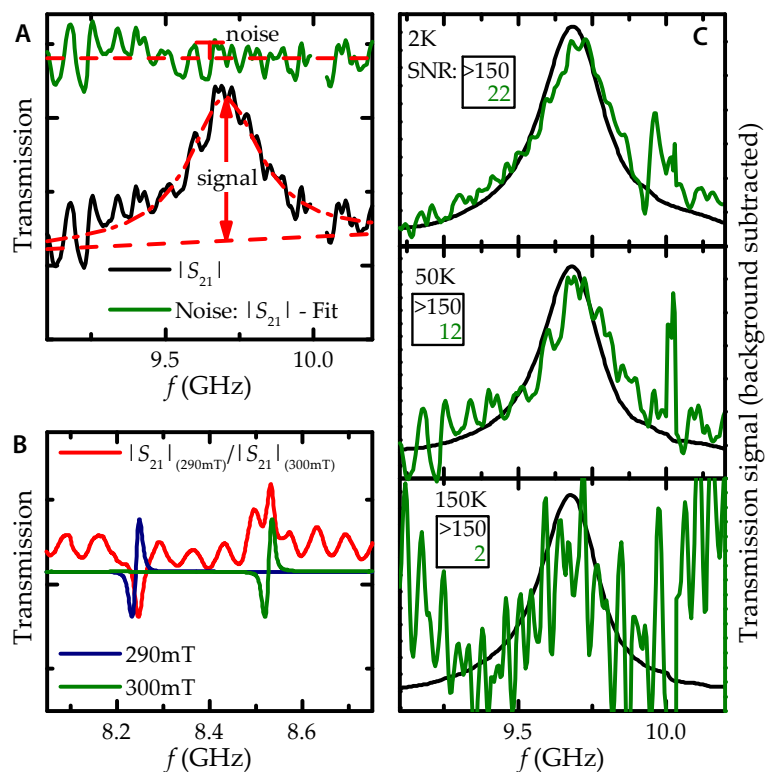


FIG. 2.14 *Instrument Performance* (A) Absorption spectrum and its noise floor.  $\text{SNR} = A_{\text{Signal}}/\sigma_{\text{Noise}}$ . (B) ESR spectra of DPPH at 300 K. Red: transmission spectrum divided by spectrum at 10 mT higher field to reduce background. Blue and green: corresponding spectra recorded with field modulation. (C)  $|m_S\rangle = +1/2$  to  $|m_S\rangle = +3/2$  transition in ruby at  $B_0 = 200$  mT; green: transmission signal, black: transmission obtained from field-modulated signal by integration. (reproduced from [M1], with the permission of AIP Publishing)

SNR for the transmission spectra decreases with increasing temperature. At 150 K the signal can hardly be distinguished from the noise floor anymore. In comparison the transmission obtained by integrating the field-modulated spectra shows almost no noise within the instrument's resolution even at 150 K.

To estimate the number of spins needed to detect a signal at room temperature, a carbon fibre sample with a line width of 0.2 mT has been used (Conrad SE carbon reinforced polymer rod with 0.75 mm diameter). The number of spins in the sample was determined with a commercial X-band spectrometer to be  $1.6 \times 10^{15}$  by double integration and calibration with a  $\gamma$ -irradiated alanine standard as shown in Fig. 2.15. The frequency-domain measurement was performed on a waveguide with 300  $\mu\text{m}$  inner conductor width  $W$  to probe a larger amount of the sample. The probed volume of the sample can be calculated from the absolute value of the microwave magnetic field  $B_1$  above the waveguide according to [69]. The ESR signal is proportional to  $B_1^2$ .

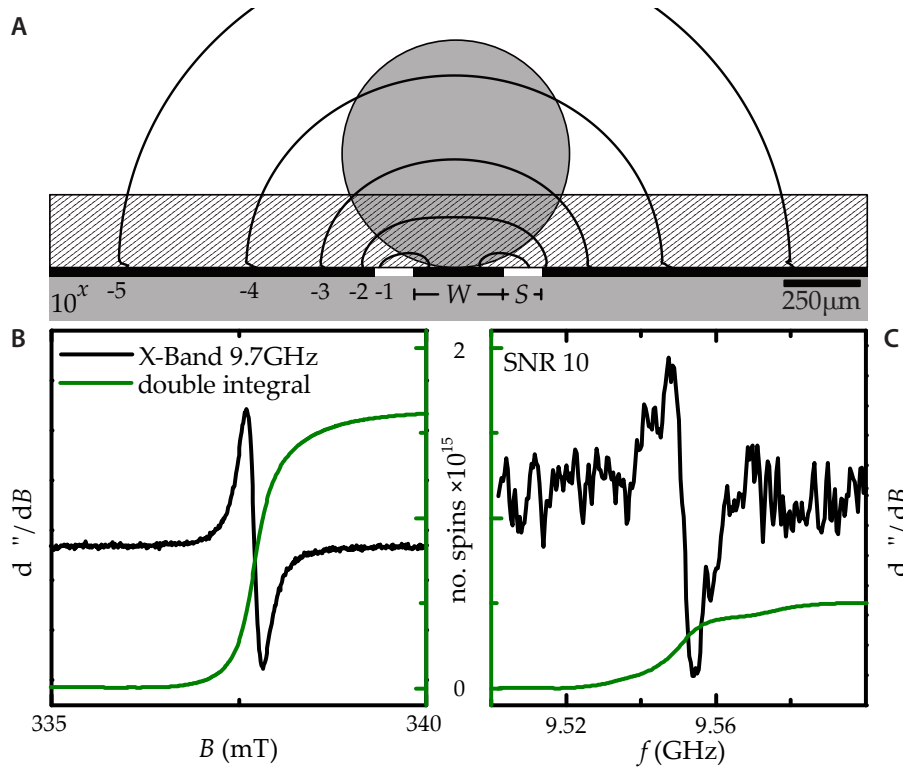


FIG. 2.15 *Estimation of Sensitivity* Room-temperature ESR spectra of a carbon fibre reinforced polymer rod (diameter  $\times$  length 0.75 mm  $\times$  1.5 mm). (A) Dimensions of the sample compared to the waveguide with inner conductor width  $W$  and gap size  $S$ . Contour lines indicate the decrease of the microwave magnetic field amplitude  $B_1$  (in powers of 10) when moving away from the waveguide. (B) Field-swept spectrum obtained with a conventional X-band spectrometer using a standard rectangular  $TE_{102}$  cavity. The number of spins in the sample is determined to be  $1.6 \times 10^{15}$  by double integration. (C) Frequency-swept spectrum recorded with the presented instrument at 337 mT. About one third of the whole number of spins contribute to the spectrum. (reproduced from [M1], with the permission of AIP Publishing)

Integrating over the lateral dimensions shows that 90 % of the ESR signal originates from the volume up to a height of  $0.8W$  above the waveguide as indicated by the hatched area in the sketch in Fig. 2.15A. For the geometries of the experiment with  $W = 300 \mu\text{m}$  and the sample diameter of  $750 \mu\text{m}$ , approximately 30 % of the sample volume contributes to the signal. Therefore  $5 \times 10^{14}$  spins yield the signal shown in Fig. 2.15C. With 1 mW of incident microwave power, 30 ms integration time and a modulation amplitude of 0.1 mT a SNR of about 10 is reached. By increasing the integration time a sensitivity of the instrument in the order of  $10^{13}$  spins per 0.1 mT line width is within reach for frequencies in the X-band. Despite the larger versatility of this instrument, the sensitivity is only two orders of magnitude lower than the  $10^{11}$  spins per 0.1 mT line width sensitivity specification of the Bruker EMXplus conventional fixed-frequency X-band ESR spectrometer with Bruker ER4102ST standard rectangular  $\text{TE}_{102}$  cavity resonator [84].

### CONCLUSION

An instrument to perform frequency-domain ESR measurements with field modulation has been presented. Operation of the instrument between 1.6 K and 300 K in the frequency range from 0.1 GHz to 25 GHz and magnetic fields up to 700 mT has been demonstrated with measurements of a ruby sample. The frequency-domain operation allows to track all six transitions of the  $S = 3/2$  system and to directly observe the zero-field splitting. Introducing the field modulation leads to a vastly improved signal-to-noise ratio as shown by the temperature-dependent experiments on ruby. The amplitude of the field modulation was calibrated with experiments on DPPH. An overall sensitivity of the instrument in the range of  $10^{13}$  spins at room temperature is within reach as shown by measurements of a carbon fibre sample.

### 2.5.2 Coplanar Waveguide Resonators

This section describing ESR measurements using CPW resonators uses and expands the prior publication in the supplementary material to [M2] **B. Miksch**, A. Pustogow, M. Javaheri Rahim, A. A. Bardin, K. Kanoda, J. A. Schlueter, R. Hübner, M. Scheffler and M. Dressel, *Gapped magnetic ground state in quantum spin liquid candidate  $\kappa\text{-(BEDT-TTF)}_2\text{Cu}_2(\text{CN})_3$* , *Science* **372**, 276 (2021).

Experiments on small samples with low spin density require levels of sensitivity out of reach for the frequency-domain approach. To be able to perform resonant experiments coplanar waveguide resonators can be employed. Using CPW resonators

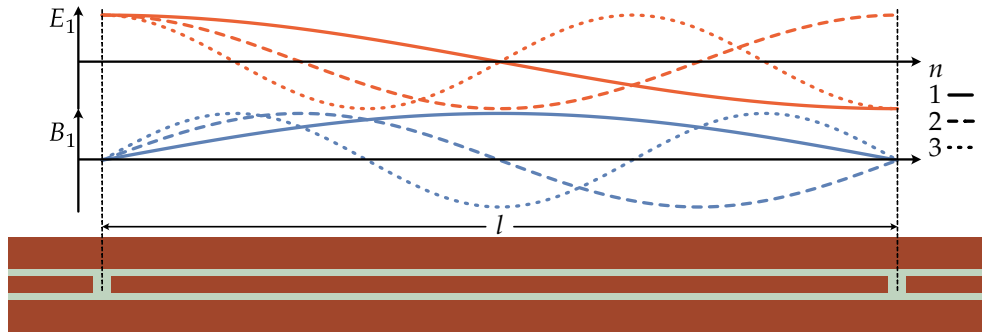


FIG. 2.16 *CPW Resonators: Modes* Electric and magnetic field components of the first three modes of a CPW resonators of length  $l$ .

similar fundamental frequencies can be reached in a much smaller form factor than the one required for a conventional resonant cavity. This enables to operate the setup in a dilution refrigerator used to reach temperatures as low as 20 mK. In addition to that, as the resonators are one-dimensional, measurements are not only possible at their fundamental frequency but also at equally spaced higher harmonics; hence multi-frequency studies are possible within a single experiment run. The details of the design and manufacturing of the resonators used for this project as well as their performance in ESR experiments have been published in a series of articles and theses over the past years [57, 79, 85–90].

A resonator can be obtained by introducing two gaps in the inner conductor of a CPW with a distance  $l$  in between. The gaps act as a capacitive coupling between the feed lines and the segment between the gaps forming a one-dimensional  $\lambda/2$  resonator. Resonances then occur at frequencies

$$f_n = n \frac{c}{2l\sqrt{\epsilon_{\text{eff}}}} \quad n \in \mathbb{N} \quad (2.36)$$

A schematic view of a CPW resonator as well as the distribution of the electric field  $E_1$  and the magnetic field  $B_1$  along the resonator for the first three modes are shown in Fig. 2.16. Note that in the middle of the resonator good conditions for ESR, i.e. nodes of the electric field and antinodes of the magnetic field, are present for modes of odd  $n$ . If small samples are investigated which only cover a small part of the resonator, they are put in the centre, thus only the odd modes can be used to study ESR. Using sapphire substrates with a resulting  $\epsilon_{\text{eff}} = 5.5$ , a length  $l \approx 6.4$  cm is needed for a fundamental frequency  $f_0 = 1$  GHz. Due to size restrictions in the fabrication as well as the cryostats used for the experiments, a meandered design has to be used to accommodate for

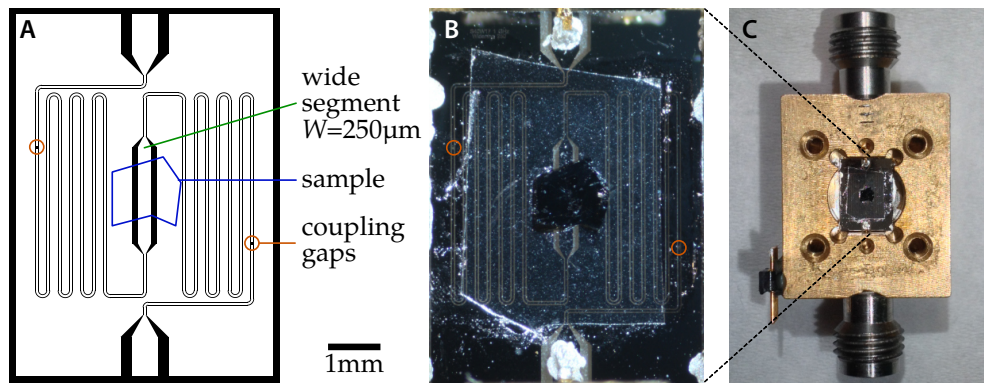


FIG. 2.17 *CPW Resonators: Design* Design (A) and photo (B) of a CPW resonator made of niobium with fundamental frequency  $f_0 = 1$  GHz. In the centre the dimensions increase from  $W = 40 \mu\text{m}$  to  $W = 250 \mu\text{m}$  to achieve better coupling of the microwaves to the sample insulated by a Mylar® foil. (C) The resonator chip is mounted in a brass sample box. The transition to V type coaxial connectors is made using sparkplug launchers contacted with conductive silver varnish. A temperature sensor is mounted on the outside of the box (left).

such lengths. To minimise crosstalk, the distance between the subsequent loops have to be larger than the CPW dimensions. A distance of  $2(W + 2S)$  has been established as a good compromise between packing density and small crosstalk [85]. Achieving low frequencies on a given chip size thus requires small CPW dimensions resulting in the magnetic field being concentrated in a very small volume above the CPW. As even for direct mounting of samples to the chip with vacuum grease a distance of approximately  $20 \mu\text{m}$  remains as a minimum [72] and conductive samples need an additional mylar foil to prevent a short-circuit of the CPW, measuring ESR on bulk samples using resonators with dimensions in the range of or smaller than this minimum distance is problematic.

To solve this problem resonator designs with increased CPW dimensions in the central part of the resonator have been developed within the scope of the Bachelor project of R. Nacke [88]. We tested several designs of resonators with a wider segment in the centre of the resonator. Using a piezo driven micro-positioning stage to move the sample, we studied the ESR sensitivity for a standard ruby sample as a function of the distance to a CPW resonator. We found that using a wider section in the centre, e.g.  $W = 200 \mu\text{m}$ , allows ESR measurements of bulk samples even on resonators with centre conductor width  $W = 20 \mu\text{m}$  elsewhere. This enables to fabricate resonators with a fundamental frequency as low as  $f_0 = 500$  MHz on a chip size of 5 mm by 7 mm

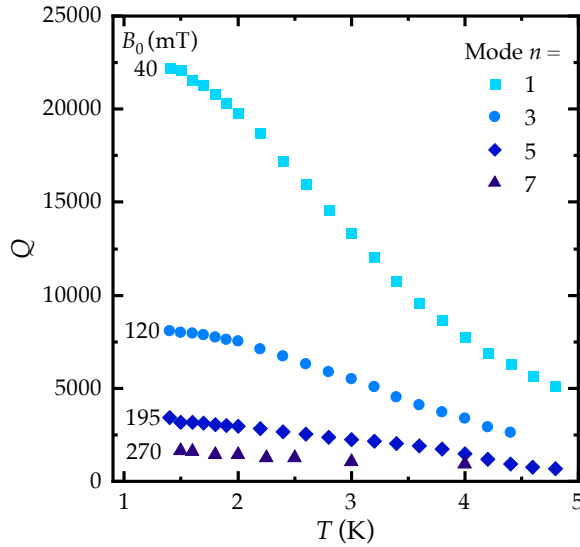


FIG. 2.18 *CPW Resonators: Quality Factor* Quality factor  $Q$  as a function of temperature  $T$  for a niobium resonator with a fundamental frequency of  $f_0 = 1.1$  GHz. The shown data is obtained for the resonator used for the low-temperature experiments presented in section 4.4. Four modes  $n = 1, 3, 5, 7$  with frequencies  $f_0 = 1.1, 3.3, 5.5,$  and  $7.6$  GHz are measured in an external magnetic field  $B_0 = 40, 120, 195,$  resp.  $270$  mT, corresponding to the resonance condition for  $g \approx 2$ . A strong decrease in  $Q$  can be observed for increasing  $B_0$  and  $T$ .

which can be incorporated in all our setups. A resonator design using this approach is shown in Fig. 2.17A.

The resonator chips are fabricated by means of optical lithography from conducting thin films – either metallic (copper or gold) [79] or superconducting (niobium or YBCO) [59, 85] – on sapphire substrates. Superconducting resonators yield higher sensitivity compared to metallic ones. Due to the vanishing Ohmic losses, they display sharper resonances characterised by a larger quality factor  $Q$ . For designs comparable to the one displayed in Fig. 2.17A metallic resonators reach a maximum  $Q \approx 500$  [79], whereas  $Q > 10^4$  is possible for superconducting resonators. The measurements with external magnetic field needed for the ESR experiments, however, cause vortices in the superconductor whose dynamics result in microwave losses [85]. The better sensitivity reached with superconductors therefore comes at the price of an immanent temperature- and magnetic field-dependence of the quality factor which has to be taken into account when analysing the obtained magnetic resonance data.

Fig. 2.18 displays the temperature-dependence of the quality factor  $Q$  reached with a niobium resonator for four different modes at approximately 1, 3, 5 and 7 GHz. The

external magnetic field  $B_0$  for each of the measurements is set to the value where the resonance condition (2.2) for  $g = 2$  would be fulfilled with the respective frequencies. A decreasing  $Q$  can be observed for increasing temperature  $T$ . The critical temperature in zero field is  $T_c = 9.2$  K for pure bulk niobium [91]. The increasing  $B_0$  is the main reason for the decreased  $Q$  seen for the higher modes. Superconductivity is fully suppressed already at a critical field of  $B_c = 820$  mT in pure niobium in the limit of  $T \rightarrow 0$  [92]. Thus, measurements are only feasible in a limited temperature and field range. In case of niobium resonators, for temperatures up to 3 K reproducible results could be obtained for fields up to 300 mT; lower fields allow for somewhat higher temperatures. ESR spectra can still be observed outside this range with lowered sensitivity, however the calibration becomes increasingly difficult as small temperature fluctuations strongly alter the quality factor  $Q$ .

Cuprate superconductors in principle allow for resonators operating in a much larger magnetic field and temperature range; e.g.  $T_c = 92$  K and  $B_c = 150$  T for optimally doped  $\text{YBa}_2\text{Cu}_3\text{O}_{7-x}$  (YBCO) [93]. They are, however, not well suited for ESR measurements as the large amount of inherent  $\text{Cu}^{2+}$  ions gives rise to an ESR signal in the vicinity of  $g = 2$  which overlaps with the signals of the studied samples [94].

A superconducting niobium resonator chip is shown in Fig. 2.17B with a sample attached to its surface. The chips are mounted inside brass boxes and contacted to the sparkplug launcher of coaxial connectors as shown in Fig. 2.17C. The whole assembly can then be loaded inside a cryostat. A  $^4\text{He}$  VTI system for temperatures between 1.5 K and 300 K also used for the frequency-domain setup as well as a dilution refrigerator reaching temperatures as low as 20 mK have been used. Both systems are operated in a helium bath including a superconducting magnet to apply fields up to 8 T.

The transmission through the resonators is measured using a vector network analyser, VNA. For all measurements with CPW resonators an Agilent PNA E8364C network analyser with a frequency range of 10 MHz to 50 GHz has been used. An exemplary transmission spectrum of the real and imaginary part as well as the absolute value of  $S_{21}(f)$  is shown in Fig. 2.19A for the  $n = 5$  mode of a resonator with fundamental frequency 1.1 GHz. The mode can be fitted with a Lorentzian function to obtain its resonance frequency  $f_0$  as well as its bandwidth  $f_B$ . Standing waves in the coaxial cables and spurious modes within the sample box lead to a background adding to the ideal transmission spectrum of the resonator in a complex way. Due to the high quality factor  $Q \approx 3000 - 10\,000$ , the resonances are typically very sharp compared to the background standing wave pattern as illustrated in Fig. 2.19B. There-

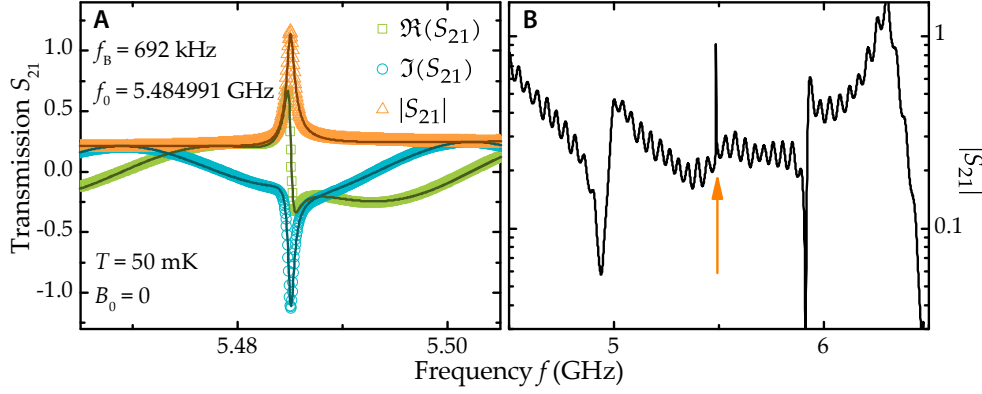


FIG. 2.19 *CPW Resonators: Spectrum* (A) Complex transmission spectra  $S_{21}$  through the coplanar waveguide resonator in the vicinity of the  $n = 5$  mode at  $B_0 = 0$ . The solid lines are fits to equation (2.37). The obtained centre frequency is  $f_0 = 5.48$  GHz, the bandwidth  $f_B = 0.69$  MHz, i.e. the quality factor of the loaded resonator is  $Q \approx 8000$ . (B) Absolute value of the transmission  $|S_{21}|$  in a larger frequency range. Notice the sharp resonance compared to much broader background features.

fore modelling the background in the vicinity of the resonance frequency  $f_0$  up to linear order is sufficient. The fits are conducted in the complex plane including the expansion of the background [95] using the following model [70]:

$$S_{21}(f) = e^{if\tau} \left( \underbrace{\frac{\tilde{v}_1}{f - \tilde{v}_2}}_{\text{resonance}} + \underbrace{\tilde{v}_3 + \tilde{v}_4 (f - \Re(\tilde{v}_2))}_{\text{background}} \right) \quad (2.37)$$

Here the exponential prefactor accounts for the signal propagation time  $\tau$  through the entire setup and  $\tilde{v}_i$  are complex fit parameters, with the resonance frequency  $f_0 = \Re(\tilde{v}_2)$  and the bandwidth  $f_B = 2\Im(\tilde{v}_2)$ .

ESR measurements are performed by stepping the external magnetic field  $B_0$  and recording the resonator modes with a VNA at each field step, giving access to  $f_0$  and  $f_B$  as a function of  $B_0$ . The ESR within the sample acts as a perturbation to the resonator under test with the ESR dispersion  $\chi'(B_0)$  and absorption  $\chi''(B_0)$  manifesting as a change in the resonator frequency  $f_0$  respectively the resonator bandwidth  $f_B$ . A spectrum obtained in this manner is presented in Fig. 2.20. The ESR features are visible in  $f_0$  as well as  $f_B$  as indicated by the arrows. The field-dependent background, increasing  $f_B$  and decreasing  $f_0$ , stems from the suppression of superconductivity of the niobium resonator with increasing field.

Treating  $f_0$  and  $f_B$  as real and imaginary parts of a complex quantity  $\tilde{F}(B_0)$ , the obtained ESR spectra can be fitted using  $n$  Lorentzian functions for the  $n$  resonances

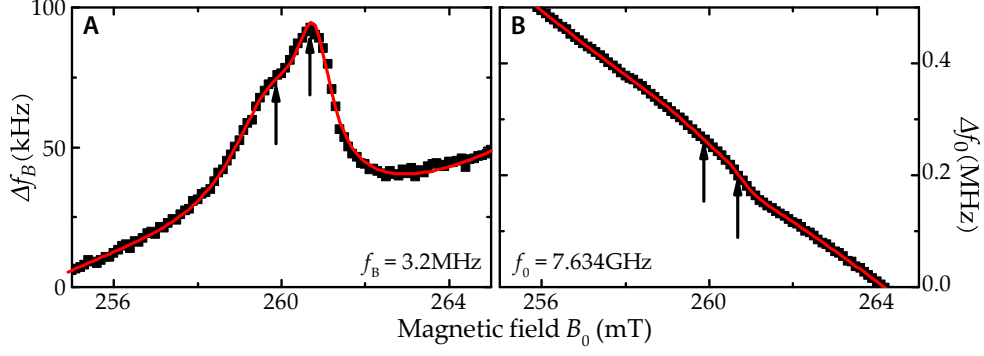


FIG. 2.20 *CPW Resonators: ESR Signal* Low-temperature ESR spectra of  $\kappa$ -(BEDT-TTF) $_2$ Cu $_2$ (CN) $_3$  from transmission measurements on a coplanar Nb resonator. (A) Fit of the bandwidth  $f_B$  and (B) centre frequency  $f_0$  of the  $n = 7$  resonator mode affected by magnetic absorption. The arrows indicate the fields where the ESR absorption features are observed. The red lines are the fit according to equation (2.38).

visible and a cubic polynomial background to fit the field-dependent background of the resonator

$$\tilde{F}_{\text{fit}}(B_0) = \underbrace{\sum_n \frac{-\tilde{A}_n \Delta B_n}{(B_0 - B_{\text{res},n}) + i\Delta B_n}}_{\text{ESR}} + \underbrace{\sum_{k=0}^3 \tilde{c}_k B_0^k}_{\text{background}} \quad (2.38)$$

Here the coefficients of the background polynomial  $\tilde{c}_k$  as well as the amplitudes of the Lorentzians  $\tilde{A}_n$  are complex quantities and thus fitted individually for the resonator frequency  $f_0$  and the resonator bandwidth  $f_B$ . The resonance fields  $B_{\text{res},n}$  as well as the line widths  $\Delta B_n$  are real numbers and therefore the same for dispersion respectively absorption.

## 2.6 Magnetic Field Calibration

Both superconducting solenoid magnets used in the VTI as well as the dilution refrigerator setup are not equipped with any magnetic field sensor such as a Hall probe or NMR teslameter. The set point for the magnetic field is converted to the applied current by a simple proportionality factor given in the solenoids data sheet. A major issue of this approach is the remanence of the magnet system which depends on the history of its magnetic field. Typical remanent fields for a simple solenoid magnet can be in the range of 10 mT [96]. In addition to that a field homogeneity of only  $10^{-3}$  within a  $1 \text{ cm}^3$  sphere is specified for the used systems leading to an additional error in the magnetic field.

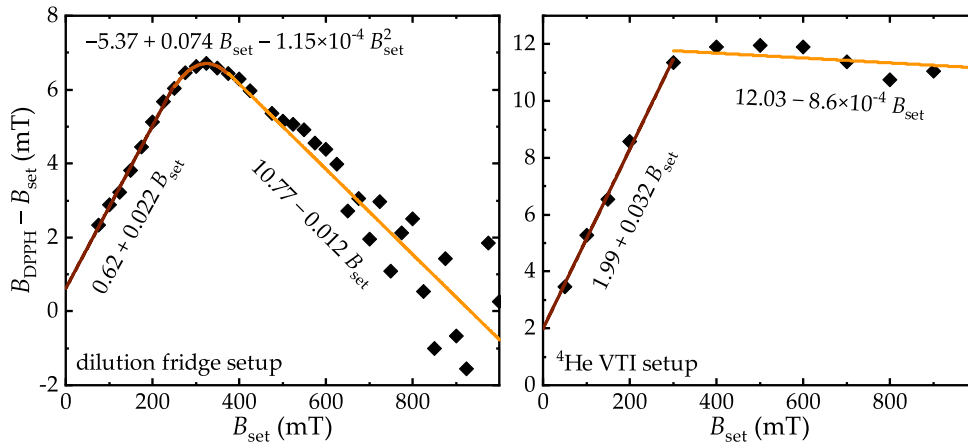


FIG. 2.21 *Magnetic Field Calibration* Frequency-domain ESR measurements on DPPH ( $g = 2.0036$ ) are performed to determine the difference between the actual and set value of the magnetic field. The piecewise fits to the data (orange) are used to correct the magnetic field values for all measurements in the dilution refrigerator and VTI setups.

To be able to use the magnet systems for ESR measurements, their magnetic field characteristics need to be calibrated. In order to minimise differences in the remanence due to the history of the magnet, a recurring operating procedure is used: the magnetic field is always swept to a field of 1 T, much larger compared to the fields present in the ESR experiments, and back to zero prior to the measurement run. As an additional effect this also reduces errors associated to the hysteretic behaviour of the vortex-induced losses within the superconducting CPWs [85].

Calibration is achieved by ESR measurements of DPPH with a known  $g = 2.0036$ . These measurements are performed in frequency-domain for different magnetic field set points. Any frequency error can be neglected as it is far below 1 ppm for both the VNA as well as the analog signal generator over the whole studied range. The main uncertainty is given by the intrinsic line width of the DPPH signal of approximately 5 MHz. Thus, the actual field can be determined to a precision of 0.1 mT. The difference of the actual field value determined from the DPPH resonance and the set point are shown in Fig. 2.21 as a function of the magnetic field set point for the two setups used. The piecewise linear and quadratic fits to the obtained calibration data are in turn used to correct the magnetic field of all ESR measurements performed in the respective setups.



## 3 Materials

The ESR experiments to investigate the magnetic properties – especially the quantum spin liquid physics – of the triangular lattice  $S = 1/2$  system were performed on samples of the  $\kappa$ -(BEDT-TTF)<sub>2</sub>X family. These are layered organic charge transfer salts with electronic properties that can be described with a quasi two-dimensional model. Within this chapter the material class of organic conductors is introduced, followed by the electronic properties and the general phase diagram for  $\kappa$ -(BEDT-TTF)<sub>2</sub>X governed by Mott physics. Afterwards the magnetic properties of the studied compounds are discussed by means of previously published experimental results revealing the open questions to be addressed by the ESR measurements performed within this project. First  $\kappa$ -(BEDT-TTF)<sub>2</sub>Cu<sub>2</sub>(CN)<sub>3</sub>, known as the archetypical quantum spin liquid, is presented including results of , magnetic (NMR,  $\mu$ SR, magnetisation), transport (DC resistivity, thermal transport) and thermodynamic (specific heat, thermal expansion) experiments. Subsequently two deduced compounds are introduced for comparison:  $\kappa$ -[(BEDT-TTF)<sub>1-x</sub>(BEDT-STF)<sub>x</sub>]<sub>2</sub>Cu<sub>2</sub>(CN)<sub>3</sub> introducing chemical pressure and disorder by molecular substitution on the BEDT-TTF site, and the sister compound  $\kappa$ -(BEDT-TTF)<sub>2</sub>Ag<sub>2</sub>(CN)<sub>3</sub> lying deeper in the Mott insulating state.

### 3.1 Organic Conductors

Most organic materials are known to be electrically insulating from everyday experience. However several classes of organic materials with metallic or even superconducting properties do exist, such as graphite intercalation compounds, fullerenes, conductive polymers or organic charge-transfer salts.

Within this project the interest is on organic charge-transfer salts, a class of materials that has been employed to study the fundamentals of various phenomena of solid state physics with low-dimensional characteristics in the last decades [18]. Two samples, a one-dimensional as well as a two-dimensional organic charge transfer compound are shown in Fig. 3.1 alongside their structure. Research on this class

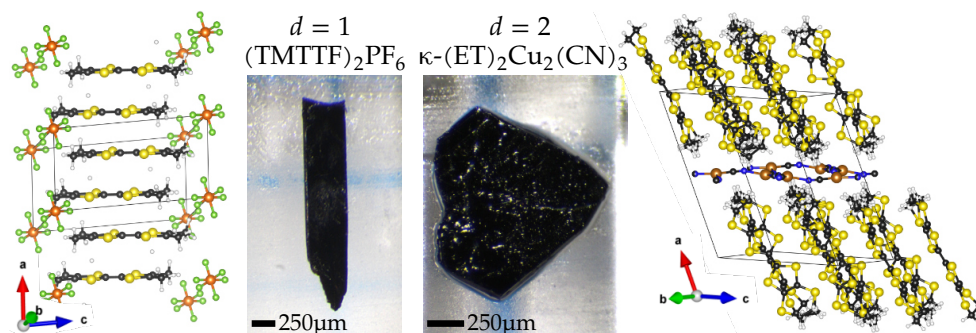


FIG. 3.1 *Examples of One- and Two-Dimensional Organic Conductors* Two specimen of one- and two-dimensional organic charge transfer salts are shown. Notice the needle-like respectively plate-like morphology of the crystals resembling the 1d and 2d structure. The conductive axis in  $(\text{TMTTF})_2\text{PF}_6$  corresponds to the stacking direction  $a$ . In  $\kappa\text{-(BEDT-TTF)}_2\text{Cu}_2(\text{CN})_3$  the conductive plane is spanned by the  $b$  and  $c$  directions. (Structures from [97] for 1d and [98] for 2d, visualised using VESTA [99])

of synthetic metals started in the 1970s with the synthesis of TTF–TCNQ, a highly conducting charge transfer complex between the electron donor tetrathiafulvalene (TTF) and the acceptor tetracyanoquinomethane (TCNQ) with the highest conductivity of any known organic compound at that time [100]. Upon this base the first organic superconductor  $(\text{TMTSF})_2\text{PF}_6$  has been synthesised [101], with tetramethyl-tetraselenafulvalene (TMTSF) as donor molecules and  $\text{PF}_6^-$  anions. The families of Bechgaard salts composed of TMTSF donor molecules and Fabre salts composed of TMTTF, where selenium is replaced by sulphur, have been intensively investigated [102]. These compounds are built up of linear stacks of the planar organic molecules separated by inorganic anions. The overlap of the atomic orbitals of organic molecules in combination with the charge transfer leads to partially filled bands and thus allows charge transport along the stacks. The result is a strongly anisotropic conductivity rendering these compounds a model system of quasi one-dimensional conductors. Electronic correlations and the low-dimensional character lead to a vast number of phenomena in the spin and charge sector which can be tuned by applying external hydrostatic pressure or chemical pressure by substitution of the anions. These include the Mott insulating state, charge order, superconductivity, antiferromagnetic order, spin density wave, the spin-Peierls transition as well as varying metallic behaviour between a purely one-dimensional Luttinger liquid and a Fermi liquid in higher dimensions. A general phase diagram of the material class has been introduced [103] and extended over the years by resistivity, optical and ESR measurements as summarised in several review articles [102].

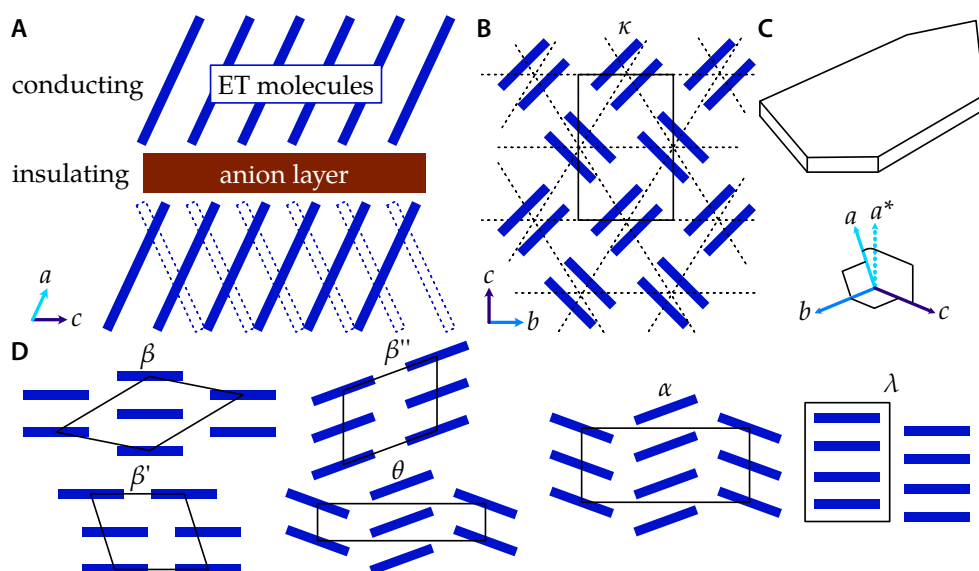


FIG. 3.2 *Schematic Structure of  $ET_2X$*  The crystals possess a layered structure consisting of conductive layers of tilted ET molecules alternating with insulating anion sheets (A). Subsequent layers can have the same or alternating orientation of ET molecules. Within the layers, the ET molecules can arrange in several motifs (D). The samples studied are ordered in the  $\kappa$ -phase with dimers of ET molecules oriented  $90^\circ$  to each other (B). The resulting crystals have a plate-like morphology with the large dimensions corresponding to the conductive plain, the  $bc$  plane in case of  $\kappa$ - $ET_2Cu_2(CN)_3$  (C).

In a similar fashion two-dimensional synthetic metals have been synthesised from bis(ethylenedithio)tetrathiafulvalene (BEDT-TTF) as discussed in the following section [18, 104].

### 3.1.1 Quasi Two-Dimensional Organic Conductors: (BEDT-TTF) $_2X$

The crystal structure and morphology of quasi two-dimensional (BEDT-TTF) $_2X$  charge transfer salts is sketched in Fig. 3.2. The BEDT-TTF, short ET, molecules (see Fig. 3.3A) act as electron donors with nominal charge  $ET^{+0.5}$ .  $ET_2X$  compounds possess a layered structure built up from planes of ET molecules. The distributed  $\pi$ -electrons form orbitals which overlap with neighbouring molecules. In combination with the charge transfer this leads to partially filled bands allowing for charge transport. The insulating anion sheets separate the planes of ET molecules. Charge transport therefore happens predominantly in two dimensions, within the ET layers. Typically the ET molecules are tilted with respect to the stacking direction leading to different possible stacking sequences.

Changing the anions allows altering the inter-layer transfer integrals as well as it leads to a different intra-layer arrangement and spacing of the ET molecules. Numerous in-plane packing motifs have been realised and named with greek symbols [105]. A selection of important motifs is depicted in Fig. 3.2B,D. As the symmetry and the unit cell size of the crystals varies depending on the intra-layer packing as well as the stacking order (uniform or alternating), the labelling of the unit cell axes is different in different compounds. The axis labelling shown in Fig. 3.2, where the  $b$  and  $c$  direction span the conducting plane, is valid for all three  $\kappa$ -ET<sub>2</sub>X compounds studied in this thesis.

The in-plane arrangement has a large influence on the electronic properties [106]. With separately arranged molecules due to the charge of +0.5 per molecule nominally a <sup>3</sup>/<sub>4</sub> band filling is realised. In some arrangements, particularly in the  $\lambda$  and  $\kappa$  phase, dimers of molecules can be identified with the transfer integral within a dimer  $t_d$  being much larger compared to the transfer integrals to molecules in neighbouring dimers. In this second case a dimerised model treating the dimers as single units can be used to describe the electronic properties. Dimerisation splits the <sup>3</sup>/<sub>4</sub>-filled band into one fully occupied and one singly occupied band resulting in an effectively half-filled system. One hole charge carrier can be associated to each of the dimers accompanied by a single  $S = 1/2$  spin. Due to the small bandwidth, electronic correlations play a crucial role in these materials. As a result Mott physics is important leading to antiferromagnetic exchange interactions as discussed in section 1.2. The materials studied for this project all crystallise in the dimerised group of  $\kappa$ -ET<sub>2</sub>X compounds, whose properties are discussed in the following.

#### 3.1.2 Properties of the $\kappa$ -(BEDT – TTF)<sub>2</sub>X Family

The crystal structure of the compounds differs within the family depending on the respective anion [18]. Within the plane in the  $\kappa$  phase, dimers of two BEDT – TTF molecules facing each other are arranged almost perpendicular to neighbouring pairs within the conductive layers as sketched in Fig. 3.2B. The exact distances of this triangular arrangement and the related transfer integrals are responsible for the degree of geometrical frustration present in the respective compound.

In addition to the differences in the in-plane arrangement one can differentiate two stacking patterns: in  $\kappa$ -ET<sub>2</sub>Cu[N(CN)<sub>2</sub>]Cl and the Br sister compound the ET molecules are tilted alternately in subsequent layers in a “herring-bone” fashion, whereas in  $\kappa$ -ET<sub>2</sub>Cu<sub>2</sub>(CN)<sub>3</sub> and the related Ag compound subsequent layers are

structurally equivalent. The different stacking patterns illustrated in Fig. 3.2A result in two different space groups: orthorhombic  $Pnma$  for the former and monoclinic  $P2_1/c$  for the latter.

Additionally the compounds also differ in the structure of the anion sheets. In  $\kappa\text{-ET}_2\text{Cu}[\text{N}(\text{CN})_2]\text{Cl}$  the anion layer consists of one-dimensional chains. In the investigated  $\kappa\text{-ET}_2\text{Cu}_2(\text{CN})_3$  and related compounds these chains are linked with additional CN groups to form a two-dimensional network as illustrated in Fig. 3.9. Within the resulting threefold coordination of Cu atoms with CN groups one of them resides on an inversion centre. As each of the Cu atoms can be linked to either one or two C atoms of the respective CN groups, the inversion symmetry is locally broken resulting in intrinsic disorder in the anion sheet. A possible transfer of this disorder to the BEDT-TTF molecules via hydrogen bonds yielding inhomogeneity throughout the whole crystal has been proposed [18, 107].

The electronic properties of the effectively half-filled  $\kappa$ -compounds are governed by Mott physics. A common feature of the materials therefore is a Mott metal insulator phase transition below a critical temperature which depends on the strength of the electronic correlations as discussed in section 1.2. The different degrees of geometrical frustration in the members of the  $\kappa$ -family of compounds play an important role for the low-temperature region of the phase diagram. Two characteristic electronic phase diagrams can be discerned for the strongly frustrated and the weakly frustrated compounds as presented in section 1.2. The less frustrated compounds, e.g.  $\kappa\text{-ET}_2\text{Cu}[\text{N}(\text{CN})_2]\text{Cl}$ , form a Mott-Heisenberg insulator with a antiferromagnetically ordered ground state. The highly frustrated members of the family do not order magnetically, forming a genuine Mott-Hubbard insulator with a proposed spin liquid state as the nonmagnetic electrically insulating ground state [19]. The two qualitatively different phase diagrams are shown in Fig. 1.3. In both cases incoherent semiconducting behaviour is observed at elevated temperatures above the Mott insulating and metallic Fermi liquid low-temperature states. At low temperatures a first order phase transition between the Mott insulator and the Fermi liquid regime with a distinct phase-coexistence has been experimentally observed [108]. Above the critical endpoint the phase boundary is a gradual crossover, the quantum Widom line [19]. In the vicinity of the metal to insulator transition a superconducting phase is present in some of the compounds at low temperature, e.g.  $\kappa\text{-ET}_2\text{Cu}_2(\text{CN})_3$  and  $\kappa\text{-ET}_2\text{Cu}[\text{N}(\text{CN})_2]\text{Cl}$  [109].

## 3.2 Frustrated Magnetism in $\kappa$ -(BEDT – TTF)<sub>2</sub>X

As discussed in the previous section, the starting point to discuss the magnetism in the  $\kappa$ -ET<sub>2</sub>X-family are the molecular dimers each hosting  $S = 1/2$  which are arranged on an anisotropic triangular lattice as indicated in Fig. 3.3C. The transfer integrals  $t$  between those dimers within the conducting layers, and therefore the related exchange interactions  $J$  of the spins, determine the magnetic properties of the individual compounds. The ratio  $t'/t$  between the nearest and next-nearest neighbour transfer integrals can act as a measure for the level of frustration of the spin system. In  $\kappa$ -ET<sub>2</sub>Cu<sub>2</sub>(CN)<sub>3</sub> first principles calculations based on the experimental crystal structures lead to an estimate  $t'/t$  value close to unity:  $t'/t = 0.83 - 0.99$ , depending on the different reported crystal structures (lower value for [110], higher for [98]) according to [111]. In comparison  $\kappa$ -ET<sub>2</sub>Cu[N(CN)<sub>2</sub>]Cl is less frustrated with a reported  $t'/t = 0.52$  [111]. The magnetic properties of the two materials are hence completely different at low temperatures: the frustrated  $\kappa$ -ET<sub>2</sub>Cu<sub>2</sub>(CN)<sub>3</sub> shows no magnetic order down to 32 mK whereas in the less frustrated  $\kappa$ -ET<sub>2</sub>Cu[N(CN)<sub>2</sub>]Cl an antiferromagnetic ordering is observed below 27 K [2].

### 3.2.1 The archetypical quantum spin liquid: $\kappa$ -(BEDT – TTF)<sub>2</sub>Cu<sub>2</sub>(CN)<sub>3</sub>

The first synthesis and crystal structure of  $\kappa$ -ET<sub>2</sub>Cu<sub>2</sub>(CN)<sub>3</sub> was described in 1991 by U. Geiser, et. al. [110]. The crystal structure of the compound is shown in Fig. 3.3. Refinement within the monoclinic space group  $P2_1/c$  results in room temperature lattice parameters of:  $a = 16.0920 \text{ \AA}$ ,  $b = 8.5813 \text{ \AA}$ ,  $c = 13.3904 \text{ \AA}$ , and  $\beta = 113.381^\circ$  [107]. A more recent study using synchrotron radiation has systemically detected reflections with weak intensity forbidden in the monoclinic  $P2_1/c$  space group [112]. Thus, the monoclinic symmetry is weakly broken and the structure has been refined in triclinic  $P\bar{1}$  including twinning, resulting in slightly different lattice parameters:  $a = 16.1221(10) \text{ \AA}$ ,  $b = 8.591(6) \text{ \AA}$ ,  $c = 13.412(8) \text{ \AA}$ ,  $\alpha = 89.99(2)^\circ$ ,  $\beta = 113.43(2)^\circ$ , and  $\gamma = 90.01(2)^\circ$ . The plane spanned by the crystallographic  $b$  and  $c$  directions hosts the two-dimensional triangular lattice spin system responsible for the peculiar magnetic properties. This plane is also coincident with the large plane of the platelet-like morphology of the single crystals. DC conductivity experiments show a semiconducting behaviour at ambient pressure; a superconducting state was observed at a pressure of 0.15 GPa below 2.8 K [110].

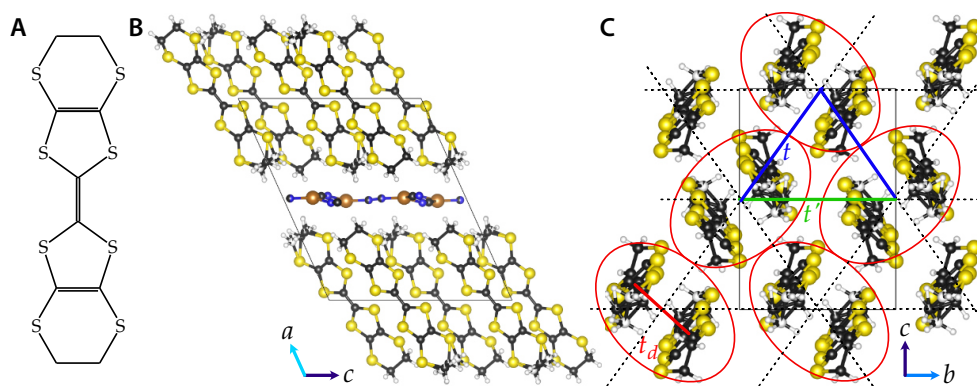


FIG. 3.3 *Crystal Structure of  $\kappa$ -ET<sub>2</sub>Cu<sub>2</sub>(CN)<sub>3</sub>* (A) BEDT-TTF molecule. (B) The organic molecules are arranged in layers alternating with polymeric Cu<sub>2</sub>(CN)<sub>3</sub> sheets. The layers are stacked along  $a^* \perp b, c$ . The colours represent the different atoms as follows: copper (orange), nitrogen (blue), carbon (black), sulfur (yellow), hydrogen (white). (C) The ET molecules are strongly dimerised with  $t_d \gg t, t'$  within the layers. The dimers each host  $S = 1/2$  interacting with the neighbouring spins via exchange coupling  $J = 4t^2/U$ . In case of  $\kappa$ -ET<sub>2</sub>Cu<sub>2</sub>(CN)<sub>3</sub> the ratio  $t'/t \approx 1$  resulting in a frustrated triangular lattice. (crystallographic data from [98], CCDC No. 850028, visualised using VESTA [99])

$\kappa$ -ET<sub>2</sub>Cu<sub>2</sub>(CN)<sub>3</sub> emerged as the first quantum spin liquid candidate material as no signs of magnetic ordering could be found even in the mK temperature regime, four orders of magnitude below the magnetic exchange interaction of  $J \approx 250$  K [2]. Many of the magnetic and thermodynamic properties of the compound have been investigated so far. However, despite the large number of experimental studies the picture of the magnetic ground state is still not conclusive [5]. In addition to that, numerical studies of the anisotropic triangular lattice Hubbard model close to the Mott transition have been performed. Their sometimes contradicting results imply a close competition between nonmagnetic spin liquid and magnetic phases with the result that small perturbations can have a large influence on the ground state [5]. The most important results motivating the present study are presented in the following paragraphs.

The magnetic susceptibility  $\chi(T)$  (Fig. 3.4A) [2] does not show any sign of magnetic order. For comparison the Néel transition in  $\kappa$ -ET<sub>2</sub>Cu[N(CN)<sub>2</sub>]Cl is observed as a divergence of the susceptibility. The overall behaviour featuring a broad peak around 50 – 100 K can be modelled by the triangular lattice Heisenberg model [113]. For low temperatures, the susceptibility neither vanishes nor shows a Curie-like upturn.

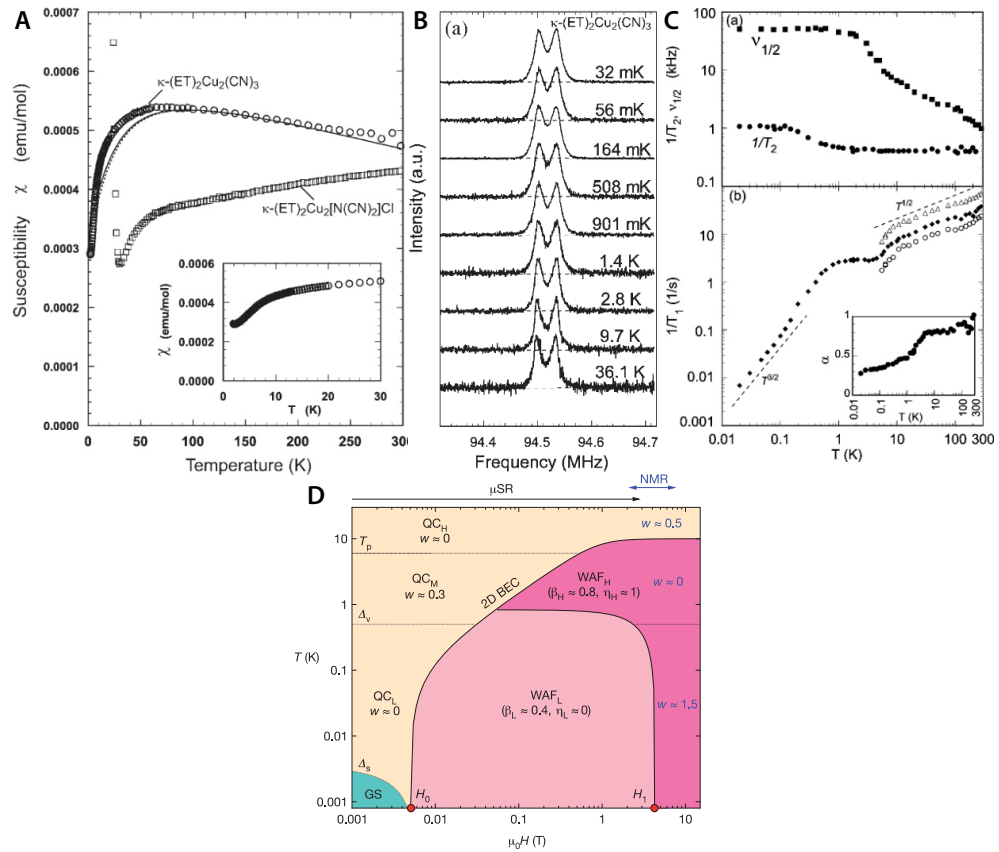


FIG. 3.4 *Experimental Data I for  $\kappa$ - $\text{ET}_2\text{Cu}_2(\text{CN})_3$*  (A) Temperature-dependence of the magnetic susceptibility measured by SQUID magnetometer for a polycrystalline sample. No signs of magnetic order are observed. (B)  $^1\text{H}$  NMR spectra of a single crystal do not show any signs of an internal field down to millikelvin temperatures. (C) Inhomogeneous moments lead to an increasing  $^{13}\text{C}$  NMR line width below 6 K. (D) Magnetic phase diagram as deduced from muon spin rotation results. ((A,B) reprinted from [2] © 2003 by the American Physical Society. (C) reprinted from [8] © 2006 by the American Physical Society. (D) reprinted from [10] © 2011 by Macmillan Publishers.)

Instead below a sharp drop around 6 K the susceptibility saturates and remains paramagnetic at least down to 1.9 K.

Temperature-dependent <sup>1</sup>H (Fig. 3.4B) [2] and <sup>13</sup>C [8] NMR spectra do not show a splitting down to 32 mK, respectively 20 mK. This rules out the presence of static internal fields, thereby ruling out any conventional magnetic order. Below 6 K a strong increase of the <sup>13</sup>C NMR line width is observed (Fig. 3.4C) [8], indicating the emergence of inhomogeneous moments. The relaxation rate  $T_1^{-1}$  shows a power-law tail below a dominant maximum at  $\sim 1$  K which is suppressed upon increasing the magnetic field. This behaviour closely resembles the observations for  $\kappa$ -ET<sub>2</sub>Hg(SCN)<sub>2</sub>Cl, where the low-temperature contribution was related to dipolar coupling to impurity spins and thus extrinsic magnetic contributions [9]. Measurements of the high frequency susceptibility display a similar field-dependent contribution around 1 K [114]. One possible source of impurity spins are magnetic Cu<sup>2+</sup> ions present in the anion layer of the crystals as observed by the ESR measurements shown in Fig. 3.5B [115, 116].

It was found that some samples of  $\kappa$ -ET<sub>2</sub>Cu<sub>2</sub>(CN)<sub>3</sub> are metallic at room temperature and show superconductivity even at ambient pressure, when grown with different supporting electrolytes in the electro-crystallisation process. Komatsu et. al. [115] studied these samples with ESR spectroscopy among other methods and compared them to the pristine compound. The samples, called  $\kappa'$ -(BEDT-TTF)<sub>2</sub>Cu<sub>2</sub>(CN)<sub>3</sub> in the publication, show the same lattice parameters as the pristine compound within the measurement errors. ESR measurements have revealed a comparatively large content of Cu<sup>2+</sup> ions in those samples. The content varies from sample to sample, but cannot be controlled reproducibly. The authors, concluded that substituting Cu<sup>+</sup> by Cu<sup>2+</sup> changes the band-filling away from the half-filled, Mott-insulating, pristine sample resulting in the observed metallic and superconducting behaviour even at ambient pressure. The ESR parameters of the pristine sample are shown in Fig. 3.5A. For larger Cu<sup>2+</sup> content these are altered. At an impurity content of 1200 ppm the low-temperature drop of the spin susceptibility vanishes, the linewidth is overall larger and the  $g$ -factors starts to increase at low temperature, all related to the increased inhomogeneity within the system. For low temperatures an additional narrow signal was observed in the vicinity of the ET cation signal. However, no further analysis is shown within the publication.

Padmalekha et. al. [116] showed with ESR measurements that even crystals grown with the conventional recipe from [110] can contain Cu<sup>2+</sup> ions. They investigated the additional narrow Lorentzian signal, mentioned above, in further detail. It emerges at

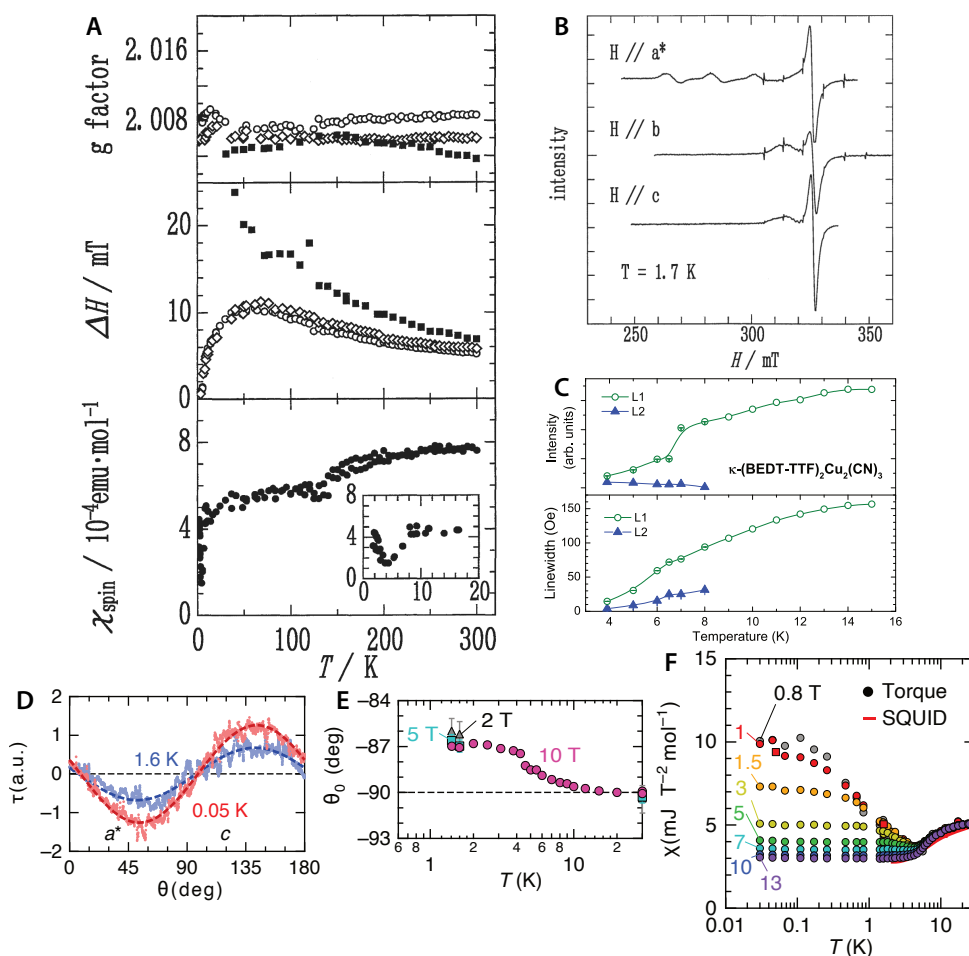


FIG. 3.5 *Experimental Data II* for  $\kappa\text{-ET}_2\text{Cu}_2(\text{CN})_3$  (A) Temperature-dependent X-band ESR parameters of ET cation radicals. Open circles, closed squares and open diamonds represent measurements with  $B_0 \parallel a^*, b, c$ . (B) ESR spectra at  $T = 1.7$  K of  $\kappa\text{-ET}_2\text{Cu}_2(\text{CN})_3$  with 830 ppm  $\text{Cu}^{2+}$  impurities. The larger signal stems from the ET cation radicals, whereas the lower field, broad signals are associated with  $\text{Cu}^{2+}$  (C) Low-temperature ESR intensity and linewidth of  $\kappa\text{-ET}_2\text{Cu}_2(\text{CN})_3$ . Notice the emergence of a second narrower Lorentzian below 8 K. (D,E) Anisotropy of the magnetic torque with respect to the applied magnetic field in the  $a^*c$ -plane. A shift of  $\theta_0 \approx 3^\circ$  with respect to the crystal axes is observed for low temperatures. (F) Magnetic susceptibility as estimated from the torque data as a function of temperature for different magnetic fields. ((A,B) reprinted from [115] © 1996 by T. Komatsu et. al., CC by 4.0. (C) reprinted from [116] © 2015 by Elsevier B.V. (D,E,F) reprinted from [7] © 2016 by T. Isono et. al., CC by 4.0.)

the same resonance field as the ET cation signal below 8 K with its intensity growing upon further cooling. They suggest that the additional contribution with different linewidth is due to a second, different relaxation mechanism becoming important for low temperature. A “Dzyalishinskii-Moriya-like” interaction is suggested to be responsible for the appearance of the additional contribution to the ESR signal, however, no conclusive explanation is given.

Results of a muon spin rotation study have been interpreted to show a field-induced emergence of staggered moments at low temperatures consistent with the <sup>13</sup>C NMR results [10]. This field-induced behaviour was attributed to the importance of spin-orbit coupling resulting in anisotropic exchange interactions [117]. The phase diagram shown in Fig. 3.4D was suggested based on the  $\mu$ SR study predicting a quantum critical point (QCP) at a small but finite field of 5.2 mT and a spin liquid phase hosted only in a small region located in the mK range at even lower fields [10].

Magnetic torque measurements have been performed in a similar range of temperatures and magnetic fields by Isono et. al. [7]. The field-angle dependence of the magnetic torque within the  $a^*c$ -plane is shown in Fig. 3.5D for low temperature. At room temperature, the angles where the torque is zero coincide with those expected from the  $g$ -factor anisotropy. For low temperature an angle shift  $\theta_0$  is observed. This shift appears below approx. 10 K and increases saturating to 3° for lower temperatures as depicted in Fig. 3.5E. The temperature dependence of the spin susceptibility as estimated from the magnetic torque is shown in Fig. 3.5F for various magnetic fields. A power law divergence of the susceptibility  $\chi \propto T^{-0.8}$  is observed, suppressed by increasing magnetic field. The authors interpret the diverging susceptibility obtained from the magnetic torque data for  $B \rightarrow 0$  as quantum critical behaviour above a zero field QCP [7]. In contrast to the  $\mu$ SR study however the torque data do not show any signs of antiferromagnetic correlations at elevated fields suggesting a growing quantum spin liquid phase with increasing magnetic field.

It has been shown that these magnetic torque experimental results can also be explained within a scenario without critical scaling; local spin defects hosted in a valence bond glass state are able to give rise to the observed magnetic properties in a consistent picture that can also explain the aforementioned inhomogeneous NMR response [31]. The authors suggest, that below  $T^* = 6$  K the resonating valence bonds get randomly pinned. In this state unpaired orphan spins can occur either as defects in the static valence bond pattern or due to anion layer vacancies. The angle shift observed in the field-angle dependence can then be explained by the fact that the total magnetic torque is the sum of the bulk contribution and a low-temperature impurity

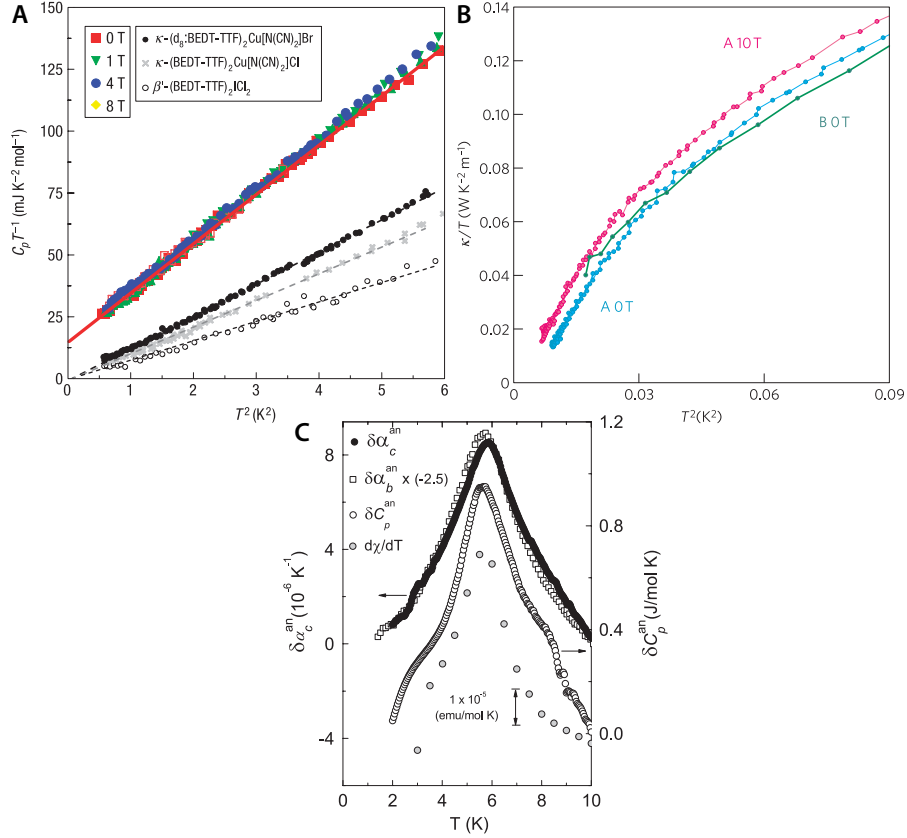


FIG. 3.6 *Experimental Data III for  $\kappa$ - $\text{ET}_2\text{Cu}_2(\text{CN})_3$*  (A) Low-temperature specific heat data shows a linear contribution in contrast to other  $\kappa$ - $\text{ET}_2\text{X}$  salts. (B) Thermal conductivity vanishes towards low temperatures. (C) Anomalies at  $T^* = 6 \text{ K}$  can be observed in the thermal expansion coefficient  $\alpha$ , the specific heat  $C$  as well as the magnetic susceptibility  $\chi$ . ((A) reprinted from [118] © 2008 by Nature Publishing Group. (B) reprinted from [119] © 2009 by Nature Publishing Group. (C) reprinted from [120] © 2010 by the American Physical Society.)

contribution whose  $\mathbf{g}$ -tensor differs from the bulk due to the finite DM interaction. The field and temperature dependence of the torque susceptibility can also be explained in this framework. In the high-field limit the impurity contribution is temperature independent and diverges with field as  $\chi \propto H^{-\zeta_I}$  with  $2/3 \leq \zeta_I \leq 1$ ; in the low-field limit it is field independent and approximately follows a power law as a function of temperature  $\chi \propto T^{-\omega_I}$  with  $2 - \zeta_I^{-1} \leq \omega_I \leq 1$  at intermediate temperatures. This is in accord with the experimental data [7] shown in Fig. 3.5F.

Specific heat (Fig. 3.6A) [118] as well as thermal transport (Fig. 3.6B) [119] measurements have been performed to investigate the thermodynamic properties of  $\kappa$ - $\text{ET}_2\text{Cu}_2(\text{CN})_3$ . A vanishing electronic specific heat contribution for  $T \rightarrow 0$  is expected

ted for insulators and indeed observed in the antiferromagnetic  $\kappa$ -ET<sub>2</sub>X compounds. In contrast to that, in  $\kappa$ -ET<sub>2</sub>Cu<sub>2</sub>(CN)<sub>3</sub> a linear specific heat contribution was observed even at the lowest temperatures. This has been attributed to fermionic excitations in the spin sector, supposedly the gapless spinon excitations predicted by various models for spin liquid ground states [118]. However, the thermal conductivity vanishes with decreasing temperature incompatible with the idea of freely mobile spinon excitations [119].

At  $T^* = 6$  K anomalous features can be observed in various physical quantities. The aforementioned anomalies in the magnetic properties observed in susceptibility, NMR, ESR and  $\mu$ SR measurements are accompanied by a hump in the specific heat and a shoulder in the thermal conductivity. In addition to that also at  $T^*$ , the thermal expansion coefficient is strongly anisotropic and shows a cusp-like feature as shown in Fig. 3.6C [120]. Additionally a lattice softening can be observed as a minimum in the ultrasonic velocity [121]. This has led to the conclusion, that the 6 K-anomaly is connected with spin-lattice coupling [5].

The temperature  $T^*$  at which the anomalous features are observed is not affected by applying an external magnetic field at least up to 8 T. Experiments on various physical properties with varying external field have not yielded any changes. This includes the cusp-like feature in the thermal expansion coefficient [120] as well as the hump in the specific heat [118]. The <sup>13</sup>C NMR linewidth behaves linear in the magnetic field and extrapolates to the nuclear dipole field value at  $B_0 = 0$ , indicating that internal fields are non-existent and the inhomogeneous magnetisation is purely field-induced. This points towards the presence of non- or at least weakly interacting local moments induced by impurities or grain boundaries within the sample. As discussed above, the field-dependent behaviour of the magnetic torque measurements further corroborates the presence of local orphan spins [31].

Recently, the importance of disorder for the magnetic properties has been intensively discussed as it has been shown, that the introduction of randomness can lead to the emergence of a spin liquid from an ordered state [30, 122].

Despite the intensive investigations by various methods, the nature of the ground state of  $\kappa$ -ET<sub>2</sub>Cu<sub>2</sub>(CN)<sub>3</sub> remains an open question to date. This includes the mechanism how magnetic order is prevented, as well as the spin excitation spectrum. In particular, the nature of the anomalies observed at  $T^* = 6$  K has not been unambiguously identified. The results of the ESR measurements performed in the course of this project and the implications for this questions are presented within chapter 4.

Beside the open issues regarding the well studied  $\kappa$ -ET<sub>2</sub>Cu<sub>2</sub>(CN)<sub>3</sub> exploring the

magnetic properties throughout the different electronic phases allows to study the coupling of the electronic and magnetic degrees of freedom in the system. The main motivation is the longstanding question, if the vicinity to the Mott transition does play a crucial role for the magnetic ground state of  $\kappa\text{-ET}_2\text{Cu}_2(\text{CN})_3$ ? ESR investigations on different compounds with varying degree of electronic correlations are shown and discussed in chapter 5. The investigated samples are introduced in the following sections.

### 3.2.2 Introducing Pressure and Disorder:



Analogous molecular substitution of  $\kappa\text{-ET}_2\text{Cu}_2(\text{CN})_3$  at the BEDT-TTF site can be used to locally change the transfer integrals and exert chemical pressure onto the system. In addition to that, disorder is introduced through the random distribution of the substitution sites. Recently a series of samples with varying substitution level of unsymmetrical bis(ethylenedithio)diselenadithiafulvalene (BEDT-STF) has been synthesised [123]. In this molecule in one of the central rings S is replaced with Se atoms as shown in Fig. 3.7A. The substitution leads to a local increase of the transfer integrals around the substituted dimer of approximately 23% [123]. Tab. 3.1 gives the experimentally determined  $U/W$  ratio for different substitution levels for  $\kappa\text{-}[\text{ET}_{1-x}\text{STF}_x]_2\text{Cu}_2(\text{CN})_3$ . An increasing substitution leads to a decreasing  $U/W$  ratio and therefore drives the systems towards the metallic side of the phase diagram.

The magnetic properties of  $\kappa\text{-}[\text{ET}_{1-x}\text{STF}_x]_2\text{Cu}_2(\text{CN})_3$  with  $x = 0.05$  substitution have been shown to be similar to those of the pure sample as determined by NMR measurements at the bulk as well as the substituted sites [123].

Using a series of samples with varying substitution, a phase diagram can be experimentally determined by DC transport measurements. Fig. 3.8 shows the phase diagram as a function of substitution in comparison to applying hydrostatic pressure to the pristine sample [124]. Both experiments yield similar results with a substitution level of  $x = 0.05$  approximately corresponding to a chemical pressure of 1 kbar.

Making use of the substituted samples, various interesting regions of the phase diagram can be reached without the need for applying hydrostatic pressure. Of particular interest is the low-temperature phase boundary between the metallic and insulating phases which should be of first order type in case of a conventional Mott transition. DC resistivity measurements on the pristine sample under hydrostatic pressure, however, show barely recognisable hysteresis at the transition [126]. This

TABLE 3.1 *Electronic correlations in different  $\kappa$ -ET<sub>2</sub>X compounds* Values for the  $U/W$  ratio of coulomb repulsion  $U$  and bandwidth  $W$  as experimentally determined from infrared spectroscopy. The electronic properties are more and more dominated by electronic correlations, the larger the  $U/W$  ratio becomes. As a result for large  $U/W$  a Mott-insulating ground state is expected, whereas metallic behaviour is present for lower numbers.

Compound	$(U/W)_{\text{exp}}$	Ref.
$\kappa$ -ET <sub>2</sub> Ag <sub>2</sub> (CN) <sub>3</sub>	1.96	[19]
$\kappa$ -ET <sub>2</sub> Cu <sub>2</sub> (CN) <sub>3</sub>	1.52	[19]
$\kappa$ -[ET <sub>1-x</sub> STF <sub>x</sub> ] <sub>2</sub> Cu <sub>2</sub> (CN) <sub>3</sub> $x = 0$	1.61	[124]
$x = 0.04$	1.56	
$x = 0.12$	1.42	
$x = 0.28$	1.34	
$x = 0.44$	1.33	
$x = 0.78$	1.32	
$x = 1$	1.31	

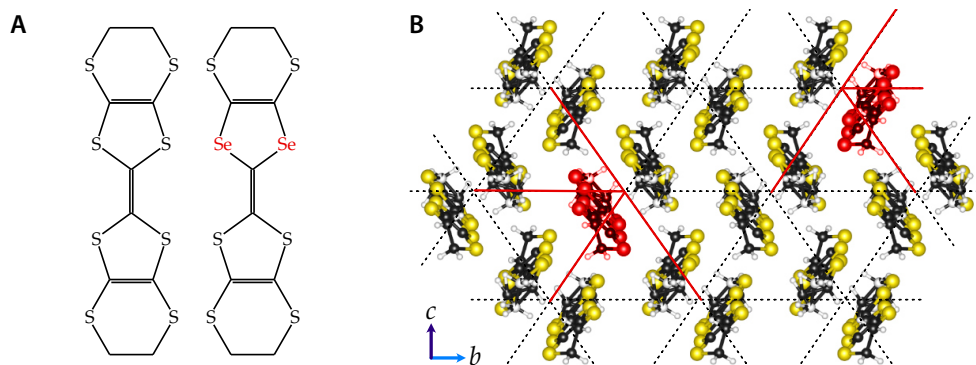


FIG. 3.7 *Molecular Substitution:  $\kappa$ -[ET<sub>1-x</sub>STF<sub>x</sub>]<sub>2</sub>Cu<sub>2</sub>(CN)<sub>3</sub>* (A) BEDT-TTF molecule (left) and the substituted BEDT-STF (right) where the S atoms in one of the two central rings are replaced by Se atoms. (B) The large spread of the Se 4d orbital in the substituted molecules (red) leads to a local increase of the transfer integrals. (visualised with VESTA [99])

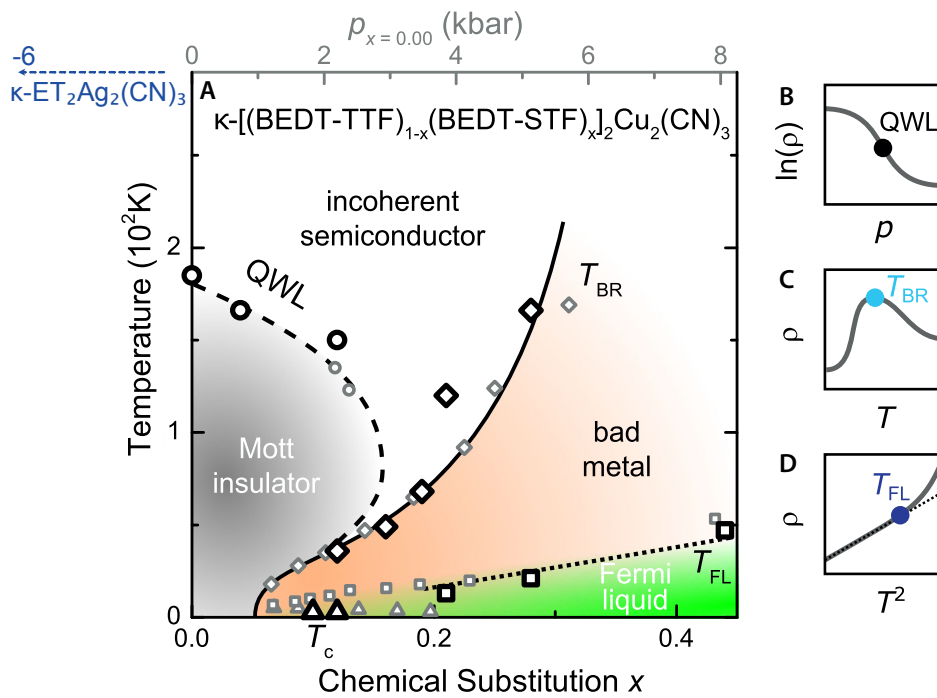


FIG. 3.8 *Pressure-Temperature Phase Diagram for  $\kappa$ - $[(\text{BEDT-TTF})_{1-x}(\text{BEDT-STF})_x]_2\text{Cu}_2(\text{CN})_3$*   
 (A) Phase diagram obtained from DC transport measurements as a function of chemical substitution (black symbols) and hydrostatic pressure on the pristine compound (grey) yield the same phase diagram. (B,C,D) illustrate how the features indicated in the phase diagram: the quantum Widom line (QWL), the Brinkman-Rice temperature  $T_{\text{BR}}$ , and the Fermi liquid onset temperature  $T_{\text{FL}}$  are obtained from the resistivity measurements. ((A) reproduced from [124], sketches (B,C,D) from [108]). The sister compound  $\kappa$ - $\text{ET}_2\text{Ag}_2(\text{CN})_3$  shows a similar phase diagram with a pressure offset of approx. 6 kbar [125].

indicates a very weak first-order nature and thus a quasi-continuous Mott transition. A phase coexistence region, expected for a first-order transition, has nevertheless been found in the vicinity of the transition by dielectric measurements [108]. Above the critical endpoint a quantum critical region is present in the phase diagram between the metallic and insulating phases [109]. Recently has been shown to be present already at ambient pressure for substitution levels of  $x = 0.10 - 0.12$ . The critical temperature  $T_c$  at ambient pressure reaches up to approximately 3 K. A superconducting dome with a maximum in  $T_c$  can be found as function of pressure [127].

An ESR study addressing the properties in different regions of the phase diagram has been performed as part of this project and is reported in section 5.1.

### 3.2.3 Deeper in the Mott Insulating State: $\kappa$ -(BEDT – TTF)<sub>2</sub>Ag<sub>2</sub>(CN)<sub>3</sub>

In analogy to  $\kappa$ -ET<sub>2</sub>Cu<sub>2</sub>(CN)<sub>3</sub> the sister compound  $\kappa$ -ET<sub>2</sub>Ag<sub>2</sub>(CN)<sub>3</sub> with Ag ions instead of Cu within the anion sheet has been synthesised [128]. The introduction of Ag ions increases the unit cell volume by approximately 4% applying a negative chemical pressure to the system. The expanded triangular lattice in the  $bc$  plane retains its large degree of frustration with a reported ratio between the transfer integrals  $t/t' = 0.97$  [125]. This leads to smaller orbital overlap and thus smaller transfer integrals between the neighbouring dimers.  $\kappa$ -ET<sub>2</sub>Ag<sub>2</sub>(CN)<sub>3</sub>, thus shows an even stronger influence of electronic correlations compared to  $\kappa$ -ET<sub>2</sub>Cu<sub>2</sub>(CN)<sub>3</sub>, reflected by the larger  $U/W$  ratio (see Tab. 3.1). It is located further away from the metal to insulator phase transition, deep in the Mott insulating state. The pressure temperature phase diagram is similar to that of  $\kappa$ -ET<sub>2</sub>Cu<sub>2</sub>(CN)<sub>3</sub> shifted by a pressure offset of 6 kbar [125]. NMR measurements have shown that no magnetic order occurs down to the lowest measured temperature of 0.11 K and a low-temperature linear specific heat contribution has been found analogous to  $\kappa$ -ET<sub>2</sub>Cu<sub>2</sub>(CN)<sub>3</sub>. Magnetisation measurements yielded similar results as for  $\kappa$ -ET<sub>2</sub>Cu<sub>2</sub>(CN)<sub>3</sub> [125]: the high temperature behaviour is well described by an antiferromagnetic Heisenberg model on a triangular lattice with exchange energy  $J = 175$  K, lower than the Cu case in accord with the smaller transfer integral; the susceptibility decreases below 20 K before it saturates to about half the room temperature value; for the Cu compound a more pronounced decrease was observed below 7 K [2]. Specific heat measurements reveal a finite linear specific heat contribution as in  $\kappa$ -ET<sub>2</sub>Cu<sub>2</sub>(CN)<sub>3</sub> with about half of the magnitude [125]. These results point to the fact that the compound hosts a quantum spin liquid

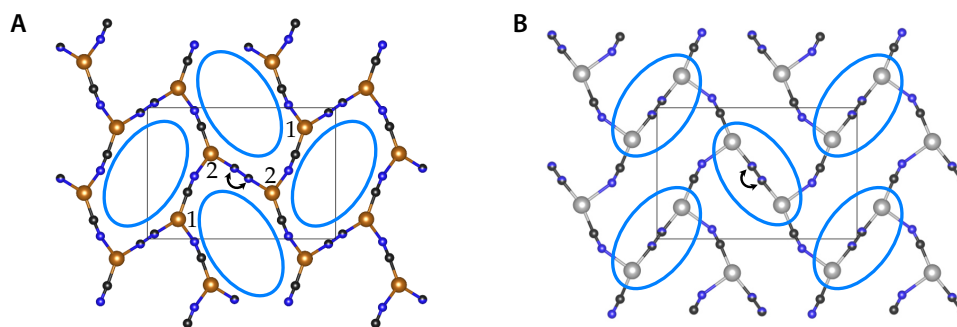


FIG. 3.9 Anion Sheets in  $\kappa\text{-ET}_2\text{Cu}_2(\text{CN})_3$  and  $\kappa\text{-ET}_2\text{Ag}_2(\text{CN})_3$ . In the copper (A) as well as the silver (B) analogues the anions form a two-dimensional polymeric network. The colours represent the different atoms as follows: copper (orange), silver (silver), nitrogen (blue), carbon (black). Notice the CN group located at the inversion centre. Both possible arrangements of carbon and nitrogen atoms are present in the crystals resulting in intrinsic disorder. The blue ellipses indicate the different relative positions of the ET dimers in the adjacent conducting layers. The two distinct configurations of Cu ions are indicated (1,2). (crystallographic data for Cu: [98], CCDC No. 850028; for Ag: [128], CCDC No. 1023571, visualised with VESTA [99])

ground state with gapless excitations similar to what has been generally assumed for  $\kappa\text{-ET}_2\text{Cu}_2(\text{CN})_3$ .

A lower intrinsic disorder level is expected in  $\kappa\text{-ET}_2\text{Ag}_2(\text{CN})_3$  compared to  $\kappa\text{-ET}_2\text{Cu}_2(\text{CN})_3$  [129]. The arrangement of the BEDT–TTF dimers with respect to the anion sheets differs in both compounds as illustrated in Fig. 3.9. Whereas in  $\kappa\text{-ET}_2\text{Cu}_2(\text{CN})_3$  the dimers sit in the opening of the hexagons of the polymeric anion layers, in the case of  $\kappa\text{-ET}_2\text{Ag}_2(\text{CN})_3$  the centre of the dimer is located on top of the bridging CN groups. This results in a larger distance of the terminal ethylene groups of the ET molecules to the CN group. Less perturbation of the molecular layers due to the intrinsically disordered sequence of CN is therefore expected for  $\kappa\text{-ET}_2\text{Ag}_2(\text{CN})_3$ , which manifests in a lower in-plane dielectric strength [129]. A recent X-ray diffraction study has indeed shown that the terminal ethylene groups are ordered in  $\kappa\text{-ET}_2\text{Ag}_2(\text{CN})_3$ , while these groups are disordered in  $\kappa\text{-ET}_2\text{Cu}_2(\text{CN})_3$  [130].

In addition to the lower intrinsic disorder, no intrinsic magnetic impurities are expected in the Ag compound in contrast to the case of  $\kappa\text{-ET}_2\text{Cu}_2(\text{CN})_3$  where  $\text{Cu}^{2+}$  ions act as magnetic impurities [116]. Usually nonmagnetic  $\text{Ag}^+$  should be the only present ion due to the significantly larger second ionisation energy to form  $\text{Ag}^{2+}$  compared to  $\text{Cu}^{2+}$  [131].

Temperature-dependent ESR measurements on a single crystal of  $\kappa\text{-ET}_2\text{Ag}_2(\text{CN})_3$  have been performed as part of this project. The results are presented within section 5.2

### 3.3 Studied Samples

All experiments were performed on crystals grown by electro-crystallisation methods [110]. The specimen have plate-like shape with a typical size in the range of  $1\text{ mm} \times 1\text{ mm} \times 100\ \mu\text{m}$  as shown in Fig. 3.1. The measurements were performed on the crystals as grown without further treatment. Crystals from each batch were characterised within the institute by DC resistivity as a function of temperature. To select specimen of the correct phase and determine their crystallographic orientation, measurements of the polarised infrared reflectivity have been used. Precise alignment (within  $5^\circ$ ) for the ESR measurements was achieved in-situ using the goniometer on the X-band spectrometer.

The samples were mostly provided by external collaborators. In the case of  $\kappa\text{-ET}_2\text{Cu}_2(\text{CN})_3$  samples from collaborators from four different laboratories have been investigated:

- #1 A.A. Bardin, Institute of Problems of Chemical Physics, Russian Academy of Sciences, Chernogolovka, Russia
- #2 K. Kanoda, Department of Applied Physics, University of Tokyo, Tokyo, Japan
- #3 R. Hübner, 1. Physikalisches Institut, University of Stuttgart, Stuttgart, Germany
- #4 J.A. Schlueter, Material Science Division, Argonne National Laboratory, Argonne, Illinois, USA

The variation of the ESR parameters for  $T > 4\text{ K}$  between the different samples is inconsiderable. However, significant differences arise for lower temperatures as discussed in section 4.3. The studied  $\kappa\text{-ET}_2\text{Ag}_2(\text{CN})_3$  crystal was provided by T. Hiramatsu, Y. Yoshida and G. Saito (Meijo University, Nagoya, Japan) [128]. The substituted  $\kappa\text{-}[\text{ET}_{1-x}\text{STF}_x]_2\text{Cu}_2(\text{CN})_3$  crystals with different amounts  $x$  of BEDT – STF have been synthesised at the Department of Physics, Hokkaido University, Sapporo, Japan [123].



## 4 Gapped Magnetic Ground State in Quantum Spin Liquid Candidate

### $\kappa$ -(BEDT – TTF)<sub>2</sub>Cu<sub>2</sub>(CN)<sub>3</sub>

The main results presented in this section have been published in [M2] **B. Miksch**, A. Pustogow, M. Javaheri Rahim, A. A. Bardin, K. Kanoda, J. A. Schlueter, R. Hübner, M. Scheffler and M. Dressel, *Gapped magnetic ground state in quantum spin liquid candidate  $\kappa$ -(BEDT – TTF)<sub>2</sub>Cu<sub>2</sub>(CN)<sub>3</sub>*, *Science* **372**, 276 (2021) and the corresponding supplementary materials.

In 2003, NMR measurements have shown that conventional magnetic order is absent in  $\kappa$ -(BEDT – TTF)<sub>2</sub>Cu<sub>2</sub>(CN)<sub>3</sub> even at temperatures orders of magnitude below the exchange energies in the system [2]. The material has since been considered to be the prime candidate for hosting a quantum spin liquid state. Several review articles on quantum spin liquids have summarised the experimental studies [3–6].

Nevertheless, despite the large number of experimental studies, crucial open questions have remained unanswered as summarised in section 3.2.1. In particular the system's exact ground state is still undetermined; the nature of the anomalies observed at  $T^* = 6$  K remains unresolved and it is unclear whether a spin gap exists and how the spin excitation spectrum looks like.

ESR measurements have been performed with conventional spectrometers as well as broadband techniques to tackle those questions. The results of the measurements are presented and discussed within this chapter. In the final section a ground state scenario is proposed based on the findings. It is shown to be compatible to most of the previous experimental results and allows to resolve so far contradicting conclusions.

Exemplary raw data obtained with the conventional X-band spectrometer are shown in Fig. 4.1A to give an overview of the temperature-dependent behaviour of the ESR spectra for a single crystal of  $\kappa$ -ET<sub>2</sub>Cu<sub>2</sub>(CN)<sub>3</sub>. At room temperature a Dysonian line shape is observed which transforms into a symmetric Lorentzian shape upon

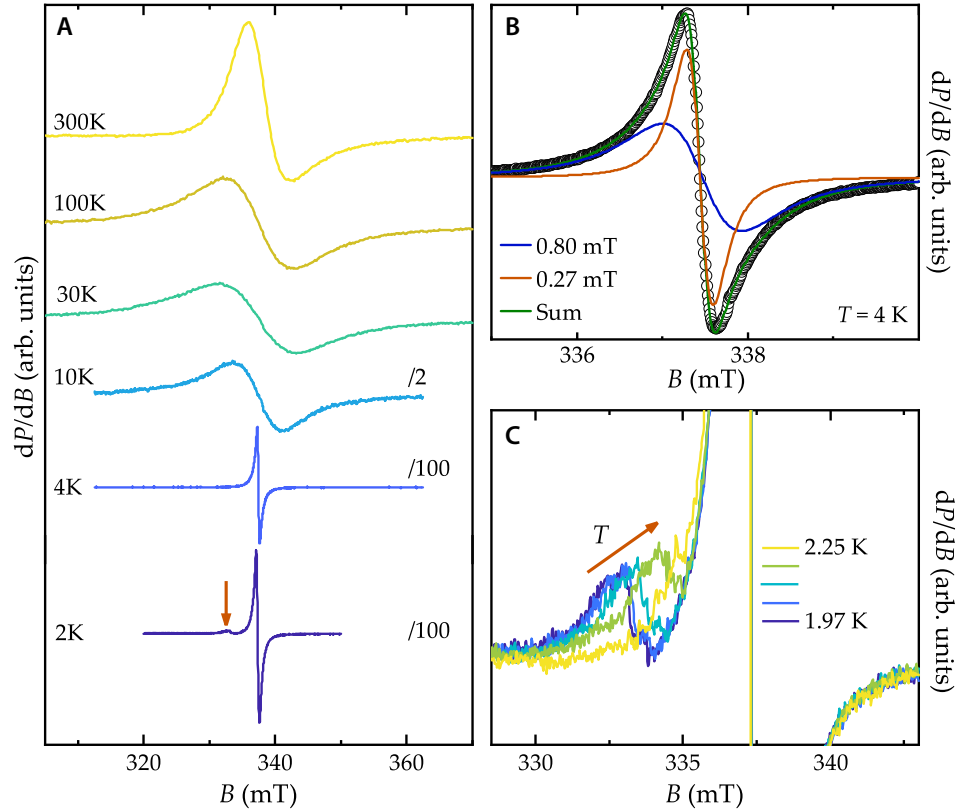


FIG. 4.1 X-Band ESR Spectra (A) Evolution of the X-band spectra as a function of temperature with magnetic field  $B_0 \parallel c$ . The signal is divided by 2, respectively 100, for  $T \leq 10$  K to account for the increasing peak height as the line sharpens upon cooling. (B) Below  $T^*$  an additional narrower component emerges at the resonance field of the main signal requiring a second Lorentzian function for a satisfying fit to the spectra. This signal can be assigned to defect spins not involved in the singlet formation at low temperatures. The respective decomposition is shown exemplarily for the 4 K spectrum. (C) The defect signal separates below  $T_{\text{loc}} \approx 2.5$  K and shifts towards lower resonance fields upon further cooling.

cooling as a result of the decreasing conductivity. This is in accordance with the semi-conducting temperature-dependence of the conductivity revealed by DC transport measurements [107, 110]. The resonance field does not show any significant change for all spectra through the whole temperature range from 300 K to 2 K. In contrast to that, the line width  $\Delta B$  initially increases for the first three spectra shown, reaching a maximum. For lower temperatures it decreases again, first moderately, then, starting below 10 K in the vicinity of  $T^* = 6$  K, strongly by more than a factor of ten. This behaviour is also resembled by the intensity corresponding to the spin susceptibility  $\chi_S$ : After an increase, a broad maximum is followed by a moderate decrease, before it drops abruptly starting near  $T^*$ . This decrease is accompanied by a change of the line shape. A single Lorentzian model does not give a satisfying fit to the data any more. Fitting two Lorentzian functions reveals the appearance of a second component with smaller line width below  $T^*$ . As illustrated in Fig. 4.1B it emerges at the same resonance field of  $B_{\text{main}} = 337$  mT as the signal in the paramagnetic state. Upon further cooling, below  $T_{\text{loc}} \approx 2.5$  K part of the second component splits off as an additional signal and shifts away from  $B_{\text{main}}$  as indicated in Fig. 4.1C.

In the following, results of the ESR measurements mostly in the paramagnetic state at elevated temperatures are shown and discussed in detail (section 4.1). Afterwards, evidence for the opening of a spin gap at  $T^*$  is presented alongside an argumentation on the nature of the ground state of  $\kappa\text{-ET}_2\text{Cu}_2(\text{CN})_3$  (section 4.2). Subsequently, follows an in-depth discussion of additional contributions to the ESR spectra including the feature introduced in Figs. 4.1B,C (section 4.3) accompanied by a comparison of different samples. Then, frequency-dependent experimental results for temperatures down to the mK regime are presented. This allows a discussion of the influence of disorder on the low-temperature magnetic properties (section 4.4). In a final conclusion a ground state scenario is proposed based on the presented experiments (section 4.5). This includes a discussion upon the role of impurities in concealing the nature of the ground state to previous experiments. Unless otherwise stated, all results presented within this chapter are obtained with a single batch of samples from Chernogolovka, Russia (sample #1).

## 4.1 Temperature-Dependence of the ESR Parameters

The starting point to characterise the magnetic properties of  $\kappa\text{-ET}_2\text{Cu}_2(\text{CN})_3$  are temperature-dependent X-band ESR measurements. Measurements have been per-

formed with the static magnetic field  $\mathbf{B}_0$  oriented along the three crystallographic axes  $a^*, b, c$  as a first characterisation for crystals from the four different labs mentioned in section 3.3. The sample to sample variation in the observed ESR parameters (spin susceptibility  $\chi_S$ ,  $g$ -factor, and line width  $\Delta B$ ) is small for temperatures  $T > 4$  K as can be seen in the side by side comparison in Fig. 4.2.

As the samples are oriented with the conductive  $bc$ -plane perpendicular to the microwave magnetic field  $\mathbf{B}_1$ , screening eddy currents form, leading to a reduced skin depth  $\delta$  at elevated temperatures. The effect of the increased conductivity can be seen in the ESR measurements as an increasing dispersion-absorption ratio  $\alpha$  represented by the open symbols in Fig. 4.2A. The skin depth  $\delta$  can be estimated using the DC resistivity within the  $bc$  plane of approximately  $\rho_{300\text{K}} = 0.1 \Omega\text{cm}$  at room temperature and  $\rho_{100\text{K}} = 10 \Omega\text{cm}$  at 100 K from [107], the X-band frequency of  $\omega = 2\pi \cdot 9.8 \text{ GHz}$  and a permeability of  $\mu \approx \mu_0$ . Using

$$\delta = \sqrt{\frac{2\rho}{\omega\mu}} \quad (4.1)$$

one obtains  $\delta(300 \text{ K}) = 160 \mu\text{m}$  and  $\delta(100 \text{ K}) = 1.6 \text{ mm}$ . As the thickness of the crystal platelets along the  $a^*$  direction is in the same order of magnitude as the skin depth (several  $100 \mu\text{m}$  to  $1 \text{ mm}$ ), at room temperature the inner part of the crystal is screened from the microwaves and thus does not contribute to the ESR absorption. The large difference in the spin susceptibility  $\chi_S$  between the crystals can thus be attributed to their different dimensions, in particular the thickness.  $\chi_S$  cannot be trusted for temperatures where the dispersion-absorption ratio  $\alpha \gg 0$ , i. e.  $T > 100 \text{ K}$  rendering the normalisation of  $\chi_S$  at room temperature impossible. The qualitative behaviour of  $\chi_S$  is nevertheless similar for all three samples as can be seen in Fig. 4.2A.

The  $g$  factor (Fig. 4.2B) does not show a significant difference between samples # 1 and # 2 within an assumed error of 5 % of the line width. For sample # 4 the  $g$  factor is larger by approximately 0.003 for the measurement shown. This corresponds to a change in resonance field of 0.5 mT which can be explained well by the recalibration of the magnet which has been done in between the earlier measurements of sample # 4 and the later experiments on samples # 1 and # 2.

The line width shown in panel C for the three samples is indistinguishable. All ESR parameters shown coincide moreover well with previously published results [115, 116, 132].

Fig. 4.3 gives a detailed view of the ESR parameters as a function of temperature

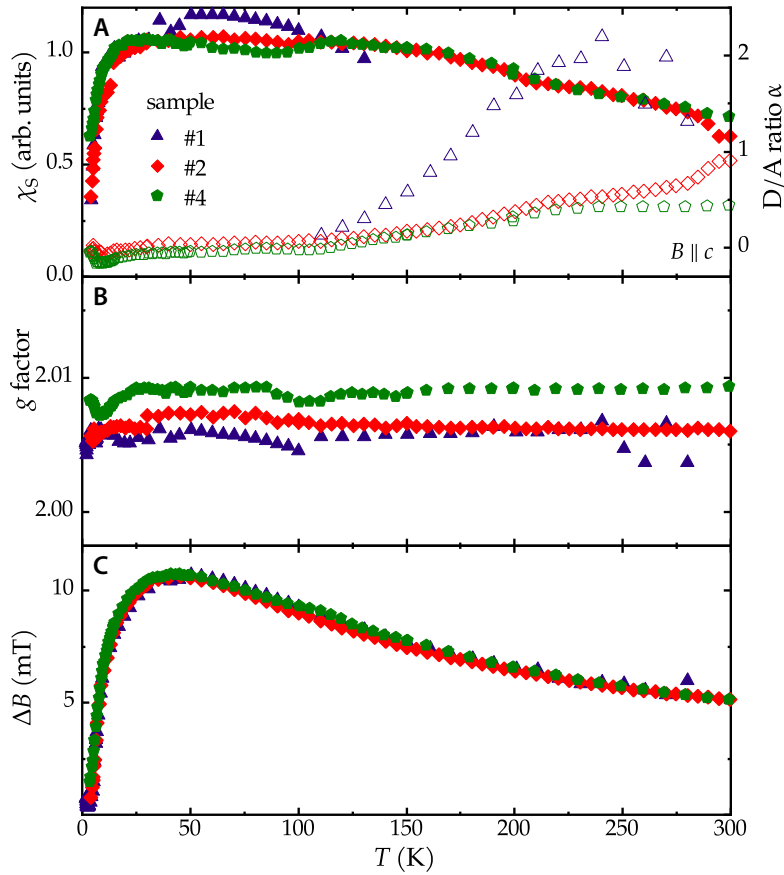


FIG. 4.2 *Sample-Dependence of ESR Parameters* Spin susceptibility  $\chi_s$  and dispersion-absorption ratio  $\alpha$  (A),  $g$  factor (B) and line width  $\Delta B$  (C) as a function of temperature with magnetic field  $B_0 \parallel c$  for samples from three different labs. The overall sample-dependence is small. The increasing dispersion-absorption ratio  $\alpha$  represented by the open symbols in (A) indicates the increased conductivity at elevated temperatures. The absolute value of  $\alpha$  depends on the relative dimensions of the sample with respect to the skin depth. Due to the finite skin depth the ESR absorption and thus the extracted values of  $\chi_s$  are artificially reduced. A normalisation at room temperature is in this case impossible. Therefore the curves have been manually scaled on top of each other to allow a comparison of the relative behaviour.

for a crystal of sample #1 presented with a logarithmic temperature scale. For high temperatures the spin susceptibility  $\chi_S(T)$  can be described by the antiferromagnetic Heisenberg model on a triangular lattice given in equation (1.20). Taking into account only interactions of strength  $J$  between nearest neighbours on the triangular lattice, the susceptibility values can be obtained by high temperature series expansion extrapolated to lower  $T$  using Padé approximants as described in [113]. The black curve in Fig. 4.3A is the [7/7] Padé approximant with a Heisenberg exchange interaction of  $J = 250$  K in accordance with previous results [2].

Below  $T^*$  valence bonds between the spins form resulting in a spin singlet state as evidenced by the exponential decrease of  $\chi_S(T)$  pointing to the opening of a spin gap. Details of this behaviour, appropriate models and the implications for the ground state are discussed in section 4.2.

An additional narrower component to the signal appears at  $T^*$  as shown in Figs. 4.1B. This change of the line shape has also been previously described in [116] where it was vaguely attributed to the influence of a Dzyaloshinskii–Moriya-like interaction. The signal appears simultaneously to the beginning formation of the spin singlet state and its intensity increases upon further cooling as the orange symbols in Fig. 4.3A indicate. Unpaired defect spins not taking part in the formation of the spin singlet state are a likely source of the increasing defect signal. The intensity of the defect contribution is strongly sample-dependent implying that intrinsic disorder is playing an important role for the low-temperature properties. The detailed behaviour and sample-dependence is discussed in section 4.3.

The  $g$ -factor of the main signal is temperature independent within the experimental uncertainty as can be seen in Fig. 4.3B for all three orientations. Values of  $g_{a^*} = 2.008$  for out of plane and  $g_b = 2.004$  and  $g_c = 2.006$  for in plane orientation were found in agreement with published data [115, 116]. The same temperature independent values have also been found for W-band measurements at ten times larger frequency of 95 GHz.

Fig. 4.3C depicts the behaviour of the line width  $\Delta B(T)$ :  $\Delta B(T)$  increases upon cooling reaching a broad maximum around 40 K and is strongly reduced below 10 K. Along the  $b$ -direction  $\Delta B$  is twice as large compared to the  $a^*$  and  $c$  directions.

Inhomogeneities can lead to a distribution of the  $g$ -factor between individual sites and thus result in Gaussian broadening of the absorption lines depending on the external magnetic field. Identical values of the line width are however found in W-band measurements for temperatures between 5 K and 100 K as shown in Fig. 4.4. The fact that a ten times larger magnetic field does not broaden the ESR absorption rules

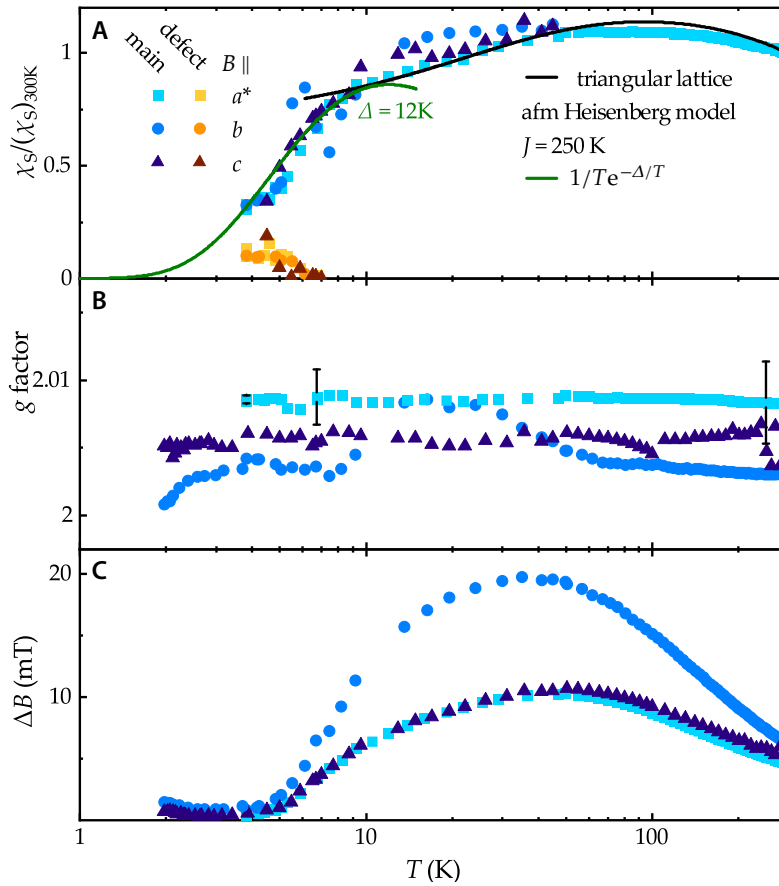


FIG. 4.3 *Temperature-Dependence of ESR Parameters* The spin susceptibility  $\chi_S$  (A),  $g$  factor (B) and line width  $\Delta B$  (C) are obtained from fits to the X-band (9.5 GHz) ESR spectra measured along the three orthogonal directions  $B_0 \parallel a^*, b, c$ . At elevated temperatures  $\chi_S$  is well described by spin susceptibility of a Heisenberg antiferromagnet on a triangular lattice. Below  $T^*$  the intensity of the main signal drops exponentially hinting at the opening of a spin gap. The susceptibility of the simultaneously emerging defect contribution is shown by the orange symbols. No change can be observed in the  $g$ -factor within the experimental uncertainty estimated as 5% of the line width. The line width  $\Delta B(T)$  increases starting from room temperature while the largest values are observed along the  $b$ -direction. A maximum followed by a moderate decrease is reached around 40 K for all three directions. Below 10 K the line narrows drastically reaching a minimum around  $T_{loc}$ .

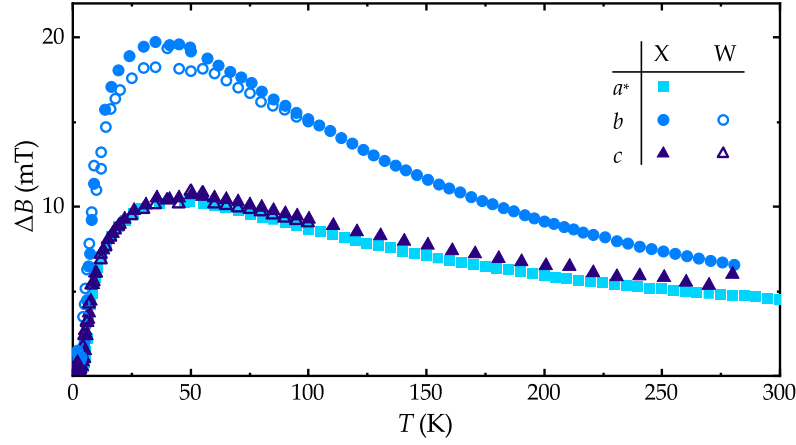


FIG. 4.4 *ESR Line Width at Different Magnetic Fields* Spectra measured in X-band (closed symbols) at  $B_0 \approx 340$  mT and W-band (open symbols) at 10 times higher field  $B_0 \approx 3.4$  T show almost identical line width over the whole temperature range 5 – 100 K.

out any influence of inhomogeneity within the samples for the given temperature range.

A magnified graph of the low-temperature line width is given in Fig. 4.5 for both the main as well as the defect signal. Around  $T_{\text{loc}} = 2.5$  K a minimum in the line width is observed coinciding with the emergent shift of the defect signal away from  $B_{\text{main}}$ . As the separated defect signal has a complex line shape a single line width cannot be given for that. The intrinsic signal is almost frozen out at this temperature, thus the increasing line width has to be attributed to extrinsic contributions remaining at  $B_{\text{main}}$  as discussed in section 4.4.2. One explanation could be an increasing contribution of dipole-dipole interaction of the emerging defect spins with local magnetic impurities that become increasingly polarised at lower temperatures.

An exchange narrowed ESR line can be expected from the large exchange coupling of  $J = 250$  K. Thus, as described in section 2.3, Kubo-Tomita theory can be used to approximate  $\Delta B$ . In the insulating state three electronic contributions have to be considered as a perturbation contributing to the ESR line width: dipole-dipole interaction between neighbouring spins, anisotropic exchange and antisymmetric DM exchange. Here, the latter two are introduced by spin-orbit coupling which is often assumed to be negligible in organics due to the light elements, but has been recently shown to be of great importance for the magnetic properties of  $\kappa\text{-ET}_2\text{Cu}_2(\text{CN})_3$  [117]. Hyperfine interactions can technically also contribute to the ESR line width. In the case of  $\kappa\text{-ET}_2\text{Cu}_2(\text{CN})_3$  they can be neglected as the predominant isotopes of carbon

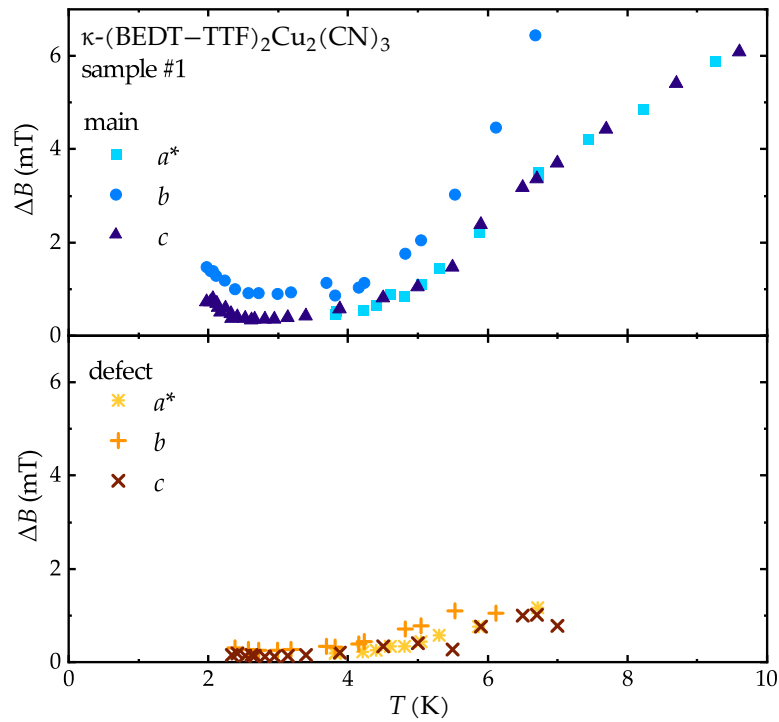


FIG. 4.5 *Low-Temperature ESR Line Width* Magnifying the low-temperature range from Fig. 4.3C reveals a minimum in the line width  $\Delta B$ . While the main signal as well as the defect line continuously sharpen upon cooling down to  $T = 3$  K, a pronounced broadening can be observed below 2.5 K

and sulphur which form the molecules hosting the spins under consideration do not carry nuclear spin.

The contribution of the three individual interactions can be estimated as follows according to [49]. Omitting the intricate angular-dependence the second moments  $M_2(J/k_B T)$  used in equation (2.32) are

$$M_2^{DD} = \frac{3g^4\mu_B^4}{2\hbar^2} S(S+1) \frac{6}{|r|^6} \quad (4.2)$$

$$M_2^{AE} = \frac{3}{2\hbar^2} A^2 S(S+1) \quad (4.3)$$

$$M_2^{DM} = \frac{1}{3\hbar^2} S(S+1) |D|^2 \quad (4.4)$$

in the high temperature limit  $J/T \rightarrow 0$ . The inter-dimer distance  $r_{ij}$  is almost equal for the six neighbouring sites and taken as  $|r| \approx 8 \text{ \AA}$  from the crystallographic data (8.58  $\text{\AA}$  along  $b$ , 7.95  $\text{\AA}$  along  $c \pm b$ ) [107]. Values for the isotropic exchange coupling  $J$ , the DM vector  $D$  and the traceless anisotropic exchange tensor  $\Gamma$ , with diagonal  $(2A, -A, -A)$ , are taken from previous calculations via cluster exact diagonalisation [117]. Here, the values  $J = 250 \text{ K}$ ,  $D = (3.30, 0.94, 0.99) \text{ K}$  and  $A = 6.65 \text{ mK}$  are used. The calculations reveal the DM interaction as the dominant contribution to the line width in the order of  $\Delta B^{DM} \approx 10 \text{ mT}$ . This is in good agreement with the observed line width  $\Delta B_{a^*,c} \approx 10 \text{ mT}$  and  $\Delta B_b \approx 20 \text{ mT}$  at the broad maximum around 40 K. In comparison the contributions from dipole-dipole interaction  $\Delta B^{DD} \approx 5 \times 10^{-4} \text{ mT}$  and anisotropic exchange  $\Delta B^{AE} \approx 1.5 \times 10^{-4} \text{ mT}$  are negligible.

Multiple effects contribute to the temperature-dependence of the line width: Owing to the increasing conductivity at higher temperatures the spin diffusion increases according to Elliott's relation [46]. As a result the line width  $\Delta B$  is reduced. According to [49] a decrease of the dominant DM contribution is expected upon cooling. This explains the overall decrease below 30 K.

In conclusion, the temperature-dependent behaviour of the ESR parameters is similar in all investigated samples in the paramagnetic state above  $T^* = 6 \text{ K}$  and is in agreement with previously published results [115, 116]. The behaviour resembles other  $\kappa\text{-ET}_2X$  organic conductors [132]. A  $S = 1/2$  Heisenberg antiferromagnet on a triangular lattice with exchange interaction  $J = 250 \text{ K}$  models the spin system in this temperature range appropriately. It allows a prediction of the spin susceptibility with good agreement to the experimental data. The observed broad line width of the ESR absorption in this strongly exchange coupled system can be explained by

DM exchange, supporting the discovery of the importance of spin orbit coupling in  $\kappa\text{-ET}_2\text{Cu}_2(\text{CN})_3$  [117].

## 4.2 Opening of the Spin Gap

The starting point to clarify the nature of the ground state as well as the  $T^*$  anomaly is the temperature-dependence of the spin susceptibility  $\chi_S(T)$  plotted in Fig. 4.6 as derived from the ESR measurements. As discussed in the previous section, at elevated temperature  $T > T^*$ ,  $\chi_S(T)$  is well described by the antiferromagnetic Heisenberg model. However, below  $T^*$  the spin susceptibility sharply drops below the model's prediction. The formation of long range magnetic order or any other well defined local moments can be ruled out because the  $g$ -factor remains unchanged [see Fig. 4.3]. Magnetic transitions to an ordered state would be accompanied by internal fields exposed by an altered  $g$ -factor. This behaviour is in accord with the previous NMR results [2] discussed in section 3.2.1 that did not show any splitting in the spectra. It can be concluded that  $\kappa\text{-ET}_2\text{Cu}_2(\text{CN})_3$  hosts a nonmagnetic ground state. One possibility for such a ground state is a spin singlet state emerging from the paramagnetic phase by the formation of valence bonds between the spins on two adjacent BEDT–TTF dimers.

The exponential decay of the spin susceptibility as a function of temperature below  $T^*$  indicates the opening of an energy gap in the spin excitation spectrum. This is in stark contrast to the gapless quantum spin liquid ground state widely suggested by former publications [2, 118] as described in section 3.2.1. Itinerant spinons with a gapless continuous excitation spectrum as predicted on a resonating valence bond state are not compatible with the observed energy gap. A gapped valence bond state with an energy gap associated to the singlet-triplet excitations is nevertheless imaginable. This and other possible scenarios for the ground state in  $\kappa\text{-ET}_2\text{Cu}_2(\text{CN})_3$  have to be considered as a consequence.

### 4.2.1 Modelling the Temperature-Dependent Spin Susceptibility

In order to discuss possible ground states, the properties of the phase transition have to be quantified. Two models were fitted to the susceptibility data to extract those

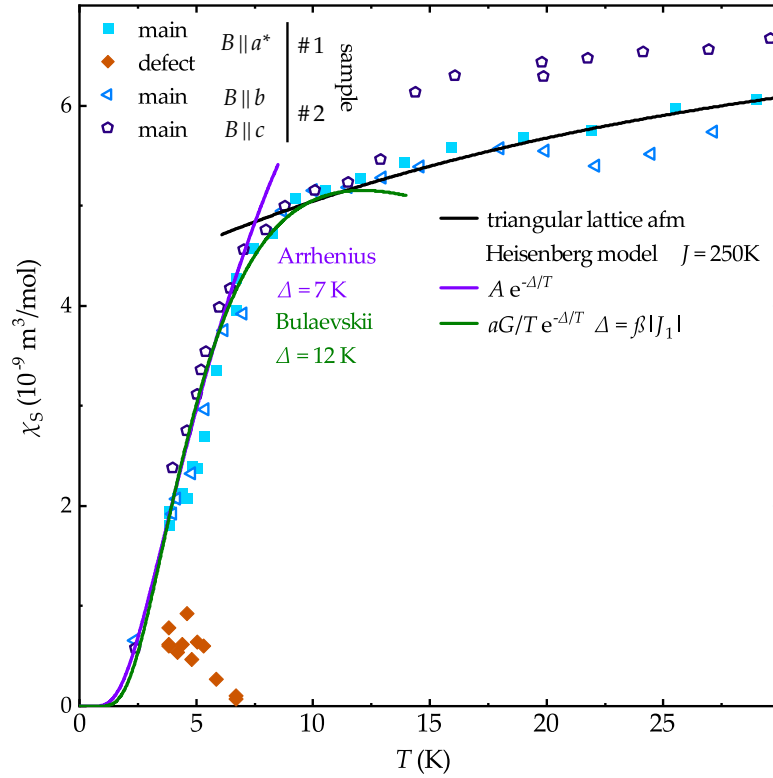


FIG. 4.6 *Gapped Magnetic Ground State* Temperature-dependence of the spin susceptibility  $\chi_S$  as determined from X-band ESR measurements along different directions. Absolute values have been obtained via a room temperature calibration with a DPPH standard. The data shown for  $B \parallel b, c$  are for sample #2. For elevated temperatures,  $\chi_S(T)$  is well described by the susceptibility of a Heisenberg antiferromagnet on a triangular lattice with exchange coupling  $J = 250\text{ K}$  (black line). Below the  $T^*$ -anomaly around 6 K the opening of a spin gap can be observed as evidenced by the exponential decay of the main signal. The orange symbols show the increasing contribution of the defect spins for  $T < T^*$ . Two models are fitted to the exponential decay: a simple Arrhenius law (violet) resulting in a gap of  $\Delta = 7\text{ K}$  as well as the Bulaevskii model (green) describing alternating spin chains resulting in  $\Delta = 12\text{ K}$ .

attributes, in particular the size of the spin gap  $\Delta$ :

$$\chi_S^A(T) = Ae^{-\frac{\Delta}{T}} \quad (4.5)$$

$$\chi_S^B(T) = \frac{\alpha\Gamma}{T} e^{-\frac{\beta|J_1|}{T}} \quad (4.6)$$

The fits are shown in Fig. 4.6 as the violet and green curves. The simple case of a thermally activated behaviour of the singlet-triplet excitations (violet) described by Arrhenius' law (4.5) results in a value of  $\Delta = 7.3$  K for the spin gap with a prefactor of  $A = 1.02 \times 10^{-3}$  emu/mol.

In one-dimensional systems the Bulaevskii model (4.6) [25] can be used to describe the temperature-dependent susceptibility for spin chains with alternating exchange couplings  $J_1$  and  $J_2$  along the chain. Some spin chain systems show a spin-Peierls phase transition, where a lattice distortion doubling the period is coupled to the dimerisation of neighbouring spins to a singlet state, resulting in an overall lower energy state. This phenomenon can be modelled by extending the Bulaevskii model to include lattice dynamics to account for the temperature-dependent spin dimerisation [26–28, 133] and has been successfully applied to one-dimensional organic charge transfer salts [38].

The model is applied to the shown results; using the constant  $\Gamma = N_A g^2 \mu_B^2 / k_B = 15\,012$  emuK/mol one obtains the molar susceptibility in units of  $10^{-4}$  emu/mol. The dimerisation strength  $J_2/J_1 = \gamma$  can be estimated from the fit parameters  $\alpha$  and  $\beta$  and the exchange coupling above the dimerisation  $J$  as described in [38]. By using the exchange coupling  $J = 250$  K the shown fit is obtained with  $\alpha = 9.0 \times 10^{-3}$ ,  $\beta = 0.047$  with a resulting dimerisation strength  $\gamma = 0.97$  and a spin gap  $\Delta = 12.1$  K.

As shown in section 3.2.1 a pronounced feature in the thermal expansion can be observed around the phase transition temperature  $T^*$  in  $\kappa$ -ET<sub>2</sub>Cu<sub>2</sub>(CN)<sub>3</sub> [120]. This suggests that the  $T^*$  magnetic phase transition is coupled to the lattice leading to the development of an increasingly one-dimensional character. Therefore, the described model was applied as the simplest approach to capture the relevant spin dimerisation. The obtained dimerisation strength  $\gamma$  indicates a small enhancement of the exchange coupling in the valence bonds of  $\leq 2\%$ . Mean-field calculations show a BCS-like relation of the dimerisation temperature to the gap for the one-dimensional systems:  $2\Delta(0\text{ K})/T^* = 3.53$  [26]. With the obtained spin gap from the model fit this leads to a temperature  $T^* = 6.9$  K in good agreement with the temperature at which the features have been observed in the spin susceptibility  $\chi_S(T)$  and the thermal expansion.

## 4.2.2 Possible Ground State Scenarios

Various possible ground states have to be considered now as the widely proposed gapless quantum spin liquid (QSL) scenario with a spinon Fermi surface [2, 3, 118] is clearly ruled out by the observation of a spin gap. Different alternative scenarios are discussed in literature as a ground state for frustrated spin  $S = 1/2$  systems on weakly distorted triangular lattices.

An introduction into the different considered models with static valence bonds, as well as the spin liquid models is given in section 1.4 following the overview given in the recent review articles [4–6]. The possibilities include different spin singlets states where the formed valence bonds are localised on the lattice. Two options are a symmetry broken valence bond solid (VBS) where the valence bonds are arranged in a crystalline manner and a random singlet or valence bond glass (VBG) phase with disordered arrangement [24, 30, 31, 134]. In addition to that more intricate resonating valence bond models have been suggested to explain a gapped spin liquid state. These include a  $Z_2$  spin liquid phase found in the triangular-lattice dimer model, that predicts gapped spinons [35]; and an Amperean pairing instability in the  $U(1)$  spin liquid state with spinon Fermi surface, which imposes a gap to the mobile spinons [36].

First, the resemblance of the temperature-dependent spin susceptibility to the spin-Peierls transition described in the previous section in conjunction with the structural anomaly with anisotropic thermal expansion observed in  $\kappa\text{-ET}_2\text{Cu}_2(\text{CN})_3$  leverages the idea of a symmetry broken VBS scenario. Similar models have also been proposed in kagomé lattices [135] as well as in three-dimensional frustrated lattices [136]. The formation of spin singlet valence bonds in crystalline arrangement with bonds oriented predominantly along a certain direction would explain the similarities to the spin-Peierls transition in spin chains as well as the anisotropic thermal expansion. The underlying magnetoelastic coupling is further corroborated by a pronounced lattice softening observed in an ultrasound investigation [121]. The shrinkage observed along the  $c$  axis below  $T^*$  [120] suggest the  $(b \pm c)$  directions as the preferable orientations. A VBS scenario is thus consistent with the observations made by the ESR measurements. However, a certain amount of unpaired spins seems to remain present in the system being ultimately responsible for the additional signals observed at low temperatures as shown in Fig. 4.1B,C. In a VBS scenario these could be represented by defects in the valence bond lattice as discussed previously in the theory section within the illustration Fig. 1.9.

A random pinning of the valence bonds in a glassy state is also compatible with the observed spin defects [24, 31]. The inhomogeneity introduced in the crystals by the intrinsically disordered anion sheets [18, 107] as illustrated in Fig. 3.9 could be a reason for such a random pinning. In the framework of such a random singlet model even the low-temperature behaviour of the spin susceptibility stemming from the spin defects can be explained [134] as will be elucidated in section 4.4.2.

One possibility of a resonating valence bond state compatible to the observed spin gap would be a topological  $Z_2$  spin liquid hosting gapped spinon excitations. Such a state has been shown to exist in perfect triangular lattice dimer models for a finite parameter range [35]. However, it is difficult to imagine a state like this bearing in mind the present in-plane anisotropy in the ESR measurements as well as the thermal expansion.

For a  $U(1)$  spin liquid with spinon Fermi surface, it has been suggested that an Amperean attractive interaction between two spinons can lead to a pairing of the spinons imposing a gap in the Fermi surface [36]. This scenario is able to explain the  $T^*$  phase transition as well as several other low-temperature properties, but it is difficult to reconcile with the presence of unscreened orphan spins which would pin the spinons in their vicinity.

As the ESR results unambiguously show that the ground state in  $\kappa\text{-ET}_2\text{Cu}_2(\text{CN})_3$  is a gapped spin-singlet phase, one important question arises: Why did the gapped nature of the ground state remain unresolved despite the numerous experimental studies in the last decades? To answer this question and to show why ESR has been able to circumvent the problems of many other methods applied so far, an in-depth discussion of the different contributions to the ESR signal of the crystals at low temperatures is given in the following sections.

A scenario with localised spin singlet valence bonds will be the working hypothesis throughout the rest of the chapter. Even though the ESR observations made for different extrinsic contributions as well as the low-temperature behaviour of the intrinsic defect spins give more insight, an unambiguous decision for a specific ground state model remains difficult. Precise structural studies through  $T^*$  to deduce the valence bond arrangement may help to finally distinguish between different specific scenarios. One feasible model for the low-temperature state is suggested in the concluding section alongside a discussion of its compatibility to available experimental data for various quantities 4.5.

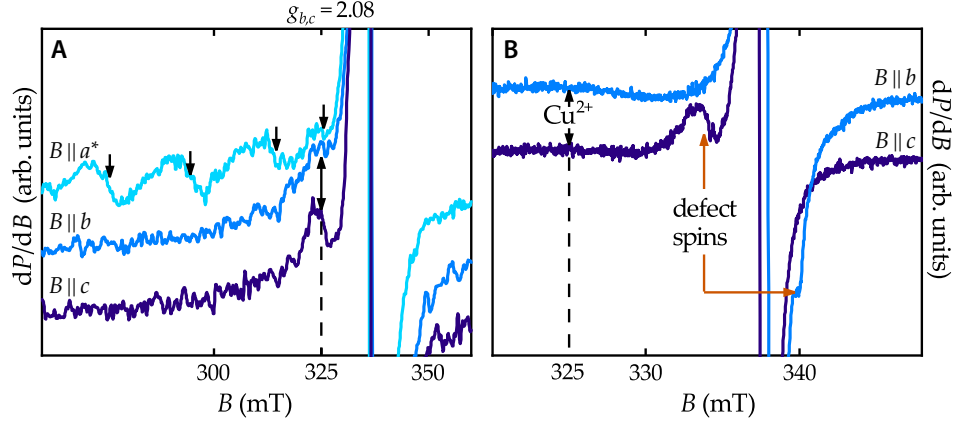


FIG. 4.7  $\text{Cu}^{2+}$  Impurities Comparison of the distinct  $\text{Cu}^{2+}$  signal (A) present in all studied samples of  $\kappa\text{-(BEDT-TTF)}_2\text{Cu}_2(\text{CN})_3$  and the observed  $(\text{BEDT-TTF})_2$  low-temperature defect signal (B). No anisotropy can be resolved for the  $\text{Cu}^{2+}$  signal shows within the  $bc$ -plane with  $g_{\parallel bc} = 2.08$ . Contrastingly, the low-temperature defect signal possesses a pronounced anisotropy as it moves from the low-field side of the main peak for  $B \parallel c$  to the high-field side for  $B \parallel b$ .

### 4.3 Additional Contributions to the ESR Spectra below $T^*$

ESR spectroscopy is advantageous compared to bulk susceptibility measurements performed by magnetisation or magnetic torque experiments as it is able to distinguish different contributions to the overall susceptibility of a sample. Nuclear magnetic resonance (NMR) measurements are also susceptible to impurities as any kind of unpaired spins effect the NMR spin-lattice relaxation rate. In the event that a spin gap opens these impurities will dominate the signal concealing the intrinsic properties of the material. In contrast to other microscopic probes, ESR probes the electron spins directly, giving direct access to the intrinsic magnetic properties.

In addition to the main signal emerging from spins hosted on the  $\text{ET}_2^+$  dimers, which vanishes as the spin gap opens, other contributions to the ESR spectra can be observed. One of them is the emerging signal below  $T^*$  as shown in Fig. 4.1B,C. The resonance field of the two features is indistinguishable just below  $T^*$ . Upon further cooling a component splits off as an additional peak shifting away from the main signal at  $B_{\text{main}}$ . The temperature-dependence and anisotropy of this features as well as other signal contributions are discussed below one after the other.

### 4.3.1 Cu<sup>2+</sup> Impurities

Although, nominally only nonmagnetic Cu<sup>+</sup> ions should be present in  $\kappa$ -ET<sub>2</sub>Cu<sub>2</sub>(CN)<sub>3</sub>, it is known that  $\kappa$ -ET<sub>2</sub>Cu<sub>2</sub>(CN)<sub>3</sub> crystals can host Cu<sup>2+</sup> impurities [115, 116]. Cu<sup>2+</sup> are paramagnetic ions with a spin  $S = 1/2$ . The first hypothesis for the origin of the emerging ESR signal below  $T^*$  as shown in Fig. 4.1B,C was thus the presence of Cu<sup>2+</sup> ions.

The ESR spectra at  $T = 4$  K shown in Fig. 4.7A give indeed clear evidence for the presence of Cu<sup>2+</sup> impurities in the the studied  $\kappa$ -ET<sub>2</sub>Cu<sub>2</sub>(CN)<sub>3</sub> sample # 3. Four characteristic absorption lines are expected due to the hyperfine splitting induced by the copper nuclei with spin  $I = 3/2$ . The characteristic ESR spectrum for the Cu<sup>2+</sup> ions with its four ESR lines can be observed clearly. All four equidistantly spaced lines marked by the black arrows in Fig. 4.7A are only visible in the  $B \parallel a^*$ -direction perpendicular to the layers. Within the  $bc$ -plane of the crystal the lines collapse into a single line with almost no anisotropy. The  $g$ -factors of  $g_{b,c} = 2.08$  and  $g_{a^*} = 2.22$  fit well to numerical values obtained by molecular orbital calculations in [115]. Depending on the individual crystal the features only appear below a certain temperature,  $T = 10$  K in case of the crystal used for the shown spectra. The ESR intensity of those localised spins follows a paramagnetic temperature-dependence allowing to determine the concentration of Cu<sup>2+</sup> ions in the crystal. It is strongly sample-dependent ranging from around 50 ppm to a maximum 1350 ppm for the sample shown in Fig. 4.7, though no crystals without any indications for Cu<sup>2+</sup> have been found in any of the batches that have been investigated. Despite the presence of Cu<sup>2+</sup> ions is evident, the characteristic signal of those impurities is incompatible with the behaviour of the additional signal component emerging at  $B_{\text{main}}$  below  $T^*$  and thus cannot be its origin.

By taking a closer look at the  $T = 2$  K spectra, as shown in panel B, a distinct in-plane anisotropy of the emergent defect signal can be observed. For magnetic field  $B \parallel c$  the feature appears at lower field compared to the main signal and moves through the main signal to the higher field side upon rotation in the  $bc$ -plane. This is fundamentally different from the aforementioned Cu<sup>2+</sup> signal, also indicated in Fig. 4.7B, providing further evidence for the fact that the emergent defect signal is not originating from Cu<sup>2+</sup> ions. Moreover the Cu<sup>2+</sup> signal exhibits a much broader line width in comparison.

As shown Cu<sup>2+</sup> ions can be ruled out as the direct cause for the emergent low-temperature signal. An indirect role in precipitating the formation of unpaired orphan spins at the ET<sub>2</sub> sites is, however, still conceivable and is discussed below.

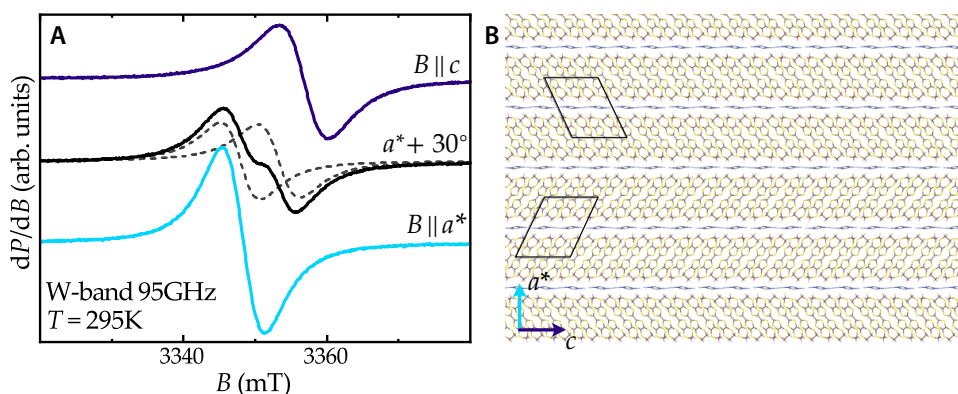


FIG. 4.8 *Crystal Twinning* Crystal twinning is disclosed by the angular-dependence of the W-band signal (A) when rotating the magnetic field  $B$  within the  $a^*c$ -plane. Most samples exhibit a splitting of the ESR signal for intermediate angles (black), inferring that the crystals are twinned as sketched in panel (B). The two lines always collapse in the  $a^*$  direction along the stack as well as the perpendicular  $c$  direction.

### 4.3.2 Structural Twinning

Many of the studied crystals show indications of twinning in the ESR spectra. The implications of twinning on the experimental data are important to consider for analysing their angular-dependence. It is therefore discussed here prior to discussing the anisotropy of the low-temperature spectra.

Crystal twinning can be observed clearly in the room temperature W-band spectra displayed in Fig. 4.8A. Due to the lower energy resolution in the X-band, the effects of twinning on the spectra are only visible at low temperature where the line width is sufficiently narrow. Along the crystallographic  $a^*$  and  $c$ -directions a single Lorentzian line shape is always observed. In many crystals a splitting of the spectra into two lines is evident for intermediate angles while rotating in the  $a^*c$ -plane. As shown here by the dotted lines the signal can be described by two Lorentzians with the magnetic field pointing along  $a^* + 30^\circ$ . The observed splitting in the spectra is known for the orthorhombic  $\kappa$ -ET<sub>2</sub>X compounds, such as  $\kappa$ -ET<sub>2</sub>Cu[N(CN)<sub>2</sub>]Cl. In this case the ET molecules are tilted in a “herring bone” fashion within alternating layers. As a result for general magnetic field orientations those magnetically inequivalent layers can show different resonance fields in ESR measurements if the exchange coupling between them is small enough [137].

In case of the monoclinic  $\kappa$ -ET<sub>2</sub>Cu<sub>2</sub>(CN)<sub>3</sub> crystals, where the tilt of the ET molecules is alike in consecutive layers such a behaviour is unexpected. The observation of a splitting thus indicates crystal twinning conceivable as sketched in Fig. 4.8B: Different

domains of “left-tilted” as well as “right-tilted” layers are present, separated by stacking faults. The same angular-dependence is observed in almost all crystals with only very few exceptions which possess more or less a single line and can thus be considered single domain. Different ratios of the “left-” and “right-tilted” domains manifest in varying intensities of the two observed lines.

Overall the structural twinning leads to a doubling of all intrinsic contributions in the angular-dependence of the ESR spectra which can become visible for narrow absorption features. Impurities occurring at specific crystallographic sites are also subject to this doubling in contrast to any isotropically distributed sources.

### 4.3.3 Defect Signal Contribution

This section is focusing on the signal emerging below  $T_{\text{loc}} \approx 2.5$  K as shown in Fig. 4.1C. The emergence of the feature from the main ESR line at  $B_{\text{main}}$  leads to the conclusion that the responsible spins are located at the molecular dimer sites and remain unpaired despite the opening of the spin gap.

To ensure that the signal is not only stemming from impurities present in a specific crystal, X-band ESR spectra at  $T = 2$  K have been recorded for crystals from all four different laboratories. In Fig. 4.9 it can be seen that its intensity is much more pronounced for sample # 3 as compared to the other samples. Nevertheless a similar feature can also be observed for samples # 1 and # 2; in sample # 4 the larger line width of the signal at  $B_{\text{main}}$  possibly hides the feature. The sample to sample variation amongst crystals from one batch from a certain laboratory is smaller. Here the intensity varies by less than a factor of 2. This pronounced sample to sample-dependence points towards the importance of intrinsic disorder for the low-temperature properties.

Similar findings of a large sample to sample variation have also been made for the anomaly at  $T^* = 6$  K in thermal expansion measurements [138]. In those measurements, even though the feature is always present at the same temperature, the magnitude of the anomalous peak in the thermal expansion coefficient varies significantly amongst different crystals.

As already shown in Fig. 4.7B the signal displays a pronounced anisotropy of its resonance field. In Fig. 4.10 the anisotropy of the ESR signals is visualised for samples # 1 (A) and # 3 (B). Spectra have been recorded in steps of  $10^\circ$  respectively  $5^\circ$  at  $T = 2$  K. For sample # 1 the anisotropy within the  $bc$ -plane is presented. In case of sample # 3 the full anisotropy is shown with three panels displaying the  $bc$ -plane (upper), the  $a^*c$ -plane (middle) and the  $a^*b$ -plane (lower). The signal at  $B_{\text{main}}$  identified by the

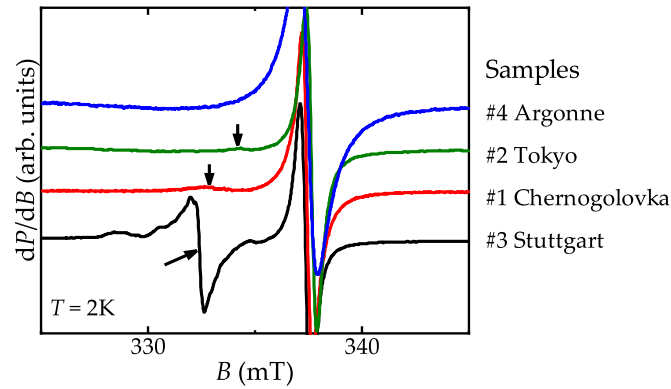


FIG. 4.9 *Sample to Sample Variation of Defect Contribution* X-Band ESR spectra at  $T = 2$  K for four crystals from different labs reveal the large sample to sample variation of the emerging defect signal, indicated by the black arrows. All spectra are normalised to the amplitude of the main signal.

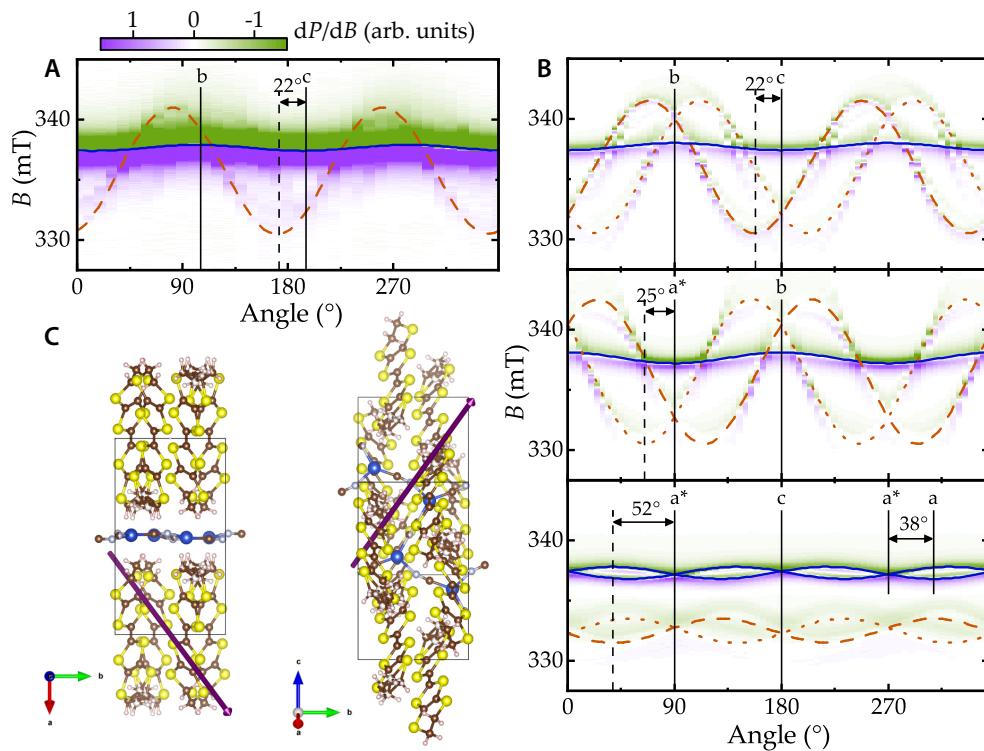


FIG. 4.10 *Low-Temperature Anisotropy of the ESR Signal* Besides the main signal from the  $\text{ET}_2^+$  ions (solid blue lines) at  $T = 2$  K an additional resonance is visible (orange dashed and dotted lines). The anisotropy of this defect signal is consistent in both samples shown: (A) a single-domain crystal, sample #1, and (B) a twinned crystal from sample #3. (C) The purple arrows indicate the orientation of the dipole interaction likely responsible for the anisotropy of the defect signal (view: left along  $a^*$ , right along  $c$ ).

zero-crossing of  $dP/dB$  only shows a small angular variation; 0.3 mT for measurement in the  $bc$ -plane. This small relative shift of approximately  $10^{-3}$  upon rotation can be fully explained by the  $\mathbf{g}$ -tensor anisotropy of the BEDT–TTF molecules owing to spin-orbit coupling. Within the principal axis system the  $g$ -factor is given by

$$g = \sqrt{g_{a^*} \cos^2 \theta + g_b \sin^2 \theta \cos^2 \phi + g_c \sin^2 \theta \sin^2 \phi} \quad (4.7)$$

where  $\theta$  describes the angle of the external magnetic field with respect to the out-of-plane  $a^*$ -direction, and  $\phi$  the angle within the  $bc$ -plane. Thus, the resonance field follows a  $\cos^2$  angular-dependence along any chosen axis of rotation.

The splitting of the main signal (for rotation within the  $a^*c$  plane, bottom panel) as well as the doubling of the defect signal can be related to twinning in the crystal. Therefore crystal twinning has to be considered to fully describe the anisotropy of the ESR signals. On the one hand, sample #1 does not show any splitting of the main signal, proving that the crystal is single domain in accord with the observation of only one set of defect lines. On the other hand clear signs of twinning are observed for sample #3: within the  $a^*c$ -plane a doubling of the main signal can be clearly observed. The minima in both branches are symmetrically shifted by  $\pm 38^\circ$  with respect to the  $a^*$  direction as indicated in Fig. 4.10B. This is the same behaviour that can be observed with W-band measurements already at room temperature as shown in 4.8. The shift angle exactly reproduces the tilt angle of the BEDT–TTF molecules in the  $a^*c$ -plane coincident with the principal axes of the  $\mathbf{g}$ -tensor of the molecules. The doubled main signal can thus be explained by the two distinct orientations of the molecules that occur due to twinning as discussed in section 4.3.2.

As indicated by the dashed and dotted lines in Fig. 4.10B in addition to the doubling of the main signal, two sets of defect signals with a pronounced symmetric anisotropy are visible. This anisotropy is distinct from the signal at  $B_{\text{main}}$ . Whereas the main absorption line has its maximum along the  $b$ -direction within the  $bc$ -plane, the maxima of the defect signals are shifted by an angle of  $\pm 22^\circ$  for both samples #1 and #3. Equivalent shifts can be identified for the other directions:  $25^\circ$  in the  $a^*b$ -plane and  $\pm 52^\circ$  in the  $a^*c$ -plane.

As evident from Fig. 4.10, the defect signal is subject to an order of magnitude larger anisotropy of approximately 10 mT, in particular within the  $bc$  and  $a^*c$ -planes. Despite the very different intensities of the defect contribution as shown in Fig. 4.9, the angular-dependence of the resonance field is alike in different samples, specifically shown here for samples #1 and #3 in Fig. 4.10A and B. The variation in resonance

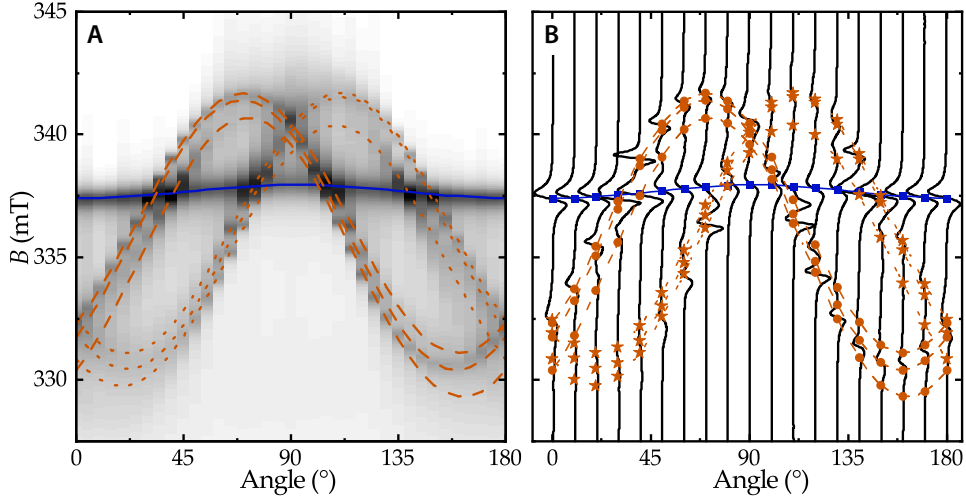


FIG. 4.11 *Components of the Defect Signal* Detailed view of the anisotropy in the  $bc$ -plane for sample #3 at  $T = 2$  K. Three components can be disentangled by fitting the two sets of defect lines (dashed, dotted) in the twinned sample with 3 Lorentzians each. The resonance fields of the main signal (blue) and the three doubled defect components (orange) are shown. Two different views of the spectra are given to allow the visualisation of different details: (A) absorbed power  $P$  indicated by the grey level intensity, (B) derivative spectra  $dP/dB$  as vertically stacked lines every  $10^\circ$ .

field follows the characteristic  $(3 \cos^2 \alpha - 1)$ -dependence related to a dipole-dipole interaction. A local dipole field

$$B_{\text{loc}}(\alpha) = -\frac{\mu_0 \mu_{\text{B}} g S}{4\pi r^3} (3 \cos^2(\alpha) - 1) \quad (4.8)$$

caused by localised moments in a distance of about  $6 - 7 \text{ \AA}$  acting on the defect spins located on the  $(\text{BEDT-TTF})_2^+$  can quantitatively describe the observed behaviour. Here,  $\alpha$  describes the angle between the external magnetic field  $B_0$  and the vector connecting the spin defect and the impurity responsible for the local field. The respective vector is indicated in Fig. 4.10C as a purple arrow within the unit cell of  $\kappa\text{-ET}_2\text{Cu}_2(\text{CN})_3$ . Its direction and thus the direction of strongest interaction is not lying in the  $bc$ -plane, specifically ruling out that the local field is caused by regular dimers within the plane.

Upon closer look the defect feature is actually comprised of two or three individual absorption lines with slightly different angular-dependence. Sample #3 is chosen for further analysis despite the strong twinning as it exhibits significantly more defects. The resulting resonance fields of fits to the spectra with three defect components

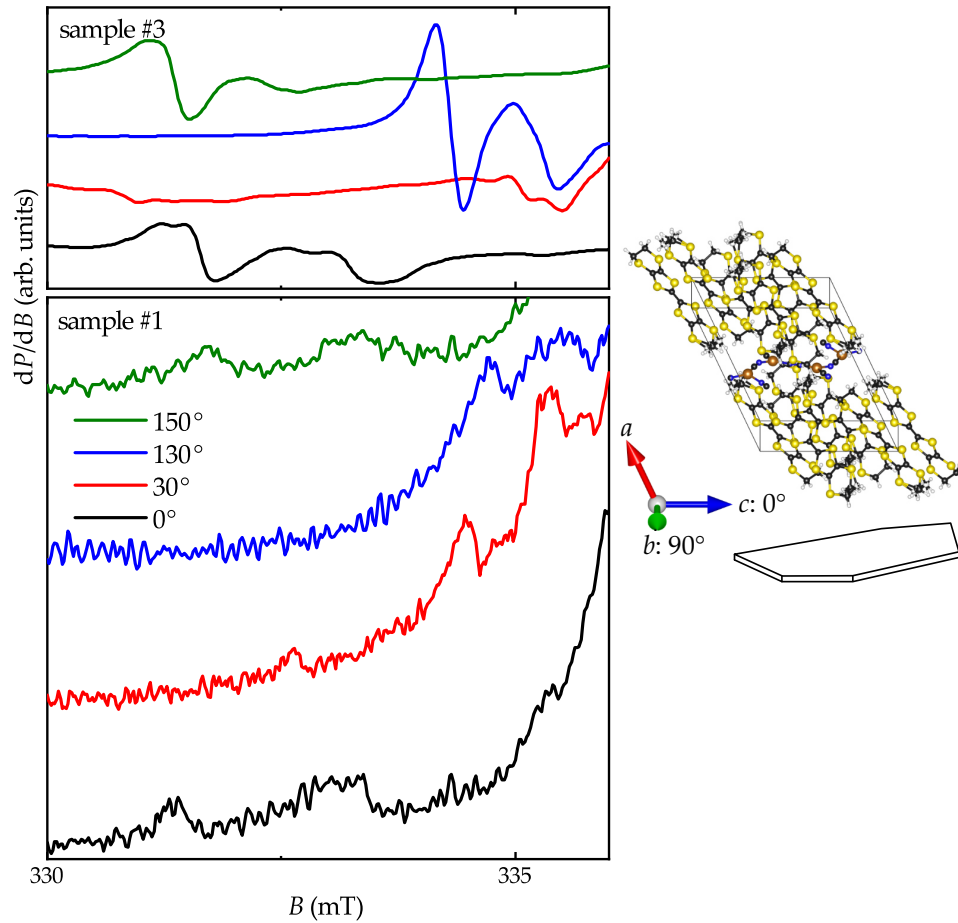


FIG. 4.12 *Defect Components in Different Samples* Comparing the defect signal for four different angles in the  $bc$ -plane for samples #1 and #3 at  $T = 2$  K reveals a close match in the anisotropy even on the level of the individual components.

are shown in Fig. 4.11. In spite of the much smaller intensity of the defect signals for sample #1 multiple components can also be identified in the spectra. Fig. 4.12 shows four spectra at different angles of  $B_0$  within the  $bc$ -plane for both samples. In comparison the defect signals exhibit the same angle-dependence down to the level of the individual components within a small offset angle of  $5 - 10^\circ$  explainable by mounting uncertainties.

In conclusion, the emergent defect signal stems from unpaired spins located on the  $(BEDT-TTF)_2^+$  dimer sites. Local impurities are increasingly polarised at lower temperature causing an emerging local field below  $T_{loc}$ . Dipole-dipole interaction between the unpaired defect spins and the localised impurities causes the observed angular-dependence of the defect signal which is robust against different amounts of disorder in the spin system, albeit the intensity strongly varies between different crystals. The structure of the defect signal consisting of multiple absorption lines suggests that there are several possible impurity sites relevant for the dipolar interaction. One possible source of local magnetic moments are the  $S = 1/2$   $Cu^{2+}$  ions detected in the samples (Fig. 4.7). A possible coupling of the  $Cu^{2+}$  impurities to the occurrence of unpaired spins on the  $(BEDT-TTF)_2^+$  dimers is discussed in the next section 4.3.4.

#### 4.3.4 Possible Coupling of the Defect Spins to the $Cu^{2+}$ Impurities

As shown before, the defect signal arises from unpaired spins amongst the valence bonds in the  $BEDT-TTF$  layers and is distinct from absorption lines related to the  $Cu^{2+}$  impurities. An interaction between the defect spins' magnetic moments and the  $Cu^{2+}$  impurities is nevertheless conceivable. The  $Cu^{2+}$  impurities are located within the anion sheets separating the organic layers that host the  $(BEDT-TTF)_2^+$  defect spins. As shown in Fig. 3.9 the anion sheets can be pictured as a hexagonal structure with copper ions in each corner. The four copper ions within the unit cell are located in two distinct configurations: two  $Cu$  close to the inversion centre and two closer to the edge (see Fig. 3.9).

From the anisotropy of the defect signal the axis connecting the defect spin to the searched-for local moment responsible for the dipole-dipole interaction was deduced as shown in shown in Fig. 4.10C. As it points at a considerable angle out of the layers, dipolar coupling among the neighbouring organic dimers could be ruled out as an explanation for the observed anisotropy. Dipolar interaction of the defect spins to the  $Cu^{2+}$  also carrying  $S = 1/2$  could be an explanation. With the two organic dimers and the two distinct configurations of copper ions in the unit cell, there are four

distinct distances to account for. For parallel alignment along the axis connecting the spins ( $\alpha = 0$ ) one obtains local magnetic fields of 1.6 mT, 2.2 mT, 3.5 mT, and 4.4 mT, according to (4.8). The experimentally observed local fields are also in the range of several mT, thus interactions beyond the unit cell do not need to be considered in view of the rapid  $r^{-3}$  decay.

A shift of  $\sim 6$  mT compared to the main signal is experimentally observed for an angle of  $22^\circ$  from the  $c$ -axis when rotating within the  $bc$ -plane, as can be seen in Fig. 4.10A,B. This value is larger compared to the 4.4 mT associated to the nearest Cu position to an organic dimer. Two effects have to be considered to explain this discrepancy: firstly, it is known that the crystal structure is altered for low temperatures, particularly below  $T^*$  [120]. Small changes of the distances in the order of  $1 \text{ \AA}$  would be sufficient to explain the experimentally observed local fields. As the structural data used to determine the distances has been acquired at  $T \simeq T^*$  [98], but not for significantly lower temperatures, further alterations are imaginable. Secondly and more importantly, the occurrence of  $\text{Cu}^{2+}$  ions will cause local distortions due to the additional charge which may also alter the distances.

The observation of multiple defect lines as shown in Fig. 4.12 suggests that several possible configurations of Cu sites and nearby defect spins are realised. Some of them may occur more likely than others depending on properties of the individual crystals, e.g. growth conditions.

Moreover, the  $\text{Cu}^{2+}$  impurities can not only cause the local field responsible for the anisotropy of the defect spins' signal, but can also be causal for the emergence of the unpaired spins. If the additional electron from the formation of  $\text{Cu}^{2+}$  is doped to the closest  $(\text{BEDT-TTF})_2$  dimer, this dimer will acquire  $S = 0$ . As a result of this vacancy one of the spins on a neighbouring  $(\text{BEDT-TTF})_2^+$  dimers will automatically not be included in a valence bond but remain unpaired. Due to this mechanism the  $\text{Cu}^{2+}$  impurities are likely a relevant source of the localised defect spins that contribute to the low-temperature spin susceptibility albeit the presence of the spin gap. The defect spins created this way are always localised in the vicinity of the  $\text{Cu}^{2+}$  impurity resulting in the observed dipolar interaction.

Other sources of defects can however explicitly not be excluded. As shown in the following section 4.4 the signal at a temperature of a few tens of mK consists of the discussed defect line and another absorption at the original resonance field of the main line. This second absorption with zero local field implies that no other nearby local moments are present to its source. Different sources other than  $\text{Cu}^{2+}$  impurities responsible for the formation of defect spins thus have to be taken into account.

## 4.4 Frequency-Dependent ESR below $T^*$

In order to investigate the different magnetic contributions for temperatures below  $T = 2$  K, the limit for the utilised conventional X-band ESR spectrometer, measurements on CPW resonators have been performed in a temperature range of  $T = 25$  mK – 4 K. A superconducting resonator with a fundamental mode at 1.1 GHz allowed measurements at 4 different frequencies of  $f_0 = 1.1, 3.3, 5.5, 7.6$  GHz enabling a frequency-, respectively magnetic field-, dependent analysis of the magnetic properties.

A temperature evolution of representative ESR absorption spectra is shown upon cooling from 4 K to 25 mK in Fig. 4.13 for all 4 investigated frequencies. The ESR absorption is visible as a change of the resonator's quality factor. The defect signal separates from  $B_{\text{main}}$  at a temperature  $T_{\text{loc}}$  depending on the investigated frequency and thus resonance field. For the fundamental mode the splitting from  $B_{\text{main}} = 40$  mT is visible below  $T_{\text{loc}} \simeq 1$  K. With increasing external field  $B_0$  the splitting can be observed already at higher temperatures. Upon lowering the temperature further the field offset of the defect signal from  $B_{\text{main}}$  saturates. The intensity of the defect component increases upon cooling as expected for local moments. The signal at  $B_{\text{main}}$  first loses intensity below  $T^*$  as already seen in the X-band measurements. However, despite the presence of the spin gap, a signal at  $B_{\text{main}}$  is unexpectedly still visible at the base temperature  $T_{\text{base}} = 25$  mK as will be discussed in further detail in section 4.4.2.

Fitting the ESR absorption and dispersion signal with a model consisting of two Lorentzian signals – one at  $B_{\text{main}}$  and one defect component – is performed according to equation 2.38. The resulting parameters are displayed in Fig. 4.14: the resonance field shown as an offset  $B - B_{\text{main}}$  from the high temperature value of  $B_{\text{main}}$ , and the ESR line width  $\Delta B$ . Due to the lower sensitivity of the technique compared to the commercial X-band spectrometer and an increasing line width below  $T_{\text{loc}}$  leading to overlapping signals, the data is subject to substantial noise but qualitative trends can still be extracted: Firstly, the resonance field of the signal at  $B_{\text{main}}$  is constant within an error of one line width  $\Delta B$  for all modes shown. Secondly, the defect signal separates at  $T_{\text{loc}}$  depending on the external magnetic field. Its resonance field offset  $B - B_{\text{main}}$  saturates for temperatures in the mK range. Within the error bar of one line width the same value  $B_{\text{loc}} \simeq 5.5$  mT is reached for all modes for  $T \rightarrow 0$ . Thirdly, the line width of both components of the signal significantly increases below  $T_{\text{loc}}$ ; the behaviour above

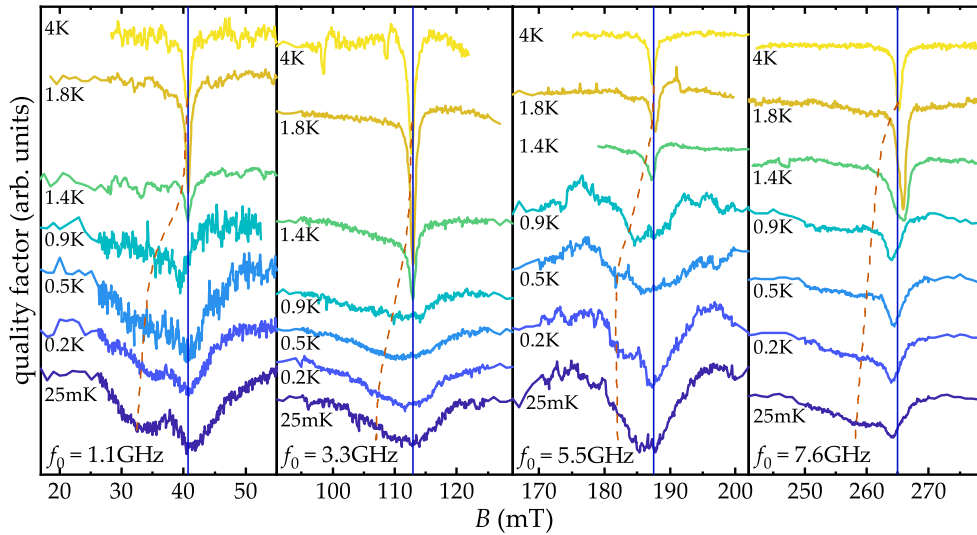


FIG. 4.13 *Temperature Evolution of ESR Spectra in the mK Range* ESR absorption spectra are shown for different frequencies and temperatures down to 25 mK with  $\mathbf{B}_0 \parallel c$ . The resonance fields of the main signal  $B_{\text{main}}$  (solid blue) and the evolution of the defect signal (dashed orange) are indicated.

2 K replicates the data obtained in the X-band shown in Fig. 4.5 with the minimum around 2.5 K. Lastly, the line width of both signals saturates below 1 K.

Similar ESR measurements on metallic CPW resonators have been performed for sample # 3 in a  $4^4\text{He}$  cryostat reaching only as low as 1.5 K by M. Javaheri [139]. The raw transmission data has been analysed again using the methods described in section 2.5.2 in the same way as for sample # 1. Exemplary spectra are shown in Fig. 4.15 for two different orientations of the external field: along  $b$  in panel A, and along  $c$  in panel B. The anisotropy observed from angle-dependent X-band measurements is reflected in the shown ESR spectra; the defect signal is shifted to higher field compared to  $B_{\text{main}}$  for  $\mathbf{B}_0 \parallel b$  and to lower field for  $\mathbf{B}_0 \parallel c$ . Spectra can be obtained with a larger signal-to-noise ratio compared to sample # 1 as sample # 3 shows a larger content of unpaired defect spins as shown in Fig. 4.9.

The resonance field and line width of both signal components are shown in Fig. 4.15 C,D,E as a function of temperature obtained by fitting the absorption spectra in the same way as for sample # 1. Regardless of the much larger intensity of the defect signal, the temperature-dependent behaviour matches the results for sample # 1. The saturation of the resonance field as well as the line width below  $T = 1$  K cannot be seen here as the temperature only reaches as low as 1.5 K.

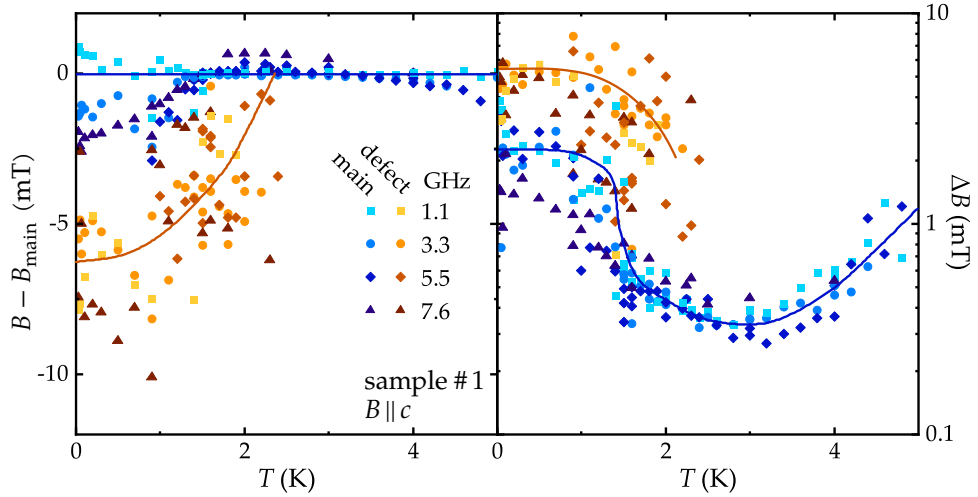


FIG. 4.14 *ESR Parameters in the mK Range* Resonance field offset from the room temperature value of  $B_{\text{main}}$  (left) and ESR line width  $\Delta B$  (right) as a function of temperature down to 25 mK determined from fits to the absorption spectra for all 4 investigated modes. The defect signal emerges from the main signal below the field-dependent temperature  $T_{\text{loc}}$  and shifts towards lower field. Values for the signal at  $B_{\text{main}}$  are indicated in blue, for the defect signal in orange. The overall trends of the main and defect signals are indicated by guides to the eye shown in the respective colours.

#### 4.4.1 Behaviour of the Defect Signal

As discussed previously (see Figs. 4.1C and 4.14), the defect signal splits off the signal at  $B_{\text{main}}$  below a temperature  $T_{\text{loc}}$  due to emerging local fields. Upon further cooling this separation in resonance field increases before a saturation is observed in the limit  $T \rightarrow 0$ . The most likely explanation for this observation is an increasing polarisation of the localised  $\text{Cu}^{2+}$  impurity moments for lower temperatures resulting in an increased local field as discussed in section 4.3.4.

The resonance field of both signal components at the base temperature  $T = 25$  mK is displayed in Fig. 4.16A for all four frequencies at which measurements have been performed. This graph illustrates the approximately field-independent offset  $B_{\text{loc}} \approx 5.5$  mT of the defect signal with respect to  $B_{\text{main}}$  expected for the interaction with the suggested  $\text{Cu}^{2+}$  impurity moments.

As seen from the low-temperature spectra, the temperature  $T_{\text{loc}}$  below which the separation of the defect signal is visible varies for the different frequencies and related magnetic fields used for the measurement. For higher fields the separation is observed already at higher temperatures. This is also in accord with the assumption of impurity moments as the source of the emergent local fields, as for higher external fields these

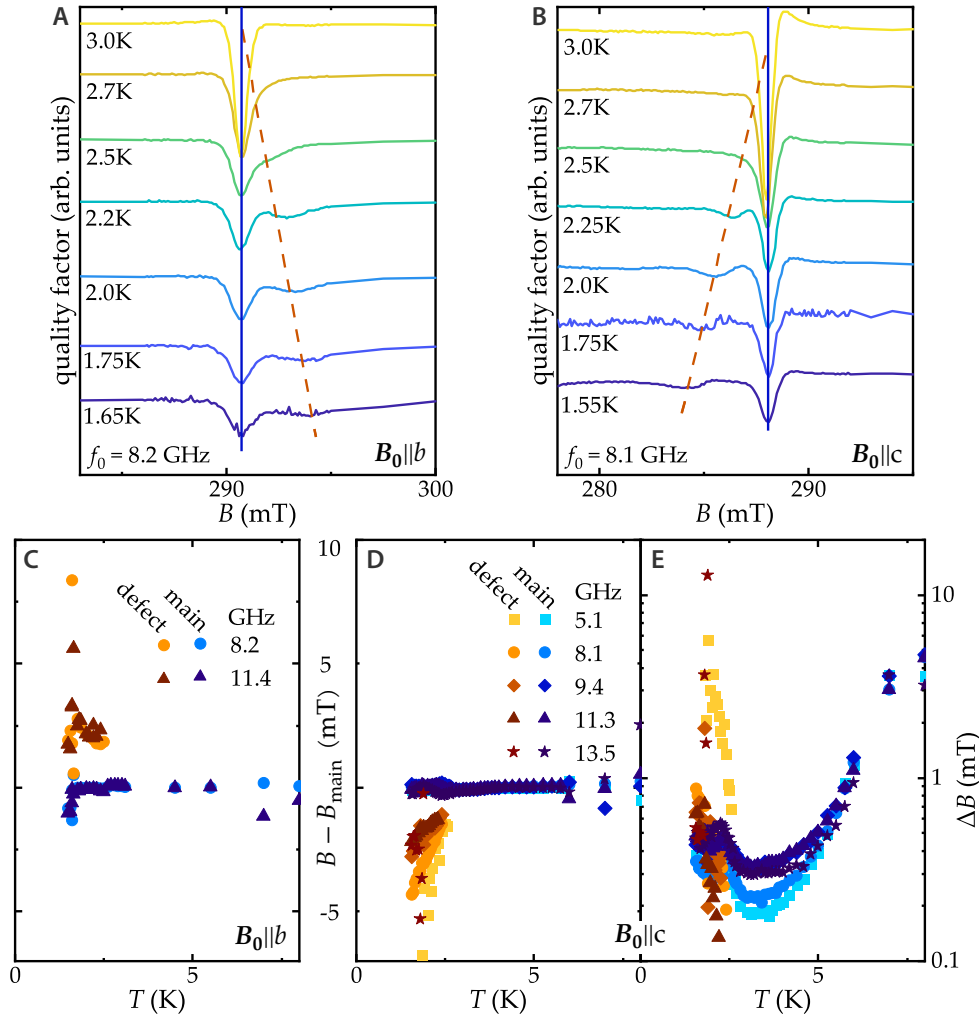


FIG. 4.15 *Low-Temperature ESR Results for Sample #3* The behaviour of the ESR spectra is similar compared to sample #1. Due to the larger amount of unpaired defect spins the ESR signals have a better signal-to-noise ratio in this case. (A,B) show the emergence of the defect signal (dashed orange) below  $T_{\text{loc}}$  in the ESR spectra from the signal at  $B_{\text{main}}$  (solid blue) for  $B_0 \parallel b$  respectively  $B_0 \parallel c$ . (C,D) The defect signal (orange) shifts to higher respectively lower resonance field compared to the signal at  $B_{\text{main}}$ . (E) Line width  $\Delta B$  of both signal components. A minimum is observed around  $T = 3$  K. Upon further cooling the signals significantly broaden with  $\Delta B$  of the defect signal being significantly larger compared to the component at  $B_{\text{main}}$ . (experiments performed by M. Javaheri [139])

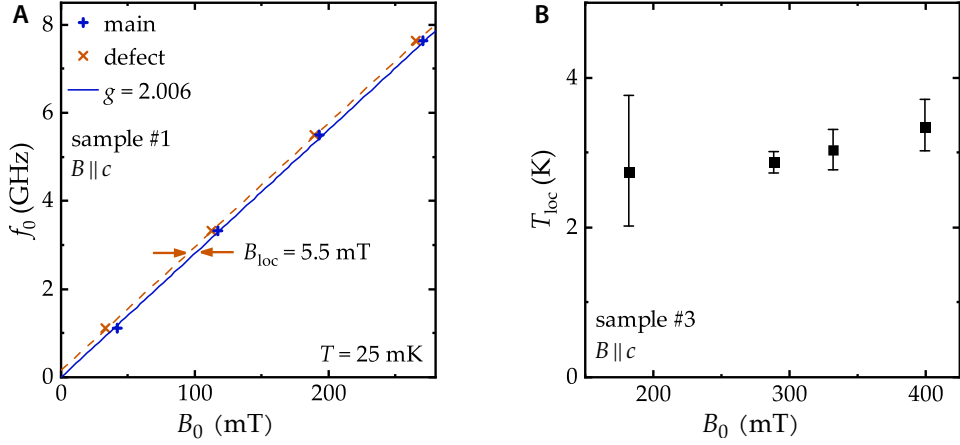


FIG. 4.16 *Field-Dependence of Local Field  $B_{loc}$  and Onset Temperature  $T_{loc}$*  (A) Saturated low-temperature peak positions for varying resonance frequencies and fields for  $B_0 \parallel c$  and  $T = 25$  mK reveal a constant shift between the signal at  $B_{main}$  and the defect signal. (B) Onset temperature of the emergent defect signal as a function of the external magnetic field  $B_0$  for sample #3.

moments are polarised already at higher temperatures. Fig. 4.16B shows the addressed temperature  $T_{loc}$  as function of the applied magnetic field for sample #3. The trend of the presented field-dependence is in good agreement with the suggested phase boundary of the weak antiferromagnetic phase discussed for the  $\mu$ SR data [10] shown in Fig. 3.4D. There the phase was related to the emergence of field-induced moments within the frustrated spin system. A recent NMR study [9] has shown that even a small amount of impurity moments can fully conceal the intrinsic relaxation properties of the spin system. The observed defect signal in the presented ESR measurements related to local spin defects and the local field acting upon them due to  $Cu^{2+}$  impurity moments is a likely source of the observed field-induced behaviour observed at low temperatures in the  $\mu$ SR and NMR studies.

#### 4.4.2 Remaining Signal at $B_{main}$

Having discussed the behaviour of the defect signal comprehensively, this section focuses on the ESR contribution at  $B_{main}$ . Having a look at the ESR spectra in Fig. 4.13 one can see that a strong absorption is present at  $B_{main}$  even at the base temperature  $T_{base} = 25$  mK. Close to  $T^*$  thermal excitations across the spin gap lead to an ESR signal exceeding the defect contribution as shown in Fig. 4.6. However, at  $T_{base} \simeq \Delta/500$ , far below the spin gap, no contribution is expected. In reality the intensity of the

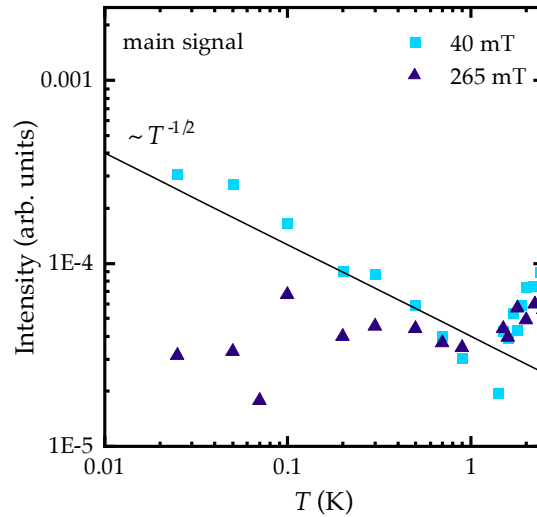


FIG. 4.17 *Intensity of the Remaining Signal at  $B_{\text{main}}$*  Intensity of the ESR absorption at  $B_{\text{main}}$  between 25 mK and 2.5 K for the two modes with resonance fields of 40 mT respectively 265 mT. The black line indicates a  $T^{-1/2}$  power law.

observed signal even increases upon cooling starting from 1 K for the modes with lower frequency or at least stays approximately constant for the highest frequency.

What is the origin of this ESR absorption? As discussed in the theory section 1.4.3 there are various possibilities for the formation of unpaired defect spins within a valence bond state. One possibility are the  $\text{Cu}^{2+}$  impurities inducing a nearby vacancy and related unpaired defect spin responsible for the shifted defect signal. In addition to that valence bond imperfections are conceivable, e.g. due to domain walls in a VBS state or as orphan spins in a state with randomly pinned singlets, a VBG state. In the absence of a nearby magnetic moment the related ESR absorption is not subject to any local field and thus remains at  $B_{\text{main}}$ .

In Fig. 4.17 the ESR intensity obtained from the amplitude and width of a Lorentzian fit to the absorption is shown as a function of temperature for the two modes giving the clearest data: one at a frequency  $f_0 = 1.1$  GHz corresponding to a magnetic field  $B_0 = 40$  mT and one at  $f_0 = 7.6$  GHz corresponding to  $B_0 = 265$  mT. Below 2.5 K at first the intensity, proportional to the spin susceptibility  $\chi_S$ , drops drastically continuing the trend observed by X-band ESR. This is related to the formation of spin singlets causing the signal to decay exponentially. Higher temperatures cannot be analysed properly as the used superconducting Nb resonator loses sensitivity which influences the observed ESR intensity. Below approximately 1 K the trend does not continue. Instead an increasing signal intensity is observed. For the mode with low magnetic

field this divergence continues down to the lowest temperature with the increase roughly following a  $T^{-1/2}$  power law. For higher field, in this case  $B_0 = 265$  mT, the increase of  $\chi_S$  is suppressed below  $T = 0.5$  K.

The observed behaviour is in accord with a magnetic torque study [7]. There, the authors show the spin susceptibility  $\chi_S$  estimated from the magnetic torque measurements for fields from 0.8 T up to 13 T. Upon cooling  $\chi_S$  first drops strongly around  $T^*$  and starts to increase again below a minimum around 2 K. Similar to the ESR intensity the increase is suppressed for larger magnetic fields.

The presented low-temperature behaviour of  $\chi_S$  observed by measurements of the ESR intensity, respectively the magnetic torque, is in agreement with the theoretical predictions for a glassy valence bond state hosting unpaired orphan spins, i.e. with randomly pinned singlets. For a random singlet model extended to include spin-orbit coupling and DM interactions a power law divergence of the spin susceptibility in zero field, that is suppressed upon increasing the magnetic field, has been predicted, exactly as observed in the experiments [31, 134].

## 4.5 Low-Temperature Magnetic State

To conclude the investigations on  $\kappa$ -ET<sub>2</sub>Cu<sub>2</sub>(CN)<sub>3</sub> a scenario for the magnetic ground state is presented based on the ESR measurements. The main results which have to be considered are summarised in the following: First of all, the presence of a spin gap was concluded from the activated behaviour observed in the spin susceptibility below  $T^*$ . For higher temperatures paramagnetic behaviour is observed; the spin susceptibility  $\chi_S$  follows the prediction of a spin-<sup>1/2</sup> Heisenberg model on a triangular lattice. Secondly, additional defect contributions to the ESR spectra besides the intrinsic paramagnetic resonance show up below  $T^*$ . These are composed of two distinct signals: one with the same resonance field as the paramagnetic signal at  $B_{\text{main}}$  and another one that shifts in resonance field upon further cooling below  $T_{\text{loc}}$  and shows a distinct anisotropy with respect to the external magnetic field  $B_0$ . The intensity of those defect contributions vastly differs between different samples, whereas the resonance field always shows the same anisotropy. Thirdly, magnetic Cu<sup>2+</sup> impurities can be detected in the samples with a characteristic ESR signature. The local fields caused by those impurities at the ET<sub>2</sub> dimer sites within one unit cell are of comparable size to the observed anisotropy of defect signal. This suggests that the magnetic impurities are responsible for the shifted resonance field of the defect signal. Lastly, the intensity

of the defect signal at  $B_{\text{main}}$  diverges following a power law when approaching  $T \rightarrow 0$ . This divergence is suppressed in higher external magnetic fields.

With those results in mind, the following ground state can be proposed: The spins hosted on the  $\text{ET}_2$  dimer sites form a valence bond state. The valence bond arrangement is fixed within the crystal lattice and shows some degree of anisotropy, i.e. bonds are preferably formed along a certain direction. However, no perfect crystalline arrangement and thus a valence bond solid is formed. The arrangement instead is subject to a certain degree of randomness. This can be on a local scale in the form of a random arrangement of the valence bonds or on a larger scale in the form of grain boundaries between region with different preferential bond directions. In both cases, as a result of the disorder, unpaired orphan spins are hosted within the ground state otherwise comprised of spin singlet valence bonds. In addition to that magnetic impurities are present in the form of  $\text{Cu}^{2+}$ . Due to their different charge, they can induce a spin vacancy on a nearby  $\text{ET}_2$  dimer site also resulting in an unpaired orphan spin in the vicinity. A local field surrounds the magnetic impurities acting upon those nearby orphan spins. In summary, instead of the gapless spin liquid ground state with spinon Fermi surface proposed in literature, a gapped valence bond state hosting unpaired orphan spins is proposed as the magnetic ground state of  $\kappa\text{-ET}_2\text{Cu}_2(\text{CN})_3$ .

#### 4.5.1 Compatibility to Existing Experimental Results

In order to discuss the compatibility of the presented model for the low-temperature magnetic state of  $\kappa\text{-ET}_2\text{Cu}_2(\text{CN})_3$ , one has to first recall the benefits of the applied ESR techniques. First of all ESR is a spectroscopic technique that allows to distinguish different contributions to the magnetic susceptibility compared to bulk techniques such as SQUID magnetometry or magnetic torque measurements. The microscopic probes,  $\mu\text{SR}$  and NMR, probe the local magnetism indirectly by recording its influence on the spectral and relaxation properties of muons respectively nuclei. Whereas those indirect probes are susceptible to the influence of extrinsic contributions, ESR directly probes the excitation spectrum of the electron spins and can therefore unambiguously distinguish the intrinsic response from other contributions.

The localised unpaired spins dispersed in the realised valence bond state have been shown to manifest themselves in the form of two contributions to the ESR response far below  $T^*$ : Some are possibly pinned to  $\text{Cu}^{2+}$  impurities leading to the observed anisotropic defect signal; others are formed as orphan spins at defects or grain boundaries of a partially ordered valence bond state and are responsible for

the signal at  $B_{\text{main}}$  not affected by local fields with its characteristic temperature and magnetic field-dependence of the ESR intensity. The ESR experiments allow to distinguish these contributions from the intrinsic paramagnetic response above  $T^*$  which exponentially decays upon formation of the spin gapped valence bond state.

As discussed in section 3.2.1, data yielded by different experimental methods led to controversial and sometimes even contradicting conclusions concerning the magnetic properties of  $\kappa\text{-ET}_2\text{Cu}_2(\text{CN})_3$ . Many of those issues can be resolved when considering the different contributions to those properties disentangled by the presented ESR experiments.

First of all, the spin susceptibility  $\chi_S$  as measured by SQUID magnetometry shows a weak and smeared-out drop below  $T^*$  with the value remaining finite down to the lowest temperature [2]. In contrast to that ESR measurements were able to clearly show the activated behaviour of  $\chi_S$  related to the spin gap. As the bulk susceptibility measurements determine the sum of all unpaired spins in the sample, the defect contribution as well as the present  $\text{Cu}^{2+}$  impurities are also included explaining the observed difference.

Secondly, NMR measurements show a drop in  $(T_1T)^{-1}$  below  $T_*$  in accord with the decreasing spin susceptibility, however a strong increase is observed for lower temperatures alongside an inhomogeneous broadening of the NMR line width [8]. Because the NMR spin-lattice relaxation rate is susceptible to any kind of unpaired spins within the sample, unpaired orphan spins in a valence bond state can dominate the relaxation in the event that a spin gap opens. NMR work on related compounds of the  $\kappa\text{-ET}_2X$  family has shown that the defect spin contribution indeed dominates the intrinsic relaxation for the mentioned low-temperature region but is suppressed for fields above  $B = 10$  T [9]. The observed low-temperature increase of the ESR intensity of the defect contribution at  $B_{\text{main}}$  and its suppression with increasing magnetic field, in accord with magnetic torque data [7], is a direct proof for the presence of unpaired moments responsible for the described NMR relaxation. This behaviour observed for the low-temperature spin susceptibility is a strong indication for the presence of a valence bond state hosting unpaired orphan spins according to theoretical considerations. For a proposed VBG state in  $\kappa\text{-ET}_2\text{Cu}_2(\text{CN})_3$  [31] and for random singlet states in other frustrated spin systems [134] the observed power law increase at low temperature suppressed with magnetic field has been predicted.

Furthermore, the inhomogeneous broadening of the NMR signal observed in  $^{13}\text{C}$  studies yields a line width  $\Delta\nu_{1/2} = 50$  kHz corresponding to 4.7 mT for low temperatures [8]. This is of comparable strength to the observed local field responsible for the

anisotropy of the shifted defect signal. The NMR study explains the increased line width with field-induced inhomogeneous moments. These inhomogeneous moments can, therefore, be identified with the local field from impurity moments, in particular the observed  $\text{Cu}^{2+}$  ions, acting upon the unpaired orphan spins.

Additionally, the low-temperature phase diagram proposed based on  $\mu\text{SR}$  measurements hosts a weak antiferromagnetic phase at low temperatures and elevated magnetic fields, therein related to field-induced staggered moments [10]. The proposed phase boundary coincides with the emergence of the observed anisotropic defect signal at  $T_{\text{loc}}$ . In addition to that the  $\mu\text{SR}$  study proposed a  $T = 0$  quantum critical point between a spin liquid phase and a field-induced weak antiferromagnetic phase at a magnetic field of 5.2 mT similar to the local fields observed in the presented ESR data. The similar phase boundaries are an indication that the signatures in the  $\mu\text{SR}$  data interpreted as the weak antiferromagnetic phase likely stem from the orphan spins hosted in the valence bond state in the vicinity of magnetic impurities.

Magnetic impurities such as  $\text{Cu}^{2+}$  do of course not vanish at temperatures above  $T^*$ , however their influence on the magnetic properties diminishes as the large number of intrinsic paramagnetic moments dominates. Therefore their influence can only be seen in measurements at temperatures below the spin gap when most of the spins have formed nonmagnetic singlets.

In a broader picture, many experimental results beyond the magnetic measurements also fit to the presented low-temperature scenario. Firstly, high densities of  $\text{Cu}^{2+}$  would dope the system into a metallic state [115] not seen in the investigated samples. However, the small amount of present impurities responsible for the observed magnetic properties is also a potential source for the controversially discussed relaxor-like dielectric response [107, 140]: the charged impurities could be a source of electric polarisation in the Mott insulator.

As discussed before, signs of a phase transition around  $T^*$  are visible in the lattice parameters. The anisotropic signatures observed in the thermal expansion [120] backs the proposed scenario that the valence bonds are not pinned in a fully random fashion. Instead the singlet pairs are formed in an ordered way at least on a local scale leading to spin-lattice coupling analogous to the spin Peierls transition in spin chains. Such a scenario is also compatible with the two types of orphan spins present at low temperatures: one type formed in the vicinity of magnetic impurities as a result of their change of the local charge distribution; and the other one unrelated to impurities, but formed at intrinsic defects in the valence bond arrangement.

Unpaired localised spins dispersed in the valence bond state can also solve the con-

troversty that vanishing thermal transport  $\kappa/T$  is observed for  $T \rightarrow 0$  [119], albeit the observation of a strong linear specific heat contribution. This specific heat contribution has been related to gapless spin excitations, namely spinons in a quantum spin liquid state [118] which should be able to move freely and thus contribute substantially to the thermal transport. Orphan spins in a random singlet state enable local cluster-type low energy spin excitations bearing  $T$ -linear specific heat at low temperature [30]. Due to their localised nature they do, on the other hand, not contribute to the thermal transport in accord with the experimental observations [119].

All in all, the proposed valence bond state based on the presented ESR experiments is in agreement with studies utilising numerous different experimental methods. Many of the so far outstanding controversies can be resolved, when leaving behind the gapless quantum spin liquid ground state with spinon Fermi surface as a result of the observed spin gap.

## 5 ESR Investigations on Related Frustrated $\kappa$ -(BEDT – TTF)<sub>2</sub>X Compounds

Building upon the thorough investigation of the magnetic properties of  $\kappa$ -ET<sub>2</sub>Cu<sub>2</sub>(CN)<sub>3</sub> their interplay with different material attributes has been investigated by ESR measurements. Of particular interest here, is tuning the ratio  $U/t$  of electronic correlations and the transfer integral and thus moving through the phase diagram from the Mott insulating state towards a metallic state. As the spins relevant for the magnetic properties stem from the conduction electrons in the system, varying the electronic properties should have a direct influence also on the magnetic properties. It has been shown, that by varying the band width  $W$  proportional to the transfer integral  $t$  by applying hydrostatic pressure,  $\kappa$ -ET<sub>2</sub>Cu<sub>2</sub>(CN)<sub>3</sub> can be tuned from the Mott-insulating state at ambient pressure to a Fermi liquid at higher pressure for low temperatures [126].

Applying hydrostatic pressure in ESR experiments is technically very challenging as the commonly used clamp type pressure cells fabricated from metal cannot be used inside the microwave cavity. Another approach, instead of applying external hydrostatic pressure, is to use chemical pressure and perform experiments on related frustrated  $\kappa$ -(BEDT – TTF)<sub>2</sub>X compounds. Two different types of compounds have been investigated by ESR measurements and compared to  $\kappa$ -ET<sub>2</sub>Cu<sub>2</sub>(CN)<sub>3</sub> in order to explore the influence of the correlation strength. The ESR results are shown and discussed in the following two sections: first for  $\kappa$ -[ET<sub>1-x</sub>STF<sub>x</sub>]<sub>2</sub>Cu<sub>2</sub>(CN)<sub>3</sub>, where a varying fraction  $x$  of the organic BEDT – TTF molecules is substituted by BEDT – STF, and afterwards for  $\kappa$ -ET<sub>2</sub>Ag<sub>2</sub>(CN)<sub>3</sub> the sister compound with Ag<sup>+</sup> - instead of Cu<sup>+</sup> -ions within the anion sheets. As discussed in section 3.2.2, upon increasing the substitution,  $\kappa$ -[ET<sub>1-x</sub>STF<sub>x</sub>]<sub>2</sub>Cu<sub>2</sub>(CN)<sub>3</sub> is located further on the higher pressure, metallic side of the phase diagram.  $\kappa$ -ET<sub>2</sub>Ag<sub>2</sub>(CN)<sub>3</sub> on the other hand is subject to negative chemical pressure and therefore electronic correlations play a larger role compared to  $\kappa$ -ET<sub>2</sub>Cu<sub>2</sub>(CN)<sub>3</sub>. It is thus located deeper in the Mott insulating state, the lower pressure side of the phase diagram (see section 3.2.3 for details). As a result studying

those compounds allows to cover a region of the phase diagram extending in both directions compared to  $\kappa$ -ET<sub>2</sub>Cu<sub>2</sub>(CN)<sub>3</sub>.

In order to obtain comparable results it is important that the degree of frustration of the system, i. e. the ratio of the transfer integrals  $t'/t$ , does not change due to the substitution. For  $\kappa$ -ET<sub>2</sub>Ag<sub>2</sub>(CN)<sub>3</sub> this is fulfilled with a ratio close to unity ( $t'/t \sim 0.97$  [125]) similar to  $\kappa$ -ET<sub>2</sub>Cu<sub>2</sub>(CN)<sub>3</sub> ( $t'/t \sim 0.97$  [111]). In the substituted system the situation is more difficult. Even though the substituted samples have been shown to be isostructural to the pristine compound [124] the transfer integrals can be locally disturbed due to the more extended orbitals related to the selenium containing molecules. NMR measurements on  $\kappa$ -[ET<sub>1-x</sub>STF<sub>x</sub>]<sub>2</sub>Cu<sub>2</sub>(CN)<sub>3</sub> have, however, shown similar behaviour at the bulk as well as the substituted sites [123]. In addition the substitution has the same effect on  $\kappa$ -ET<sub>2</sub>Cu<sub>2</sub>(CN)<sub>3</sub> as applying hydrostatic pressure as shown in the electronic phase diagram in Fig. 3.8 [124]. Thus, the substitution mainly changes the electronic bandwidth of the system [124].

Nevertheless, disorder in the systems remains an important second aspect. As shown for  $\kappa$ -ET<sub>2</sub>Cu<sub>2</sub>(CN)<sub>3</sub>, disorder plays a major role for the low-temperature magnetic properties manifesting in the form of unpaired defect spins. It has also been shown that by targeted introduction of disorder through x ray irradiation an antiferromagnet can be driven into a quantum spin liquid state [122]. Alongside the different chemical pressure, the partial chemical substitution in  $\kappa$ -[ET<sub>1-x</sub>STF<sub>x</sub>]<sub>2</sub>Cu<sub>2</sub>(CN)<sub>3</sub> introduces more disorder into the system, whereas  $\kappa$ -ET<sub>2</sub>Ag<sub>2</sub>(CN)<sub>3</sub> is subject to less intrinsic disorder compared to  $\kappa$ -ET<sub>2</sub>Cu<sub>2</sub>(CN)<sub>3</sub> as explained in section 3.2.3. Thus, when discussing the effect of a different  $U/t$  for the different compounds, the different disorder levels have to be kept in mind.

## 5.1 Magnetic Properties of Chemically Substituted



Introducing chemical pressure through molecular substitution has proven to be an effective way to study the phase diagram of  $\kappa$ -ET<sub>2</sub>Cu<sub>2</sub>(CN)<sub>3</sub> with various experimental methods including NMR [123], DC transport and magnetisation [124, 127], infrared spectroscopy [124] as well as dielectric spectroscopy [108]. ESR experiments have been conducted as part of this project for further insight into the magnetic properties analogous to the new findings presented for the pristine  $\kappa$ -ET<sub>2</sub>Cu<sub>2</sub>(CN)<sub>3</sub>. Performing temperature-dependent ESR measurements on a series of substituted

$\kappa$ -[ET<sub>1-x</sub>STF<sub>x</sub>]<sub>2</sub>Cu<sub>2</sub>(CN)<sub>3</sub> samples of different substitution level  $x$  is a promising approach to explore the magnetic properties of frustrated  $\kappa$ -ET<sub>2</sub>X compounds for different vertical cuts of the pressure temperature phase diagram shown in Fig. 3.8. ESR measurements have been performed on single crystals with seven different substitution levels of  $x = 4\%, 10\%, 12\%, 16\%, 19\%, 21\%$ , and  $25\%$ .

In addition to studying the ground state properties, ESR is a promising technique to distinguish the spatially separated phases around the first order metal to insulator transition at low temperatures that have been identified by dielectric measurements [108]. Due to the different relaxation properties of the metallic and insulating regions, a distinction and possibly even a determination of the volume fractions could be possible, analogous to the ESR results on  $\kappa$ -ET<sub>2</sub>Hg(SCN)<sub>2</sub>Cl [141]. The quantum critical region above the critical endpoint proposed in [109] can also be accessed by samples with higher substitution. The superconducting phase has a reported maximum  $T_c$  at ambient pressure below 3 K [127], rendering investigations of this phase difficult with the conventional ESR spectrometer.

### 5.1.1 Room Temperature Behaviour for Varying Substitution

As a starting point, room temperature spectra have been recorded for different STF substitutions  $x$  of up to 100%. Due to the larger conductivity of the higher substituted samples, the microwave losses get substantial. All samples have therefore been only measured in a configuration where the microwave magnetic field  $B_1$  lays within the conduction plane and the static magnetic field  $B_0$  is parallel to the out of plane direction  $a^*$ . Nevertheless no spectra could be recorded for substitution levels above 25%. This has three main reasons: firstly, microwave losses in the samples deteriorate the sensitivity of the instrument; secondly, the SNR worsens quadratically with the increasingly large line width  $\Delta B$  due to the recorded first derivative spectra; and thirdly, the available crystals are very small, especially for the larger substitutions.

The line width  $\Delta B$  as well as the  $g$  factor as a function of the varying substitution  $x$  are shown in Fig. 5.1 including the results for the pristine sample. A larger  $g$ -shift relative to the free electron value is expected when substituting sulphur with selenium due to the larger spin-orbit coupling in the element with larger atomic number. This effect has been extensively studied on one dimensional organic charge transfer salts [38, 142].

The line width increases approximately linearly with a slope of 5 mT per 5% of STF. The much larger spin-orbit coupling when substituting S with Se is the reason for an

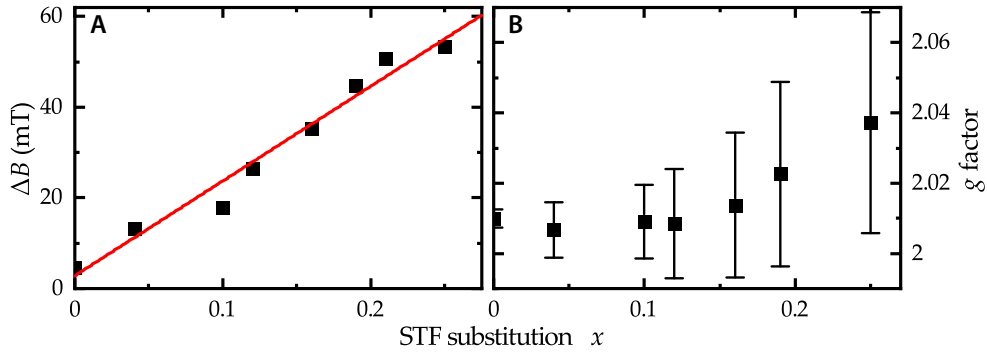


FIG. 5.1 Room-Temperature ESR Parameters for  $\kappa$ - $[ET_{1-x}STF_x]_2Cu_2(CN)_3$ . The parameters are obtained from Lorentzian fits to the ESR spectra recorded at  $T = 300$  K with samples of varying STF substitution  $x$  for  $B_0 \parallel a^*$ . (A) The line width  $\Delta B$  increases linearly as a function of  $x$ . (B) For low substitution levels the  $g$  factor remains at a constant offset from the free electron value  $g_e$ ; starting from  $x > 0.12$  an increase can be observed. The error bars represent 5% of the line width.

increase of  $\Delta B$ . In the case of non-interacting spins this would lead to inhomogeneous broadening due to the different  $g$  factors in a partially substituted sample. The present strong exchange coupling, however, leads to mixing of the inhomogeneous components, as discussed in section 2.3, resulting in a homogenous line shape with larger line width as compared to the pristine sample. Antisymmetric DM interaction has been identified as the largest contribution to the line width already for the pristine sample. As DM interaction is caused by spin-orbit coupling, an even larger contribution is expected in the case of BEDT-STF consistently explaining the linearly increasing line width as a function of the substitution level.

The  $g$  factor has a constant shift from  $g_e$  to about  $x = 12\%$  and starts to increase above. The increased spin-orbit coupling is seen as a larger  $g$ -shift. For lower substitutions exchange coupling mainly results in a broadened absorption line as discussed above. Only at higher substitution levels an overall shift starts to become visible. The broadening absorption for higher substitutions leads to an increasing uncertainty in determining the  $g$ -factor from the fits to the spectra.

### 5.1.2 Temperature-Dependence of the ESR Parameters

To investigate the temperature-dependence, ESR measurements have been performed with all chosen substitutions for temperatures between 300 K and 4 K. Fig. 5.2 gives an overview of the ESR spectra for different  $x$  at temperatures  $T = 300$  K, 75 K, 20 K,

and 4 K. As the samples with  $x = 21\%$  were particularly small, the spectra could not be analysed due to very bad SNR and are thus not shown in the following.

Overall, the qualitative behaviour is similar compared to the pristine sample. The ESR absorption first broadens upon cooling. For both of the intermediate temperatures shown the line width for  $x > 12\%$  gets so large that the signal can hardly be recognised anymore. Towards 4 K the signal narrows again. In contrast to the pristine sample, which shows a very narrow absorption of strongly decreased intensity, the substituted samples give spectra resembling the room temperature ones for  $x = 4, 10, 12\%$ .

Due to the larger line width the SNR is worse for the higher substitutions. Starting from  $x = 16\%$ , the maximum modulation amplitude of 3 mT had to be used to be able to recognise the spectra. Using such high sensitivity settings, any contamination within the cavity gives rise to a large temperature-dependent background signal, especially paramagnetic species at low temperatures. Therefore, background spectra had to be recorded and subtracted for all temperatures. The narrow pointed features visible for 20 K and more strongly at 4 K in the spectra are at resonance fields where such background signals are present. The visible signals are thus, most likely remains of those background features that could not be completely eliminated by the background subtraction, rendering a detailed analysis of those spectra impossible.

The parameters of Lorentzian fits to the ESR spectra, including the susceptibility  $\chi_S$ ,  $g$  factor, and line width  $\Delta B$  are shown in Fig. 5.3. As the noise level of the spectra as well as  $\Delta B$  increases with increasing  $x$ , the fits are subject to more and more uncertainty. Thus, only the substitution  $x \leq 12\%$  are shown for temperatures below 150 K

Having a look at the low-temperature behaviour of the spin susceptibility first, it can be noticed that for  $x \leq 10\%$  a decrease is visible similar to the pristine sample. A detailed view of  $\chi_S$  in this range is given in Fig. 5.4. For  $x = 4\%$   $\chi_S$  starts to strongly decrease below  $T = 7$  K similar to the pristine sample, however towards the lowest temperature a larger susceptibility remains in comparison. Increasing the substitution to  $x = 10\%$  the decreasing behaviour sets in at an even lower temperature of  $T = 5$  K. For  $x = 12\%$  no decrease is visible any more within the measurement range down to 4 K. At this lowest observed temperature the normalised susceptibility is significantly larger compared to  $\kappa$ -ET<sub>2</sub>Cu<sub>2</sub>(CN)<sub>3</sub>. Starting from  $x = 16\%$  the analysis of  $\chi_S$  completely fails due to the large noise, the broad absorption feature and strong influence of the background. The larger transfer integrals lead to more hopping of the charge carriers between the sites. Thus, the spin system is subject to larger fluctuations. As shown in the phase diagram (Fig. 3.8), samples with  $x > 10\%$  do possess a metallic ground state. Spin-singlet valence bonds are less stable in such a

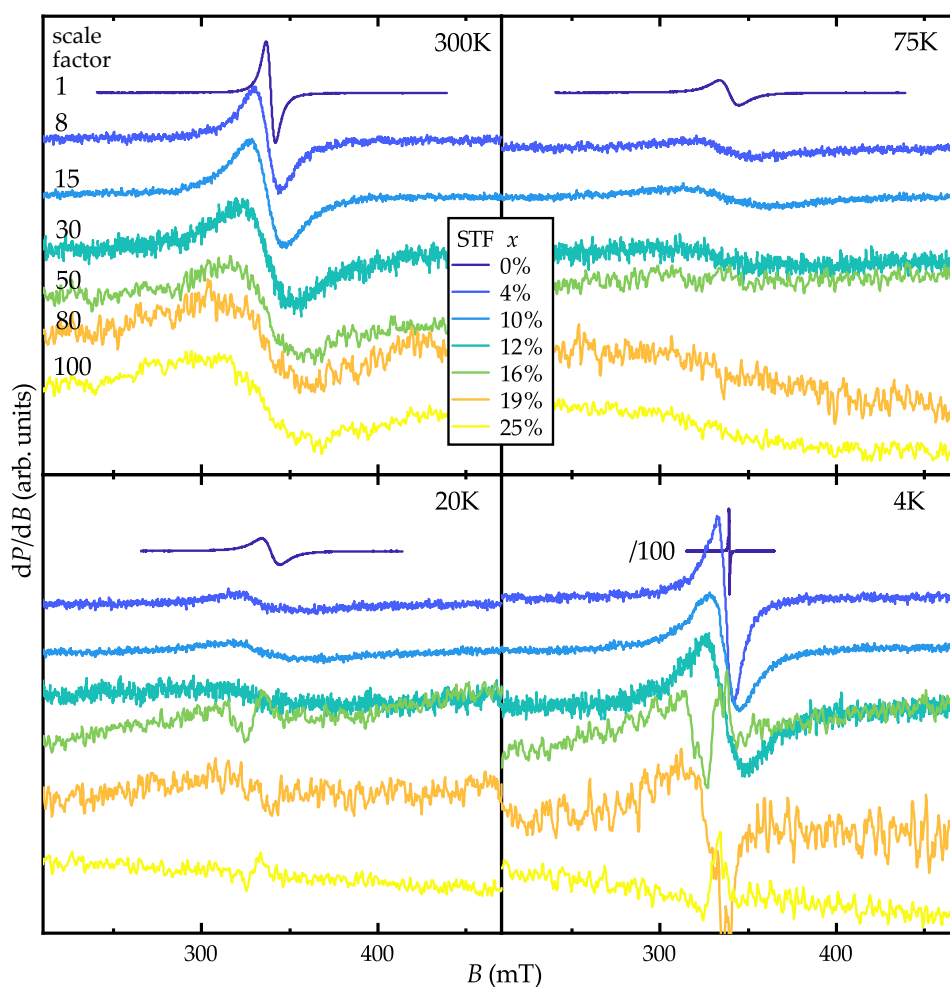


FIG. 5.2 X-Band ESR Spectra of  $\kappa$ -[ET<sub>1-x</sub>STF<sub>x</sub>]<sub>2</sub>Cu<sub>2</sub>(CN)<sub>3</sub> Evolution of the X-band ESR spectra for six different STF substitutions  $x$  and four different temperatures  $T$  with magnetic field  $B_0 \parallel a^*$ . The spectra for each substitution level are normalised to their room temperature intensity and scaled by an individual factor for better visibility as the amplitude quadratically decreases with increasing line width. The same scale is used for all temperatures, except for 4 K where the signal of the pristine sample is divided by 100 to account for the increasing peak height as the line drastically sharpens upon cooling. Note that the narrow pointed features occurring for the 3 high substitutions at 20 K and 4 K are most likely remains of a contaminant signal of the spectrometer still present after background removal.

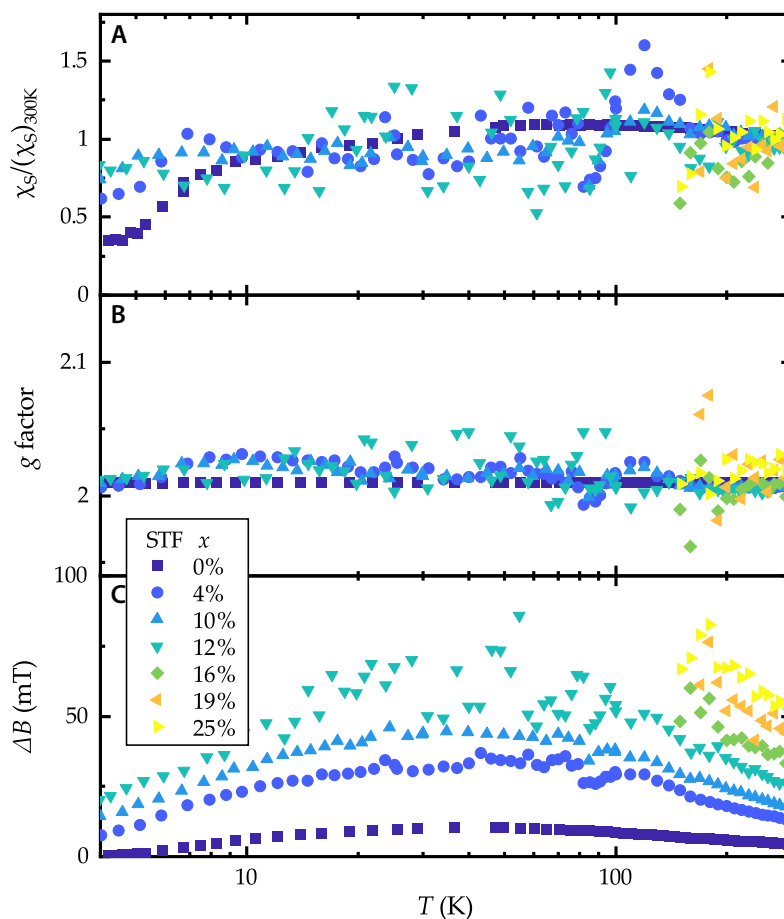


FIG. 5.3 *Temperature-Dependent ESR Parameters for  $\kappa$ -[ET<sub>1-x</sub>STF<sub>x</sub>]<sub>2</sub>Cu<sub>2</sub>(CN)<sub>3</sub>*  
 The normalised spin susceptibility  $\chi_S$  (A),  $g$  factor (B) and line width  $\Delta B$  (C) are obtained from fits to the X-band (9.5 GHz) ESR spectra measured for six different substitution levels with  $B_0 \parallel a^*$ . The parameters for  $\kappa$ -ET<sub>2</sub>Cu<sub>2</sub>(CN)<sub>3</sub> ( $x = 0$ ) are shown for comparison.

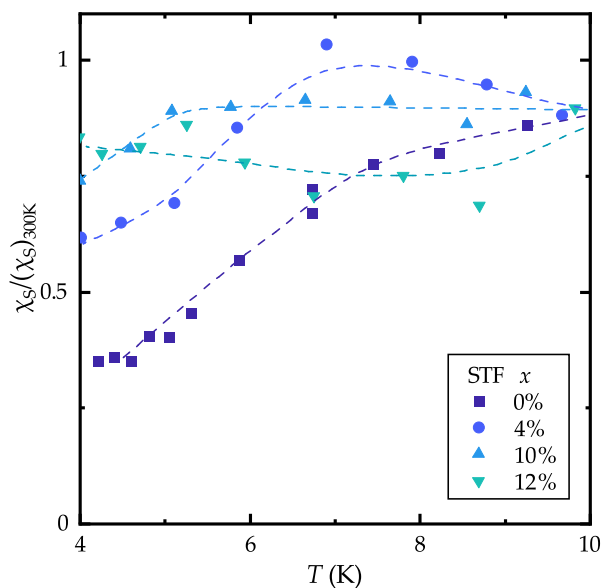


FIG. 5.4 Low-Temperature Spin Susceptibility for  $\kappa$ -[ET<sub>1-x</sub>STF<sub>x</sub>]<sub>2</sub>Cu<sub>2</sub>(CN)<sub>3</sub> Detailed view of the low-temperature behaviour of the normalised spin susceptibility  $\chi_S$  from Fig. 5.3A. The trends are visualised by the dashed lines serving as a guide to the eye.

more fluctuating system, thus they do form only at lower temperatures and more spins do still participate in the magnetic resonance. In addition to that, when the valence bonds finally form, the larger disorder will strongly localise them creating a larger amount of unpaired orphan spins as compared to  $\kappa$ -ET<sub>2</sub>Cu<sub>2</sub>(CN)<sub>3</sub> which can also contribute to the low-temperature ESR signal. The two contributions can, however, not be distinguished here, in the same way as it was possible for  $\kappa$ -ET<sub>2</sub>Cu<sub>2</sub>(CN)<sub>3</sub>. One likely reason is that the stronger exchange coupling mixes the different contributions. Additionally the overall larger line widths and asymmetries of the ESR signals lead to a worsened resolution for distinguishing different components that are close in their resonance field.

Precisely determining the  $g$  factor is difficult for the presented spectra. As the inhomogeneous broadening as well as present background signals lead to slightly asymmetric signals for temperatures below 150 K, an uncertainty of at least 10 % of the line width has to be assumed. At  $\Delta B = 50$  mT this corresponds to an uncertainty of  $\pm 0.03$  for the  $g$  factor. Thus, within this range no significant temperature-dependent change can be observed for  $x \leq 12$  which is in accord with the results for the pristine sample. For higher substitutions the analysis did again not work satisfactorily especially due to large influence of background signals.

The line width is shown in Fig. 5.3C. Its analysis is more successful due to the minima and maxima in the recorded derivative signals being the most robust features. Above 10 K the line widths of all measured substitutions follow the temperature-dependence of the pristine compound scaled with the room temperature value. Already at  $x = 4\%$   $\Delta B$  is three times larger compared to unsubstituted  $\kappa$ -ET<sub>2</sub>Cu<sub>2</sub>(CN)<sub>3</sub>. The width further increases linearly with increasing  $x$  as shown for  $T = 300$  K in Fig. 5.1. As discussed earlier, the main contribution to the line width is the DM interaction, which is larger in case of the heavier selenium analogue of the organic molecules in the crystals. For the larger substitutions  $x \geq 16\%$   $\Delta B$  grows so large upon cooling that the signal is hardly visible any more.

The strong decrease of  $\Delta B$  by a factor of ten seen for  $\kappa$ -ET<sub>2</sub>Cu<sub>2</sub>(CN)<sub>3</sub> below 10 K is not observed for the substituted samples. The line widths are less than a factor of two smaller at 4 K compared to 300 K. The much larger intrinsic line width for the spins associated with the substituted sites is likely the cause of masking the sharpening below  $T^*$  in the pristine sample.

### 5.1.3 Discussion

In order to explain the observations a closer look to the behaviour of the resistivity is given in this paragraph following the results and interpretations from [124]. As can be seen from the DC transport measurements reproduced in Fig. 5.5, for low substitution levels up to  $x = 10\%$  no metallic behaviour is observed for the full temperature range from 300 K down to 4 K. The resistivity is in this case increasing upon cooling for all temperatures. Starting from  $x = 12\%$  a maximum in the resistivity  $\rho(T)$  is observed corresponding to the onset of metallic transport. For very low temperature Fermi-liquid behaviour is observed. Upon increasing the temperature  $\rho(T)$  deviates from the  $\propto T^2$  behaviour; the system enters a bad metal regime. The observation of a displaced Drude peak in optical conductivity has shown that quasiparticles still play a crucial role for the charge transport in this regime. The quasiparticles get however dynamically localised due to the inherently disordered nature of the materials and thus lead to the altered temperature dependence. The maximum in resistivity occurs when the temperature exceeds the kinetic energy of the quasiparticles at the Brinkman-Rice scale. For larger temperature the metallic behaviour is completely lost and the resistivity behaves as in a thermally activated semiconductor just as for the lower substitution levels.

For  $x = 12\%$  the resistivity at 4 K is still slightly larger than the room temperature

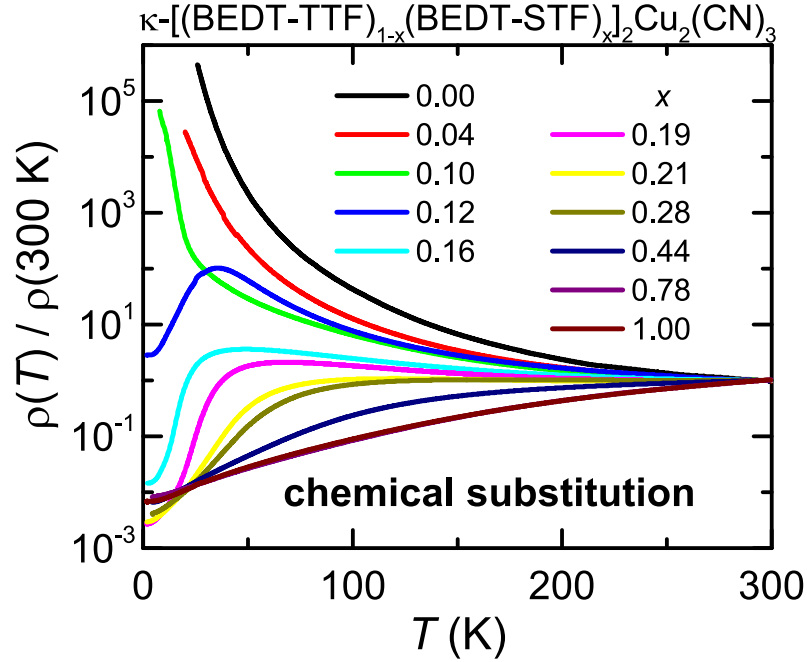


FIG. 5.5 DC Resistivity for  $\kappa$ -[ET<sub>1-x</sub>STF<sub>x</sub>]<sub>2</sub>Cu<sub>2</sub>(CN)<sub>3</sub> Evolution of the DC resistivity  $\rho(T)$  as function of substitution  $x$ . For higher substitution  $\rho(T)$  is reduced and metallic behaviour is observed towards lower temperatures. (reproduced from [124], Supplementary Fig. 2)

value, whereas for higher substitutions it drops to much lower values, e. g.  $\sim 100$  times lower for  $x = 16\%$ . This coincides with the vanishing ESR signal for lower temperature starting from  $x = 16\%$ . The strong decrease of  $\rho$  sets in within the range between 30 K and 75 K for substitution  $x$  between 16% and 25%. This temperature range is characterised by the largest ESR line width for all investigated samples due to the mechanism discussed for the pristine sample in section 4.1. There, antisymmetric DM interaction has been identified as the largest contribution to the line width. The overall large line width strongly impacts the sensitivity of the measurements and thus hides any potential changes due to the strongly changing resistivity. Below 20 K the ESR line width decreases again resulting in the comeback of a clear observation of the spectra for  $x \leq 12\%$ , i. e. the samples with resistivity larger or at least similar to the room temperature value. In the case of higher substitution the situation changes. As the observed spins are associated to the charge carriers which are localised in the Mott-insulating case, in the metallic state the hopping of the charge carriers results in totally different situation. No ESR signal has been observed in this metallic state of  $\kappa$ -[ET<sub>1-x</sub>STF<sub>x</sub>]<sub>2</sub>Cu<sub>2</sub>(CN)<sub>3</sub>.

A coexistence of metallic in insulating domains was observed by dielectric spectro-

scopy in the vicinity of the Mott transition reached with substitution levels between 12 % and 19 % [108]. As the ESR signal vanishes for the metallic state, only one single ESR signal is visible for all temperatures for  $x = 12$  %, whereas no clear signal was observed for low temperatures starting from  $x = 16$  %. It was, thus, impossible to further study the coexistence phase with the present ESR results.

Comparing the low temperature behaviour of the insulating samples to the pristine compound is, nevertheless, interesting. In the pristine sample an additional ESR signal has been observed for temperatures below  $T^*$  associated to unpaired orphan spins within the emerging spin singlet ground state. Despite the increased disorder compared to  $\kappa$ -ET<sub>2</sub>Cu<sub>2</sub>(CN)<sub>3</sub>, no signs of an additional ESR signal have been observed. Instead, in case of  $x = 4$  % the ESR intensity resembles the spin susceptibility as reported by static magnetisation measurements for the pristine compound: it decays and then saturates to a finite value [2]. For the higher substitutions  $x = 10$  % and 12 % the decay is even less pronounced. For  $\kappa$ -ET<sub>2</sub>Cu<sub>2</sub>(CN)<sub>3</sub> the ESR measurements have shown that this behaviour is not caused by gapless spin excitations of a quantum spin liquid ground state as it has been widely assumed [M2]. Rather, remaining unpaired orphan spins between the localised valence bonds have masked the intrinsic behaviour for other measurement techniques [M2]. In case of the substituted samples, the ESR measurements are now subject to similar problems that other techniques already had for the pristine sample. Because of the vastly increased line width, the capability of ESR spectroscopy to distinguish the intrinsic response from the defect spins is diminished. It is, therefore, not possible to unambiguously determine the magnetic ground state of the substituted  $\kappa$ -[ET<sub>1-x</sub>STF<sub>x</sub>]<sub>2</sub>Cu<sub>2</sub>(CN)<sub>3</sub> samples experimentally. Assuming similar behaviour as in the pristine sample, most likely even more unpaired orphan spins remain within a spin singlet ground state due to the increased disorder levels.

#### 5.1.4 Conclusions

Overall, the analogous molecular substitution leads to a strong increase of the ESR line width. In combination with the increasing conductivity causing technical problems in ESR spectroscopy, samples with larger substitution could not be studied satisfactorily.

For the low substitutions  $x \leq 12$  % at temperatures above 10 K the ESR results are in accord to the pristine compound with molecules with different  $g$  factor substituted into it. The larger spin-orbit coupling in Se compared to S leads to an increased  $g$  factor and line width  $\Delta B$  [38, 142]. For lower temperatures the observed behaviour differs

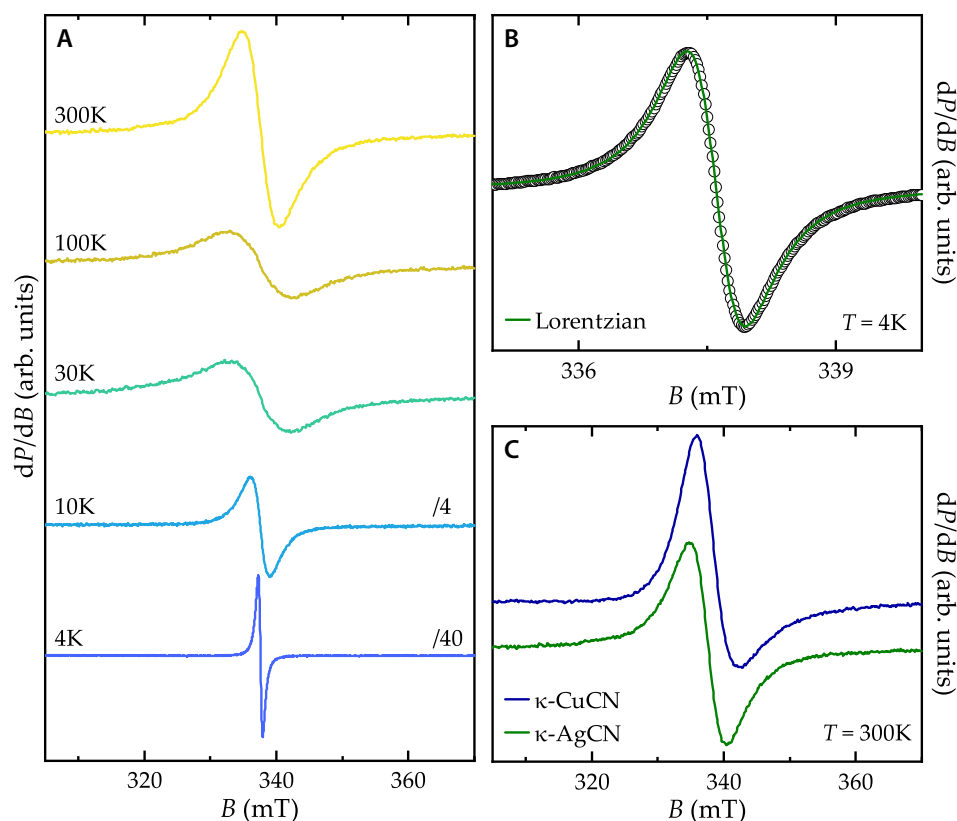


FIG. 5.6 X-Band ESR Spectra of  $\kappa$ -ET<sub>2</sub>Ag<sub>2</sub>(CN)<sub>3</sub> (A) Evolution of the X-band spectra as a function of temperature with magnetic field  $B_0 \parallel c$ . The signal is divided by 4, respectively 40, for  $T \leq 10$  K to account for the increasing peak height as the line sharpens upon cooling. (B) Single component Lorentzian signal observed down to  $T = 4$  K. (C) Due to the lower conductivity compared to  $\kappa$ -ET<sub>2</sub>Cu<sub>2</sub>(CN)<sub>3</sub> the signal stays Lorentzian all the way up to  $T = 300$  K

from  $\kappa$ -ET<sub>2</sub>Cu<sub>2</sub>(CN)<sub>3</sub>. With increasing substitution the transfer integrals in the system increase. Closer to the insulator to metal transition larger fluctuations are present within the spin system. The valence bonds, thus, start to form at lower temperatures. For the samples with low substitution level, which still have an insulating ground state, the strong disorder localises the valence bonds leaving a significant amount of unpaired orphan spins. Therefore, a random singlet state similar to the pristine compound is the most likely ground state. For the larger substitutions the ground state is metallic as shown before [124].

## 5.2 Quantum Spin Liquid Candidate $\kappa\text{-(BEDT – TTF)}_2\text{Ag}_2(\text{CN})_3$

The sister compound to  $\kappa\text{-ET}_2\text{Cu}_2(\text{CN})_3$ ,  $\kappa\text{-ET}_2\text{Ag}_2(\text{CN})_3$ , where Cu ions are replaced with Ag ions within the anion layers, has been first synthesised and studied in 2016 by NMR, DC transport and specific heat [125] as well as dielectric measurements [129]. Magnetic order is absent in the compound despite the large antiferromagnetic exchange interaction. As introduced in section 3.2.3, electronic correlations play an even larger role here, compared to  $\kappa\text{-ET}_2\text{Cu}_2(\text{CN})_3$ , as the applied negative chemical pressure reduces the transfer integrals in the system. The compound is therefore at ambient pressure located further on the insulating side of the Mott transition on the electronic phase diagram.

The first ESR experiments on the compound have been performed as part of this doctoral project. An exemplary set of ESR spectra obtained for different temperatures with a single crystal of  $\kappa\text{-ET}_2\text{Ag}_2(\text{CN})_3$  is shown in Fig. 5.6A. From room temperature to 4 K the resonance field, and thus the related  $g$ -factor, stays unchanged. The behaviour of the line width of the spectra is similar to  $\kappa\text{-ET}_2\text{Cu}_2(\text{CN})_3$ : the line first broadens upon cooling from 300 K reaching a maximum width in the range between 100 K and 30 K; below that the line width strongly decreases towards low temperatures. In contrast to the asymmetric Dysonian lineshape observed for  $\kappa\text{-ET}_2\text{Cu}_2(\text{CN})_3$ , the absorption is of Lorentzian shape already at room temperature owing to the higher resistivity as shown in Fig. 5.6C. At low temperatures just one single component Lorentzian signal has been observed. Even at the lowest temperature of 4 K shown in Fig. 5.6B, no signs of an additional ESR signal due to any kind of defect spins could be observed. This supports the assumption that  $\kappa\text{-ET}_2\text{Ag}_2(\text{CN})_3$  is subject to less intrinsic disorder and does not host magnetic impurities.

### 5.2.1 Temperature-Dependence of the ESR Parameters

Temperature-dependent X-band ESR spectra in the range from 300 K to 4 K have been recorded for three different orientations of the crystal with respect to the external magnetic field:  $\mathbf{B}_0 \parallel a^*, b, c$ . The parameters, spin susceptibility  $\chi_S$ ,  $g$  factor, and line width  $\Delta B$ , are obtained from fitting a Lorentzian line shape to the spectra. Fig. 5.7 displays the results including the parameters for  $\kappa\text{-ET}_2\text{Cu}_2(\text{CN})_3$  for comparison.

The measured  $\chi_S$  is in very good agreement with published data obtained by static magnetisation as well as NMR measurements [125]. For temperatures above 20 K the behaviour is well predicted by a Heisenberg model on a triangular lattice with

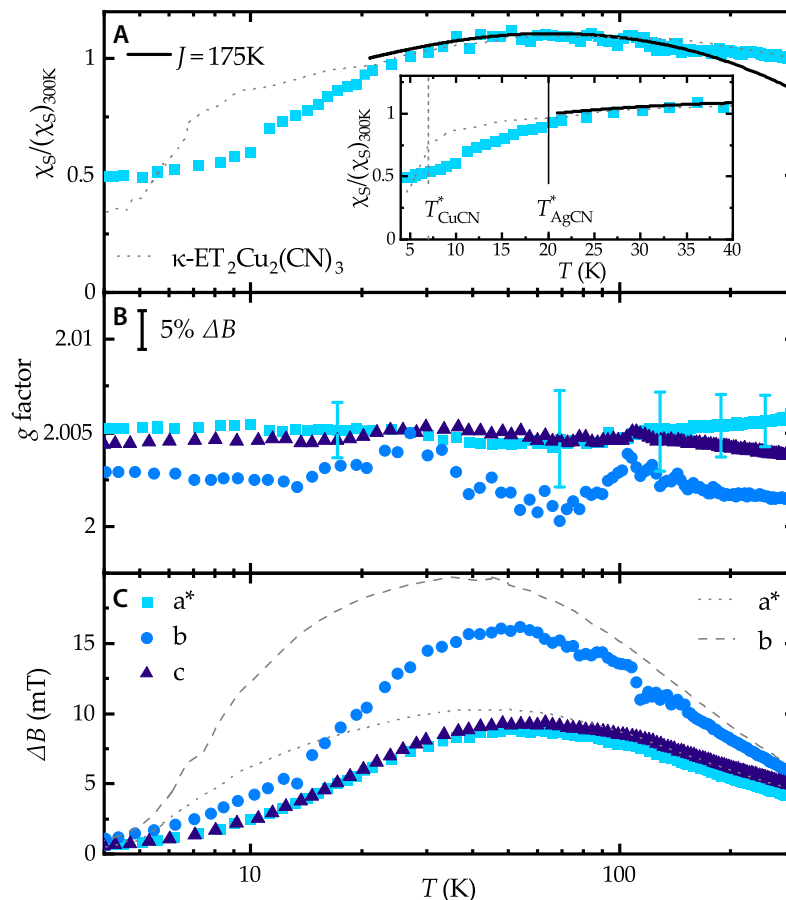


FIG. 5.7 *Temperature-Dependent ESR Parameters for  $\kappa$ -ET<sub>2</sub>Ag<sub>2</sub>(CN)<sub>3</sub>* The spin susceptibility  $\chi_S$  (A),  $g$  factor (B) and line width  $\Delta B$  (C) are obtained from fits to the X-band (9.5 GHz) ESR spectra measured along the three orthogonal directions  $B_0 \parallel a^*, b, c$ . The parameters measured for  $\kappa$ -ET<sub>2</sub>Cu<sub>2</sub>(CN)<sub>3</sub> (grey, dashed and dotted) are shown for comparison. For elevated temperatures,  $\chi_S$  is well described by a Heisenberg antiferromagnet on a triangular lattice. Below  $T^* \approx 20$  K the intensity of the signal drops (similar to the Cu compound) and eventually saturates at a value close to half of the room temperature value. No change can be observed in the  $g$ -factor within the experimental uncertainty estimated as 5% of the line width. The line width  $\Delta B(T)$  increases starting from room temperature while the largest values are again observed along the  $b$ -direction. A broad maximum is reached around 50 – 60 K for all three directions followed by a strong decrease towards lower temperatures without any distinct features.

antiferromagnetic exchange coupling  $J = 175$  K [125].  $\chi_S$  decreases significantly below 20 K, below 10 K it saturates to one half of the room temperature value. The  $g$  factor is temperature independent for all directions, i.e. it does not show any signs of internal fields. A conventional magnetic ordering can, thus, be ruled out within the observed temperature range as already indicated by NMR [125]. The  $g$  factors observed are similar to those for  $\kappa\text{-ET}_2\text{Cu}_2(\text{CN})_3$ . Also here, the small anisotropy can be explained by the  $\mathbf{g}$  tensor anisotropy of the BEDT–TTF molecules.  $\Delta B$  shows a broad maximum located around 50 K for all three directions. At room temperature the line widths even quantitatively agree to the ones measured for  $\kappa\text{-ET}_2\text{Cu}_2(\text{CN})_3$ .

While most of the temperature-dependent behaviour closely resembles the parameters for the Cu compound, distinct differences can be observed: the maximum in the line width as well as the drop of the susceptibility below the predicted value from the Heisenberg model are shifted towards higher temperatures by approximately 15 K; and the low-temperature susceptibility saturates, whereas an exponential decay was observed for the main signal for  $\kappa\text{-ET}_2\text{Cu}_2(\text{CN})_3$ .

The strong decay of the spin susceptibility below the prediction of the Heisenberg model accompanied by distinct anomalies in other physical properties, including the thermal expansion as well as the specific heat, has been related to the formation of spin singlet valence bonds below  $T^*$  in  $\kappa\text{-ET}_2\text{Cu}_2(\text{CN})_3$ . This decay of  $\chi_S$  sets in at higher temperature in the case of  $\kappa\text{-ET}_2\text{Ag}_2(\text{CN})_3$ , indicating a higher  $T^*$ . Even though the kink is less pronounced a temperature of  $T^* \approx 20$  K can be determined as shown in the inset of Fig. 5.7. Precise measurements of the lattice parameters as well as a detailed analysis of the specific heat as done for  $\kappa\text{-ET}_2\text{Cu}_2(\text{CN})_3$  in [120] remain a future task to confirm  $T^*$ .

Formation of valence bonds at a higher temperature is counterintuitive owing to the smaller exchange coupling of  $J = 175$  K in the compound compared to  $J = 250$  K for  $\kappa\text{-ET}_2\text{Cu}_2(\text{CN})_3$  [125]. However, the lower disorder levels in  $\kappa\text{-ET}_2\text{Ag}_2(\text{CN})_3$ , as discussed in section 3.2.3, can support the spin pairing. Dielectric measurements have shown a relaxor-ferroelectric behaviour for both compounds [107, 129]. Different possible orientations of the CN groups in the anion layer result in different almost degenerate electronic configurations. The resulting charged domain walls have been shown to be responsible for the characteristic dielectric response [129]. In case of  $\kappa\text{-ET}_2\text{Ag}_2(\text{CN})_3$  the coupling between the disordered anion layer and the BEDT-TTF dimers is weaker due their different relative arrangement, resulting in fewer and larger domains and manifesting in a reduced in-plane dielectric strength.

Even though the strong decrease of the susceptibility starts already at higher tem-

perature, 20 K versus 7 K for  $\kappa$ -ET<sub>2</sub>Cu<sub>2</sub>(CN)<sub>3</sub>, the susceptibility remains finite. It saturates below 10 K. An additional contribution like the defect signal responsible for the low-temperature  $\chi_S$  in  $\kappa$ -ET<sub>2</sub>Cu<sub>2</sub>(CN)<sub>3</sub> is not observed for  $\kappa$ -ET<sub>2</sub>Ag<sub>2</sub>(CN)<sub>3</sub>. The finite  $\chi_S$  is therefore a clear indication that low energy spin excitations persist towards the lowest measured temperature. A non gapped ground state, thus, cannot not be excluded for  $\kappa$ -ET<sub>2</sub>Ag<sub>2</sub>(CN)<sub>3</sub> in contrast to the observations presented for  $\kappa$ -ET<sub>2</sub>Cu<sub>2</sub>(CN)<sub>3</sub>.

## 5.2.2 Conclusions for the Ground State

The observed decrease of  $\chi_S$  is likely related to the formation of valence bonds just as in  $\kappa$ -ET<sub>2</sub>Cu<sub>2</sub>(CN)<sub>3</sub>. What makes the difference is supposedly the lower intrinsic disorder level as well as the missing magnetic impurities. If defects are absent, there is a lower tendency for the valence bonds to localise. Instead, they can remain freely fluctuating forming a resonating valence bond state. As discussed in section 1.4 spinon excitations are possible in such a RVB state, which can be responsible for the observed finite susceptibility as well as linear specific heat contribution towards low temperature [125].

It is possible that at temperatures below 4 K, the limit of the presented experiments, the valence bonds also localise in  $\kappa$ -ET<sub>2</sub>Ag<sub>2</sub>(CN)<sub>3</sub> despite less inhomogeneities. A gapless quantum spin liquid ground state is nevertheless still conceivable in  $\kappa$ -ET<sub>2</sub>Ag<sub>2</sub>(CN)<sub>3</sub> with the presented ESR results.

## 6 Conclusion

NMR measurements have shown in 2003 that magnetic order is absent in  $\kappa$ -(BEDT-TTF)<sub>2</sub>Cu<sub>2</sub>(CN)<sub>3</sub> at temperatures as low as 32 mK, four orders of magnitude below the exchange energy [2]. Since then the compound was considered as the textbook example to host a quantum spin liquid ground state. This peculiar nonmagnetic state emerges from spins on a frustrated triangular lattice that do not show magnetic order down to  $T = 0$  despite their strong interactions. Instead the spins are highly entangled, forming spin singlet valence bonds that rearrange as in a liquid owing to quantum fluctuations. It has been widely assumed that a spin liquid state hosting gapless excitations, that form a spinon Fermi surface, is realised in  $\kappa$ -ET<sub>2</sub>Cu<sub>2</sub>(CN)<sub>3</sub>.

However various experiments have already proven difficult to reconcile with the gapless spin liquid scenario. Those include: anomalies in different physical properties around  $T^* = 6$  K, e.g. in the lattice expansion coefficient [120], weak antiferromagnetism observed by  $\mu$ SR [10], vanishing thermal transport for  $T \rightarrow 0$  [119] despite a strong  $T$ -linear contribution [118], and the importance of disorder [31] to explain the divergences observed in magnetic torque measurements [7]. In face of those observations the exact nature of the ground state has remained unclear.

Within the scope of this project, electron spin resonance has been chosen to investigate the magnetic properties of  $\kappa$ -ET<sub>2</sub>Cu<sub>2</sub>(CN)<sub>3</sub>. In contrast to the previously mentioned experiments that use different rather indirect methods, ESR enables to directly probe the electron spins within the material. This has big advantages: In contrast to bulk methods it allows to differentiate different contributions to the magnetic susceptibility. Indirect microscopic probes rely on the influence of the electron spins on other aspects, e.g. nuclear spins in the case of NMR. Impurity moments can therefore mask the intrinsic response of the spin system.

Conventional ESR spectrometers are very sensitive instruments, however, their parameter range concerning temperature and magnetic field is typically rather limited. Thus, in addition, setups based on coplanar waveguides have been employed in order

to overcome those limitations and study  $\kappa\text{-ET}_2\text{Cu}_2(\text{CN})_3$  in a broad range of magnetic fields down to millikelvin temperatures.

A setup using coplanar transmission lines and field modulation has been newly developed [M1]. It enables broadband frequency-swept measurements at sensitivity levels only two orders of magnitude worse compared to a conventional cavity based X-band spectrometer. The operation of the instrument has been demonstrated in the frequency range of 0.1 GHz to 25 GHz, with magnetic field up to 700 mT, and temperatures between 1.6 K and 300 K. Experiments on three different well characterised materials have been performed: ruby ( $\text{Cr}^{3+}:\text{Al}_2\text{O}_3$ ), DPPH, and carbon fibres. The frequency-swept operation allows to follow all six transitions of the  $S = 3/2$  ruby system over the whole magnetic field range including the direct observation of the zero-field splitting. A demonstration of the improved SNR by adding the field modulation resulting in an increased sensitivity was possible.

Utilising conventional spectrometers as well as the coplanar techniques to perform ESR experiments on  $\kappa\text{-ET}_2\text{Cu}_2(\text{CN})_3$  allowed to answer the question on the nature of the ground state [M2]. The opening of a spin gap at  $T^* = 6$  K has been unambiguously shown by an exponential decrease of the spin susceptibility associated to the main ESR signal.

In addition to that multiple other contributions to the ESR spectra could be observed at temperatures below  $T^*$ . Signatures of  $\text{Cu}^{2+}$  magnetic impurities within the crystals appear at low temperatures due to their increasing Curie-like ESR response. A narrow signal component appears first at the same resonance field as the main absorption feature. Upon further cooling a fraction of this component splits off and shifts to a different resonance field. The shifted part is subject to a pronounced anisotropy exactly following the expected behaviour for a dipolar interaction. Another part of the signal, however, does not shift and shows a strongly increasing intensity for temperatures below 1 K at low magnetic fields. Higher magnetic fields suppress this increase.

These observations of additional contributions allow to propose a model for the gapped magnetic ground state in  $\kappa\text{-ET}_2\text{Cu}_2(\text{CN})_3$ : Spin-singlet valence bonds form below  $T^*$  with an associated spin gap. The valence bonds are localised on the lattice in the form of a valence bond solid, in accord with anisotropic lattice expansion. Intrinsic disorder in the anion layer as well as the observed magnetic impurities, however, lead to random pinning of valence bonds and thus introduce unpaired orphan spins. Those can be formed in the vicinity of a  $\text{Cu}^{2+}$  impurity due to the compensation of the charge imbalance. These spins are then subject to the local field of the magnetic impurity and are responsible for the shifted defect signal. Other

orphan spins can be formed due to grain boundaries or glassy areas in the VBS possibly induced by the intrinsic disorder present in the anion layers. These are not subject to any local fields and are thus responsible for the unshifted signal. The characteristic temperature- and magnetic field-dependence of its susceptibility is in very good agreement to random singlet models [134] as well as the magnetic torque observations [7]. It has been discussed that the presence of unpaired orphan spins and dipolar coupling to magnetic impurities can explain numerous of the previously contradicting experimental conclusions.

$\kappa\text{-ET}_2\text{Cu}_2(\text{CN})_3$  possesses a Mott insulating ground state due to the presence of strong electronic correlations. The ratio of those correlations to the transfer integrals determine the location of the compound within a generalised phase diagram for Mott insulators [19]. Studying the sister compound  $\kappa\text{-ET}_2\text{Ag}_2(\text{CN})_3$  or partially substituting ET for STF in  $\kappa\text{-}[\text{ET}_{1-x}\text{STF}_x]_2\text{Cu}_2(\text{CN})_3$  allows to explore the magnetic properties as a function of the location of the compound on this phase diagram without the need to apply external hydrostatic pressure. The substitution with STF increases the chemical pressure, driving the system towards the metallic state.  $\kappa\text{-ET}_2\text{Ag}_2(\text{CN})_3$  is subject to negative chemical pressure and therefore located further on the insulating side. The first ESR measurements on both systems have been performed as a part of this project.

In the case of STF substitution the properties for higher temperatures are only affected by the larger  $g$  factor due to replacing sulphur with selenium. This also leads to a strong increase in the line width due to inhomogeneous broadening and rendered experiments on crystals with substitutions larger than  $x = 25\%$  impossible. The increased line width can be observed down to the lowest temperature as it is caused by the disorder introduced through the substitution. As a result different contributions could not be identified. Upon increasing the substitution, the temperature at which the susceptibility drops lowers and the 4 K susceptibility approaches the room temperature value. More and more spins remain unpaired due to two reasons: increasing metallic fluctuation prevent the formation of valence bonds in the first place; and the larger amount of disorder results in a fully random pinning of the valence bonds creating a larger number of unpaired orphan spins.

In the sister compound  $\kappa\text{-ET}_2\text{Ag}_2(\text{CN})_3$  the observed ESR parameters closely follow the ones observed for  $\kappa\text{-ET}_2\text{Cu}_2(\text{CN})_3$  while all features are shifted to approximately 15 K higher temperatures. The negative chemical pressure decreases the transfer integrals in the system, hence, moving the system deeper into the Mott insulating state. Fluctuations are therefore reduced resulting in an earlier onset of the form-

ation of valence bonds. Despite the narrow signal observed at 4 K, compared to  $\kappa$ -[ET<sub>1-x</sub>STF<sub>x</sub>]<sub>2</sub>Cu<sub>2</sub>(CN)<sub>3</sub> and similar to  $\kappa$ -ET<sub>2</sub>Cu<sub>2</sub>(CN)<sub>3</sub>, no additional signal components could be identified. The spin susceptibility nevertheless remains finite for  $T \rightarrow 0$ , an indicator for the persistence of fluctuations and thus a resonating valence bond state. Missing magnetic impurities as well as a lower intrinsic disorder level due to differences within the anion sheet can explain the lower tendency for the valence bonds to localise. Localisation might still happen at temperatures lower than the ones reached within the experiments. Nevertheless, a gapless quantum spin liquid cannot be ruled out to be the ground state of  $\kappa$ -ET<sub>2</sub>Ag<sub>2</sub>(CN)<sub>3</sub> in face of the presented experimental data.

# List of Figures

- 1.1 Curie-Weiss Law • 6
- 1.2 Hubbard Model for Half-Filling • 9
- 1.3 Schematic Phase Diagram of Mott Insulators • 10
- 1.4 Geometrical Frustration • 11
- 1.5 Frustrated Lattices • 12
- 1.6 Frustrated Magnets • 12
- 1.7 Valence Bond States • 15
- 1.8 Spinon Excitations • 16
- 1.9 Adding Anisotropy and Disorder • 18
  
- 2.1 Basic Experimental Setup • 24
- 2.2 ESR for  $S = 1/2$  • 25
- 2.3 Bloch Equations: Absorption • 30
- 2.4 ESR Spectra • 31
- 2.5 Conventional CW ESR Spectrometer • 36
- 2.6 Rectangular  $TE_{102}$  Cavity • 36
- 2.7 Coplanar Waveguides • 39
- 2.8 Coplanar Waveguide Field Components • 41
- 2.9 Frequency-Domain ESR Probe-Head • 44
- 2.10 Schematic View of the Frequency-Domain Instrumentation • 46
- 2.11 Demonstration of the Instrument's Parameter Range • 47
- 2.12 Calibration of the Modulation Amplitude • 48
- 2.13 Frequency-Domain ESR Measurement of Ruby • 49
- 2.14 Instrument Performance • 50
- 2.15 Estimation of Sensitivity • 51
- 2.16 CPW Resonators: Modes • 53
- 2.17 CPW Resonators: Design • 54
- 2.18 CPW Resonators: Quality Factor • 55
- 2.19 CPW Resonators: Spectrum • 57

- 2.20 CPW Resonators: ESR Signal • 58
- 2.21 Magnetic Field Calibration • 59
  
- 3.1 Examples of One- and Two-Dimensional Organic Conductors • 62
- 3.2 Schematic Structure of  $\text{ET}_2\text{X}$  • 63
- 3.3 Crystal Structure of  $\kappa\text{-ET}_2\text{Cu}_2(\text{CN})_3$  • 67
- 3.4 Experimental Data I for  $\kappa\text{-ET}_2\text{Cu}_2(\text{CN})_3$  • 68
- 3.5 Experimental Data II for  $\kappa\text{-ET}_2\text{Cu}_2(\text{CN})_3$  • 70
- 3.6 Experimental Data III for  $\kappa\text{-ET}_2\text{Cu}_2(\text{CN})_3$  • 72
- 3.7 Molecular Substitution:  $\kappa\text{-}[\text{ET}_{1-x}\text{STF}_x]_2\text{Cu}_2(\text{CN})_3$  • 75
- 3.8 Pressure-Temperature Phase Diagram for  $\kappa\text{-}[\text{ET}_{1-x}\text{STF}_x]_2\text{Cu}_2(\text{CN})_3$  • 76
- 3.9 Anion Sheets in  $\kappa\text{-ET}_2\text{Cu}_2(\text{CN})_3$  and  $\kappa\text{-ET}_2\text{Ag}_2(\text{CN})_3$  • 78
  
- 4.1 X-Band ESR Spectra of  $\kappa\text{-ET}_2\text{Cu}_2(\text{CN})_3$  • 82
- 4.2 Sample-Dependence of ESR Parameters • 85
- 4.3 Temperature-Dependent ESR Parameters for  $\kappa\text{-ET}_2\text{Cu}_2(\text{CN})_3$  • 87
- 4.4 ESR Line Width at Different Magnetic Fields • 88
- 4.5 Low-Temperature ESR Line Width • 89
- 4.6 Gapped Magnetic Ground State • 92
- 4.7  $\text{Cu}^{2+}$  Impurities • 96
- 4.8 Crystal Twinning • 98
- 4.9 Sample to Sample Variation of Defect Contribution • 100
- 4.10 Low-Temperature Anisotropy of the ESR Signal • 100
- 4.11 Components of the Defect Signal • 102
- 4.12 Defect Components in Different Samples • 103
- 4.13 Temperature Evolution of ESR Spectra in the mK Range • 107
- 4.14 ESR Parameters in the mK Range • 108
- 4.15 Low-Temperature ESR Results for Sample # 3 • 109
- 4.16 Field-Dependence of Local Field  $B_{\text{loc}}$  and Onset Temperature  $T_{\text{loc}}$  • 110
- 4.17 Intensity of the Remaining Signal at  $B_{\text{main}}$  • 111
  
- 5.1 Room-Temperature ESR Parameters for  $\kappa\text{-}[\text{ET}_{1-x}\text{STF}_x]_2\text{Cu}_2(\text{CN})_3$  • 120
- 5.2 X-Band ESR Spectra of  $\kappa\text{-}[\text{ET}_{1-x}\text{STF}_x]_2\text{Cu}_2(\text{CN})_3$  • 122
- 5.3 Temperature-Dependent ESR Parameters for  $\kappa\text{-}[\text{ET}_{1-x}\text{STF}_x]_2\text{Cu}_2(\text{CN})_3$  • 123
- 5.4 Low-Temperature Spin Susceptibility for  $\kappa\text{-}[\text{ET}_{1-x}\text{STF}_x]_2\text{Cu}_2(\text{CN})_3$  • 124
- 5.5 DC Resistivity for  $\kappa\text{-}[\text{ET}_{1-x}\text{STF}_x]_2\text{Cu}_2(\text{CN})_3$  • 126
- 5.6 X-Band ESR Spectra of  $\kappa\text{-ET}_2\text{Ag}_2(\text{CN})_3$  • 128

5.7 Temperature-Dependent ESR Parameters for  $\kappa\text{-ET}_2\text{Ag}_2(\text{CN})_3 \cdot 13\text{O}$



# References

- [1] P. W. Anderson, *Resonating valence bonds: A new kind of insulator?*, Mater. Res. Bull. **8**, 153 (1973).
- [2] Y. Shimizu, K. Miyagawa, K. Kanoda, M. Maesato and G. Saito, *Spin liquid state in an organic Mott insulator with a triangular lattice*, Phys. Rev. Lett. **91**, 107001 (2003).
- [3] L. Balents, *Spin liquids in frustrated magnets*, Nature **464**, 199 (2010).
- [4] L. Savary and L. Balents, *Quantum spin liquids: a review*, Rep. Prog. Phys. **80**, 016502 (2016).
- [5] Y. Zhou, K. Kanoda and T.-K. Ng, *Quantum spin liquid states*, Rev. Mod. Phys. **89**, 025003 (2017).
- [6] C. Broholm, R. J. Cava, S. A. Kivelson et al., *Quantum spin liquids*, Science **367**, eaay0668 (2020).
- [7] T. Isono, T. Terashima, K. Miyagawa, K. Kanoda and S. Uji, *Quantum criticality in an organic spin-liquid insulator  $\kappa$ -(BEDT-TTF)<sub>2</sub>Cu<sub>2</sub>(CN<sub>3</sub>)*, Nat. Commun. **7**, 13494 (2016).
- [8] Y. Shimizu, K. Miyagawa, K. Kanoda, M. Maesato and G. Saito, *Emergence of inhomogeneous moments from spin liquid in the triangular-lattice Mott insulator  $\kappa$ -(ET)<sub>2</sub>Cu<sub>2</sub>(CN<sub>3</sub>)*, Phys. Rev. B **73**, 140407 (2006).
- [9] A. Pustogow, T. Le, H.-H. Wang et al., *Impurity moments conceal low-energy relaxation of quantum spin liquids*, Phys. Rev. B **101**, 140401 (2020).
- [10] F. L. Pratt, P. J. Baker, S. J. Blundell et al., *Magnetic and non-magnetic phases of a quantum spin liquid*, Nature **471**, 612 (2011).
- [11] S. Blundell, *Magnetism in condensed matter*, Oxford Master Series in Condensed Matter Physics (Oxford University Press, Oxford, UK, 2001).
- [12] R. Gross and A. Marx, *Festkörperphysik*, 2. ed. (De Gruyter, Berlin Boston, 2014).

## References

- [13] A. Auerbach, *Interacting electrons and quantum magnetism* (Springer, New York, USA, 1994).
- [14] F. Gebhard, *The mott metal-insulator transition, Models and methods*, Springer Tracts on Modern Physics (Springer, Berlin Heidelberg, 1997).
- [15] J. Hubbard and B. H. Flowers, *Electron correlations in narrow energy bands*, Proc. R. Soc. Lond. A **276**, 238 (1963).
- [16] R. Rösslhuber, *Pressure-dependent dielectric spectroscopy measurements on organic spin liquid compounds*, PhD thesis (Universität Stuttgart, 2019).
- [17] A. Pustogow, *Unveiling electronic correlations in layered molecular conductors by optical spectroscopy*, PhD thesis (Universität Stuttgart, 2017).
- [18] M. Dressel and S. Tomić, *Molecular quantum materials: electronic phases and charge dynamics in two-dimensional organic solids*, Adv. Phys. **69**, 1 (2020).
- [19] A. Pustogow, M. Bories, A. Löhle et al., *Quantum spin liquids unveil the genuine mott state*, Nat. Mater. **17**, 773 (2018).
- [20] Y. Okamoto, M. Nohara, H. Aruga-Katori and H. Takagi, *Spin-liquid state in the  $S = 1/2$  hyperkagome antiferromagnet  $\text{Na}_4\text{Ir}_3\text{O}_8$* , Phys. Rev. Lett. **99**, 137207 (2007).
- [21] A. P. Ramirez, *Strongly geometrically frustrated magnets*, Annu. Rev. Mater. Sci. **24**, 453 (1994).
- [22] L. Seabra, T. Momoi, P. Sindzingre and N. Shannon, *Phase diagram of the classical heisenberg antiferromagnet on a triangular lattice in an applied magnetic field*, Phys. Rev. B **84**, 214418 (2011).
- [23] S. Sachdev, *Quantum magnetism and criticality*, Nat. Phys. **4**, 173 (2008).
- [24] I. Kimchi, A. Nahum and T. Senthil, *Valence bonds in random quantum magnets: theory and application to  $\text{YbMgGaO}_4$* , Phys. Rev. X **8**, 031028 (2018).
- [25] L. N. Bulaevskii, *Magnetic susceptibility of a chain of spins with antiferromagnetic interaction*, Sov. Phys. – Solid State **11**, 921 (1969).
- [26] E. Pytte, *Peierls instability in heisenberg chains*, Phys. Rev. B **10**, 4637 (1974).
- [27] J. W. Bray, L. V. Interrante, I. S. Jacobs and J. C. Bonner, *The spin-peierls transition*, in *Extended linear chain compounds: Volume 3* (Springer, Boston, MA, 1983).

- [28] D. C. Johnston, R. K. Kremer, M. Troyer et al., *Thermodynamics of spin  $S = 1/2$  antiferromagnetic uniform and alternating-exchange Heisenberg chains*, Phys. Rev. B **61**, 9558 (2000).
- [29] I. Affleck, T. Kennedy, E. H. Lieb and H. Tasaki, *Valence bond ground states in isotropic quantum antiferromagnets*, Commun. Math. Phys. **115**, 477 (1988).
- [30] H. Kawamura and K. Uematsu, *Nature of the randomness-induced quantum spin liquids in two dimensions*, J. Phys. Condens. Matter **31**, 504003 (2019).
- [31] K. Riedl, R. Valentí and S. M. Winter, *Critical spin liquid versus valence-bond glass in a triangular-lattice organic antiferromagnet*, Nat. Commun. **10**, 2561 (2019).
- [32] O. I. Motrunich, *Variational study of triangular lattice spin-1 / 2 model with ring exchanges and spin liquid state in  $\kappa$ - $\text{ET}_2\text{Cu}_2(\text{CN})_3$* , Phys. Rev. B **72**, 045105 (2005).
- [33] S.-S. Lee and P. A. Lee,  *$U(1)$  Gauge theory of the hubbard model: spin liquid states and possible application to  $\kappa$ -(BEDT-TTF) $_2\text{Cu}_2(\text{CN})_3$* , Phys. Rev. Lett. **95**, 036403 (2005).
- [34] O. I. Motrunich, *Orbital magnetic field effects in spin liquid with spinon fermi sea: possible application to  $\kappa$ -(ET) $_2\text{Cu}_2(\text{CN})_3$* , Phys. Rev. B **73**, 155115 (2006).
- [35] R. Moessner and S. L. Sondhi, *Resonating valence bond phase in the triangular lattice quantum dimer model*, Phys. Rev. Lett. **86**, 1881 (2001).
- [36] S.-S. Lee, P. A. Lee and T. Senthil, *Amperean pairing instability in the  $U(1)$  spin liquid state with Fermi surface and application to  $\kappa$ -(BEDT-TTF) $_2\text{Cu}_2(\text{CN})_3$* , Phys. Rev. Lett. **98**, 067006 (2007).
- [37] A. Kitaev, *Anyons in an exactly solved model and beyond*, Ann. Phys. (NY) **321**, January Special Issue, 2 (2006).
- [38] M. Dumm, *Elektronenspinresonanz an niedrigdimensionalen organischen Systemen*, PhD thesis (Universität Augsburg, 1999).
- [39] C. P. Poole, *Electron spin resonance: A comprehensive treatise on experimental techniques*, 2. ed. (Wiley, New York, USA, 1983).
- [40] G. Jeschke, *Electron paramagnetic resonance*, in *Lecture notes on physical chemistry IV* (ETH Zürich, 2016).

## References

- [41] E. Tiesinga, P. J. Mohr, D. B. Newell and B. N. Taylor, *The CODATA 2018 recommended values of the fundamental physical constants*, NIST, (2020)  
<http://physics.nist.gov/constants>.
- [42] D. Di Gianni and A. Weis, *Magnetic resonance and bloch equations*, Wolfram Demonstrations Project, (2008)  
<http://demonstrations.wolfram.com/MagneticResonanceAndBlochEquations>.
- [43] F. J. Dyson, *Electron spin resonance absorption in metals. II. Theory of electron diffusion and the skin effect*, *Phys. Rev.* **98**, 349 (1955).
- [44] G. Feher and A. F. Kip, *Electron spin resonance absorption in metals. I. Experimental*, *Phys. Rev.* **98**, 337 (1955).
- [45] G. Jeschke, *Kurze Einführung in die elektronenparamagnetische Resonanzspektroskopie*, Vorlesungsskript (Universität Konstanz, 2008).
- [46] R. J. Elliott, *Theory of the effect of spin-orbit coupling on magnetic resonance in some semiconductors*, *Phys. Rev.* **96**, 266 (1954).
- [47] R. Kubo and K. Tomita, *A general theory of magnetic resonance absorption*, *J. Phys. Soc. Jpn.* **9**, 888 (1954).
- [48] S. Taniguchi, Y. Kobayashi, M. Kasai, K. Kodama and M. Sato, *ESR studies on  $\text{CaV}_4\text{O}_9$  and  $\text{CaV}_3\text{O}_7$* , *J. Phys. Soc. Jpn.* **66**, 3660 (1997).
- [49] I. Yamada, M. Nishi and J. Akimitsu, *Electron paramagnetic resonance governed by the Dzyaloshinsky-Moriya antisymmetric exchange interaction in  $\text{CuGeO}_3$* , *J. Phys. Condens. Matter* **8**, 2625 (1996).
- [50] D. Ehlers, *Spektrolyst*, Universität Augsburg,  
<http://myweb.rz.uni-augsburg.de/~ehlersdi/spektrolyst/>.
- [51] R. T. Weber, *An EPR primer*, in *Xenon user's guide* (Bruker BioSpin Corporation, Billerica, MA USA, 2011).
- [52] T. Schwarze, J. Waizner, M. Garst et al., *Universal helimagnon and skyrmion excitations in metallic, semiconducting and insulating chiral magnets*, *Nat. Mater.* **14**, 478 (2015).
- [53] Y. Onose, Y. Okamura, S. Seki, S. Ishiwata and Y. Tokura, *Observation of magnetic excitations of skyrmion crystal in a helimagnetic insulator  $\text{Cu}_2\text{OSeO}_3$* , *Phys. Rev. Lett.* **109**, 037603 (2012).

- [54] K. Y. Povarov, A. I. Smirnov, O. A. Starykh, S. V. Petrov and A. Y. Shapiro, *Modes of magnetic resonance in the spin-liquid phase of  $\text{Cs}_2\text{CuCl}_4$* , Phys. Rev. Lett. **107**, 037204 (2011).
- [55] U. Schaufuß, V. Kataev, A. A. Zvyagin et al., *Evolution of the Kondo state of  $\text{YbRh}_2\text{Si}_2$  probed by high-field ESR*, Phys. Rev. Lett. **102**, 076405 (2009).
- [56] A. Schwartz, M. Scheffler and S. M. Anlage, *Determination of the magnetization scaling exponent for single-crystal  $\text{La}_{0.8}\text{Sr}_{0.2}\text{MnO}_3$  by broadband microwave surface impedance measurements*, Phys. Rev. B **61**, R870 (2000).
- [57] M. Scheffler, K. Schlegel, C. Clauss et al., *Microwave spectroscopy on heavy-fermion systems: probing the dynamics of charges and magnetic moments*, Phys. Status Solidi B **250**, 439 (2013).
- [58] H. Malissa, D. I. Schuster, A. M. Tyryshkin, A. A. Houck and S. A. Lyon, *Superconducting coplanar waveguide resonators for low temperature pulsed electron spin resonance spectroscopy*, Rev. Sci. Instrum. **84**, 025116 (2013).
- [59] A. Ghirri, C. Bonizzoni, D. Gerace et al.,  *$\text{YBa}_2\text{Cu}_3\text{O}_7$  microwave resonators for strong collective coupling with spin ensembles*, Appl. Phys. Lett. **106**, 184101 (2015).
- [60] C. Schlegel, M. Dressel and J. van Slageren, *Broadband electron spin resonance at 4 – 40 GHz and magnetic fields up to 10 T*, Rev. Sci. Instrum. **81**, 093901 (2010).
- [61] H. Mahdjour, W. G. Clark and K. Baberschke, *High-sensitivity broadband microwave spectroscopy with small nonresonant coils*, Rev. Sci. Instrum. **57**, 1100 (1986).
- [62] K. A. Rubinson, *Broadband (up to 10 GHz) electron-paramagnetic-resonance spectrometer: cw implementation with direct detection*, Rev. Sci. Instrum. **60**, 392 (1989).
- [63] V. P. Denysenkov and A. M. Grishin, *Broadband ferromagnetic resonance spectrometer*, Rev. Sci. Instrum. **74**, 3400 (2003).
- [64] F. Giesen, J. Podbielski, T. Korn et al., *Hysteresis and control of ferromagnetic resonances in rings*, Appl. Phys. Lett. **86**, 112510 (2005).
- [65] I. Harward, T. O’Keevan, A. Hutchison, V. Zagorodnii and Z. Celinski, *A broadband ferromagnetic resonance spectrometer to measure thin films up to 70 GHz*, Rev. Sci. Instrum. **82**, 095115 (2011).

## References

- [66] E. Montoya, T. McKinnon, A. Zamani, E. Girt and B. Heinrich, *Broadband ferromagnetic resonance system and methods for ultrathin magnetic films*, J. Magn. Mater. **356**, 12 (2014).
- [67] C. Clauss, D. Bothner, D. Koelle et al., *Broadband electron spin resonance from 500 MHz to 40 GHz using superconducting coplanar waveguides*, Appl. Phys. Lett. **102**, 162601 (2013).
- [68] Y. Wiemann, J. Simmendinger, C. Clauss et al., *Observing electron spin resonance between 0.1 and 67 GHz at temperatures between 50 mK and 300 K using broadband metallic coplanar waveguides*, Appl. Phys. Lett. **106**, 193505 (2015).
- [69] R. N. Simons, *Coplanar waveguide circuits, components, and systems*, 1. ed. (Wiley, New York, USA, 2001).
- [70] D. M. Pozar, *Microwave engineering*, 4. ed. (Wiley, Hoboken, NJ USA, 2012).
- [71] R. N. Simons and R. K. Arora, *Coupled slot line field components*, IEEE Trans. Microw. Theory Tech. **30**, 1094 (1982).
- [72] N. G. Ebensperger, B. Ferdinand, D. Koelle et al., *Characterizing dielectric properties of ultra-thin films using superconducting coplanar microwave resonators*, Rev. Sci. Instrum. **90**, 114701 (2019).
- [73] M. Belmeguenai, F. Zighem, Y. Roussigné et al., *Microstrip line ferromagnetic resonance and Brillouin light scattering investigations of magnetic properties of Co<sub>2</sub>MnGe Heusler thin films*, Phys. Rev. B **79**, 024419 (2009).
- [74] S. S. Kalarickal, P. Krivosik, M. Wu et al., *Ferromagnetic resonance linewidth in metallic thin films: Comparison of measurement methods*, J. Appl. Phys. **99**, 093909 (2006).
- [75] Y. Chen, X. Wang, H. Chen, Y. Gao and N. X. Sun, *Novel ultra-wide band (10 MHz – 26 GHz) permeability measurements for magnetic films*, IEEE Trans. Magn. **54**, 1 (2018).
- [76] S. Beguhn, Z. Zhou, S. Rand et al., *A new highly sensitive broadband ferromagnetic resonance measurement system with lock-in detection*, J. Appl. Phys. **111**, 07A503 (2012).
- [77] I. S. Maksymov and M. Kostylev, *Broadband stripline ferromagnetic resonance spectroscopy of ferromagnetic films, multilayers and nanostructures*, Physica E **69**, 253 (2015).

- [78] K. Herb, R. Tschaggelar, G. Denninger and G. Jeschke, *Double resonance calibration of g factor standards: Carbon fibers as a high precision standard*, J. Magn. Reson. **289**, 100 (2018).
- [79] M. Javaheri Rahim, T. Lehleiter, D. Bothner et al., *Metallic coplanar resonators optimized for low-temperature measurements*, J. Phys. D: Appl. Phys. **49**, 395501 (2016).
- [80] J. E. Geusic, *Paramagnetic fine structure spectrum of  $Cr^{+++}$  in a single ruby crystal*, Phys. Rev. **102**, 1252 (1956).
- [81] E. O. Schulz-Du Bois, *Paramagnetic spectra of substituted sapphires — Part I: Ruby*, Bell Labs Tech. J. **38**, 271 (1959).
- [82] D. I. Schuster, A. P. Sears, E. Ginossar et al., *High-cooperativity coupling of electron-spin ensembles to superconducting cavities*, Phys. Rev. Lett. **105**, 140501 (2010).
- [83] T.-T. Chang, D. Foster and A. H. Kahn, *An intensity standard for electron paramagnetic resonance using chromium-doped corundum ( $Al_2O_3:Cr^{3+}$ )*, J. Res. Natl. Inst. Stand. Technol. **83**, 133 (1978).
- [84] G. Eaton, S. Eaton, D. Barr and R. Weber, *Quantitative EPR*, 1. ed. (Springer, Wien, 2010).
- [85] C. Clauß, *On-chip broadband magnetic resonance spectroscopy down to ultralow temperatures*, PhD thesis (Universität Stuttgart, 2014).
- [86] C. Clauss, M. Dressel and M. Scheffler, *Optimization of coplanar waveguide resonators for ESR studies on metals*, J. Phys. Conf. Ser. **592**, 012146 (2015).
- [87] W. Voesch, M. Thiemann, D. Bothner, M. Dressel and M. Scheffler, *On-chip esr measurements of DPPH at mK temperatures*, Phys. Procedia **75**, 503 (2015).
- [88] R. Nacke, *Optimierte koplanare Resonatoren für Elektronenspinresonanz-Spektroskopie*, Bachelor's thesis (Universität Stuttgart, 2017).
- [89] L. Bondorf, M. Beutel, M. Thiemann et al., *Angle-dependent electron spin resonance of  $YbRh_2Si_2$  measured with planar microwave resonators and in-situ rotation*, Physica B **536**, 331 (2018).
- [90] D. S. Rausch, M. Thiemann, M. Dressel et al., *Superconducting coplanar microwave resonators with operating frequencies up to 50 GHz*, J. Phys. D: Appl. Phys. **51**, 465301 (2018).

## References

- [91] B. T. Matthias, T. H. Geballe and V. B. Compton, *Superconductivity*, Rev. Mod. Phys. **35**, 1 (1963).
- [92] J. Eisenstein, *Superconducting elements*, Rev. Mod. Phys. **26**, 277 (1954).
- [93] G. Grissonnanche, O. Cyr-Choinière, F. Laliberté et al., *Direct measurement of the upper critical field in cuprate superconductors*, Nat. Commun. **5**, 3280 (2014).
- [94] D. K. De, *Electron spin resonance and infrared studies of  $\text{Cu}^{2+}$  site symmetry in the high- $T_c$  superconductor  $\text{YBa}_2\text{Cu}_3\text{O}_{7-x}$* , J. Phys. C: Solid State Phys. **21**, 4481 (1988).
- [95] M. Thiemann, *Microwave investigations on superconducting Nb-doped  $\text{SrTiO}_3$* , PhD thesis (Universität Stuttgart, 2018).
- [96] S. Spassov and R. Egli, *Method for correcting remanent fields in magnetic property measurement systems without field compensation*, Technical Note (COST Action TD1402 RADIOMAG, 2016).
- [97] T. Granier, B. Gallois, L. Ducasse, A. Fritsch and A. Filhol, *4 K crystallographic and electronic structures of  $(\text{TMTTF})_2\text{X}$  salts ( $\text{X}^- : \text{PF}_6^-, \text{AsF}_6^-$ )*, Synth. Met. **24**, 343 (1988).
- [98] H. O. Jeschke, M. de Souza, R. Valentí et al., *Temperature dependence of structural and electronic properties of the spin-liquid candidate  $\kappa\text{-(BEDT-TTF)}_2\text{Cu}_2(\text{CN}_3)$* , Phys. Rev. B **85**, 035125 (2012).
- [99] K. Momma and F. Izumi, *VESTA3 for three-dimensional visualization of crystal, volumetric and morphology data*, J. Appl. Crystallogr. **44**, 1272 (2011).
- [100] J. Ferraris, D. O. Cowan, V. Walatka and J. H. Perlstein, *Electron transfer in a new highly conducting donor-acceptor complex*, J. Am. Chem. Soc. **95**, 948 (1973).
- [101] D. Jérôme, A. Mazaud, M. Ribault and K. Bechgaard, *Superconductivity in a synthetic organic conductor  $(\text{TMTSF})_2\text{PF}_6$* , J. Phys. Lett. **41**, 95 (1980).
- [102] M. Dressel, *Spin-charge separation in quasi one-dimensional organic conductors*, Naturwissenschaften **90**, 337 (2003); *Ordering phenomena in quasi-one-dimensional organic conductors*, ibid. **94**, 527 (2007).
- [103] D. Jérôme, *The physics of organic superconductors*, Science **252**, 1509 (1991).
- [104] G. Saito, T. Enoki, K. Toriumi and H. Inokuchi, *Two-dimensionality and suppression of metal-semiconductor transition in a new organic metal with alkylthio substituted TTF and perchlorate*, Solid State Commun. **42**, 557 (1982).

- [105] T. Mori, *Structural genealogy of BEDT-TTF-based organic conductors I. Parallel molecules:  $\beta$  and  $\beta'$  phases*, Bull. Chem. Soc. Jpn. **71**, 2509 (1998); T. Mori, H. Mori and S. Tanaka, *Structural genealogy of BEDT-TTF-based organic conductors II. Inclined molecules:  $\theta$ ,  $\alpha$ , and  $\kappa$  phases*, *ibid.* **72**, 179 (1999); T. Mori, *Structural genealogy of BEDT-TTF-based organic conductors III. Twisted molecules:  $\delta$  and  $\alpha'$  phases*, *ibid.* **72**, 2011 (1999).
- [106] M. Dressel and N. Drichko, *Optical properties of two-dimensional organic conductors: signatures of charge ordering and correlation effects*, Chem. Rev. **104**, 5689 (2004).
- [107] M. Pinterić, M. Čulo, O. Milat et al., *Anisotropic charge dynamics in the quantum spin-liquid candidate  $\kappa$ -(BEDT-TTF) $_2$ Cu $_2$ (CN) $_3$* , Phys. Rev. B **90**, 195139 (2014).
- [108] A. Pustogow, R. Rösslhuber, Y. Tan et al., *Low-temperature dielectric anomaly arising from electronic phase separation at the Mott insulator-metal transition*, npj Quantum Mater. **6**, 1 (2021).
- [109] T. Furukawa, K. Miyagawa, H. Taniguchi, R. Kato and K. Kanoda, *Quantum criticality of mott transition in organic materials*, Nat. Phys. **11**, 221 (2015).
- [110] U. Geiser, H. H. Wang, K. D. Carlson et al., *Superconductivity at 2.8 K and 1.5 kbar in  $\kappa$ -(BEDT-TTF) $_2$ Cu $_2$ (CN) $_3$ : the first organic superconductor containing a polymeric copper cyanide anion*, Inorg. Chem. **30**, 2586 (1991).
- [111] T. Koretsune and C. Hotta, *Evaluating model parameters of the  $\kappa$ - and  $\beta'$ -type Mott insulating organic solids*, Phys. Rev. B **89**, 045102 (2014).
- [112] P. Foury-Leylekian, V. Ilakovac, V. Balédent et al., *(BEDT-TTF) $_2$ Cu $_2$ (CN) $_3$  Spin liquid: Beyond the average structure*, Crystals **8**, 158 (2018).
- [113] N. Elstner, R. R. P. Singh and A. P. Young, *Finite temperature properties of the spin-1/2 Heisenberg antiferromagnet on the triangular lattice*, Phys. Rev. Lett. **71**, 1629 (1993).
- [114] M. Poirier, S. Parent, A. Côté et al., *Magnetodielectric effects and spin-charge coupling in the spin-liquid candidate  $\kappa$ -(BEDT-TTF) $_2$ Cu $_2$ (CN) $_3$* , Phys. Rev. B **85**, 134444 (2012).
- [115] T. Komatsu, N. Matsukawa, T. Inoue and G. Saito, *Realization of superconductivity at ambient pressure by band-filling control in  $\kappa$ -(BEDT-TTF) $_2$ Cu $_2$ (CN) $_3$* , J. Phys. Soc. Jpn. **65**, 1340 (1996).

- [116] K. G. Padmalekha, M. Blankenhorn, T. Ivek et al., *ESR studies on the spin-liquid candidate  $\kappa$ -(BEDT-TTF) $_2$ Cu $_2$ (CN) $_3$ : Anomalous response below  $T=8$ K*, Physica B: Condens. Matter, Special Issue on Electronic Crystals (ECRYS-2014) **460**, 211 (2015).
- [117] S. M. Winter, K. Riedl and R. Valentí, *Importance of spin-orbit coupling in layered organic salts*, Phys. Rev. B **95**, 060404 (2017).
- [118] S. Yamashita, Y. Nakazawa, M. Oguni et al., *Thermodynamic properties of a spin-1/2 spin-liquid state in a  $\kappa$ -type organic salt*, Nat. Phys. **4**, 459 (2008).
- [119] M. Yamashita, N. Nakata, Y. Kasahara et al., *Thermal-transport measurements in a quantum spin-liquid state of the frustrated triangular magnet  $\kappa$ -(BEDT-TTF) $_2$ Cu $_2$ (CN) $_3$* , Nat. Phys. **5**, 44 (2009).
- [120] R. S. Manna, M. de Souza, A. Brühl, J. A. Schlueter and M. Lang, *Lattice effects and entropy release at the low-temperature phase transition in the spin-liquid candidate  $\kappa$ -(BEDT-TTF) $_2$ Cu $_2$ (CN) $_3$* , Phys. Rev. Lett. **104**, 016403 (2010).
- [121] M. Poirier, M. de Lafontaine, K. Miyagawa, K. Kanoda and Y. Shimizu, *Ultrasonic investigation of the transition at 6 K in the spin-liquid candidate  $\kappa$ -(BEDT-TTF) $_2$ Cu $_2$ (CN) $_3$* , Phys. Rev. B **89**, 045138 (2014).
- [122] T. Furukawa, K. Miyagawa, T. Itou et al., *Quantum spin liquid emerging from antiferromagnetic order by introducing disorder*, Phys. Rev. Lett. **115**, 077001 (2015).
- [123] Y. Saito, T. Minamidate, A. Kawamoto, N. Matsunaga and K. Nomura, *Site-specific  $^{13}$ C NMR study on the locally distorted triangular lattice of the organic conductor  $\kappa$ -(BEDT-TTF) $_2$ Cu $_2$ (CN) $_3$* , Phys. Rev. B **98**, 205141 (2018).
- [124] A. Pustogow, Y. Saito, A. Löhle et al., *Rise and fall of landau's quasiparticles while approaching the mott transition*, Nat. Commun. **12**, 1571 (2021).
- [125] Y. Shimizu, T. Hiramatsu, M. Maesato et al., *Pressure-tuned exchange coupling of a quantum spin liquid in the molecular triangular lattice  $\kappa$ -(ET) $_2$ Ag $_2$ (CN) $_3$* , Phys. Rev. Lett. **117**, 107203 (2016).
- [126] T. Furukawa, K. Kobashi, Y. Kurosaki, K. Miyagawa and K. Kanoda, *Quasi-continuous transition from a fermi liquid to a spin liquid in  $\kappa$ -(BEDT-TTF) $_2$ Cu $_2$ (CN) $_3$* , Nat. Commun. **9**, 307 (2018).

- [127] Y. Saito, A. Löhle, A. Kawamoto, A. Pustogow and M. Dressel, *Pressure-tuned superconducting dome in chemically-substituted  $\kappa$ -(BEDT-TTF) $_2$ Cu $_2$ (CN) $_3$* , Crystals **11**, 817 (2021).
- [128] T. Hiramatsu, Y. Yoshida, G. Saito et al., *Design and preparation of a quantum spin liquid candidate  $\kappa$ -(ET) $_2$ Ag $_2$ (CN) $_3$  having a nearby superconductivity*, Bull. Chem. Soc. Jpn. **90**, 1073 (2017).
- [129] M. Pinterić, P. Lazić, A. Pustogow et al., *Anion effects on electronic structure and electrodynamic properties of the mott insulator  $\kappa$ -(BEDT-TTF) $_2$ Ag $_2$ (CN) $_3$* , Phys. Rev. B **94**, 161105 (2016).
- [130] P. Foury-Leylekian, V. Ilakovac, P. Fertey et al., *New insights into the structural properties of  $\kappa$ -(BEDT-TTF) $_2$ Ag $_2$ (CN) $_3$  spin liquid*, Acta Crystallogr. B **76**, 581 (2020).
- [131] J. Rumble, ed., *Crc handbook of chemistry and physics*, 102nd ed. (CRC Press, 2021).
- [132] T. Nakamura, T. Nobutoki, T. Takahashi et al., *ESR properties of  $\kappa$ -type organic superconductors based on BEDT-TTF*, J. Phys. Soc. Jpn. **63**, 4110 (1994).
- [133] J. W. Bray, H. R. Hart, L. V. Interrante et al., *Observation of a spin-peierls transition in a Heisenberg antiferromagnetic linear-chain system*, Phys. Rev. Lett. **35**, 744 (1975).
- [134] I. Kimchi, J. P. Sheckelton, T. M. McQueen and P. A. Lee, *Scaling and data collapse from local moments in frustrated disordered quantum spin systems*, Nature Communications **9**, 4367 (2018).
- [135] M. R. Norman, N. J. Laurita and D. Hsieh, *Valence bond phases of herbertsmithite and related copper kagome materials*, Phys. Rev. Research **2**, 013055 (2020).
- [136] M. Hermanns, S. Trebst and A. Rosch, *Spin-Peierls instability of three-dimensional spin liquids with Majorana fermi surfaces*, Phys. Rev. Lett. **115**, 177205 (2015).
- [137] Á. Antal, T. Fehér, A. Jánossy, E. Tátrai-Szekeres and F. Fülöp, *Spin diffusion and magnetic eigenoscillations confined to single molecular layers in the organic conductors  $\kappa$ -(BEDT-TTF) $_2$ Cu[N(CN) $_2$ ]X (X=Cl, Br)*, Phys. Rev. Lett. **102**, 086404 (2009).
- [138] R. S. Manna, S. Hartmann, E. Gati et al., *Low-temperature lattice effects in the spin-liquid candidate  $\kappa$ -(BEDT-TTF) $_2$ Cu $_2$ (CN) $_3$* , Crystals **8**, 87 (2018).

## References

- [139] M. Javaheri Rahim, *High frequency spin dynamics investigation of quantum critical matters by metallic coplanar resonators*, PhD thesis (Universität Stuttgart, 2018).
- [140] M. Abdel-Jawad, I. Terasaki, T. Sasaki et al., *Anomalous dielectric response in the dimer mott insulator  $\kappa$ -(BEDT-TTF)<sub>2</sub>Cu<sub>2</sub>(CN)<sub>3</sub>*, Phys. Rev. B **82**, 125119 (2010).
- [141] E. Gati, J. K. H. Fischer, P. Lunkenheimer et al., *Evidence for electronically driven ferroelectricity in a strongly correlated dimerized BEDT-TTF molecular conductor*, Phys. Rev. Lett. **120**, 247601 (2018).
- [142] S. Flandrois, C. Coulon, P. Delhaes et al., *On the structure and properties of tmttf and tmtsf salts: experimental evidence for the importance of interchain couplings*, Mol. Cryst. Liq. Cryst. **79**, 663 (1982).

# Acknowledgements

Many people contributed to the progress of this work in different areas. I want to thank all of them for the support during my doctoral studies.

First of all, I would like to particularly thank Prof. Dr. Martin Dressel for giving me the opportunity to work in the highly interesting and topical field of quantum spin liquids at his institute. He supported the presented work and the publications through frequent critical discussions and ideas on the topic.

I would like to thank Prof. Dr. Gert Denninger not only for accepting to co-examine this thesis, but also for supporting our ESR laboratory with his expertise and equipment.

I am grateful to Marc Scheffler who welcomed me warmly in his group. He was always open for lively discussions and shared his great expertise on all aspects of microwave spectroscopy.

I want to thank all members of our institute, who spent their time for scientific exchange, particularly to Andrej Pustogow for the vivid support and great ideas while preparing our joint publication.

Sincere thanks are given to our ESR team: Mamoun, Guilherme and Lena who did not only jointly ran the ESR lab and shared the office with me. You were always helpful in any regards, be it scientific, technical or personal. We spent a great time together at work as well as in the evenings.

I am very grateful for our amazing “basement” microwave team: Markus, Nikolaj, Desirée, Alessandro and Mario. You turned into close friends over the last years. You have always been there with an open ear in times of great successes and failures. I look back with joy to our joint time at PI1 and forward to our joint activities still to come. Many thanks to all of you.

Finally and most importantly I want to thank my beloved wife April. You have always been there with moral support, and advice, and patience. Without you the presented work and this thesis would not have been possible to complete.

# Erklärung

Die eingereichte Dissertation zum Thema „Electron Spin Resonance Investigations on Organic Spin Liquid Compounds“ stellt meine eigenständig erbrachte Leistung dar.

Ich habe ausschließlich die angegebenen Quellen und Hilfsmittel benutzt. Wörtlich oder inhaltlich aus anderen Werken übernommene Angaben habe ich als solche kenntlich gemacht.

Die Richtigkeit der hier getätigten Angaben bestätige ich und versichere, nach bestem Wissen die Wahrheit erklärt zu haben.

Stuttgart, den 31. Januar 2022

Björn Miksch